

## ABSTRACT

Title of Dissertation: QUASI-STATIC CHARACTERIZATION AND MODELING OF THE BENDING BEHAVIOR OF SINGLE CRYSTAL GALFENOL FOR MAGNETOSTRICTIVE SENSORS AND ACTUATORS

Supratik Datta, Doctor of Philosophy, 2009

Dissertation Directed By: Professor Alison B. Flatau,  
Department of Aerospace Engineering

Iron-gallium alloys (Galfenol) are structural magnetostrictive materials that exhibit high free-strain at low magnetic fields, high stress-sensitivity and useful thermo-mechanical properties. Galfenol, like smart materials in general, is attractive for use as a dynamic actuator and/or sensor material and can hence find use in active shape and vibration control, real-time structural health monitoring and energy harvesting applications. Galfenol possesses significantly higher yield strength and greater ductility than most smart materials, which are generally limited to use under compressive loads. The unique structural attributes of Galfenol introduce opportunities for use of a smart material in applications that involve tension, bending, shear or torsion. A principal motivation for the research presented in this dissertation is that bending and shear loads lead to development of non-uniform stress and magnetic fields in Galfenol which introduce significantly more complexity to the considerations to be modeled, compared to modeling of purely axial loads.

This dissertation investigates the magnetostrictive response of Galfenol under different stress and magnetic field conditions which is essential for understanding and modeling Galfenol's behavior under bending, shear or torsion. Experimental data are used to calculate actuator and sensor figures of merit which can aid in design of adaptive structures. The research focuses on the bending behavior of Galfenol alloys as well as of laminated composites having Galfenol attached to other structural materials. A four-point bending test under magnetic field is designed, built and conducted on a Galfenol beam to understand its performance as a bending sensor. An extensive experimental study is conducted on Galfenol-Aluminum laminated composites to evaluate the effect of magnetic field, bending moment and Galfenol-Aluminum thickness ratio on actuation and sensing performance.

A generalized recursive algorithm is presented for non-linear modeling of smart structures. This approach is used to develop a magnetomechanical plate model (MMPM) for laminated magnetostrictive composites. Both the actuation and sensing behavior of laminated magnetostrictive composites as predicted by the MMPM are compared with results from existing models and also with experimental data obtained from this research. It is shown that the MMPM predictions are able to capture the non-linear magnetomechanical behavior as well as the structural couplings in the composites. Model simulations are used to predict optimal actuator and sensor design criteria. A parameter is introduced to demarcate deformation regimes dominated by extension and bending. The MMPM results offer significant improvement over existing model predictions by better capturing the physics of the magnetomechanical coupled behavior.

QUASI-STATIC CHARACTERIZATION AND MODELING OF THE BENDING  
BEHAVIOR OF SINGLE CRYSTAL GALFENOL FOR MAGNETOSTRICTIVE  
SENSORS AND ACTUATORS

By

Supratik Datta

Dissertation submitted to the Faculty of the Graduate School of the  
University of Maryland, College Park, in partial fulfillment  
of the requirements for the degree of  
Doctor of Philosophy  
2009

Advisory Committee:  
Professor Alison B. Flatau, Chair/Advisor  
Professor Abhijit Dasgupta  
Professor Sung Lee  
Professor Norman M. Wereley  
Professor Manfred Wuttig

© Copyright by  
Supratik Datta  
2009

To the memory of my late grandfather

Pravash Chandra Dutta

## Acknowledgements

First and foremost, I would like to thank my advisor Dr. Alison Flatau for her unwavering support at all times that helped me to meet several challenges in graduate school. I am thankful to her for her confidence in me and for allowing me to pursue several ideas in the past six years, some of which helped me towards my PhD dissertation. She has been an excellent mentor who took active initiative in my professional development as an independent researcher. She always encouraged me to interact and collaborate with peers and facilitated interactions with them at many occasions. Her guidance on public speaking helped me win accolades at many conferences. Most importantly, I would like to thank her for being such a nice human being and teaching me how to remain calm and keep a smile on your face no matter how difficult a situation you are in.

I would like to thank all my committee members, Dr. Wereley, Dr. Wuttig, Dr. Dasgupta and Dr. Lee, for their thoughtful suggestions during the oral exam and pre-defense. I was particularly influenced by Dr. Wereley's class on composites and ended up using a significant amount of the knowledge gained in that course in this dissertation. I would especially like to thank Dr. Wuttig for taking time out often to interact with me and for introducing me to the intriguing world of material science. It was a pleasure attending his classes on smart materials and kinetics. I am also thankful to Dr. Dasgupta for helping me to develop an appreciation of application of mathematical principles in unifying different engineering areas through his course on energy methods. The opportunity to discuss my work with him at "College Perk" completely changed my way of thinking about modeling smart materials. I would like

to thank Dr. Inderjit Chopra whose course on smart structures taught me several useful modeling techniques that I have used in this work. I would also like to thank Dr. Mary Bowden for recommending me for the Wylie dissertation fellowship.

I would like to acknowledge the financial support from ETREMA Products Inc. under contract number 05C0165 and the US Office of Naval Research under MURI contract number N000140610530. I would also like to thank Dr. Jon Snodgrass, Dr. Julie Slaughter and Eric Summers from ETREMA and Dr. Arthur Clark, Dr. James Restorff and Marilyn Wun-Fogle from NSWC Carderock for stimulating discussions and for providing me with valuable resources for my research. I would also like to acknowledge the encouragement that I received from Dr. Thomas Lograsso of Materials Preparation Center, Ames, during our occasional meetings at workshops and conferences. I am also thankful to Late Dr. William Armstrong for his criticism of my early work which motivated me to develop the coupled model discussed in this dissertation.

I would like to thank Pat Baker, Becky Sarni, Debora Chandler, Julia John, Rita Woodell, LaVita Williams, Peter Alexander, Otto Fandino, Kevin Lewy and all other staff members in the Aerospace Engineering Department for making my stay at the University of Maryland a wonderful experience. I would particularly like to thank Rosalia for encouraging me to apply for the AIAA graduate award. Special thanks to Howard Grosenbacher at the Engineering machine shop and David Cogswell at the Physics machine shop for helping me with the fabrication of my experimental setup and for sharing their insights which helped me to learn a great deal. Dr. Phil Piccoli deserves a special mention for helping me with composition analysis using EDS and

WDS. I would also like to thank a number of people in the Manufacturing Building who have helped me in designing and conducting experiments. Dr. V. K. Pavlin, Dr. Y. T. Choi, Dr. Jin-Hyeong Yoo, Dr. Suok-Min Na and Dr. Wei Hu have been of great help at many a times. Dr. Patrick Downey and Dr. Anirban Chaudhuri have been of immense help in teaching me a number of things in the lab and for always coming up with useful suggestions and advice. I particularly need to thank Kunal Kothari for sharing his design insights on the four-point bending test fixture. I would also like to thank Luke Twarek, Mark Staley, Sarah Haack, Baran Sahin, Marie Schroeder and Frank Graham for helping me at different times during the period of my graduate studies.

I need to specially mention two of my colleagues, Dr. Jayasimha Atulasimha and Chaitanya Mudivarthi. Atul has been an excellent mentor and Chaitanya has been the best office-mate. The honest feedback and friendly advice that I received from them deeply influenced my work. Thanks to both of you for being such great friends. I would also like to thank my personal friends Subhamoy, Anyesha, Ayush, Theron and Indrajit, for all their help and personal advice which made my stay at Maryland a memorable experience.

I must thank my parents for inculcating in me the urge for advanced education at a tender age which finally motivated me to pursue a doctoral degree. I am particularly indebted to my father for supporting my decision to join graduate school and for instilling in me the belief that I should do my best and leave the rest to God. This belief helped me to overcome many uncertain times that I faced in the past six years.

Finally, I would like to thank my wife Ritaja for making my home and making me the person that I am today. She is the sweetest thing I found in grad school but I must confess that I haven't been able to return her unconditional love because of my pre-occupation with research. I hope she forgives me for that knowing that I could not have completed this journey without her hand in my hand.

# Table of Contents

<b>Acknowledgements .....</b>	<b>iii</b>
<b>Table of Contents .....</b>	<b>vii</b>
<b>Chapter 1: Introduction .....</b>	<b>1</b>
1.1. Smart structures .....	2
1.1.1. Applications of smart structures .....	3
1.1.2. Role of smart materials .....	4
1.2. Overview of smart materials .....	6
1.2.1. Introduction to ferroic materials .....	7
1.2.2. A unified view of ferroic materials .....	14
1.3. Physics of ferromagnetism.....	16
1.3.1. Fundamental magnetic quantities .....	17
1.3.2. Demagnetization and its significance .....	21
1.3.3. Electromagnetism and magnetic circuit.....	23
1.3.4. Maxwell's equations and their significance.....	26
1.3.5. Classification of magnetic materials .....	28
1.3.6. Magnetism at the atomic scale.....	30
1.3.7. Magnetic domains and process of magnetization .....	33
1.4. Phenomenon of magnetostriction .....	40
1.4.1. Magnetoelastic effects .....	41
1.4.2. Fundamental relations in magnetostriction.....	43
1.4.3. Magnetostrictive actuation and sensing .....	46
1.4.4. History of the development of magnetostrictive materials .....	50
1.5. Iron-gallium alloys (Galfenol) .....	53
1.5.1. Metallurgy of Fe-Ga alloys .....	53
1.5.2. Magnetostriction and other properties of Fe-Ga alloys .....	57
1.5.3. Processing of Fe-Ga alloys .....	61
1.5.4. Applications of Fe-Ga alloys .....	63
1.6. Overview of magnetomechanical models .....	65
1.6.1. Constitutive material models .....	65
1.6.2. Device-level models.....	71
1.7. Objectives and organization of the dissertation .....	72
<b>Chapter 2: Experimental studies and model simulations of actuator and sensor figures of merit .....</b>	<b>75</b>
2.1. Background and scope of this work.....	75
2.2. Experiment.....	76
2.2.1. Sample description.....	77
2.2.2. Description of transducer.....	78
2.2.3. Instrumentation .....	79
2.2.4. Actuator characterization under constant stress.....	81
2.2.5. Sensor characterization under constant magnetic field.....	82

2.3.	Energy-based non-linear constitutive magnetomechanical model .....	87
2.3.1.	Energy formulation .....	87
2.3.2.	Modeling of constitutive behavior .....	90
2.4.	Model validation .....	94
2.4.1.	Model fitting of actuator behavior .....	94
2.4.2.	Model prediction of sensor behavior .....	100
2.4.3.	Error estimation .....	105
2.5.	Evaluation of stress and magnetic field-dependent material properties ...	106
2.5.1.	Experimental method .....	107
2.5.2.	Model simulations .....	107
2.5.3.	Magnetomechanical properties .....	108
2.5.4.	Discussion on the trend in material properties .....	113
2.6.	Energy density .....	116
2.7.	Magnetomechanical coupling factor .....	120
2.8.	Gage factor .....	126
2.9.	Evaluation of clamped material properties .....	130
2.9.1.	Young's modulus at constant magnetic induction .....	130
2.9.2.	Permeability at constant strain .....	134
2.10.	Summary .....	136
<b>Chapter 3: Experimental studies on Galfenol beam as a sensor in bending .....</b>		<b>140</b>
3.1.	Classical beam theory .....	140
3.2.	Motivation and scope of this work .....	143
3.3.	Design of experiment .....	146
3.3.1.	Mechanical components .....	146
3.3.2.	Magnetic components .....	149
3.4.	Magnetomechanical four-point bending test .....	153
3.4.1.	Sample description .....	153
3.4.2.	Test procedure .....	154
3.5.	Results and discussion .....	155
3.5.1.	Sensor characterization in bending .....	156
3.5.2.	Discussion on experimental trends .....	158
3.6.	Summary .....	161
<b>Chapter 4: Experimental studies on laminated Galfenol-Aluminum composite .....</b>		<b>163</b>
4.1.	Classical laminated beam theory with induced-strain actuation .....	164
4.2.	Motivation and scope of this work .....	167
4.3.	Description of experiment .....	168
4.3.1.	Description and characterization of Galfenol lamina .....	168
4.3.2.	Choice of thickness of Aluminum laminae .....	171
4.3.3.	Description of no-load actuator characterization .....	172
4.3.4.	Description of pre-load actuator characterization .....	174
4.3.5.	Description of sensor characterization .....	177
4.4.	Magnetic analysis of test setup .....	179
4.4.1.	Estimation of magnetic flux variation .....	179

4.4.2.	Estimation of demagnetization .....	185
4.5.	Mechanical analysis of test setup.....	187
4.5.1.	Effect of free strain .....	189
4.5.2.	Effect of free strain and bending load.....	192
4.6.	Actuator characterization results.....	194
4.6.1.	Effect of laminate thickness under no-load condition .....	195
4.6.2.	Effect of bending loads in absence of magnetic field.....	201
4.6.3.	Effect of bending loads in presence of magnetic field.....	205
4.7.	Sensor characterization results.....	211
4.7.1.	Self-consistency in sensor data .....	212
4.7.2.	Effect of bias magnetic fields .....	214
4.7.3.	Analysis of sensor parameters .....	217
4.8.	Summary .....	223
<b>Chapter 5: Modeling of magnetostrictive laminated composite.....</b>		<b>225</b>
5.1.	Background and scope of this work.....	226
5.2.	Model formulation .....	228
5.2.1.	Magnetostrictive device modeling approach .....	229
5.2.2.	Energy-based constitutive magnetostrictive model .....	233
5.2.3.	Classical laminated plate theory .....	235
5.2.4.	Lumped parameter magnetic model.....	240
5.2.5.	Algorithm of Magnetomechanical Plate Model.....	242
5.3.	Model simulation results.....	245
5.3.1.	Comparison with existing models.....	246
5.3.2.	Effect of actuating magnetic field and pre-load.....	249
5.3.3.	Effect of laminate thickness and stiffness.....	258
5.3.4.	Effect of applied force and bias magnetic field .....	268
5.3.5.	Comparison of experimental data and model prediction .....	271
5.4.	Summary and conclusions .....	277
<b>Chapter 6: Conclusions .....</b>		<b>280</b>
6.1.	Summary of research .....	280
6.2.	Contributions of this research .....	284
6.3.	Recommendations and future work .....	287
<b>References.....</b>		<b>292</b>

## Chapter 1: Introduction

This dissertation explores the possibilities of using iron-gallium alloys as an active material in smart structures. These alloys, which are also known by the name of Galfenol, offer a combination of structural and magnetostrictive properties which can be utilized in novel devices. The design of such devices would require an in-depth knowledge of the material's response to mechanical and magnetic forces as well as its nature of interaction with other materials in a smart device. These factors are investigated in this work using both experimental techniques and physics-based modeling tools.

The introduction attempts to provide sufficient background to the reader to aid in appreciation and comprehension of the contributions of this dissertation. The following sections will introduce the concept of smart structures and their applications and also provide an overview of commonly used smart materials. A discussion on the relative merits and demerits of smart materials will be used to motivate the study of magnetostrictive materials. This overview will be followed by a deeper discussion of the physics of magnetism and magnetostriction. A brief history of magnetostrictive materials and the state of the art in research related to iron-gallium alloys will be presented. An introduction to modeling techniques using active materials in smart devices will also be presented. Finally the motivation, objectives and organization of this dissertation will be stated.

1.1. Smart structures

A “smart structure,” also known as adaptive or intelligent structure, is a name given to a system which can perform an operation as a response to a stimulus. The classic example of such a smart system is the human body. For example, when we touch a hot object, the skin senses the temperature and this information is transmitted to the brain by nerves. The brain processes this information and sends a signal to the muscles to actuate and remove our hand from the hot object. A smart structure comprises of a sensor (skin), actuator (muscle), controller (brain) and information flow channels (nerve).

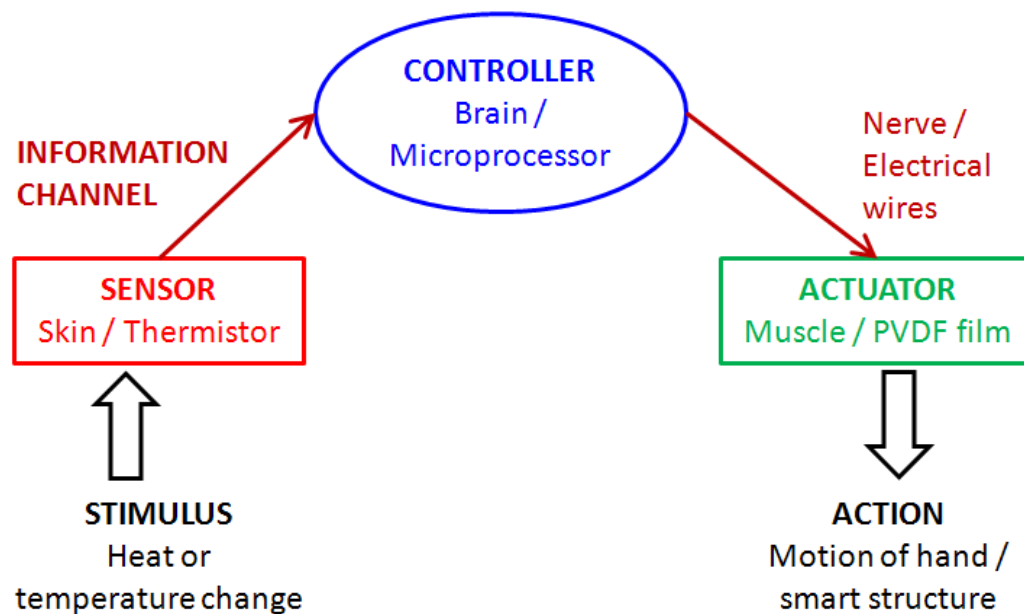


**Figure 1.1. Flow diagram of a smart system’s response to temperature.**

Figure 1.1 shows the flow of information in such a smart system where an artificial intelligent system can be created using engineered materials which will respond to temperature changes in the same way as a biological organism.

In most present day smart structures, the controller is usually a single microprocessor or an appropriate electronic circuit with electrical conductors serving

as information flow channels. The controller receives the information from a sensor, processes it and sends an appropriate signal to an actuator which performs the desired action.

Smart structures are used in several applications as they offer a number of advantages over conventional systems. Mechanical, pneumatic and hydraulic power-based technology can be bulky and may have limitations on the dynamic conditions at which they can be operated. Moreover, these conventional techniques may also require several mechanical components which can act as sources of significant noise and power loss and also create reliability issues due to wear and tear. On the other hand, smart structures can reduce weight which in turn can cut cost and power requirements. Additionally, the tunable nature and faster response time of smart structures enable them to be operated not only at different dynamic conditions but also over a larger bandwidth than most conventional devices.

#### 1.1.1. Applications of smart structures

Smart structure technology has been broadly used [1, 2] for active damping or vibration control, active shape control, stroke amplification, damage detection or structural health monitoring and energy harvesting. Several applications in the area of aerospace and automotive industries use smart structures.

Both fixed wing aircraft and rotorcraft applications have used concepts such as smart wing [3, 4] and smart rotor [4] respectively. The ideas behind a smart rotor [1] include actuation and control of leading/trailing edge flap angle (Figure 1.2), blade twist/camber and blade tip position. Such concepts could be used to mitigate the effects of flutter and blade-vortex interaction and thereby enhance flight safety.

Furthermore, structural health monitoring [5] and self-healing techniques [6] can be used to address problems related to fatigue. Other applications in the aerospace industry can be for morphing wings [7-9], synthetic jet actuators [10] and swash-plate-less active pitch links [11].

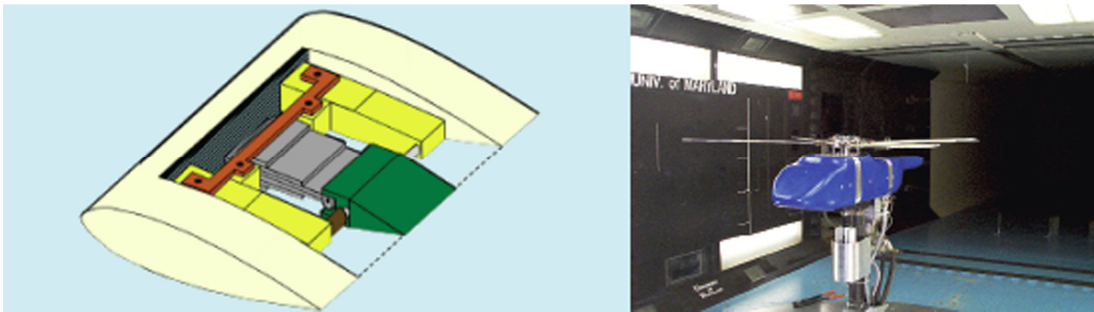


**Figure 1.2. Smart structure application in rotorcrafts. Rotor model with trailing edge flaps actuated with piezobimorphs.**

**Source: <http://www.agrc.umd.edu/research/smart-structures.html>**

Some of the possible areas of using smart structures in automotive applications [12] can be in active suspension systems to improve ride, minimize vibration and noise in engine mounts, improve performance of pumps and valves, shock absorbers, dampers and large energy-absorbing bumpers for improved crashworthiness. Some of the specific applications may include controlling the stiffness of seat belt and use of information from an accelerometer to deploy air bags in the event of an accident.

#### 1.1.2. Role of smart materials

Smart structures use smart or active materials as sensors and actuators. Active materials can transduce one form of energy to another. For example, a piezoelectric material can convert electrical energy to mechanical energy by deforming itself when

subjected to an electric field and thereby working as an actuator. On the other hand it can also convert mechanical energy to electrical energy by creating an electric field when subjected to pressure. The capability of energy transduction in active materials makes them different from a passive device such as a hydraulic press which only transmits (not transduce) mechanical energy through a fluid thereby producing a mechanical advantage.

Although both sensing and actuation requires active materials, the requirements of desirable sensor [13] can be slightly different from that of an actuator as summarized in Table 1.1. Some of the common desirable characteristics for sensor and actuator materials are small size, low specific weight, low cost, high bandwidth, linearity, low hysteresis, low sensitivity to temperature or other factors which can interfere with the desired operation, structural integrity (not brittle) and minimum associated electronics.

**Table 1.1. Desirable characteristics of actuators and sensors.**

<b>Actuator</b>	<b>Sensor</b>
Large stroke	High sensitivity
Large blocked force	Large range
High stiffness	High resolution
High coupling factor	Low drift
Impedance matching	High accuracy and precision

In order to understand the behavior of smart materials and deploy them in smart structures, it is important to understand the physics of these materials. Such understanding can contribute in better materials processing and development of

accurate modeling techniques for predicting and controlling the response of these active materials. Some of the roadblocks for development of smart structures have been manufacturing cost of smart materials, operational reliability and structural integrity at extreme environments. A better understanding of the physics of these materials along with extensive characterization for evaluating material properties and development of appropriate modeling techniques and control algorithms could pave the way for design of advanced smart structures.

### *1.2. Overview of smart materials*

Smart materials are either naturally available elements and compounds or engineered alloys and compounds which transduce one form of energy to another. The energy transduction is manifested as a change in shape and physical properties of the materials when they are exposed to an external energy field which produces a change in their atomic arrangement. Such changes in shape and properties of the material are used in actuator and sensor applications. Table 1.2 shows the different effects related to energy transduction between electrical, magnetic, mechanical and thermal fields.

This section will present some of the commonly used smart materials and discuss more common areas of application. Section 1.2.1 will discuss the more widely used smart materials such as piezoelectric, magnetostrictive and shape memory alloy (SMA). These materials are grouped together due to certain common physical and functional characteristics shared by them which will be discussed in Section 1.2.2. Information on other active materials, such as electro-rheological (ER) and magneto-

rheological (MR) fluids which are used in vibration dampers and fiber optics which are used as optical sensors, can be obtained in Ref. [1].

**Table 1.2. Effects related to change of one form of energy to another. The input and output/stored energy are listed along the rows and columns respectively.**

	<b>Mechanical</b>	<b>Magnetic</b>	<b>Thermal</b>	<b>Electrical</b>
<b>Mechanical</b>	Elastic, Plasticity, Pseudoelastic	Magnetostrictive	Friction	Piezoresistive, Piezoelectric, Electrostrictive
<b>Magnetic</b>	Magnetostrictive, Ferromagnetic shape memory, Magneto- rheological effect	Magnetization	Magnetocaloric effect	Magneto-resistance, Hall-effect, Electromagnetic induction
<b>Thermal</b>	Thermal expansion, Shape memory effect	Paramagnetic- ferromagnetic phase transformation	Temperature change	Seebeck and Peltier effects
<b>Electrical</b>	Piezoelectric, Electrostrictive, Electro- rheological effect	Electromagnetic induction	Joule heating, Seebeck and Peltier effects, Pyroelectric	Polarization

### 1.2.1. Introduction to ferroic materials

The most commonly used active materials are the ones which show piezoelectric effect. Piezoelectric literally means pressure induced electricity which

refers to the fact that these materials exhibit an electrical polarity when subjected to mechanical stress. This direct effect is used for sensing purposes. An inverse effect describes a strain in these materials under the influence of an electric field which is used for actuation purposes. Piezoelectric materials can be ferroelectric (e.g. BaTiO<sub>3</sub>) or antiferroelectric (e.g. PbZrO<sub>3</sub>). Piezoelectricity is also exhibited by materials which are not ferroelectric (e.g. quartz) and can also be engineered in materials (e.g. PZT). The polarization can be reversed in a ferroelectric material which may not be the case in all piezoelectric materials. Piezoelectric materials need to be poled by applying a very high electric field along a particular direction in order to preferentially align the polarization along that direction. This helps in obtaining linear, reversible and bi-directional strains from the material when it is subjected to moderate variations in electric field. Piezoelectricity develops as a result of non-centrosymmetric crystal structure which induces a spontaneous polarization in the crystal below the Curie temperature. The electromechanical coupling in these materials causes the distortion of the crystal from a cubic to a tetragonal shape which manifests as increasing strain with increasing polarization.

Piezoelectric materials are used in a variety of actuator and sensor applications [1, 2]. They are widely used in several transducers like accelerometers, load cells and pressure sensors. Engineered piezoelectric transducers such as RAINBOW and THUNDER are used in valves, linear motors, configurable mirrors and synthetic jet actuators. Other aerospace applications include active control of twist and flap in rotor blades and development of configurable airfoils. Piezoelectric

stacks are also used in ultrasonic motors, sonars and for nano-positioning in AFM and STM stages.

Piezoelectric materials offer several advantages such as large blocked stress (~ 50 MPa) and free strain (~ 1000  $\mu\epsilon$ ), fast response as they are activated by electric field (voltage) with an operational bandwidth of upto 20 MHz and low impedance at high frequencies. These materials also exhibit certain restriction in their capabilities at high stresses (~ 500 MPa) at which they can get depoled and fractured. Depoling also takes place above Curie temperature. Another problem is the capacitive nature of the electrical behavior of these materials due to which they offer high impedance and drift in electrical signal at low frequencies. Moreover, the large hysteresis manifests as significant self-heating at high frequencies.

Certain polymers (e.g. PVDF) also exhibit piezoelectricity due to an inherent polarity developed in the polymer chain. Such piezo-polymers can be used to make flexible smart fabrics for energy harvesting [14, 15], pressure sensor [12] and tactile sensor for posture recognition in vehicle seats [12].

A different type of electromechanically coupled material known as relaxor ferroelectrics or electrostrictives do not exhibit spontaneous polarization and hence show negligible hysteresis and low self-heating in dynamic applications which is extremely important for devices such as deformable mirrors [16] and pumps [17]. These materials show uni-directional strain i.e. the strain is always positive irrespective of the direction of applied electric field although the polarization is induced in the same direction as that of the electric field. Electrostrictive materials like PMN-PT (Lead Magnesium Niobate-Lead Titanate) exhibit about 1000  $\mu\epsilon$  but

require very high electric field (voltage) and are brittle and extremely sensitive to temperature which restricts them from being used in harsh environments. Due to the absence of a spontaneous polarization, electrostrictives can be used as a sensor only in the presence of a bias electric field.

Magnetostrictive materials, which are the primary focus of this dissertation, function like electrostrictive materials except that they are actuated by magnetic field instead of electric field. All ferromagnetic materials and some anti-ferromagnetic and ferrimagnetic materials exhibit magnetostriction. Magnetostrictive effect develops due to the reorientation of magnetization by both magnetic field and stress and hence is also known as magnetomechanical or magnetoelastic effect. The phenomena will be explained in greater depth in Sections 1.3 and 1.4.

Magnetostrictive materials are used in a variety of applications [2] such as sonar, ultrasonic shaker, position controller for machine tool head, linear motor, torque sensor [18-23] acoustic devices and magnetic field sensor [24]. A number of works have shown use of magnetostrictive materials in hydrophone [25], linear position sensor [26] and non-contact position [27], strain [28] and stress [29] sensors. Magnetostrictive materials have also been used in conjunction with piezoelectric materials in hybrid tonpilz transducers [30, 31] and in other devices such as inchworm actuator [32] and rotational motor [33]. Use of magnetostrictive particulate composites has been proposed [34] for micro-positioners, vibration dampers and platform stabilizers. Magnetostrictive thin films are being used for monitoring biomechanical movements [35] and in micro-actuators [36], micro-biosensors [37] and several other MEMS applications [38]. A schematic of a wireless

magnetostrictive biosensor is shown in Figure 1.3. Magnetostrictive powered trailing edge [39] in smart wings has shown promise to reduce drag and save fuel in aircrafts. A review of the application in actuators and comparison of their performance with piezoelectric actuators can be found in Ref. [36]. A review of sensing applications of magnetostrictive materials can be found in Refs. [40-42].

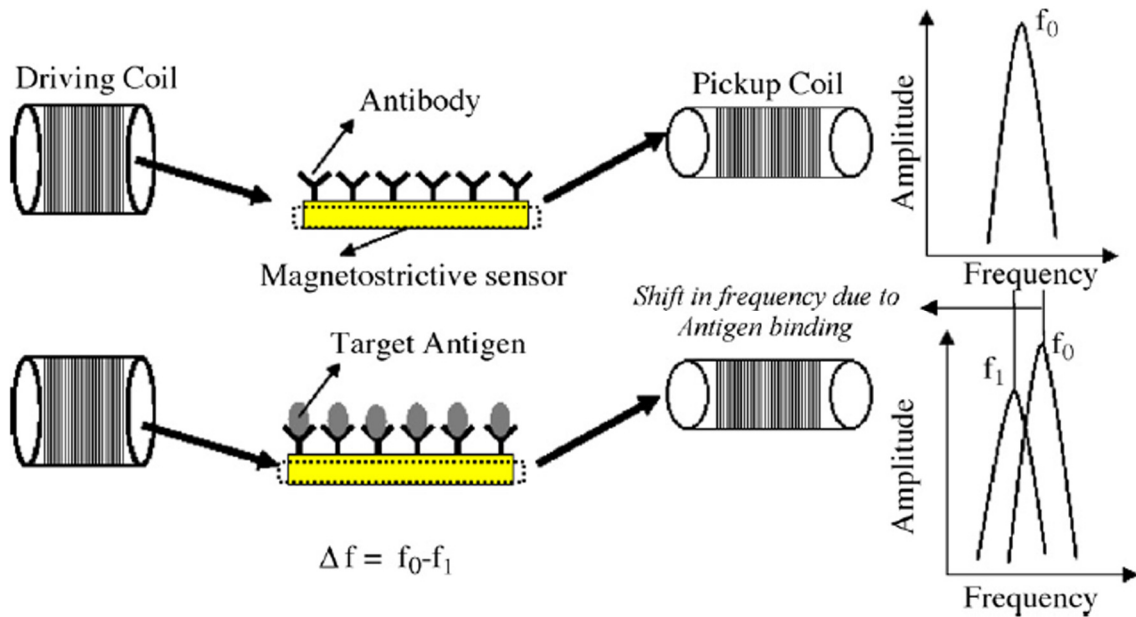


**Figure 1.3. Schematic of a wireless magnetostrictive biosensor. A shift in the resonance of the device takes place when bacterial cells get attached to it. The resonance shift can be observed in the pick-up coil signal [37].**

Magnetostrictive materials such as Terfenol-D show high strain and blocked stress. In general, all magnetostrictives show fast response as magnetic field can be controlled by changing current which can be changed as fast as electric field. Unlike piezoelectric, these materials can be used under static and low frequency conditions with very low impedance but they offer high impedance at high frequencies (kHz range) due to the inductive nature of the materials. Another problem at high

frequency is related to formation of eddy current in the material which prevents excitation of the core of the material. Such problems can be overcome by using laminated materials. Most magnetostrictive materials have higher Curie temperature than piezoelectric materials as shown in Table 1.3 and hence can be operated at higher temperatures. Moreover, these materials do not need to be poled and hence there is no limitation in applying stress which can cause depoling. The small hysteresis shown by these materials translates to negligible self-heating, and the need for less complicated control algorithms for actuation and precise sensing output. Some of the challenges of using magnetostrictive materials are related to flux leakage and demagnetization effects which demands efficient design of transducer magnetic circuit.

Another class of smart material which exhibit large strains due to twin boundary motion is known as ferroelastic material. These materials can respond to stress (pseudo-elasticity), temperature (shape memory alloys - SMA) or magnetic field (ferromagnetic shape memory alloys - FSMA).

Traditional SMA such as Nitinol ( $\text{Ni}_{55}\text{Ti}_{45}$ ) exists in a low temperature martensite phase and a high temperature austenite phase which can be reversibly obtained by cycling temperature. This is known as the two-way shape memory effect and is used for obtaining strains much larger than that due to simple thermal expansion. This effect can be used for low frequency and large stroke actuation. On the other hand, a material which is in the martensite phase will elongate when pulled but will regain its shape on heating even in the presence of the pulling force. This phenomenon is known as the one-way shape memory effect where the martensitic

phase elongates due to de-twinning but transforms to the austenitic phase on heating and regains its shape. It should be noted that this observation is contrary to thermal expansion. The shape recovery effect is used in applications such as braces, eyeglass frames and antennas. Also, the martensite phase can exhibit large strains at a constant stress due to de-twinning, which can be used in clamps and fasteners. The pseudo or super-elastic effect describes a large change in strain at almost a constant stress which occurs due to stress-induced martensite formation in a material which was originally in the austenite phase. Such materials exhibit almost complete strain recovery even from strains of as high as  $50000 \mu\epsilon$  [1].

The FSMA such as  $\text{Ni}_2\text{MnGa}$  and  $\text{Fe}_{70}\text{Pd}_{30}$  exhibit similarly high strains due to de-twinning. The twin boundary motion is produced by magnetic field. The main advantage of FSMA over traditional SMA is that they can be used for high frequency applications as they are actuated by magnetic field and not temperature. On the other hand most FSMA are brittle and their bandwidth is limited by eddy current formation.

Table 1.3 summarizes the properties of commonly used ferroic smart materials. It can be seen that Galfenol exhibits moderate free strain but has very low power requirements. Moreover, it shows much better structural properties and can be operated at temperatures higher than other materials. These benefits offered by Galfenol have motivated further research in this dissertation, particularly to utilize its structural properties.

**Table 1.3. Properties of ferroic smart materials [1, 43-52].**

<b>Properties</b>	<b>PZT-5H</b>	<b>PVDF</b>	<b>PMN-PT</b>	<b>Terfenol-D</b>	<b>Galfenol</b>	<b>Nitinol</b>
<b>Free strain</b>	1000 $\mu\epsilon$	700 $\mu\epsilon$	1000 $\mu\epsilon$	2000 $\mu\epsilon$	350 $\mu\epsilon$	60,000 $\mu\epsilon$
<b>Actuation field</b>	$5 \times 10^5$ V/m	$10^8$ V/m	$10^6$ V/m	240 kA/m	10 kA/m	100 MPa (depends on temperature)
<b>Young's modulus</b>	69 GPa	2 GPa	14 GPa	48 GPa	65 GPa	27/90 GPa (martensite / austenite)
<b>Tensile strength</b>	76 MPa (Brittle)	43 MPa (Ductile)	30 MPa (Brittle)	28 MPa (Brittle)	515 MPa (Ductile)	750 MPa (Ductile)
<b>Bandwidth</b>	0.1 Hz – 1 MHz	0.1 Hz – 1 MHz	0.1 Hz – 1 MHz	0 – 100 kHz	0 – 1 kHz	0 – 1 Hz
<b>Phase transition or Curie temperature</b>	193 °C	177 °C	166 °C	380 °C	675 °C	40 – 65 °C (martensite to austenite)

### 1.2.2. A unified view of ferroic materials

This section presents a view of the ferroic materials which can be unified based on energy and structural considerations. Although there are fundamental differences between the phenomena of ferroelectricity, ferromagnetism and ferroelasticity, nevertheless a unified view is appreciative of the underlying physics and is helpful for modeling purposes [2]. It is assumed that the reader is familiar with

basic material science and hence some of the terms used in this section are not explained in details. The terms relevant for ferromagnetic materials will be explained in details in Section 1.3 and 1.4.

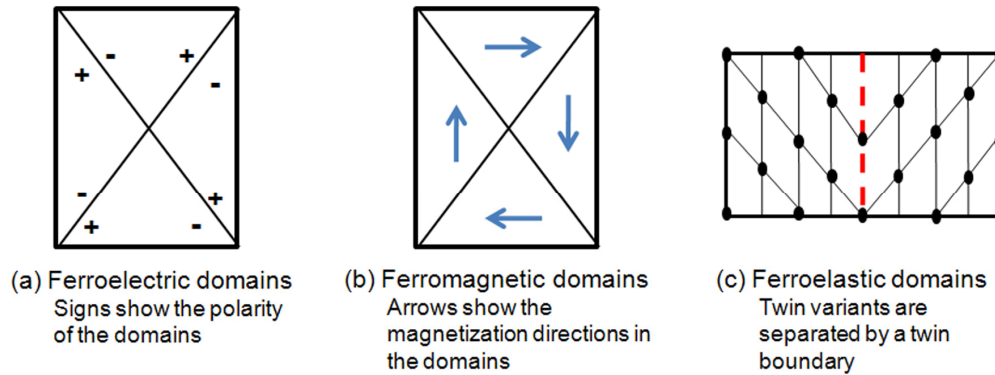


**Figure 1.4. Domains in ferroic materials.**

As shown in Figure 1.4, all three ferroic materials have a fundamental structural unit which is a domain. It can be an electric or magnetic domain or an elastic domain (twin variant). Domains are formed below a critical temperature in order to reduce electrostatic, magnetostatic or elastic energy. The phase transformation at this critical temperature is of an order-disorder type. The high temperature phases, such as paraelectric, paramagnetic and austenite are disordered phases. The low temperature phases, such as ferroelectric, ferromagnetic and martensite are ordered phases. The ordering involves that of electric dipoles, magnetic moments or atoms in the crystal lattice. The domains are characterized by order parameters, such as polarization, magnetization and strain. Adjacent ferroelectric and ferromagnetic domains have polarization and magnetization in different direction respectively. Adjacent ferroelastic domains have different twin variants. The domains are separated by domain walls which form at pinning sites, i.e. at locations of material defects or stress inhomogeneities.

Ferroc materials respond to different fields which change their order parameter. Electric fields change the polarization and also cause electrostriction due to lattice distortion in ferroelectric materials. Magnetic fields change the magnetization and also cause magnetostriction in ferromagnetic materials. Whereas the polarization or magnetization follows the sign (direction) of the electric or magnetic field, the striction is always of the same sign (i.e. either elongation or contraction) in a given material irrespective of the sign of the field. Similarly stress fields can produce pseudo-elastic strains in ferroelastic materials.

Inspite of such similarities, fundamental differences exist between the three types of ferroic materials. Ferroelectric such as  $\text{BaTiO}_3$  and ferroelastic materials exhibit first order phase transition which is marked by a discontinuity in the order parameter at the critical phase transition temperature. Other ferroelectrics such as  $\text{KH}_2\text{PO}_4$  and ferromagnetic materials exhibit a second order phase transition which is evident from the monotonic change in the order parameter with temperature. Albeit, in both cases the order parameter becomes zero beyond the phase transition temperature. Ferroelectric materials have an actual fundamental unit which is an electric charge and hence there can be monopoles but such fundamental units do not exist for ferromagnetic and ferroelastic materials.

### *1.3. Physics of ferromagnetism*

The comparative background provided in the previous section sets the stage to delve in further details of ferromagnetism which will be required to understand the behavior of magnetostrictive materials.

The knowledge of magnetism dates back to the days when Greeks in Magnesia observed that a loadstone ( $\text{Fe}_3\text{O}_4$ ) always points along the same direction. Magnetic theory in materials developed in allusion to the concept of earth's magnetic field which conceptualizes earth as a huge permanent magnet with its magnetic north pole facing nearly towards the geographical south pole and its magnetic south pole facing nearly towards the geographical north pole. Unlike mechanical forces, forces of magnetism are non-contact forces which are manifested in the form of dipoles (known as the north and south poles), where the like poles repel each other and unlike poles attract each other.

In this section, the terms related to the study of magnetism are reviewed and the concept of electromagnetism and its description using the Maxwell's equations is introduced. The origin of magnetism at the atomic scale is explained using a combination of classical physics and introductory quantum physics. Finally, the idea of magnetic domains as a result of energy balance is introduced. The motion of magnetic domains is related to the process of magnetization and magnetostriction.

### 1.3.1. Fundamental magnetic quantities

Hans Christian Oersted (1820) observed that a current carrying conductor produces a magnetic field and attributed it to the motion of charges that constitute an electric current. The "magnetic field strength" ( $H$ ) is defined as the magnetic vector quantity at a point in a magnetic field which measures the ability of electric currents or magnetized bodies to produce magnetic induction at the given point [53]. Magnetic field strength is measured in oersted (cgs) or ampere per meter (SI) where  $1 \text{ Am}^{-1} = 79.57747 \text{ Oe}$ .

The Biot-Savart law (1820) shown in Equation (1.1) which gets its name from Jean-Baptiste Biot and Felix Savart, gives the elemental field  $d\mathbf{H}$  generated at a distance  $r$  from an elemental conductor of length  $d\mathbf{l}$  carrying the current  $i$ .

$$d\mathbf{H} = \frac{id\mathbf{l}}{4\pi r^2} \times \mathbf{r} \quad (1.1)$$

The integral form of the same law shown in Equation (1.2) was developed by Andre Marie Ampere (1820). Here  $\mathbf{H}$  is the magnetic field produced by  $N$  number of current elements with current  $i$  in each of them in a closed circuit of a fixed length.

$$Ni = \oint \mathbf{H} \cdot d\mathbf{l} \quad (1.2)$$

It is possible to find the field generated at the center of an infinitely long solenoid by the simple application of Ampere's Law. The field ( $H$ ) at the center of a long solenoid of length  $l$  having  $N$  turns of a conductor carrying a current  $i$  is given by Equation (1.3) [54].

$$H = \frac{Ni}{l} \quad (1.3)$$

Magnetic force is visualized in the form of imaginary lines known as lines of magnetic flux ( $\Phi$ ). The units of magnetic flux are maxwell (cgs) or weber (SI) where  $1 \text{ Wb} = 10^8 \text{ Mx}$ . These units were named after James Clerk Maxwell and Wilhelm Eduard Weber. The lines of flux are continuous, starting from the north pole and ending in the south pole. These lines can never intersect each other and the tangent to a line of force at a point gives the direction of the magnetic induction. The density of the flux lines determines the strength of the magnetic induction.

The "magnetic induction" or "magnetic flux density" is denoted by ( $\mathbf{B}$ ) and gives a measure of the strength of magnetic flux induced in a material due to the

application of the external magnetic field. Magnetic induction is measured in gauss (cgs) or tesla (SI) where  $1 \text{ T} = 1 \text{ Wbm}^{-2} = 10^4 \text{ G}$ . These units were named after Johann Carl Friedrich Gauss and Nikola Tesla. The magnetic flux through a material of area  $A$  can be related to the magnetic induction using Equation (1.4).

$$\Phi = \mathbf{B} \cdot \mathbf{A} \quad (1.4)$$

The lines of induction always form a closed path, i.e. through any closed surface, the amount of flux entering and leaving are equal. This statement is also known as Gauss's Law [55] and can be expressed by Equation (1.5). Note that the elemental area ( $d\mathbf{A}$ ) is a vector whose direction is normal to the surface.

$$\oint \mathbf{B} \cdot d\mathbf{A} = 0 \quad (1.5)$$

Magnetic induction and magnetic field can be related using the linear constitutive Equation (1.6).

$$\mathbf{B} = \mu \mathbf{H} \quad (1.6)$$

Here  $\mu$  is known as the magnetic permeability of the material. The magnetic permeability of vacuum ( $\mu_o$ ) has a constant value of  $4\pi \times 10^{-7} \text{ Hm}^{-1}$  (SI) or 1 (cgs). The SI unit of permeability is henry per meter and is derived from the concept of inductance which will be introduced in Section 1.3.3. Permeability is a material property and can be a complicated function of magnetic field, stress, material temperature, thermal history, etc. Usually materials are characterized by their relative permeability ( $\mu_r$ ) which is defined by Equation (1.7).

$$\mu_r = \frac{\mu}{\mu_o} \quad (1.7)$$

Another term known as the magnetization ( $\mathbf{M}$ ) of a material indicates the amount of magnetic moment ( $\mathbf{m}$ ) per unit volume, aligned in the material due to an externally applied field  $\mathbf{H}$ . In cgs unit system volume magnetization is denoted by  $4\pi\mathbf{M}$  and is measured in gauss whereas in SI system magnetization is denoted by  $\mathbf{M}$  and is measured in  $\text{Am}^{-1}$ . Hence the total magnetic induction in a material is given by Equations (1.8) or (1.9).

$$\mathbf{B} = \mu_o\mathbf{H} + \mu_o\mathbf{M} \quad \text{in SI system} \quad (1.8)$$

$$\mathbf{B} = \mathbf{H} + 4\pi\mathbf{M} \quad \text{in cgs system} \quad (1.9)$$

Furthermore, magnetization is also related to magnetic field using the linear constitutive Equation (1.10) using a property called magnetic susceptibility ( $\chi_m$ ).

$$\mathbf{M} = \chi_m\mathbf{H} \quad (1.10)$$

Using Equations (1.6) – (1.10), a relationship between permeability and susceptibility can be stated using Equation (1.11).

$$\chi_m = \mu_r - 1 \quad (1.11)$$

Permeability gives a measure of the extent of magnetic flux that will pass through a material when it is kept in a magnetic field. Susceptibility gives a measure of the magnetic moment that will be aligned in the material by the externally applied magnetic field.

The  $B$  (or  $M$ ) vs.  $H$  curve represents the magnetic behavior of a material. These are also known as ‘hysteresis’ plots and were first observed in iron by Warburg (1881) [56] and named such by Ewing (1900) [57] to emphasize on the fact that the  $B$  or  $M$  of the materials lags behind the  $H$  in response. This behavior will be explained in details in Section 1.3.7.

### 1.3.2. Demagnetization and its significance

When a ferromagnetic material of finite size is magnetized by an external magnetic field ( $\mathbf{H}$ ), the free poles which appear on its ends produce a magnetic field directed opposite to the magnetization [58]. This field is called the demagnetizing field ( $\mathbf{H}_d$ ). The demagnetizing field is proportional to the pole strength of the magnetized material and is a function of geometry and can be expressed using Equation (1.12) for a uniformly magnetized material.

$$\mathbf{H}_d = N_d \mathbf{M} \quad (1.12)$$

Here  $N_d$  is a demagnetizing factor which is dependent on the specimen geometry. In the SI system  $N_d$  is dimensionless and can be expressed as a tensor as shown in Equation (1.13) which satisfies the condition  $N_{xx} + N_{yy} + N_{zz} = 1$ .

$$\begin{bmatrix} H_{dx} \\ H_{dy} \\ H_{dz} \end{bmatrix} = \begin{bmatrix} N_{xx} & N_{xy} & N_{xz} \\ N_{yx} & N_{yy} & N_{yz} \\ N_{zx} & N_{zy} & N_{zz} \end{bmatrix} \begin{bmatrix} M_x \\ M_y \\ M_z \end{bmatrix} \quad (1.13)$$

Here  $N_{xx}$  is the demag factor that determines the contribution to the demag field ( $H_{dx}$ ) along the  $x$ -axis due to the magnetization ( $M_x$ ) along the  $x$ -axis.

The phenomenon of demagnetization severely affects measurement of magnetic properties of specimens with finite length as shown in Figure 1.5. A sample of infinite length has  $N_d = 0$  whereas the effect of a smaller length is shown in Figure 1.5 by considering an  $N_d = 0.005$ . A smaller value of susceptibility is obtained for a sample of smaller length.

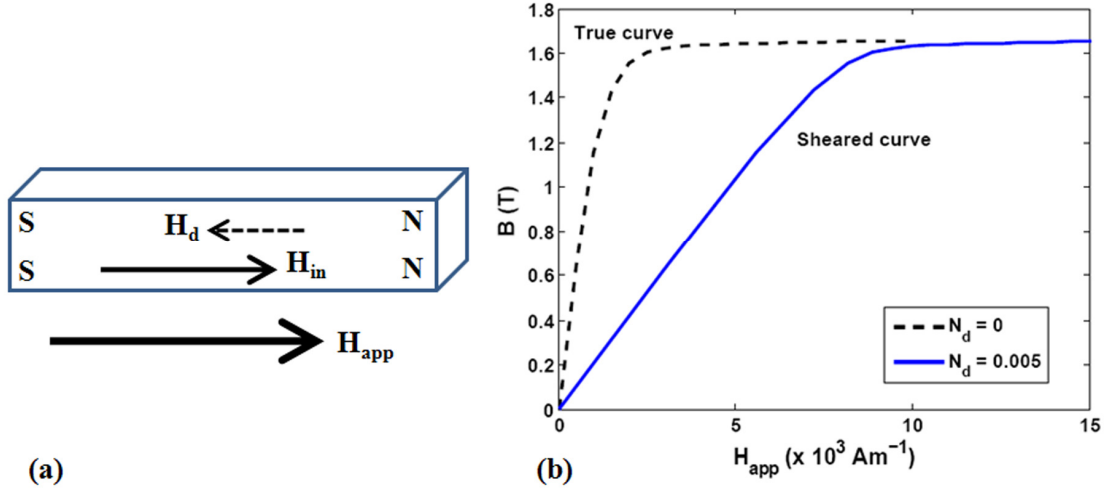


**Figure 1.5. (a) Demagnetization field in a sample of finite length created due to development of magnetic polarities. (b) Effect of demagnetization field on B vs. H curve of the material.**

A scheme of calculation can be used to correct the field inside the sample ( $H_{in}$ ) if the applied field ( $H_{app}$ ), the magnetic flux density ( $B$ ) and demag factor ( $N_d$ ) are known. The internal field can be expressed using Equation (1.14).

$$H_{in} = H_{app} - N_d M \quad (1.14)$$

Replacing  $M$  in Equation (1.14) by using Equation (1.8) with  $H = H_{in}$ , the corrected internal magnetic field can be obtained using Equation (1.15).

$$H_{in} = \frac{H_{app} - \frac{N_d B}{\mu_0}}{1 - N_d} \quad (1.15)$$

The underlying assumption in such correction considers a homogenous magnetic material and applies the correction uniformly across the material. In reality the magnetic properties are not constant across the material.

Analytical formulae for  $N_d$  were initially developed for prolate and oblate ellipsoids [59] and much later for rectangular prisms [60]. The demag factor ( $N_d$ ) is

zero for toroid and along the length of an “infinitely” long cylinder [61].  $N_d$  has been calculated for cylinders based on the aspect ratio ( $l/d$ ). For a sphere or a cube  $N_{xx} = N_{yy} = N_{zz} = 1/3$ . For a thin circular plate having its diameter in the  $x$ - $y$  plane,  $N_{xx} = N_{yy} = 0$  and  $N_{zz} = 1$ . A more generalized approach for finding demag factors for arbitrary particle shape has been developed by Beleggia *et al.* [62].

### 1.3.3. Electromagnetism and magnetic circuit

The concept of demagnetization brings forth the idea of magnetic circuit such that  $N_d = 0$  and 1 correspond to perfectly closed and open circuits respectively. Before presenting the idea of a magnetic circuit analogous to an electric circuit, it is important to be aware of certain postulates of electromagnetism.

The phenomenon of electromagnetic induction can be best described by the laws proposed by Michael Faraday (1831) and Heinrich Lenz (1834). Faraday’s law states that the voltage induced in an electrical circuit is proportional to the rate of change of magnetic flux linking the circuit. Lenz’s law states that this induced voltage is in a direction which opposes the flux change producing it. These laws can be combined as shown in Equation (1.16) [54].

$$V = -N \frac{d\Phi}{dt} \quad (1.16)$$

Here  $V$  is the induced electro-motive force (emf) produced by the flux  $\Phi$  changing at the rate  $d\Phi/dt$  and passing through a coil of  $N$  turns. Equation (1.16) can be written as Equation (1.17) in terms of the cross-section area  $A$  of the coil and flux density  $B$ . The principle of electromagnetic induction is used to measure  $B$  with a pick-up coil.

$$V = -NA \frac{dB}{dt} \quad (1.17)$$

The phenomenon of self-inductance discovered by Joseph Henry (1832), described that a change in the direction of current flowing through a coil sets up an emf so as to oppose the change of the direction of the current. This effect is evident when an alternating current flows through a coil. An inductor stores electrical energy in the form of magnetic energy unlike a resistor which dissipates the electrical energy in the form of heat energy. Self-inductance ( $L$ ) is defined as the ratio of back-emf ( $E_{back}$ ) induced in a coil by a changing current to the rate of change of current ( $di/dt$ ) through coil or total flux linkage per unit current [54] as shown in Equation (1.18).

$$L = \frac{E_{back}}{di/dt} = \frac{N\Phi}{i} = \frac{\mu_r\mu_0 N^2 A}{l} \quad (1.18)$$

Here  $\Phi$  is the flux linkage through a coil of length  $l$  and cross-section area  $A$  having  $N$  number of turns when an electric current  $i$  flows through it. The unit of inductance is henry. Power loss due to inductive impedance can be appreciable at higher frequencies and hence it poses an impediment in the design of dynamic magnetostrictive transducers.

One significance of Ampere's law is that it defines a magneto-motive force (mmf) which is analogous to the emf of an electrical system. Conceptually, a magnetic circuit can be created analogous to the electrical circuit where the magnetic flux ( $\Phi$ ) is equivalent to the electric current, the mmf ( $F_m$ ) is equivalent to the emf and the magnetic reluctance ( $R_m$ ) is equivalent to the electrical resistance. In a form that is analogous to Ohm's law (actually a different form of the Ampere's Circuital Law) [63] the relationship between these quantities can be as expressed as Equation (1.19) where  $F_m = Ni$  and  $R_m = l/\mu A$ . A schematic of a magnetic circuit representation of a system is shown in Figure 1.6.

$$F_m = \Phi R_m \quad (1.19)$$

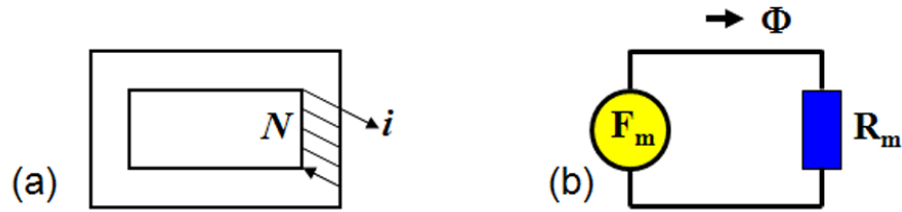


**Figure 1.6. (a) A coil with current  $i$  and  $N$  turns wrapped around a closed ferromagnetic rectangular lamina having permeability  $\mu$ , of perimeter  $l$  and cross-section area of each arm being  $A$ . (b) An equivalent magnetic circuit representation of the scenario shown in (a).**

Another electromagnetic phenomenon which should be introduced is the Hall-effect, named after Edwin Hall (1879). This effect is a manifestation of Lorentz force, postulated by Hendrik Lorentz, and describes that a force ( $F$ ) acts on a charge ( $q$ ) moving with velocity ( $v$ ) in the presence of an electric field ( $E$ ) and magnetic induction ( $B$ ) [54]. The Lorentz force can be calculated from Equation (1.20).

$$F = q[E + (v \times B)] \quad (1.20)$$

The Hall-effect states that when a current carrying conductor is placed in a magnetic field where the magnetic flux lines are perpendicular to the direction of current, a potential difference, known as a Hall voltage ( $V_H$ ), will develop along a direction which is perpendicular to both the direction of current and magnetic flux. This effect arises as the charge carriers are deflected inside the conductor in the presence of a magnetic field thereby developing a polarity which gives rise to the potential difference. The Hall voltage can be calculated from Equation (1.21) where  $i$

is the current,  $B$  is the flux density,  $t$  is the thickness of the conductor,  $n$  is the number of charge carriers and  $e$  is the unit of charge ( $= 1.609 \times 10^{-19}$  coulomb).

$$V_H = -\frac{iB}{tne} \quad (1.21)$$

The Hall-effect is illustrated in Figure 1.7 and its use as a magnetic field sensor will be discussed in Section 1.3.4.

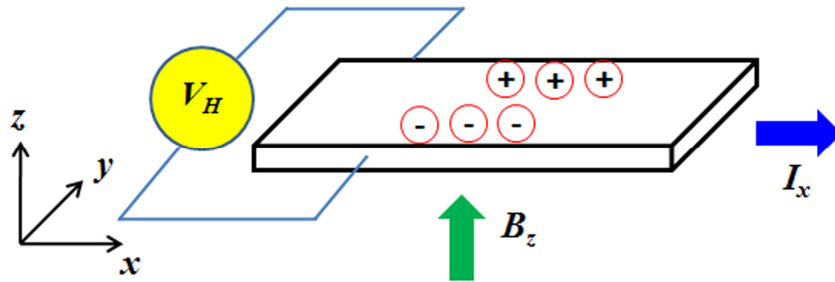


**Figure 1.7. Illustration of Hall-effect showing the development of Hall voltage along  $-y$  due to polarization of the conductor under the combined effect of a magnetic field and electric current along  $+z$  and  $+x$  directions respectively.**

#### 1.3.4. Maxwell's equations and their significance

Equations (1.22) – (1.25) are known as Maxwell's equations which are used in classical physics to describe an electromagnetic field [55].

$$\nabla \times \mathbf{H} = \mathbf{J}_f + \frac{\partial \mathbf{D}}{\partial t} \quad (\text{Ampere's Law}) \quad (1.22)$$

$$\nabla \times \mathbf{E} = -\frac{\partial \mathbf{B}}{\partial t} \quad (\text{Faraday's Law}) \quad (1.23)$$

$$\nabla \cdot \mathbf{B} = 0 \quad (\text{Gauss's Law}) \quad (1.24)$$

$$\nabla \cdot \mathbf{D} = \rho_f \quad (\text{Gauss's Law}) \quad (1.25)$$

Here  $\nabla = \frac{\partial}{\partial x} \hat{i} + \frac{\partial}{\partial y} \hat{j} + \frac{\partial}{\partial z} \hat{k}$  is the gradient operator,  $\mathbf{J}_f$  is the free current density (current per unit area-perpendicular-to-flow due to the motion of free charges, unit:  $\text{Am}^{-2}$ ),  $\mathbf{D}$  is the electric displacement (unit:  $\text{Cm}^{-2}$ ),  $\mathbf{E}$  is the electric field (unit:  $\text{Vm}^{-1}$ ) and  $\rho_f$  is the free charge density (unit:  $\text{Cm}^{-3}$ ). The electric displacement can be related to the electric field using the constitutive Equation (1.26) [55] where  $\mathbf{P}$  is the polarization (unit:  $\text{Cm}^{-2}$ ) of the dielectric material and  $\epsilon$  is the electrical permittivity (unit: farad per meter or  $\text{Fm}^{-1}$ ). Note that  $\epsilon_0 = 8.854 \times 10^{-12} \text{ Fm}^{-1}$  is the permittivity of vacuum.

$$\mathbf{D} = \epsilon_0 \mathbf{E} + \mathbf{P} = \epsilon \mathbf{E} \quad (1.26)$$

The free current density can be expressed by Equation (1.27) [55] where  $\mathbf{v}$  is the velocity of the charge flow.

$$\mathbf{J}_f = \rho_f \mathbf{v} \quad (1.27)$$

Maxwell's equations summarize the relationships between the magnetic and electrical parameters in ferromagnetic conductive media. They also define the boundary conditions across magnetic media as illustrated in Figure 1.8. Since the divergence of  $\mathbf{B}$  is zero, using Gauss' law and divergence theorem we can get Equation (1.28) which shows that the normal component of  $\mathbf{B}$  is continuous across magnetic media. This implies that a pick-up coil can only measure the component of  $\mathbf{B}$  which is normal to its cross-section.

$$\nabla \cdot \mathbf{B} = \mathbf{B}_2 \cdot \hat{n} - \mathbf{B}_1 \cdot \hat{n} = 0 \Rightarrow B_{2n} = B_{1n} \quad (1.28)$$

Similarly, in absence of any surface current and under static (or quasi-static) condition, the curl of  $\mathbf{H}$  is zero. Using Ampere's circuital law and curl theorem we

can get Equation (1.29) which shows that the tangential component of  $\mathbf{H}$  is continuous across the boundary of magnetic media.

$$\nabla \times \mathbf{H} = {}_t H_1 - {}_t H_2 = 0 \Rightarrow {}_t H_1 = {}_t H_2 \quad (1.29)$$

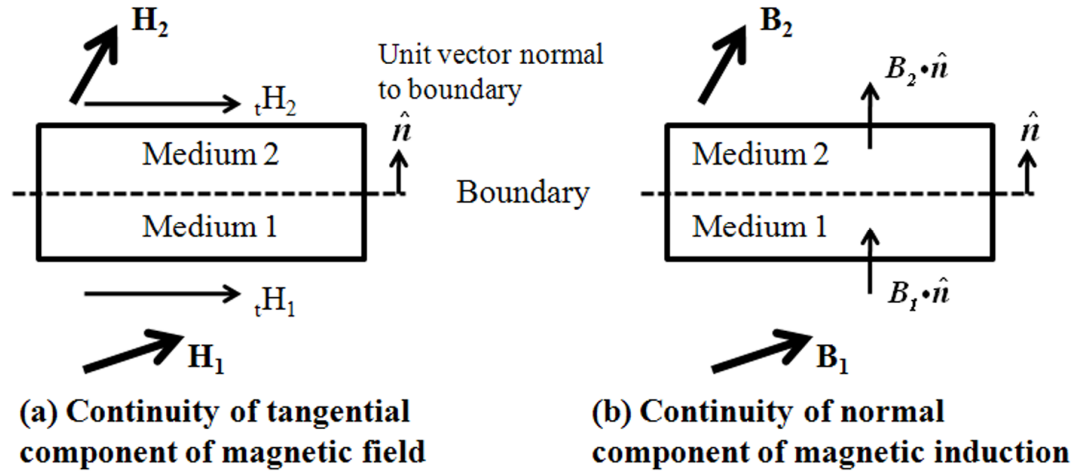


**Figure 1.8. (a) Continuity of tangential component of  $\mathbf{H}$  across the boundary of magnetic media having no surface current. (b) Continuity of normal component of  $\mathbf{B}$  across the boundary of magnetic media.**

This idea can be used to measure the tangential component of  $\mathbf{H}$  at the surface of a ferromagnetic sample. A Hall-effect sensor adhered to the sample's surface can measure the tangential component of  $\mathbf{B}$  in air at the surface. This is same as measuring the tangential component of  $\mathbf{H}$  in air at the surface as the relative permeability of air is unity. Since the tangential components of  $\mathbf{H}$  inside and outside the sample at the boundary are equal, an approximate value of  $\mathbf{H}$  inside the sample can be measured using this idea. This technique will be used in Chapter 2.

### 1.3.5. Classification of magnetic materials

The magnetostrictive effect introduced in Section 1.2.1 was related to ferromagnetic material but in general all materials can be classified into *diamagnetic*,

*paramagnetic* or *ferromagnetic* substances based on their susceptibility or the effect of externally applied magnetic field on the magnetic moments [64]. Diamagnetic substances develop a very weak induction only when an external magnetic field is applied. The induction in the material is in the direction opposite to that of the applied field as these materials have a negative susceptibility ( $\sim 10^{-5}$ ). Paramagnetic substances have magnetic moments which cancel each other's effect in the absence of an external magnetic field due to their random orientation in the bulk material. On applying a magnetic field, such materials develop a small induction in the same direction as the applied field. Paramagnetic materials have susceptibility in the range of  $10^{-5}$  to  $10^{-2}$ .

When paramagnetic substances are cooled below their Curie temperature ( $T_c$ ) the magnetic moments inside them become ordered which can produce a net polarity in these substances even in the absence of an external magnetic field. This phase of the material is known as the ferromagnetic phase. Materials such as iron (BCC  $\alpha$  phase), cobalt, nickel and some rare earth metals which exist in their ferromagnetic phase at room temperature are known as ferromagnetic materials. They can have susceptibility of as high as  $10^6$ . In these materials the value of  $M \gg H$ . The maximum value of  $M$  is known as saturation magnetization ( $M_s$ ) which is obtained when the applied  $H$  is able to align all the magnetic moments in the material in the direction of the applied field. Saturation magnetization can be defined as the product of the magnetic moment of each atom and the number of atoms in the material divided by the volume of the material.

The magnetic moment mentioned here is due to the electron spin and orbital motion of electrons around the nucleus. The reason for development of magnetic moment and their ordering in ferromagnetic materials will be discussed in Sections 1.3.6 and 1.3.7 respectively.

Net magnetism and magnetostriction are also observed in *ferrimagnetic* materials (e.g.  $MFe_2O_4$  where  $M^{2+}$  = metallic ion). This class of materials has an inverse spinel crystal structure where the  $M^{2+}$  ions are situated in the octahedral lattice site and the  $Fe^{3+}$  ions are situated in the octahedral as well as tetrahedral sites. The net magnetic moment arises due to incomplete cancellation of the spin moments of the  $M^{2+}$  and  $Fe^{3+}$  ions.

The coupling of magnetic moments between adjacent ions or atoms can occur in materials other than ferromagnetic materials. In spite of this there might be no net macroscopic magnetic moment if the spins of adjacent atoms or ions are arranged in opposite directions. This phenomenon is called *antiferromagnetism* (e.g.  $MnO$ ).

### 1.3.6. Magnetism at the atomic scale

An obvious question that arises after learning about electromagnetism and magnetic materials is regarding the principle that give rise to magnetism in materials. The existence of magnetism can be attributed to the magnetic moments of electrons in atoms. This section assumes the familiarity of the reader with the Bohr model of an atom and the basic postulates of quantum mechanics [65]. According to the classical model (Bohr model) of an atom, both the orbital angular momentum which can be visualized as revolution of electrons around the nucleus and the spin angular momentum which can be visualized as rotation of electrons about its own axis,

contribute to the magnetic moment. A pictorial representation of the revolving electron based on the Bohr model can be seen in Figure 1.9.

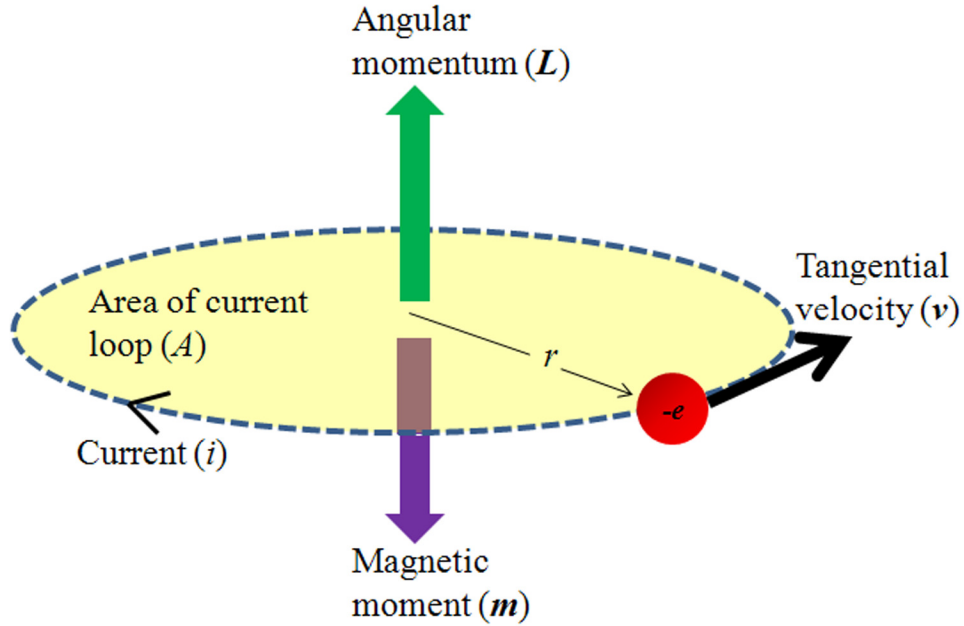


**Figure 1.9. Visualization of an electron in an orbit as a current carrying loop.**

The orbital magnetic moment can be derived as follows. A revolving electron can be visualized as a current loop where the current is given by Equation (1.30). Here  $e$  is the charge on the electron ( $= 1.602 \times 10^{-19}$  C),  $v$  is the orbital speed of the electron and  $r$  is the orbital radius.

$$i = \frac{ev}{2\pi r} \quad (1.30)$$

The magnetic moment ( $m_{orbital}$ ) due to this current loop is given by Equation (1.31).

$$m_{orbital} = iA = \left( \frac{ev}{2\pi r} \right) \pi r^2 = \frac{1}{2} evr \quad (1.31)$$

Equation (1.31) can be written in terms of the orbital angular momentum ( $L$ ) as Equation (1.32) where  $m_e$  ( $= 9.11 \times 10^{-31}$  kg) is the mass of an electron and  $L = m_e vr$ .

$$m_{orbital} = \left( \frac{e}{2m_e} \right) L \quad (1.32)$$

Applying principles of quantum physics,  $L = \sqrt{l(l+1)}\hbar$  where  $\hbar = \frac{h}{2\pi} = 1.05 \times 10^{-34}$  Js and the orbital quantum number  $l = 0, 1, 2, n - 1$ ;  $n$  being the principal quantum number. See Ref. [65] for more background on quantum numbers.

The spin magnetic moment can be derived as follows. The magnetic moment due to electron spin ( $m_{spin}$ ) can be expressed by Equation (1.33) where  $\omega$  is the angular speed of an electron about its own axis.

$$m_{spin} = iA = \left( \frac{e\omega}{2\pi} \right) \pi r^2 = \frac{1}{2} e\omega r^2 \quad (1.33)$$

Equation (1.33) can be written as Equation (1.34) in terms of the spin angular momentum ( $S$ ). As per classical mechanics,  $S = I\omega = \left( \frac{1}{2} m_e r^2 \right) \omega$ , where  $I$  is the moment of inertia of the electron.

$$m_{spin} = \frac{e}{m_e} S \quad (1.34)$$

Applying principal of quantum mechanics,  $S = \sqrt{s(s+1)}\hbar = \frac{\sqrt{3}}{2}\hbar$  where  $s = \pm 1/2$  is the spin quantum number. The total magnetic moment of an electron can be expressed by Equation (1.35).

$$m = m_{orbital} + m_{spin} = \left( \frac{e}{2m_e} \right) L + \left( \frac{e}{2m_e} \right) 2S \quad (1.35)$$

The term  $(e\hbar/2m_e)$  is known as Bohr magneton ( $\mu_B = 9.27 \times 10^{-24}$  JT<sup>-1</sup>). Atomic magnetic moments are expressed as multiples of Bohr magneton. Note  $1 \text{ JT}^{-1} = 1$

$\text{Am}^2$ . The contribution due to orbital magnetic moment is low, as electrons with opposite spins cancel each other's effect. This also holds for the contribution due to spin magnetic moment except for the unpaired electrons. Thus the majority of magnetism arises due to the presence of unpaired electrons in an atom. The pairing up of electrons in different orbitals is based on Pauli's exclusion principle and Hund's rule of maximum multiplicity.

The classical model gives a simplified explanation of the origin of magnetism in atomic level. This has been modified using the quantum mechanical model which also takes into account the effect of a magnetic field on electrons (Zeeman effect) and introduces the magnetic quantum number in order to fully describe an electron along with the principal, orbital and spin quantum numbers. A further wave-mechanical correction was done based on Schrodinger's wave equation for electrons. Further details on this topic can be obtained in standard textbooks on magnetism [58, 63, 66].

#### 1.3.7. Magnetic domains and process of magnetization

In order to bridge the gap between magnetism at atomic scale and the magnetization process observed in bulk materials, it is imperative to discuss the idea of magnetic domains which was introduced in Section 1.2.2.

During the mid 19<sup>th</sup> century, Weber tried to explain the phenomena of magnetism by considering molecular magnets which were free to turn about their center like a compass needle. On the other hand, James Alfred Ewing tried to model the magnetization behavior using minimization of magnetic potential energy [57]. Although these hypotheses had some initial success, Ewing's theory failed to comply with the numeric values of the magnetic moments of ferromagnetic materials once

they were experimentally found. Based on the initial works of Weber, Paul Langevin (1905) proposed the theory of paramagnetism [67]. Taking this theory a step forward, Pierre-Ernest Weiss (1907) proposed the theory of ferromagnetism [68] which is also known as “*domain theory*.”

Weiss observed the discontinuity of specific heat at the Curie temperature and related this to an order-disorder transformation that leads to ordering of the magnetic moments in small regions called “*domains*” in the ferromagnetic phase. The domains exhibit spontaneous magnetization. In general, a bulk material is comprised of a number of domains each of which can be as large as a few millimeters. All the magnetic moments of the atoms within a domain orient along the same direction. In a demagnetized state, the domains are randomly oriented in the bulk material and therefore materials such as iron or nickel do not show any net magnetization unless exposed to a magnetic field.

Magnetic domains were first observed [69] by Francis Bitter (1931) and soon Lev Davidovich Landau and Evgeny Mikhailovich Lifshitz (1935) explained [70] the formation of domains using the concept of magnetostatic energy. Theoretical studies on domain structures enabled the proposition of the concept of domain walls by Felix Bloch (1932) [71] and Louis Néel (1944) [72].

It is necessary to introduce certain energy terms in order to better understand the reason for existence of domains and how they evolve during the magnetization process.

Weiss used the concept of a “Mean field” to describe the alignment of magnetic moments inside the domain. The mean field approximation required all

magnetic moments to equally interact with each other. The origin of this interaction was later explained by Heisenberg (1928) [73] as a quantum-mechanical exchange effect due to overlapping wave functions of neighboring atoms. The exchange energy per unit volume is given by Equation (1.36) [58] where  $A$  is the exchange stiffness and  $\boldsymbol{\alpha}$  is a vector that denotes the magnetization direction.

$$E_{ex} = A \left\{ \left( \frac{\partial \boldsymbol{\alpha}}{\partial x} \right)^2 + \left( \frac{\partial \boldsymbol{\alpha}}{\partial y} \right)^2 + \left( \frac{\partial \boldsymbol{\alpha}}{\partial z} \right)^2 \right\} \quad (1.36)$$

The exchange stiffness depends on the crystal structure, inter-atomic distance and Curie temperature of the material. The exchange energy favors the alignment of all magnetic moments along the same direction. This does not happen in reality as there are other energy terms that need to be balanced.

One such term is the magnetostatic energy. The magnetostatic energy per unit volume of a magnetic dipole with magnetization  $\mathbf{M}$  in an externally applied magnetic field  $\mathbf{H}$  can be expressed using Equation (1.37).

$$E_{ms} = -\mu_o \mathbf{H} \cdot \mathbf{M} \quad (1.37)$$

Even in the absence of an external field, the magnetic dipole is subjected to its own demagnetizing field  $\mathbf{H}_d (= N_d \mathbf{M})$  such that the magnetostatic energy  $\sim \frac{\mu_o}{2} N_d M^2$ .

Hence, in order to reduce the magnetostatic energy, it is favorable to breakdown a single large dipole into multiple domains as shown in Figure 1.10, provided the reduction in magnetostatic energy is greater than the energy required to form the domain walls. Smaller domains are formed at the boundaries of larger domains and are oriented perpendicular to the larger domains. These smaller domains, known as ‘closure domains,’ eliminate the possibility of having free poles at the end of the bulk

material thus providing a closed flux path between the larger domains and reducing the magnetostatic energy to almost zero.

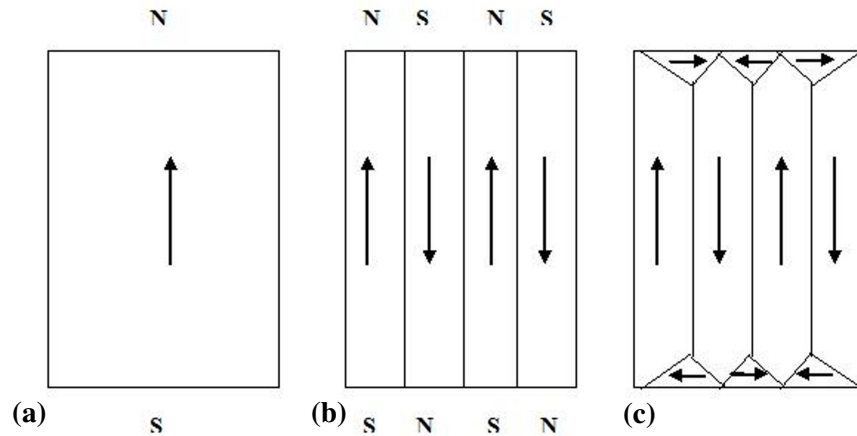


**Figure 1.10. (a) Single domain with large magnetostatic energy (b) Multiple domains reduce the magnetostatic energy (c) Formation of closure domains eliminates external magnetic poles.**

As evident from Figure 1.10, a domain wall is a region between two domains of different magnetization direction. Since it is not feasible to have two adjacent magnetic moments at the domain boundary aligned at a large angular difference due to the associated high exchange energy, the domain wall provides a layer of multiple atoms each oriented at a small angular difference from its neighbor. The cumulative change in angular difference through the domain wall thickness manifests as the difference in magnetization between the neighboring domains. This idea is schematically shown in Figure 1.11.

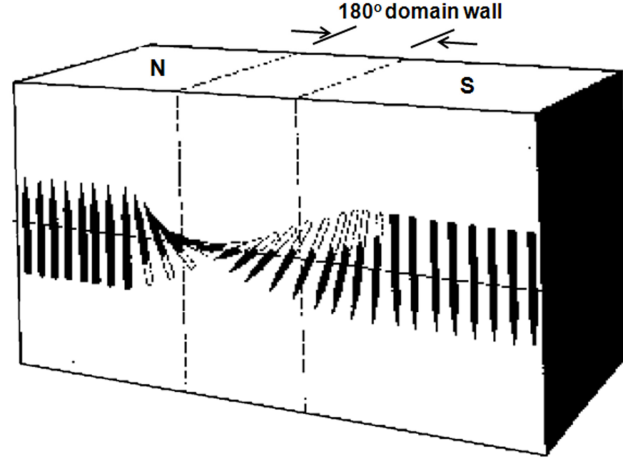


**Figure 1.11. Rotation of magnetic moments across a domain wall.**

The width of the domain wall is determined from a balance between the exchange energy and the magnetocrystalline anisotropy energy. The latter term denotes the energy required to rotate the magnetic moments away from certain “*easy directions*”. Magnetocrystalline anisotropy arises out of the coupling between spin and orbital magnetic moments [74]. As the orbital moments are constrained in their directions by the crystal lattice, the crystal symmetry influences the behavior of the spin due to the coupling. Hence, the magnetocrystalline anisotropy energy per unit volume is expressed using phenomenological expressions which are suitable to account for the symmetry. For a cubic crystal, this energy can be approximated using Equation (1.38). The energy distribution is shown in Figure 1.12.

$$E_{an} = K_1 (\alpha_1^2 \alpha_2^2 + \alpha_2^2 \alpha_3^2 + \alpha_3^2 \alpha_1^2) + K_2 \alpha_1^2 \alpha_2^2 \alpha_3^2 \quad (1.38)$$

Here  $\alpha_1 = \sin \theta \cos \varphi$ ,  $\alpha_2 = \sin \theta \sin \varphi$  and  $\alpha_3 = \cos \theta$  are the direction cosines of the magnetization ( $\mathbf{M} = M_s \boldsymbol{\alpha}$ ) with respect to the three cube edges and  $K_1$  and  $K_2$  are the 4<sup>th</sup> and 6<sup>th</sup> order anisotropy constants respectively. Based on a spherical coordinate system,  $0 \leq \theta \leq \pi$  and  $0 \leq \varphi \leq 2\pi$ .

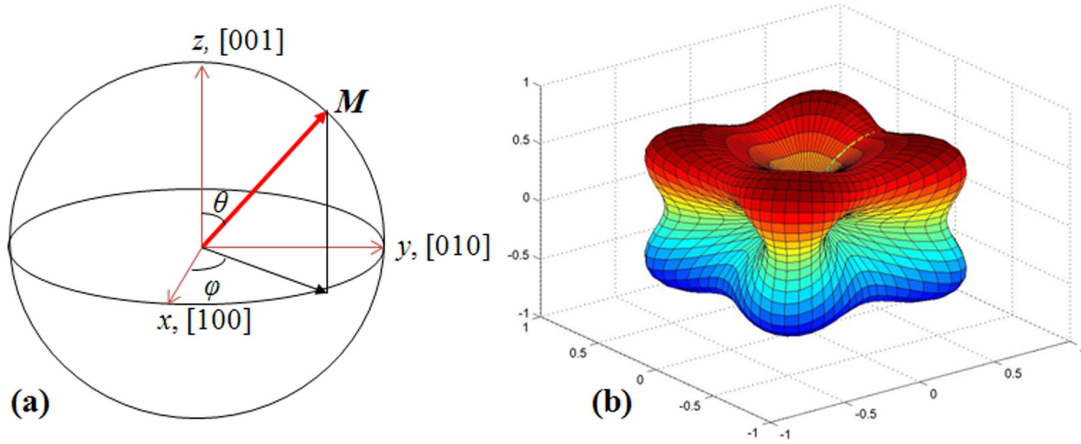


**Figure 1.12. (a) Spherical coordinate system with the  $\langle 100 \rangle$  crystal directions aligned along the coordinate axes. (b) Energy distribution in a cubic crystal in the absence of external magnetic field and mechanical stress. Energy minima (concavity) are observed along the  $\langle 100 \rangle$  directions.**

It was shown by Honda and Kaya [75], that if  $K_1 > 0$  and  $K_2 > -9K_1$  then  $\langle 100 \rangle$  are the easy directions whereas if  $K_1 < 0$  and  $K_2 > (-9/4)K_1$  then  $\langle 110 \rangle$  are the easy directions. For all other cases,  $\langle 111 \rangle$  are the easy directions.

The domain wall energy is  $\gamma_w = E_{ex} + E_{an}$  and under equilibrium the magnitude of exchange and anisotropy energies are equal at any part of the wall. The two basic types of domains walls are the Bloch and Néel walls. Bloch walls are predominant in thick specimens where the magnetic moments in the domain wall can orient normal to the plane of the sample whereas in a thin film all moments are oriented in the plane of the film and such a wall is known as Néel wall. The balance of domain wall energy and magnetostatic energy determines the size of the domains.

An external magnetic field perturbs the energy equilibrium and tends to rotate the magnetic moments along its direction which is manifested as the magnetization of the material. In terms of domain theory, the magnetization takes place in three stages

[63]. A typical magnetization and magnetic induction vs. magnetic field behavior is shown in Figure 1.13.

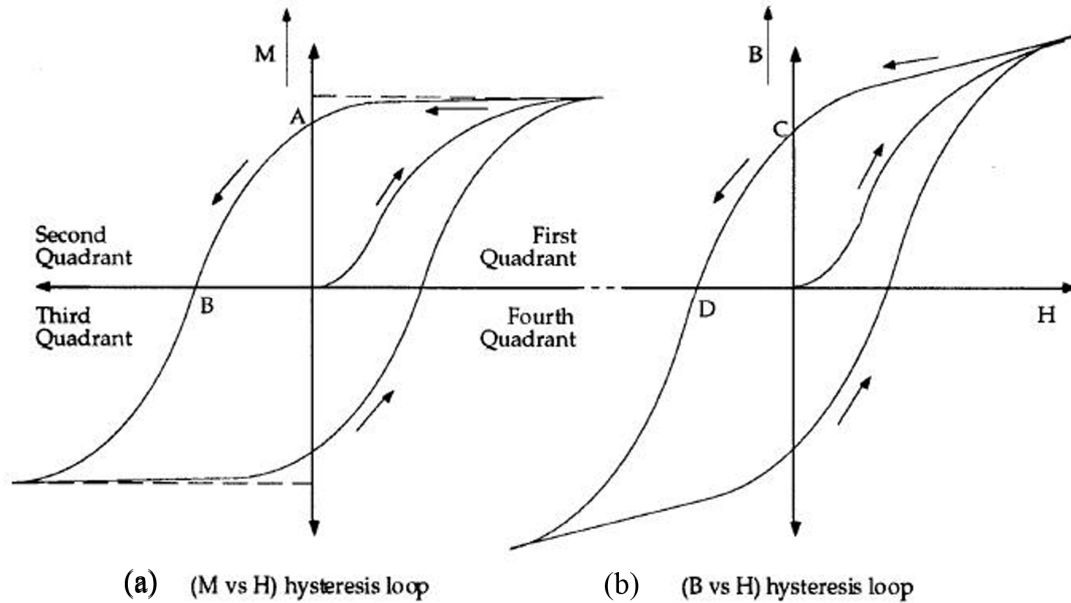


**Figure 1.13. A typical hysteretic (a) M-H and (b) B-H curve of a ferromagnet.**

At low fields, the domains oriented along the direction of field grow while those oriented opposite to the field reduce in size. The domain growth takes place by a mechanism known as *domain wall motion* in which the moments inside the domain wall flip towards the direction of the applied field thus increasing the total volume of domains aligned with the external field. At intermediate fields which are high enough to overcome the anisotropy energy, the magnetic moments in the domains which were oriented away from the field flip towards the easy axes nearest to the magnetic field direction. Finally at high fields, the magnetic moments rotate from the easy axes towards the direction of magnetic field until the material saturates and exists in a single domain state. This last step is known as *domain rotation*. Note that although

the magnetization becomes constant once the material saturates, the magnetic induction increases with increasing field with a slope of  $\mu_o$ .

The hysteresis in these curves is caused due to pinning of domains by material defects or stress inhomogeneities. It gives a measure of the loss in magnetic energy (given by the area enclosed by the B-H curve) in order to perform the mechanical work of ‘moving the domains’ against the defects. The hysteresis also signifies that the same domain orientation may not exist at the same magnetization state during magnetization and demagnetization processes. *Remanance* is the induction ( $B_r$ ) or magnetization ( $M_r$ ) that remains when the externally applied field is turned down to zero after taking the material to its saturation magnetization. The remanance is denoted by the points A and C in Figure 1.13. *Coercivity* ( $H_c$ ) is the reverse magnetic field strength that is required to reduce the material induction to zero which is denoted by the points B and D in Figure 1.13.

Section 1.4 will introduce the magnetoelastic energy which affects the energy balance in domains and domain walls in materials with significant magnetostriction thereby affecting the magnetization process in such materials.

#### 1.4. Phenomenon of magnetostriction

The discussion on ferromagnetism led to the fact that magnetic processes are guided by energy minimization principles. In this section, the phenomenon of magnetostriction will be discussed in detail and will be related to elastic and magnetoelastic energy. The actuation and sensing effects will be explained by introducing the Zeeman and stress-induced anisotropy energy. The origin of

magnetostriction will be related to the spin-orbit coupling and a brief history of magnetostrictive materials will be presented.

#### 1.4.1. Magnetoelastic effects

Magnetostriction describes the change in dimensions of a material due to a change in its magnetization. This phenomenon is a manifestation of magnetoelastic coupling which is exhibited by all magnetic materials to some extent. The effects related to magnetoelastic coupling are described by various names.

*Joule effect* [76] describes the change in length due to a change in the magnetization state of the material. This is also known as linear magnetostriction and assumes that the volume of the material remains constant. This phenomenon was first observed by James Prescott Joule (1842) in iron wires.

*Villari effect* (1865) [77] describes the mechanical stress-induced change in magnetization. A material with positive magnetostriction (e.g. iron) shows an increase in magnetization with an increase in stress whereas a material with negative magnetostriction (e.g. nickel) exhibits an increase in magnetization with a decrease in stress. Conventionally, a tensile stress is considered positive whereas a compressive stress is considered negative.

*Wiedemann effect* (1858) [78] describes a twist in the material due to a helical field produced by passing a current through the material (e.g. wire). *Matteucci effect* describes the change in magnetization in the helical direction when a ferromagnetic material is twisted.

Barrett (1882) [79] observed a change in volume of ferromagnetic materials under the influence of magnetic field and termed it as *volume magnetostriction*. The

term *forced magnetostriction* [80] describes an increase in the magnetostriction that can be obtained after attaining the saturation by increasing the temperature so that further increase in magnetic field reorders the magnetic moments which got disordered due to thermal agitation. Such an increase in magnetostriction is extremely small and has no practical application.

Conventionally, the *Joule* and *Wiedemann* effects are used for actuation purposes while the *Villari* and *Matteucci* effects are used for sensing purposes.

The observation of these macroscopic effects can be traced down to atomic scales. Magnetoelastic coupling arises from spin-orbit coupling and strong interaction between electron clouds of adjacent atoms [81]. Magnetic field applied to a material tries to orient the electron spin along the field direction but is resisted by the orbital motion which is strongly coupled to the crystal lattice structure [82]. The rotation of the orbits towards the direction of field and the associated distortion of the crystal lattice manifests as magnetostriction. Mechanical force acting on a material produces mechanical strain as the atomic bonds are stretched or twisted. At the same time the overlapping electron clouds in a bond are displaced thus affecting the electromagnetic state of the material. The change in the electromagnetic state of the material due to the applied force manifests as the inverse effect (i.e. *Villari* and *Matteucci* effects).

The spin-orbit coupling also determines the magnetocrystalline anisotropy and it is imperative that smaller spin-orbit coupling and consequently smaller magnetocrystalline anisotropy enables the orbit to reorient itself to the direction of the electron spin at smaller magnetic fields. Thus the desirable spin-orbit coupling should be large enough to produce significant lattice distortion which will manifest as a large

magnetostriction but at the same time the magnetocrystalline anisotropy should be small enough so that the lattice can be distorted by applying small magnetic fields.

#### 1.4.2. Fundamental relations in magnetostriction

The dipole-dipole interaction energy between the atoms shown in Figure 1.14 can be modeled using Equation (1.39) [58] where  $r$  is the bond length,  $[\alpha_1 \alpha_2 \alpha_3]$  are the magnetization direction cosines as defined in Equation (1.38) and  $[\beta_1 \beta_2 \beta_3]$  are the direction cosines of the bond direction.

$$w(r, \alpha) = l(r) \left\{ (\alpha_1 \beta_1 + \alpha_2 \beta_2 + \alpha_3 \beta_3)^2 - \frac{1}{3} \right\} \quad (1.39)$$

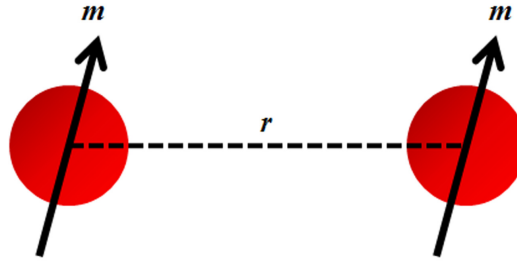


**Figure 1.14. A one-dimensional representation of interaction between neighboring dipoles with magnetic moment  $m$  separated by bond length  $r$ .**

When the crystal is strained, the bond length and consequently the interaction energy change. The sum of the change in the interaction energy for the nearest neighbor pairs can be expressed as Equation (1.40) where the tensor  $[\varepsilon_{11} \varepsilon_{22} \varepsilon_{33} \varepsilon_{23} \varepsilon_{31} \varepsilon_{12}]$  describes the strain in the crystal. The term  $E_{magel}$  is the magnetoelastic energy.

$$E_{magel} = b_1 \left\{ \varepsilon_{11} \left( \alpha_1^2 - \frac{1}{3} \right) + \varepsilon_{22} \left( \alpha_2^2 - \frac{1}{3} \right) + \varepsilon_{33} \left( \alpha_3^2 - \frac{1}{3} \right) \right\} + b_2 (\varepsilon_{23} \alpha_2 \alpha_3 + \varepsilon_{31} \alpha_3 \alpha_1 + \varepsilon_{12} \alpha_1 \alpha_2) \quad (1.40)$$

The coefficients  $b_1$  and  $b_2$  are known as magnetoelastic coupling coefficients. They depend on the number of nearest neighbor pairs, unstrained bond length, the function  $l(r)$  and its spatial gradient. The spontaneous magnetostriction or equilibrium strain in a domain in the absence of any external stress or magnetic field can be obtained by minimizing the sum of magnetoelastic and elastic energy with respect to each of the strain components. The expression for elastic energy in a cubic crystal is shown in Equation (1.41) where  $c_{11}$ ,  $c_{12}$  and  $c_{44}$  are the elastic constants.

$$E_{el} = \frac{1}{2}c_{11}(\epsilon_{11}^2 + \epsilon_{22}^2 + \epsilon_{33}^2) + \frac{1}{2}c_{44}(\epsilon_{23}^2 + \epsilon_{31}^2 + \epsilon_{12}^2) + c_{12}(\epsilon_{22}\epsilon_{33} + \epsilon_{33}\epsilon_{11} + \epsilon_{11}\epsilon_{22}) \quad (1.41)$$

The magnetostriction tensor  $[\tilde{\lambda}]$  or equilibrium strains are shown in Equation (1.42).

$$[\tilde{\lambda}] = \begin{bmatrix} \lambda_{11} \\ \lambda_{22} \\ \lambda_{33} \\ \lambda_{23} \\ \lambda_{31} \\ \lambda_{12} \end{bmatrix} = \begin{bmatrix} \frac{b_1}{c_{12} - c_{11}} \left\{ \begin{matrix} \left( \alpha_1^2 - \frac{1}{3} \right) \\ \left( \alpha_2^2 - \frac{1}{3} \right) \\ \left( \alpha_3^2 - \frac{1}{3} \right) \end{matrix} \right\} \\ -\frac{b_2}{c_{44}} \left\{ \begin{matrix} \alpha_2\alpha_3 \\ \alpha_3\alpha_1 \\ \alpha_1\alpha_2 \end{matrix} \right\} \end{bmatrix} \quad (1.42)$$

The strain along the direction cosines  $[\beta_1 \beta_2 \beta_3]$  can be expressed by Equation (1.43)

$$\epsilon_{[\beta_1 \beta_2 \beta_3]} = \epsilon_{11}\beta_1^2 + \epsilon_{22}\beta_2^2 + \epsilon_{33}\beta_3^2 + \epsilon_{23}\beta_2\beta_3 + \epsilon_{31}\beta_3\beta_1 + \epsilon_{12}\beta_1\beta_2 \quad (1.43)$$

The magnetostriction along [100] which is shown in Equation (1.44) can be obtained by substituting  $\alpha_1 = \beta_1 = 1$  and  $\alpha_2 = \beta_2 = \alpha_3 = \beta_3 = 0$  in Equations (1.42) and (1.43).

$$\lambda_{100} = \frac{2}{3} \frac{b_1}{(c_{12} - c_{11})} = -\frac{1}{3} \frac{b_1}{c'} \quad (1.44)$$

Similarly the magnetostriction along [111] which is shown in Equation (1.45) can be obtained by substituting  $\alpha_1 = \beta_1 = \alpha_2 = \beta_2 = \alpha_3 = \beta_3 = 1/\sqrt{3}$  in Equations (1.42) and (1.43).

$$\lambda_{111} = -\frac{1}{3} \frac{b_2}{c_{44}} \quad (1.45)$$

Combining Equations (1.42) – (1.45), the magnetostriction along any arbitrary direction  $[\beta_1 \beta_2 \beta_3]$  can be expressed [83] using Equation (1.46) when the magnetization direction is along  $[\alpha_1 \alpha_2 \alpha_3]$ .

$$\begin{aligned} \lambda_{\beta_1\beta_2\beta_3} = & \frac{3}{2} \lambda_{100} \left( \alpha_1^2 \beta_1^2 + \alpha_2^2 \beta_2^2 + \alpha_3^2 \beta_3^2 - \frac{1}{3} \right) \\ & + 3\lambda_{111} (\alpha_2 \alpha_3 \beta_2 \beta_3 + \alpha_3 \alpha_1 \beta_3 \beta_1 + \alpha_1 \alpha_2 \beta_1 \beta_2) \end{aligned} \quad (1.46)$$

If the equilibrium strains from Equation (1.42) are substituted back in Equations (1.40) and (1.41), the sum of the magnetoelastic and elastic energies would translate into an equivalent 4<sup>th</sup> order magnetostrictive anisotropy energy which can be expressed by Equation (1.47). The coefficient  $-\frac{9}{4} \{(c_{12} - c_{11}) \lambda_{100}^2 + 2c_{44} \lambda_{111}^2\}$  is known as  $\Delta K_1$ .

$$E_{\Delta K_1} = -\frac{9}{4} \{(c_{12} - c_{11}) \lambda_{100}^2 + 2c_{44} \lambda_{111}^2\} (\alpha_1^2 \alpha_2^2 + \alpha_2^2 \alpha_3^2 + \alpha_3^2 \alpha_1^2) \quad (1.47)$$

Hence the effective magnetocrystalline anisotropy is given by the sum of Equations (1.38) and (1.47). It should be noted that measured values of  $K_1$  include the value  $\Delta K_1$  as the magnetostrictive anisotropy ( $\Delta K_1$ ) cannot be experimentally distinguished from the pure magnetocrystalline anisotropy ( $K_1$ ).

### 1.4.3. Magnetostrictive actuation and sensing

The spontaneous magnetostriction does not contribute to any useful actuation or sensing effect. On the other hand, a magnetic field can rotate the magnetic moments from their equilibrium directions thereby producing useful magnetostriction. The effect of magnetic field is incorporated by introducing the Zeeman energy given by Equation (1.48). Note that the expression for Zeeman energy is the same as that of the magnetostatic energy shown in Equation (1.37), the only difference being that the magnetic field in Zeeman energy is an externally applied one whereas the field referred to in Equation (1.37) is created by free magnetic dipoles within the material.

$$W_{mag} = -\mu_o \mathbf{M} \cdot \mathbf{H} \quad (1.48)$$

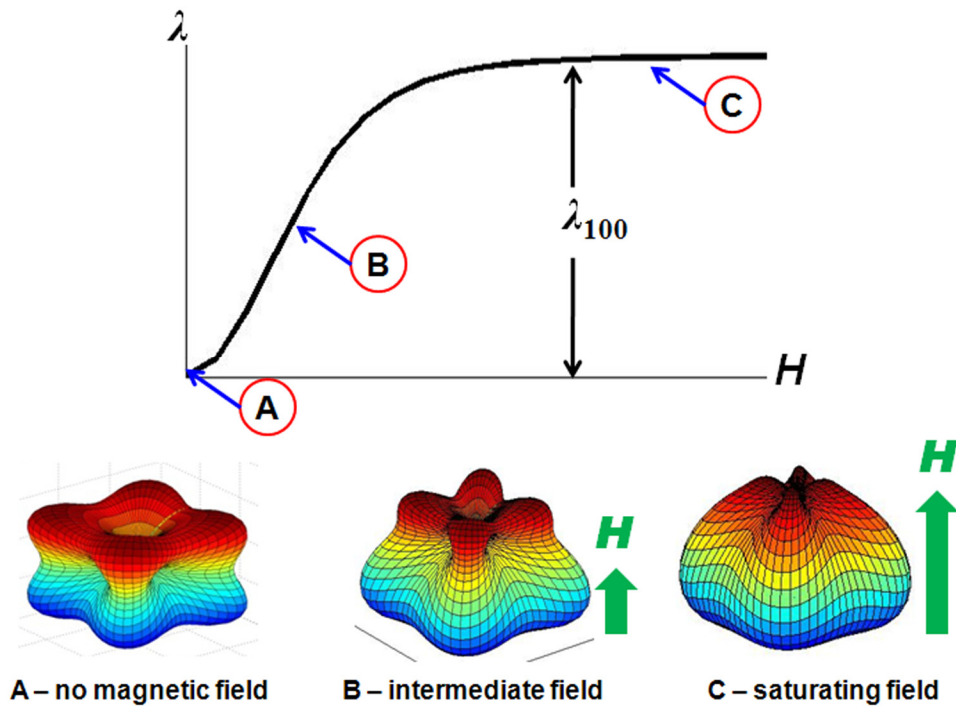


**Figure 1.15. A typical anhysteretic  $\lambda$ - $H$  curve and the energy distribution at different magnetic fields.**

Figure 1.15 shows a typical magnetostriction vs. magnetic field ( $\lambda$ -H) response along the [001] ‘easy’ direction of a cubic crystal with positive magnetostriction. The three-dimensional energy distributions for three distinct magnetic fields are shown below the  $\lambda$ -H curve. The concavities in the energy distribution denote the energy minima at a given magnetization state. The direction of energy minima are the preferred direction for alignment of magnetic moments. Magnetostriction monotonically increases with magnetic field until all the magnetic moments orient along the direction of the magnetic field. This magnetic saturation state of the material is signified by a single energy minimum oriented along the magnetic field direction.

Similarly, a mechanical stress can also rotate the magnetic moments from their equilibrium directions thereby producing a change in the net magnetization in the presence of a bias magnetic field. In the absence of a bias field, the magnetic moments reorient so as to eliminate any free poles and hence there is no net magnetization. The effect of stress is incorporated by introducing the mechanical work energy given by Equation (1.49).

$$W_{mech} = -(\sigma_{11}\epsilon_{11} + \sigma_{22}\epsilon_{22} + \sigma_{33}\epsilon_{33} + \sigma_{23}\epsilon_{23} + \sigma_{31}\epsilon_{31} + \sigma_{12}\epsilon_{12}) \quad (1.49)$$

Under the influence of stress, the equilibrium strains are obtained by minimizing the sum of Equations (1.40), (1.41) and (1.49) which yields the equilibrium strains given by Equation (1.50). Here  $[\tilde{\epsilon}_{mech}]$  is the mechanical strain tensor given by Equation (1.51).

$$[\tilde{\epsilon}] = [\tilde{\epsilon}_{mech}] + [\tilde{\lambda}] \quad (1.50)$$

$$[\tilde{\boldsymbol{\epsilon}}_{mech}] = \begin{bmatrix} c_{11} & c_{12} & c_{12} & 0 & 0 & 0 \\ c_{12} & c_{11} & c_{12} & 0 & 0 & 0 \\ c_{12} & c_{12} & c_{11} & 0 & 0 & 0 \\ 0 & 0 & 0 & c_{44} & 0 & 0 \\ 0 & 0 & 0 & 0 & c_{44} & 0 \\ 0 & 0 & 0 & 0 & 0 & c_{44} \end{bmatrix}^{-1} \begin{bmatrix} \sigma_{11} \\ \sigma_{22} \\ \sigma_{33} \\ \sigma_{23} \\ \sigma_{31} \\ \sigma_{12} \end{bmatrix} \quad (1.51)$$

Substituting Equation (1.50) into (1.49) yields a stress-induced anisotropy energy given by Equation (1.52) which influences the magnetization direction.

$$E_{\sigma} = -(\sigma_{11}\lambda_{11} + \sigma_{22}\lambda_{22} + \sigma_{33}\lambda_{33} + \sigma_{23}\lambda_{23} + \sigma_{31}\lambda_{31} + \sigma_{12}\lambda_{12}) \quad (1.52)$$

It should be noted that although Equations (1.42) and (1.46) can always be used to calculate the magnetoelastic component of strain, an appropriate technique should be used to find the equilibrium  $\boldsymbol{\alpha}$  under the influence of both magnetic field and stress. Modeling techniques which can be used to estimate the equilibrium magnetization directions will be discussed in Section 1.6.

Figure 1.16 shows a typical magnetic induction vs. compressive stress ( $B$ - $\sigma$ ) response along the [001] ‘easy’ direction of a cubic crystal with positive magnetostriction. The three-dimensional energy distributions for three distinct compressive stresses are shown below the  $B$ - $\sigma$  curve. Note that sensing can take place only when the stress-induced anisotropy energy can overcome the effect of magnetocrystalline anisotropy energy and the Zeeman energy due to the bias magnetic field. At high compressive stresses, energy minima occur along the directions which are perpendicular to the direction of stress and all magnetic moments orient in this plane normal to the stress direction. Such an orientation of the magnetic moments marks the magnetoelastic saturation and indicates that no sensing can take place for higher applied stresses.

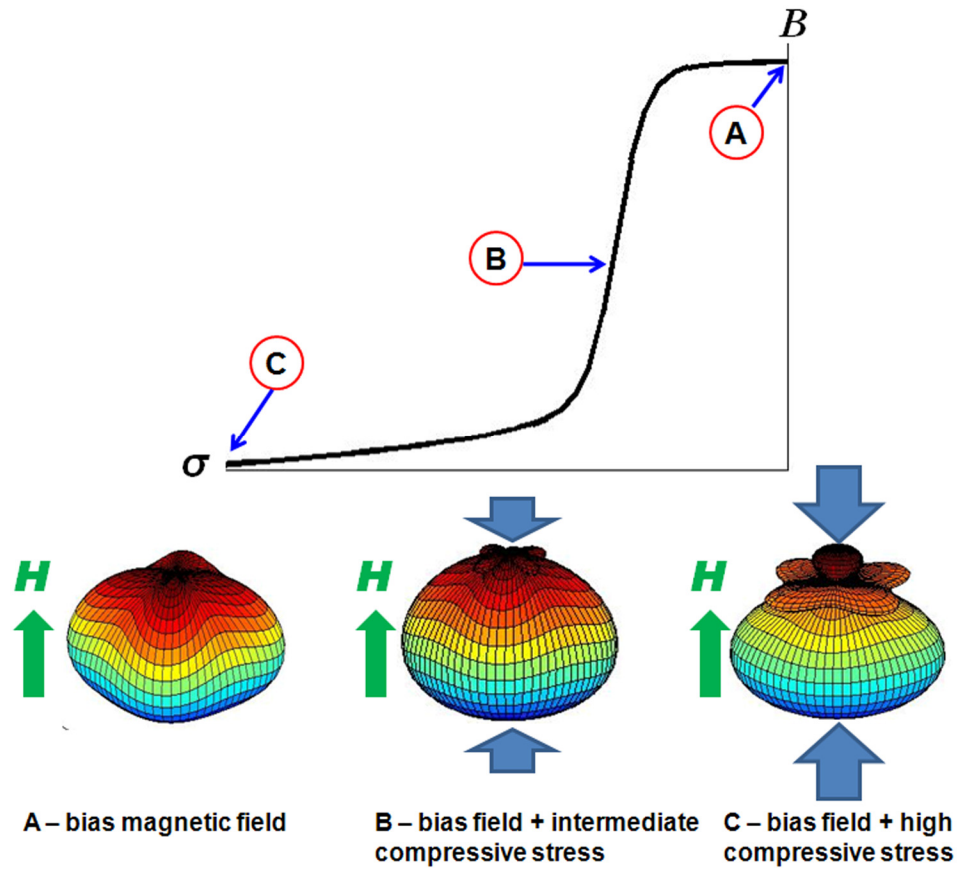


**Figure 1.16. A typical anhysteretic  $B$ - $\sigma$  curve and the energy distribution at different compressive stresses under a constant bias magnetic field.**

Analogous to a bias field in sensing applications, a pre-stress is usually applied for actuator applications to obtain more useful magnetostriction. If a compressive pre-stress applied to a demagnetized sample is large enough to overcome the crystalline anisotropy, it will orient all magnetic moments in a plane normal to the stress direction. A large enough magnetic field applied parallel to the stress direction on the pre-stressed sample can reorient all the magnetic moments in the sample thereby yielding a larger useful magnetostriction than the same magnetic field can yield if it were applied to a demagnetized sample as shown in Figure 1.15. This happens because in a demagnetized sample, some magnetic moments are already

oriented along the field direction if the field is applied along one of the easy axes and therefore these moments do not contribute to useful magnetostriction. Figure 1.17 shows the  $\lambda$ - $H$  curve of a pre-stressed sample.

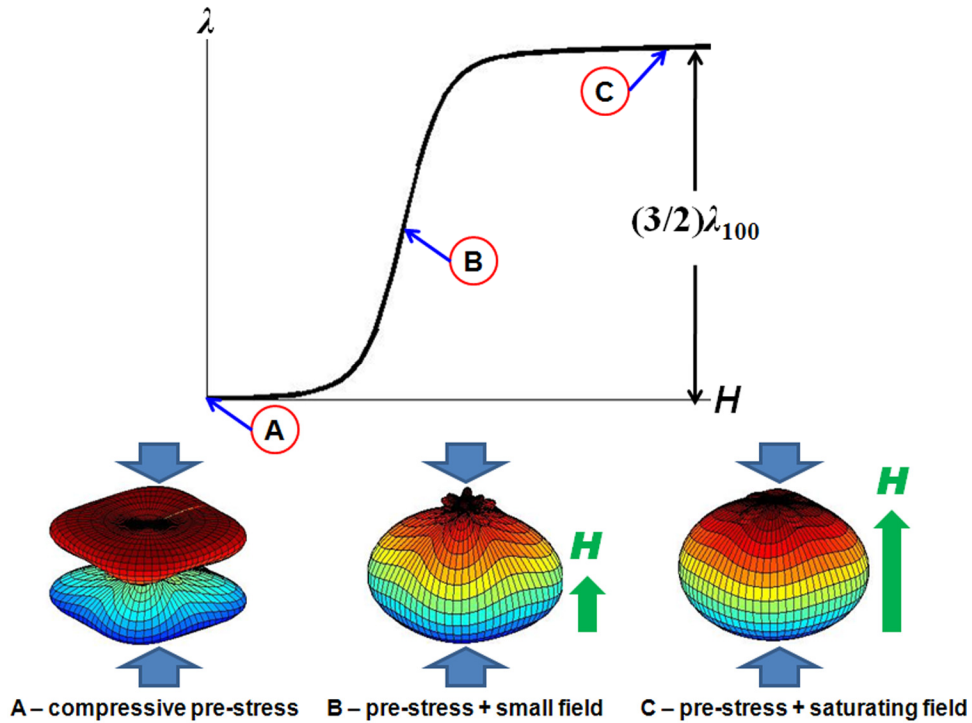


**Figure 1.17. A typical anhysteretic  $\lambda$ - $H$  curve and the energy distribution at different magnetic fields under a constant compressive pre-stress.**

#### 1.4.4. History of the development of magnetostrictive materials

After the initial discovery of magnetoelastic effects in the mid-18<sup>th</sup> century, several researchers systematically studied the magnetostriction in different binary alloys of the iron, cobalt and nickel in the next half a century. Most of these alloys showed free strain of less than 100  $\mu\epsilon$  as shown in Table 1.4. The importance of nickel as a transducer material for sonar motivated further research in magnetostrictive materials during and after World War I. However, with the

development of materials such as PZT which exhibited free strain of the order of 1000  $\mu\epsilon$ , magnetostrictive materials ended up taking the backseat.

With advancements in low temperature measurements during the 1960s, it was observed that several rare earth elements exhibit colossal magnetostriction ( $> 5000 \mu\epsilon$ ) but only at temperatures close to absolute zero and showed almost negligible magnetostriction at room temperature. Moreover, these materials showed very high magnetocrystalline anisotropy and hence required extremely high magnetic fields ( $\sim 10^6 \text{ Am}^{-1}$ ) to obtain saturation magnetostriction. In early 1980s, researchers in the Naval Ordnance Laboratory used an optimal combination of terbium, iron and dysprosium which showed high magnetostriction at room temperature finally giving rise to the giant magnetostrictive material Terfenol-D.

Commercially available [43] polycrystalline Terfenol-D exhibits about 1200  $\mu\epsilon$  at  $1.5 \times 10^5 \text{ Am}^{-1}$  but has low Young's modulus (25-35 GPa) and low tensile strength (28 MPa) which restricts its usage to applications involving only axial compression. A new era of structural magnetostrictive alloys started with the discovery of large magnetostriction in iron-gallium alloys [84, 85]. Section 1.5 will discuss iron-gallium system in details.

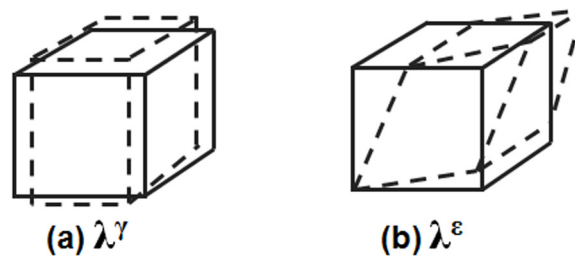


**Figure 1.18. Volume conserving magnetostriction (a)  $\lambda^\gamma$  and (b)  $\lambda^\epsilon$  [81].**

The volume-conserving magnetostriction constants  $\lambda^{\gamma}$  and  $\lambda^{\epsilon}$ , shown in Figure 1.18, are called as  $\lambda_{100}$  and  $\lambda_{111}$  in cubic materials. The values of these magnetostrictive constants for several single crystal materials are shown in Table 1.4.

**Table 1.4. Magnetostriction of single crystal materials measured at room temperature [58, 81].**

Material	$\lambda^{\gamma}$ (x $10^{-6}$ )	$\lambda^{\epsilon}$ (x $10^{-6}$ )
Fe	24	-23
Co	-248	57
Ni	-66	-29
Ni <sub>65</sub> Fe <sub>35</sub>	20	15
Ni <sub>65</sub> Co <sub>35</sub>	40	-35
Fe <sub>55</sub> Co <sub>45</sub>	130	35
Tb *	8700	20
Dy *	9400	5500
TbFe <sub>2</sub> *	-	4000
TbFe <sub>2</sub>	-	3690
DyFe <sub>2</sub> *	-70	-
DyFe <sub>2</sub>	-	1890
Tb <sub>0.27</sub> Dy <sub>0.73</sub> Fe <sub>2</sub>	-	2300
Fe <sub>97</sub> Si <sub>3</sub>	25	-7
Fe <sub>80</sub> Al <sub>20</sub>	95	5
Fe <sub>83</sub> Ga <sub>17</sub>	208	0

\* Values measured at temperatures close to absolute zero (-273 °C).

### 1.5. Iron-gallium alloys (Galfenol)

This section discusses the properties of the iron-gallium alloys which make them attractive materials for actuator and sensor applications. The focus of the discussion is on the magnetostrictive properties and relevant metallurgical aspects of single crystal material which help in understanding the variation in alloy properties as a function of composition. Finally, the state of the art in processing of Fe-Ga alloys and its significance in transducer applications is presented.

#### 1.5.1. Metallurgy of Fe-Ga alloys

It is required to have a prior knowledge of the basic metallurgical aspects of the iron-gallium system in order to understand the complexity of the relationship of Fe-Ga alloys and the magnetostriction exhibited by them.

Single crystal iron at room temperature (i.e.  $\alpha$  Fe) has a body-centered cubic (BCC) unit cell which is equivalent to an A2 structure in the strukturbericht notation. The iron-gallium equilibrium phase diagram is shown in Figure 1.19. For the purpose of this dissertation, we will only focus on the region between 0 to 30 atomic % gallium additions in iron. Figure 1.19 shows that at room temperature, the  $\alpha$  Fe (A2) phase exists upto 12 at. % Ga while the  $\alpha$  Fe<sub>3</sub>Ga (L1<sub>2</sub>) phase exists between 25 to 30 at. % Ga. The region between 12 to 25 at. % Ga is a mixture of these two phases. Other phases such as D0<sub>3</sub>, B2 and  $\beta$  Fe<sub>3</sub>Ga (D0<sub>19</sub>) exist at high temperature only.

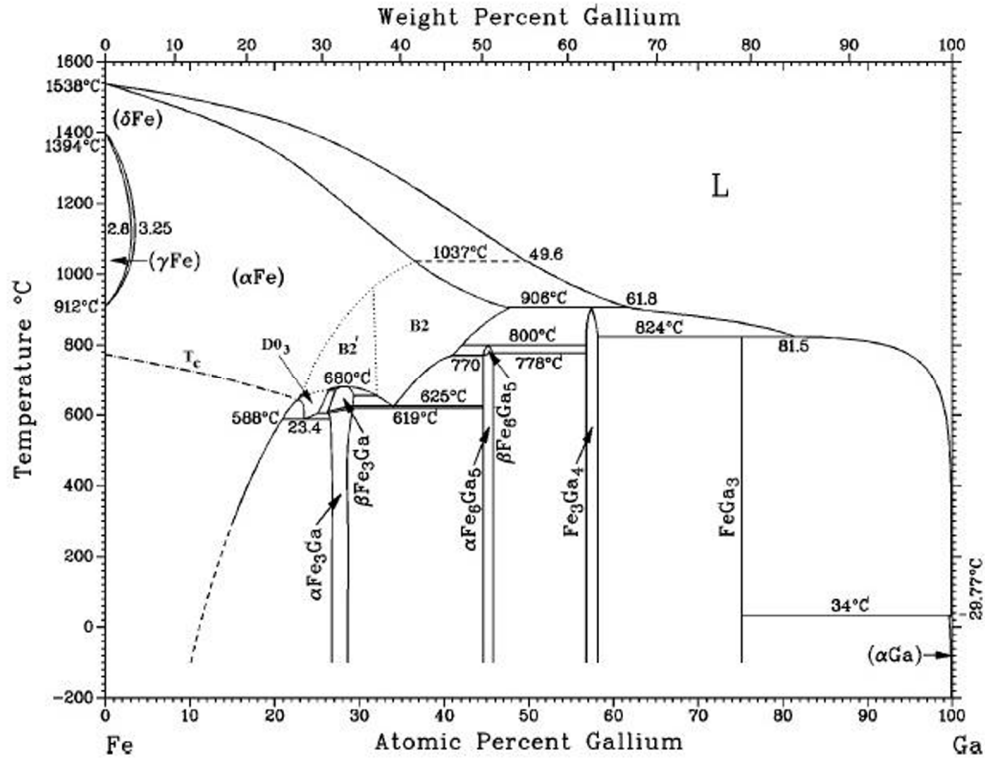


**Figure 1.19. Equilibrium phase diagram of iron-gallium system [86].**

A schematic representation of the “unit” cells of A2, D0<sub>3</sub>, L1<sub>2</sub> and B2 structures are shown in Figure 1.20. The atomic radii of iron and gallium are 0.124 and 0.122 nm respectively [64]. The size difference shown in the legend of Figure 1.20 is only meant for visual clarity. In A2 structure, which is a disordered phase, each lattice point has an equal probability of hosting an iron or gallium atom. The D0<sub>3</sub> and L1<sub>2</sub> are ordered Fe<sub>3</sub>Ga phases. The unit cell of a D0<sub>3</sub> structure consists of eight unit cells of a conventional BCC structure. The gallium atoms are situated in the body-center positions of the BCC cell or along the four alternate corners of the sub-lattice shown in green dashed line in Figure 1.20(b), i.e. along the <110> direction of this sub-lattice. The L1<sub>2</sub> is an FCC structure with Ga and Fe atoms in the corner and

face-center positions respectively. The B2 is an ordered FeGa phase with the Ga atom in the body-center position of a cube with Fe atoms in the corners.

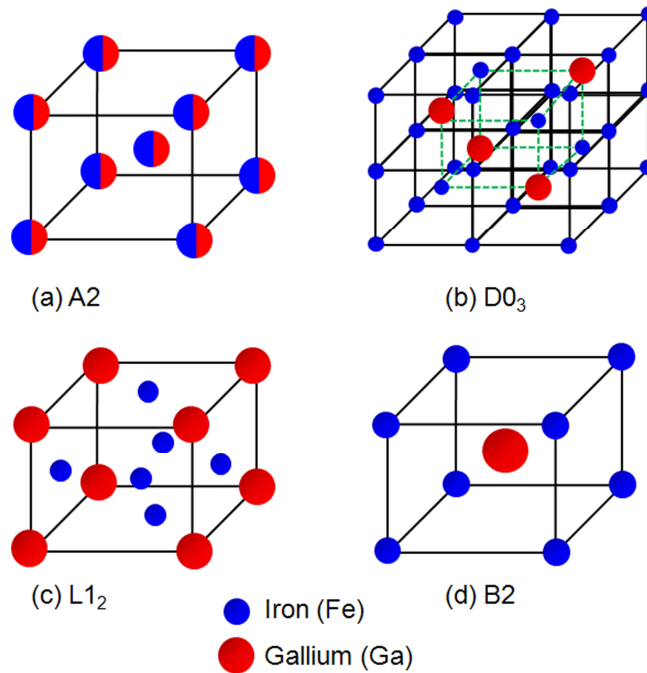


**Figure 1.20.** “Unit” cells of (a) A2, (b) D0<sub>3</sub>, (c) L1<sub>2</sub> and (d) B2 structures.

Prior work [87] showed that addition of upto 20 atomic % Ga in Fe results in a disordered A2 phase having randomly substituted gallium atoms in the iron lattice. Addition of 20 to 30 atomic % Ga in Fe can produce D0<sub>3</sub> phase if the alloy is quenched from above 730 °C or L1<sub>2</sub> phase if it is annealed at 500 °C for three days and at 350 °C for over a month. Other works [88-91] also reported a disordered FCC (A1) phase. Investigation [87] of the saturation magnetization of these phases as a function of temperature established the first magnetic phase diagram for iron-gallium alloys. Further dilatometric study [89-91] of the iron-gallium system with different thermal history was used to create a metastable phase diagram. These works showed that iron-gallium alloys have complex thermal history-dependent stable as well as meta-stable phases which also differ in their magnetic properties.

Recent work [92] using scanning and transmission electron microscopy study of the iron-rich portion of the iron-gallium system has been helpful in modifying the magnetic and metastable phase diagram of the region. This non-equilibrium phase diagram, shown in Figure 1.21, is also useful for finding the Curie temperature for different alloy composition. Further investigation [93-95] of the iron-gallium system confirmed that addition of upto 18 at. % Ga in Fe, produces an A2 phase with D0<sub>3</sub>-like or B2-like nano-precipitates. Alloys with 18 to 21 at. % Ga showed a matrix of A2 phase with structurally inhomogeneous nano-precipitates on quenching but showed a mixture of A2 and D0<sub>3</sub> phases if the alloys were slowed-cooled. Alloys with 21 to 25 at. % Ga showed a mixture of A2 and D0<sub>3</sub> phases irrespective of their thermal history. For alloys with 25 to 29 at. % Ga, quenching produced a mixture of A2, B2 and D0<sub>3</sub> phases while slow-cooling yielded only the D0<sub>3</sub> phase. The effect of these phases on the magnetomechanical properties of iron-gallium alloys will be evident in Section 1.5.2.

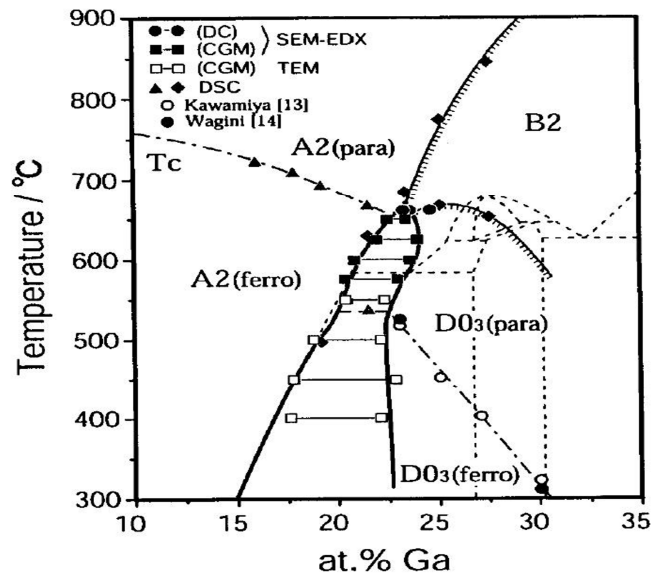


**Figure 1.21. Non-equilibrium phase diagram of iron-gallium alloys [92].**

### 1.5.2. Magnetostriction and other properties of Fe-Ga alloys

The investigation of magnetostriction of a number of binary iron alloys by Hall [96] showed that addition of aluminum in iron can increase the magnetostriction by five times. Motivated by these results, Clark *et al.* [84] investigated the effect of gallium addition in single crystal iron and found an increase in  $\lambda_{100}$  by a factor of twenty. This new alloy became known as Galfenol. The magnetostriction constants for single crystal Galfenol alloys are shown in Figure 1.22. Similar studies [85] performed on directionally cast Fe-Ga alloys showed about seven times increase in magnetostriction compared to polycrystalline iron.

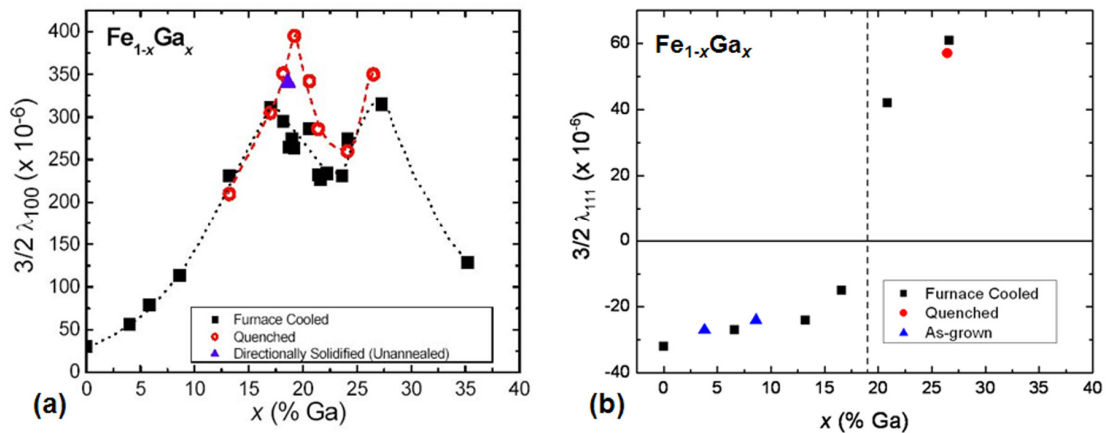


**Figure 1.22. (a)  $(3/2)\lambda_{100}$  and (b)  $(3/2)\lambda_{111}$  as functions of gallium content in iron-gallium alloys [97].**

Initial studies [97] on the effect of composition have identified Fe-Ga alloys with 15 to 30 atomic % gallium as the region of interest as the two peaks in magnetostriction occur within this composition range. As shown in Figure 1.22(a), a maximum magnetostriction of  $\sim 300 \mu\epsilon$  was shown by furnace cooled samples having 17 and 27.5 atomic % Ga. Inbetween these two compositions, a low in the magnetostriction ( $\sim 225 \mu\epsilon$ ) is observed at 24 atomic % Ga. The reason for obtaining

the first peak in magnetostriction has been attributed [98] to the presence of randomly distributed gallium atom pairs in the A2 phase of iron. It is suggested that these gallium atom pairs act as defects thereby altering the effective crystalline anisotropy and hence increasing the magnetostriction [98]. First principle calculations [99] attribute the enhanced magnetostriction to the formation of B2-like structures.

Recent measurement of atomic scale magnetostriction [100] in  $\text{Fe}_{81}\text{Ga}_{19}$  confirmed that large strains develop in the Fe-Ga bonds near the Ga-Ga environment although the strain between Ga-Ga bonds are negligible and the strain between Fe-Fe bonds show only a nominal increase from the magnetostriction observed in pure iron. Another recent work by Mudivarthi *et al.* [101] showed the reorientation of nano-clusters in an irradiated sample of  $\text{Fe}_{81}\text{Ga}_{19}$  as a response to externally applied magnetic field and mechanical stress using neutron scattering data. This work [101] may offer the experimental evidence of the correlation between magnetostriction and presence of nano-precipitates in A2 matrix which was earlier hypothesized [94, 95] and may be useful to evaluate the theory proposed by Khachatryan *et al.* [102, 103]. These observations may offer the first set of experimental evidence of the origin of magnetostriction in Galfenol and may also help in understanding the underlying mechanism that enhances the magnetostriction of iron when substituted with non-magnetic elements.

An extensive study on the effect of thermal history and gallium composition [92, 93, 104, 105] has shown that Galfenol alloys with  $\text{D0}_3$  phase has a long range ordering of Ga atoms which lowers the magnetostriction. The  $\text{D0}_3$  phase can be

expected to be present along with the A2 phase in alloys having more than 17.5 atomic % Ga.

The volume fraction of  $D0_3$  phase in Fe-Ga alloys having more than 17.5 atomic % Ga can be reduced by water-quenching which can help in increasing the saturation magnetostriction [104, 105] upto an addition of 19.5 atomic % Ga as shown in Figure 1.22(a). A possible reason for obtaining the lowest magnetostriction near 25 atomic % Ga can be due to the formation of a stoichiometric compound ( $Fe_3Ga$ ) which indicates a highly ordered structure and hence cannot be altered by water quenching. The second peak in magnetostriction is not altered significantly by heat treatment. This composition is a mixture of multiple phases and hence the reason for obtaining a high magnetostriction is not very clear. A possible reason for the high magnetostriction can be due to a marked softening of the crystal lattice [97].

The actuator behavior of single crystal [84, 104, 106-108] and polycrystalline [85, 109-111] Galfenol have been extensively characterized for the composition range of 17 to 29 at. % Ga but the sensor behavior has been characterized only for 19 at. % Ga quenched [107] and slow-cooled [108] samples and 24.7 at. % Ga slow-cooled sample [112]. The details of actuator and sensor response of Galfenol will be discussed in Chapter 2.

Although Galfenol offers only one-third the strain of commercial Terfenol-D, it requires less than one-tenth the magnetic field required to saturate Terfenol-D. This attribute can be useful for design of compact and low-weight devices by reducing the amount of coil and high power electronics which are usually required to obtain high drive current in Terfenol-D transducers. Moreover, Kellogg *et al.* [106] has shown

that  $\text{Fe}_{81}\text{Ga}_{19}$  shows a variation of only  $0.4 \mu\epsilon/^\circ\text{C}$  in its saturation magnetostriction value between  $-21^\circ\text{C}$  to  $+80^\circ\text{C}$  and hence can be used for a large range of temperature without significant loss of magnetostriction. Galfenol can be easily machined and hence can be obtained in different shapes and sizes which might be useful for innovative devices. Galfenol can also be welded to passive structures which makes it an ideal material for structural health monitoring.

The most important feature that motivates the use of Galfenol alloys in smart structures is their structural properties which give them a unique advantage over conventional smart materials such as PZT, PMN or Terfenol-D. Extensive mechanical characterization has been performed on Fe-Ga alloys. Wuttig *et al.* [113] measured the stiffness constants of Galfenol as a function of gallium content using acoustic measurement. Clark *et al.* [97] measured the elastic constants of Galfenol alloys as functions of temperature and composition using resonance ultrasound spectroscopy (RUS). Later, Petculescu *et al.* [114] used RUS to quantify the difference in the stiffness constants ( $c'$  and  $c_{44}$ ) between demagnetized and magnetically saturated conditions for 12 to 33 at. % Ga alloys at 4 K and 300 K temperatures. Kellogg *et al.* [115] used quasi-static tensile tests to measure a Young's modulus of 65 GPa, tensile strength of 515 MPa and upto 2 % strain along the  $\langle 100 \rangle$  direction of single crystal  $\text{Fe}_{83}\text{Ga}_{17}$  which showed that Galfenol is ductile and strong enough for applications involving tension. The interesting phenomenon of auxetic effect (negative Poisson's ratio) was observed [115] in a 27.2 at. % Ga sample along the  $\langle 110 \rangle$  direction. Further tensile tests [116, 117] focused on investigation of Young's modulus and

Poisson's ratio for alloys with 17.4 to 33.2 at. % Ga along the <100> and <110> directions.

Some of the other properties investigated in iron-gallium alloys include electrical resistivity [87], magnetocrystalline anisotropy [118], thermal expansion coefficient [105] and specific heat capacity [119]. Investigation [120-122] of magnetostriction in ternary Fe-Ga-X (X = Ni, Mo, Sn, Al, C, V, Cr, Mn, Co, Rh) alloys did not show any significant improvement in magnetostriction but addition of small amount (< 0.1 %) of carbon in samples with 18.6 at. % Ga increased the magnetostriction of slow-cooled alloys and appeared to have similar effect as quenching [123].

### 1.5.3. Processing of Fe-Ga alloys

Although single crystal Galfenol exhibits good magnetostrictive and mechanical properties, it may not be the best choice for commercial applications owing to the slow rate of crystal growth and high auxiliary cost involved in accurate machining along the desired orientation. Therefore, extensive research effort has gone into processing of Galfenol alloys in order to find out the best method that will provide bulk samples at low cost without significantly compromising the structural and magnetoelastic properties.

The earliest work on characterization of rolled, forged, extruded and directionally solidified polycrystalline Galfenol as well as powdered Galfenol can be attributed to Kellogg *et al.* [107, 124]. It was shown that based on the processing technique, a saturation magnetostriction between 30 to 170  $\mu\epsilon$  could be obtained.

Subsequent work at ETREMA Products Inc. [110] led to the development of research and production grade polycrystalline Galfenol. The polycrystalline ingots were grown using Float Stand Zone Melt (FSZM) technique at the rate of 25 mm/hr and 350 mm/hr respectively which were much faster than the Bridgman grown single crystal at 2 to 4 mm/hr. Measurement of saturation magnetostriction in research and production grade polycrystalline 18.4 at. % Ga samples showed 220  $\mu\epsilon$  and 168  $\mu\epsilon$  respectively which were less than the 290  $\mu\epsilon$  exhibited by a single crystal of same composition. The difference in magnetostriction was attributed to the grain size and texture [110]. The typical structural properties associated with Galfenol were exhibited by both the research (Young's modulus = 72.4 GPa, tensile strength = 370 MPa, elongation = 1.2 %) and production (Young's modulus = 86.3 GPa, tensile strength = 348 MPa, elongation = 0.81 %) grade samples.

Recent work by Na and Flatau [125, 126] on deformation processing of Fe-Ga-X (X = B, C, Mo, Nb, and NbC) alloys showed that addition of NbC can improve roll ability and produce saturation magnetostriction of 183  $\mu\epsilon$ . Moreover, appropriate atmospheric annealing and controlled doping with boron and sulfur may be used to obtain the most-wanted {100}<001> cube texture in rolled sheets as thin as 0.3 mm. These rolled sheets may offer a viable low-cost and high-performance option in applications that need structural conformation.

Other processing techniques such as stress-annealing [127, 128] and magnetic field-annealing [129] have demonstrated the development of a uniaxial anisotropy in Galfenol which can be exploited to obtain more useful magnetostriction without

applying a pre-stress and have shown to be helpful in obtaining high magnetostriction even when the material is operated under tension.

Rapid advances have taken place in the processing of Galfenol in micro and nano-scales. Weston *et al.* [130] measured the magnetic properties of 160-nm thick  $\text{Fe}_{81}\text{Ga}_{19}$  (110) oriented films deposited epitaxially on Cu(100)/Si(100) substrates. Subsequently, Butera *et al.* [131] successfully obtained (100) oriented 90-nm thick films of  $\text{Fe}_{81}\text{Ga}_{19}$  epitaxially deposited on MgO substrate. An extensive study of the effect of deposition conditions on film thickness, composition and calculated value of magnetostriction for (110) oriented Galfenol films deposited on glass as well as Si substrates showed promising results [132]. A comprehensive study of magnetostriction in Fe-Ga and Fe-Ga-Al systems performed using a high-throughput combinatorial approach [133] reflected the characteristics of bulk samples. Significant research [134, 135] has also taken place in order to develop Galfenol nanowire arrays of different composition having wires which are upto 60  $\mu\text{m}$  in length and diameter varying from 10 to 200 nm. These micro/nano-scale processing techniques would be beneficial for use of Galfenol in MEMS and NEMS applications.

#### 1.5.4. Applications of Fe-Ga alloys

Galfenol is a structural magnetostrictive material and hence it can be used to design devices which use its structural properties as well as magnetostrictive actuation and sensing capabilities. Several researchers have designed innovative proof-of-concept devices using the special attributes of Galfenol.

Yoo *et al.* [136] designed a tuning fork-based gyro sensor shown in Figure 1.23(a) which uses mm-size Galfenol patches as actuator and sensor material in bending. Downey *et al.* [137] showed that mm-scale Galfenol rods can be used as a sensor in bending and the results of this work [137] was used to conceptualize a nanowire-based broadband acoustic sensor shown in Figure 1.23(b). Further work [138] in this area led to the mechanical characterization of Galfenol nanowires which showed that although their Young's modulus is similar to that of bulk material, they possess almost three times the tensile strength. Datta and Flatau [139] showed that Galfenol could be adhered to a structural material and used as strain sensor in bending.

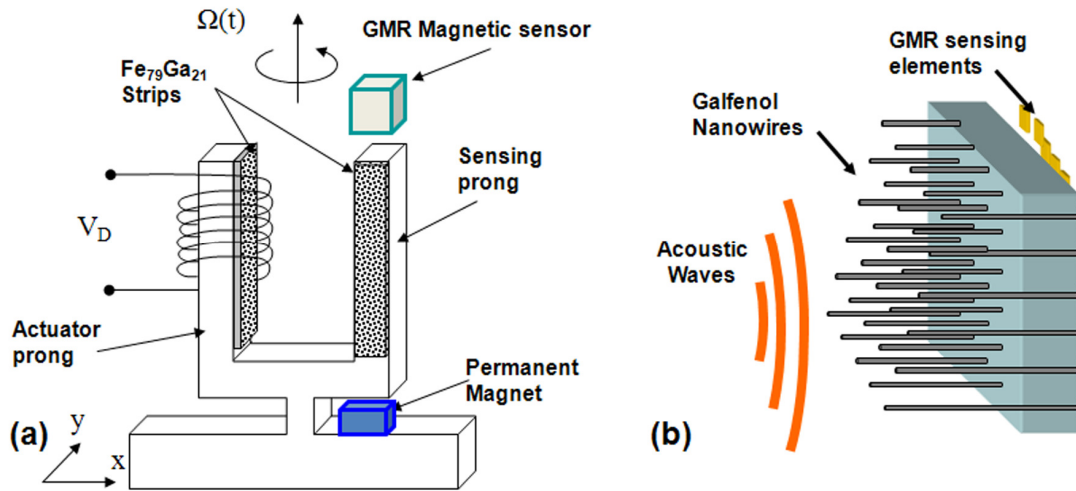


**Figure 1.23. (a) Tuning fork-based gyro sensor [136] and (b) nanowire acoustic sensor [134, 137] using Galfenol in bending mode.**

Hale and Flatau [140] and Parsons *et al.* [141] demonstrated the application of Galfenol in tactile sensing and torque sensing respectively. Ghodsi *et al.* [142] developed a positioning actuator for cryogenic environment. Ueno *et al.* developed linear actuator [143, 144], wobbler [145] and vibrator [146].

These devices showed proof-of-concept results but their performance can be improved with further knowledge of design parameters that play crucial role in determining the efficiency of these devices. In order to build an efficient prototype it is required to know the following:

- choice of active material (i.e. most suitable alloy composition)
- operating condition (pre-stress and bias magnetic field)
- size and geometry of active material
- impedance matching criteria
- location of active material in the device.

An investigation of these design parameters is performed in this dissertation.

#### *1.6. Overview of magnetomechanical models*

Modeling techniques are vital to device design. Magnetomechanical models can be used to evaluate design parameters, predict device response and control smart devices in a desired manner. An appropriate model is expected to account for the behavior of the material and its interaction with its environment. The modeling of material behavior is addressed in Section 1.6.1 and the interaction of an active material with other components of a device is discussed in Section 1.6.2. A brief review of these modeling techniques is presented in order to motivate the model proposed in Chapter 5 of this dissertation.

##### 1.6.1. Constitutive material models

Constitutive relations that describe the material behavior are usually based on energy minimization techniques. The first part of such a technique involves the

formulation of an energy functional which includes or precludes certain terms based on assumptions appropriate for the purpose of the model. The second part involves the use of mathematical techniques to extract the information about a required physical response of the material under the influence of force fields that perturb the energy.

The simplest model for magnetoelastic material is the coupled linear constitutive equations [2, 80, 81]. Considering both strain and magnetic induction in the material as functions of stress and magnetic field, a first order truncated Taylor series expansion about a given operating point  $(H_o, \sigma_o)$  can be written as Equations (1.53) and (1.54). Note that stress and magnetic field are assumed to be independent inputs to the material.

$$d\varepsilon = \left. \frac{\partial \varepsilon}{\partial \sigma} \right|_{H_o, \sigma_o} d\sigma + \left. \frac{\partial \varepsilon}{\partial H} \right|_{H_o, \sigma_o} dH \quad (1.53)$$

$$dB = \left. \frac{\partial B}{\partial \sigma} \right|_{H_o, \sigma_o} d\sigma + \left. \frac{\partial B}{\partial H} \right|_{H_o, \sigma_o} dH \quad (1.54)$$

The following Gibb's free energy formulation can be used to couple Equations (1.53) and (1.54) and also to provide physical interpretations of the differential quantities. The total workdone ( $dW$ ) on a unit volume of ferromagnetic material by a stress and magnetic field due to infinitesimal change in strain and magnetic induction can be expressed by Equation (1.55). Note that  $dW$  is not an exact differential.

$$dW = \sigma d\varepsilon + H dB \quad (1.55)$$

For a reversible process, the change in internal energy ( $dU$ ) can be expressed using Equation (1.56) which can be obtained by substituting Equation (1.55) in the 1<sup>st</sup> Law of Thermodynamics. Here  $S$  and  $T$  denote entropy and temperature respectively.

$$dU = \sigma d\varepsilon + HdB + TdS \quad (1.56)$$

The Gibb's free energy of the system is given by Equation (1.57)

$$G = U - \sigma\varepsilon - HB - TS \quad (1.57)$$

The change in Gibb's free energy in an isothermal reversible process can be expressed by Equation (1.58).

$$dG = dU - \varepsilon d\sigma - \sigma d\varepsilon - BdH - HdB - TdS \quad (1.58)$$

Combining Equations (1.56) and (1.58), the change in Gibb's free energy can be written as shown in Equation (1.59).

$$dG = -\varepsilon d\sigma - BdH \quad (1.59)$$

Equation (1.59) can be used to interpret the differential quantities in Equations (1.53) and (1.54) as follows. The mechanical compliance of the material in a process where the magnetic field ( $H_o$ ) is maintained constant while the stress is quasi-statically perturbed about a given stress ( $\sigma_o$ ) is expressed by Equation (1.60).

$$\left. \frac{\partial \varepsilon}{\partial \sigma} \right|_{H_o, \sigma_o} = - \left. \frac{\partial^2 G}{\partial \sigma^2} \right|_{H_o, \sigma_o} = s^{H_o, \sigma_o} \quad (1.60)$$

Similarly, magnetic permeability of the material in a process where the stress ( $\sigma_o$ ) is maintained constant while the magnetic field is quasi-statically perturbed about a given field ( $H_o$ ) is expressed by Equation (1.61).

$$\left. \frac{\partial B}{\partial H} \right|_{H_o, \sigma_o} = - \left. \frac{\partial^2 G}{\partial H^2} \right|_{H_o, \sigma_o} = \mu^{H_o, \sigma_o} \quad (1.61)$$

The strain coefficient ( $d = \partial\varepsilon/\partial H$ ) and stress sensitivity ( $d^* = \partial B/\partial\sigma$ ) which couple the effects of magnetic field and mechanical stress are expressed by Equations (1.62) and (1.63) respectively and are identical to each other as evident from their relation to the 2<sup>nd</sup> derivative of the Gibb's free energy.

$$\left. \frac{\partial\varepsilon}{\partial H} \right|_{H_o, \sigma_o} = - \left. \frac{\partial^2 G}{\partial\sigma\partial H} \right|_{H_o, \sigma_o} = d^{H_o, \sigma_o} \quad (1.62)$$

$$\left. \frac{\partial B}{\partial\sigma} \right|_{H_o, \sigma_o} = - \left. \frac{\partial^2 G}{\partial\sigma\partial H} \right|_{H_o, \sigma_o} = d^{*H_o, \sigma_o} \quad (1.63)$$

For small quasi-static perturbations of stress and magnetic field about a given operating stress  $[\tilde{\sigma}]$  and magnetic field ( $H$ ), the 3-D linearized coupled constitutive equations can be written as shown in Equations (1.64) and (1.65).

$$\varepsilon_i = s_{ij}\sigma_j + d_{ik}H_k \quad (1.64)$$

$$B_m = d^*_{mj}\sigma_j + \mu_{mk}H_k \quad (1.65)$$

Note that the indices  $i$  and  $j$  vary from 1 to 6 and the indices  $m$  and  $k$  vary from 1 to 3, such that  $x_4 = x_{23}$ ,  $x_5 = x_{31}$  and  $x_6 = x_{12}$  where  $x$  stands for  $\varepsilon$  or  $\sigma$ . The compliance tensor is identical to the inverse of the stiffness tensor as shown in Equation (1.51) and the stress sensitivity tensor is the transpose of the strain coefficient tensor.

Various non-linear models have also been developed to account for the magnetomechanical response of ferromagnetic materials over different operating conditions. Higher order series expansion of the free energy yielded the Landau model [147, 148]. Bergqvist and Engdahl [149] combined the effects due to stress and magnetic field into an equivalent field term and incorporated this in the Preisach operator to model the effect of stress on magnetization. A stress-induced field term

was introduced into the Langevin term by Jiles to model the effect of stress on magnetization vs. field curves [150] as well as the effect of magnetic field on magnetization vs. stress curves [151]. Ghosh and Gopalakrishnan [152] used a neural network technique to non-linearize the coupled constitutive equations and successfully predicted both the actuation and sensing characteristics of magnetostrictive materials. These models were limited to one-dimensional analysis and did not account for magnetocrystalline anisotropy which is required to capture the directional preference of magnetization orientation based on the crystal symmetry of different materials.

Armstrong [153, 154] extended the Stoner-Wohlfarth [155] model to cubic anisotropy and was able to come up with a three-dimensional model for magnetostrictive actuation. This approach was adapted to model both the actuator and predict the sensor responses of single crystal and polycrystalline Galfenol subjected to collinear stress and magnetic fields [111, 156, 157]. This approach will be discussed in detail in Chapter 2. An extension to this approach was developed [128] to add stress-annealing effect by incorporating a uniaxial anisotropy. These models included Zeeman, stress-induced anisotropy and magnetocrystalline anisotropy energy but excluded the exchange energy because it is non-zero only within the domain wall and hence forms a small fraction of the total energy of a bulk sample. Moreover, the preclusion of the magnetostatic energy incapacitates the ability of these models to account for demagnetization effects.

Smith [158] developed a homogenized energy model which included magnetostatic, stress-induced anisotropy, magnetocrystalline anisotropy and

exchange energy terms. The exchange interaction was phenomenologically incorporated using Boltzmann statistics which ironically considers only non-interacting particles. Moreover the use of Boltzmann statistics is only applicable to a large number of particles and may not be a valid assumption near saturation when the material is almost in a single domain state. Using Armstrong's [153] energy formulation and Smith's [158] framework of homogenized energy model, Evans and Dapino [159] developed a magnetomechanical model which takes into account six possible directions of magnetization orientation instead of two directions in Smith's work [158]. These approaches introduce dynamic effects into the constitutive model using thermal relaxation techniques and are particularly useful for obtaining closed minor loops when operating an actuator or sensor with DC bias magnetic field and stress respectively.

Besides these macroscopic models, micro-magnetic models [160-165] which use the Landau-Lifshitz-Gilbert (LLG) equation can also be used to predict static as well as dynamic magnetomechanical behavior. These models include all the relevant energy terms which affect the magnetization direction and hence can be more accurate for prediction of domain evolution and domain wall dynamics but they require excessive computation time and resources thereby making them not a preferred choice for prediction of bulk material response. Nevertheless, micro-magnetic models should be considered for design of MEMS and NEMS magnetostrictive devices.

### 1.6.2. Device-level models

The constitutive material models are suitable to predict the material response but they cannot be used directly to model a device. In order to do so, they need to be integrated with structural and magnetic models which can accommodate the forces or electric currents applied to the device and predict the displacement and electrical voltage response from the device.

Structural models are used to solve the mechanical boundary value problem of the device. They can be constructed using lumped parameter (mass-spring-damper) formulation [81] or continuum mechanics formulation such as beam/plate theory or finite element methods. The details of incorporating induced-strain actuation in plate theory [1, 2] will be discussed in Chapter 5.

Magnetic models are used to solve the magnetic boundary value problem of the device. They can also be constructed using lumped parameter magnetic circuit formulation [81] or by explicitly solving the Maxwell's equations with appropriate constraints in a finite element formulation [166].

The final step in device-level modeling involves integration of the constitutive material model, the structural model and the magnetic model. Traditionally, lumped parameter type “equivalent” circuit approach [81] is used to integrate the results obtained from each of the component models. The transition from mechanical to magnetic circuit takes place using a transformer ratio; known as coupling factor. The coupling factor will be discussed in detail in Chapter 2. An alternate approach [166] of model integration uses a commercial finite element package (e.g. COMSOL Multiphysics®) that offer the flexibility of coupling multiple boundary value

problems. The algorithm for traditional device-level modeling is shown in Figure 1.24.

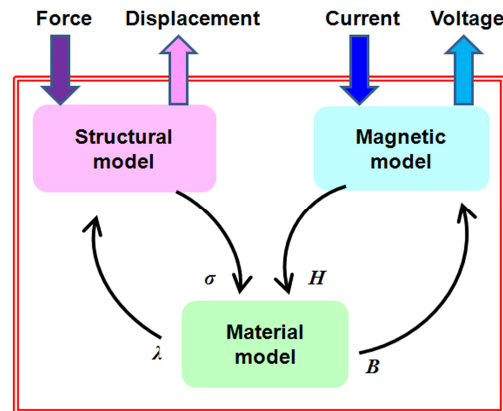


**Figure 1.24. Flow diagram of traditional device-level model.**

### 1.7. Objectives and organization of the dissertation

The broad objective of this dissertation is to understand the magnetostrictive response of Galfenol and develop design parameters and modeling tools which can be used for the development of actuators and sensors using Galfenol. The main advantage of Galfenol over other smart materials lies in its combination of structural and magnetostrictive properties which enables it to be used as a transducer material in tension, bending, shear or torsion. This dissertation attempts to understand the behavior of Galfenol particularly under bending as it encompasses the response of the material in tension as well as compression. An emphasis has been given to explain the material's response in terms of the physics of the process. All studies have been performed using single crystal Galfenol under quasi-static conditions in order to estimate the baseline performance.

Chapter 2 describes experimental studies and model simulations of the effect of stress, magnetic field and alloy composition on figures of merit such as energy

density, magnetomechanical coupling factor and sensing gage factor. The goal of this chapter is to understand the behavior of Galfenol alloys under different stress and magnetic field conditions and demonstrate a generalized technique for obtaining figures of merit which can serve as design parameters for developing adaptive transducers and control systems for such transducers. This database can be used to choose an appropriate alloy and also to optimize the performance of transducers under varying operating stress and magnetic field conditions. The outcome of this work helped in determining an appropriate alloy composition for further tests and aided in the design of the bending experiments described in Chapters 3 and 4. The experimental characterization provided the model parameters which were used in Chapter 5 for model validation.

Chapter 3 discusses the challenges related to characterization of a magnetostrictive member subjected to bending and proposes a suitable experimental technique to overcome some of these challenges. This technique, i.e., a four-point bending test, is performed on a Galfenol beam under different bias magnetic fields. The magnetic response of the beam is shown and is explained using an energy-based approach. The outcome of this work helps in determining the sensing capability of only a Galfenol member as opposed to the Galfenol being attached to a structural component. This work logically leads to the topic described in Chapter 4.

Chapter 4 introduces the concept of laminated magnetostrictive composite and describes experimental characterization of the actuator and sensor performance of cantilevered Galfenol-Aluminum unimorph. A detailed experimental study is performed by varying three parameters; applied magnetic field, tip loading and

Aluminum layer thickness. The experimental results demonstrated non-linearity in the magnetomechanical response of the structure and also exhibited structural coupling between the extensional and bending modes of the structure. In order to investigate these observations, an appropriate modeling technique had to be developed.

Chapter 5 describes a modeling approach that can couple the non-linear behavior of the active material with the structural components and magnetic circuit of a device using a recursive algorithm which combines the constitutive material model with the mechanical and magnetic boundary value problems posed by the device that is being modeled. The model simulations were used to perform a wider range of parametric study of the effect of magnetic field, mechanical stress and active/passive layer thickness ratio which was earlier introduced in Chapter 4. The simulation results were also compared to the experimental behavior presented in Chapter 4.

Finally, Chapter 6 summarizes the work of Chapters 2-5 and highlights the original contribution of this dissertation. Possible applications are described where the knowledge of this dissertation might be utilized. Future research directions are suggested to improve the modeling technique introduced in this work.

## Chapter 2: Experimental studies and model simulations of actuator and sensor figures of merit

Design of transducers using active materials requires the knowledge of certain figures of merit which provide a measure of efficiency for these active materials as an actuator or a sensor and are also helpful for comparing different active materials. The *energy density*, which gives a measure of the energy that can be obtained from the material and the *magnetomechanical coupling factor*, which is a dimensionless number that gives a measure of the transduction efficiency of the material are both commonly used as actuator figures of merit. Similarly, a dimensionless *gage factor* can serve as the figure of merit for sensing applications. These figures of merit are usually evaluated as material constants assuming a linear behavior of the material over useful operating stress and magnetic field ranges. The calculation of these figures of merit requires the knowledge of the material parameters introduced in Equations (1.60) – (1.63).

### 2.1. Background and scope of this work

Prior work by Clark *et al.* calculated stress-dependent permeability ( $\mu$ ) and strain coefficient ( $d$ ) in single crystal  $\text{Fe}_{83}\text{Ga}_{17}$  [84] and  $\text{Fe}_{78.6}\text{Ga}_{21.4}$  [104], but these calculations involved the choice of saturation magnetic field and an averaging over the entire B-H or  $\lambda$ -H curve for each pre-stress. Kellogg *et al.* [107] showed both stress and magnetic field-dependent values of stress sensitivity ( $d^*$ ) and Young's modulus ( $E$ ) of a water-quenched  $\text{Fe}_{81}\text{Ga}_{19}$  single crystal sample by using a polynomial fit of the experimental B- $\sigma$  and  $\varepsilon$ - $\sigma$  curves respectively. Since Kellogg *et*

*al.* [107] could not maintain constant magnetic field during the major-loop cyclic stress tests, the values of  $d^*$  and  $E$  were under-estimated and over-estimated respectively. Atulasimha *et al.* [167] were able to obtain better estimates of  $d^*$  and  $E$  by experimentally maintaining a constant magnetic field.

This chapter presents the actuator and sensor characterization results of  $\text{Fe}_{84}\text{Ga}_{16}$  and discusses the physical reasons for the non-linear behavior observed. The experimental results are used to obtain material properties such as permeability, Young's modulus, strain coefficient and stress sensitivity as functions of discrete operating stresses and magnetic fields which are in turn used to calculate the energy density, magnetomechanical coupling factor and gage factor of the material at these operating conditions.

An energy-based model is used to simulate the experimental behavior of  $\text{Fe}_{84}\text{Ga}_{16}$ . It is shown that all the parameters required for the energy-based model can be obtained from the actuator characterization and this single set of parameters are sufficient to model both the actuator and sensor behavior. The model is used to simulate the material properties and the figures of merit as continuous functions of stress and magnetic field in  $\text{Fe}_{84}\text{Ga}_{16}$ , which are compared with the experimental values. The effect of alloy composition as well as operating conditions on the actuator and sensor figures of merit are studied by using the model to simulate the stress and magnetic field-dependent figures of merit of  $\text{Fe}_{84}\text{Ga}_{16}$ ,  $\text{Fe}_{82.5}\text{Ga}_{17.5}$  and  $\text{Fe}_{81}\text{Ga}_{19}$ .

## 2.2. Experiment

This section describes the sample preparation technique, the experimental setup and test procedures used for characterizing the  $\text{Fe}_{84}\text{Ga}_{16}$  sample as an actuator

and sensor. The sample preparation and experimental details for  $\text{Fe}_{82.5}\text{Ga}_{17.5}$  and  $\text{Fe}_{81}\text{Ga}_{19}$ , are available in prior work by Datta *et al.* [105] and Atulasimha *et al.* [108]. An in-house built transducer [107] was used to characterize the sample under quasi-static stresses and magnetic fields applied along the  $\langle 100 \rangle$  long axis of the rod-shaped sample. Both the actuator and sensor characterization involved the measurement of strain, magnetic field and magnetic induction along the  $\langle 100 \rangle$  direction of the sample.

### 2.2.1. Sample description

All samples used in this study were prepared in Materials Preparation Center, Ames, Iowa [168]. The 25-mm long and 6.25-mm diameter rod of  $\text{Fe}_{84}\text{Ga}_{16}$  shown in Figure 2.1, was obtained from a single crystal ingot grown using the Bridgman technique in a resistance furnace [168].

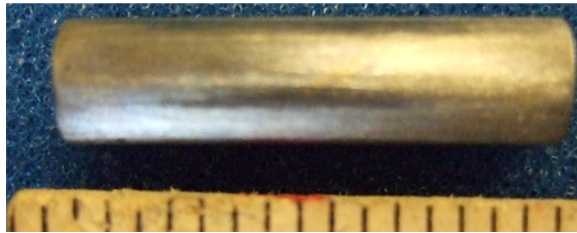


**Figure 2.1.  $\text{Fe}_{84}\text{Ga}_{16}$  rod-shaped sample. The  $\langle 100 \rangle$  crystal direction is along the length of the rod.**

Appropriate quantities of iron and gallium were cleaned and arc melted several times under an argon atmosphere. The buttons were then remelted and the alloy drop cast into a copper chill cast mold to ensure compositional homogeneity throughout the ingot. The as-cast ingot was placed in an alumina crucible and heated under a vacuum to 900 °C. After reaching 900 °C, the growth chamber was backfilled

with ultra high purity argon to a pressure of  $1.03 \times 10^5$  Pa. This over-pressurization is necessary in order to maintain stoichiometry. Following pressurization, heating was continued until the ingot reached a temperature of 1600 °C and held for 1 hour before being withdrawn from the furnace at a rate of 4 mm/hr. The ingot was annealed at 1000 °C for 168 hours using heating and cooling rates of 10 °C per minute. The ingot is considered to be in the “slow-cooled” state after this annealing process. Using back reflection Laue diffraction, the rod was oriented and sectioned from the ingot with a  $\langle 100 \rangle$  crystal axis aligned within  $\pm 0.5^\circ$  of the rod’s longitudinal axis. Energy Dispersive Spectroscopy performed on the rod showed that it contains  $83.8 \pm 0.6$  atomic % iron and  $16.2 \pm 0.6$  atomic % gallium. Sample details of  $\text{Fe}_{82.5}\text{Ga}_{17.5}$  and  $\text{Fe}_{81}\text{Ga}_{19}$  can be found in Refs. [105, 108].

### 2.2.2. Description of transducer

A schematic of the water-cooled quasi-static transducer [107] is shown in Figure 2.2. The transducer comprised of a housing that formed a closed magnetic circuit which enclosed a solenoid (drive coil) having a sample chamber in its core. A Techron LVC623 linear amplifier was used to supply current to the drive coil. It is important to obtain a closed magnetic circuit so that the characterization results are independent of the demagnetization effects which can arise due to the finite length of the sample. Annealed low carbon steel end-pieces were used as interfaces between the sample and the transducer housing to form a closed magnetic circuit. These end-pieces and an output shaft from the transducer also constituted a load path which was used to apply compressive forces upto 3650 N. As the temperature can affect the magnetization and magnetostriction data, a digital thermocouple was used to monitor

the solenoid temperature, which was maintained at 23 °C by running water through cooling tubes placed around the solenoid.

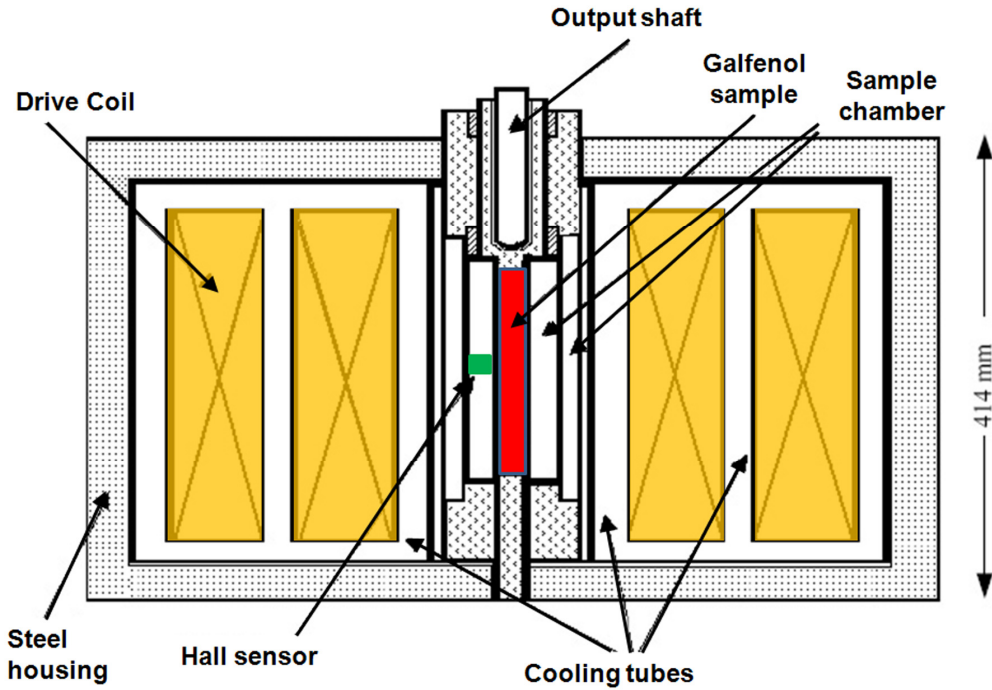


**Figure 2.2. Schematic of the transducer assembly, after Kellogg *et al.* [107].**

### 2.2.3. Instrumentation

Figure 2.3 shows the instruments mounted on the sample. The strain in the sample was measured by two resistive strain gages (Vishay Micro-Measurements: CEA-06-250UN-350) attached in a quarter bridge configuration on diametrically opposite sides of the rod at mid-length to counter the effect of any bending moment. An Allegro 1323 linear Hall-effect sensor placed parallel to the sample measured the magnetic field and a pick-up coil with 50 turns wound around the sample measured the magnetic induction using an integrating fluxmeter. The data was collected during the experiment using a computer-controlled system at 50 scans per second. A finite element model of the experimental setup showed that the magnetic induction and

magnetic field measurement can vary at most by 4 % based on the position of the pick-up coil and Hall sensor along the length of the sample [45].

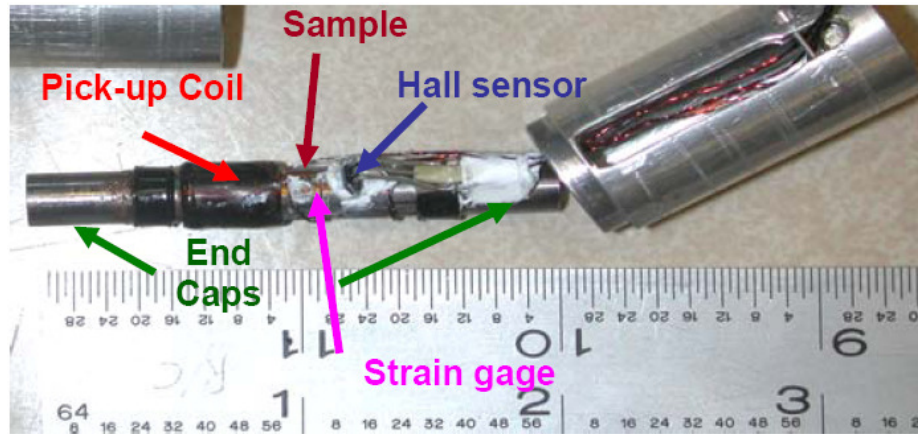


**Figure 2.3. Measurement devices mounted on the sample.**

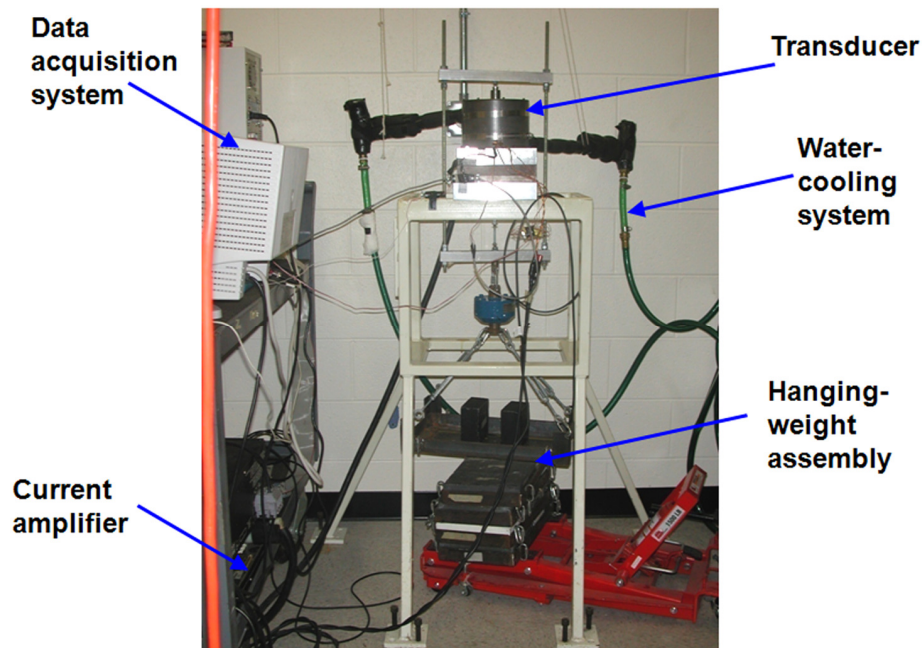
Table 2.1 describes the measurement devices used to measure the strain, magnetic field and magnetic induction. The resolution was calculated based on a 12-bit National Instruments PCI-MIO-16E-4 data acquisition card which was used to acquire the data from the measurement devices. The error estimate in measurement is calculated as the sum of the absolute values of possible errors in any quantity used to calculate the physical quantity of interest from the measured voltage.

**Table 2.1. Description of measurement devices.**

Quantity	Measurement device	Sensitivity	Resolution	Range	Error
Strain	Strain gages and Vishay 3800 strain indicator	2500 $\mu\epsilon/V$	0.61 $\mu\epsilon$	$\pm 10$ V	3 %
Magnetic field	Hall sensor and Vishay 2310 signal conditioner	31 kA/Vm	7.56 A/m	0 – 5 V	4 %
Magnetic induction	Pick-up coil and Walker MF-10D fluxmeter	1 T/V	$2.44 \times 10^{-4}$ T	$\pm 3$ V	2 %

#### 2.2.4. Actuator characterization under constant stress

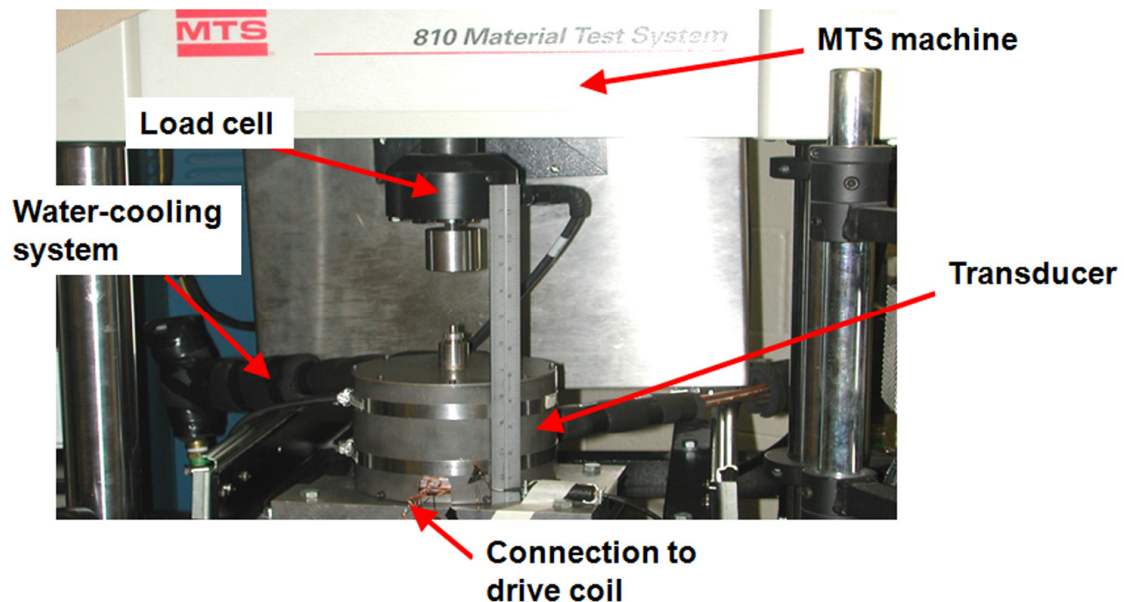
Figure 2.4 shows the different components of the actuator characterization test setup. The actuator characterization involved measurement of the magnetic induction ( $B$ ) and magnetostriction ( $\lambda$ ) of the sample under quasi-static 0.01 Hz, 70 kA/m amplitude sinusoidal applied magnetic field ( $H$ ) conditions for 4 cycles. This magnetic field cycle was repeated with the sample subjected to compressive prestresses ( $\sigma$ ) of 0, 18, 34, 50 and 66 MPa using lead dead weights arranged in a free-hanging weight assembly. Prior to each test, the sample was stabilized after applying the compressive stress and then demagnetized over 167 cycles using a 1 Hz sinusoidal magnetic field which underwent a 5 % geometric decay every 1.5 cycles from an initial amplitude of 97 kA/m. The actuator characterization provided information on material properties such as saturation magnetization ( $M_s$ ), saturation magnetostriction ( $3\lambda_{100}/2$ ), magnetic permeability ( $\mu$ ) and strain coefficient ( $d$ ).



**Figure 2.4. Actuator characterization setup.**

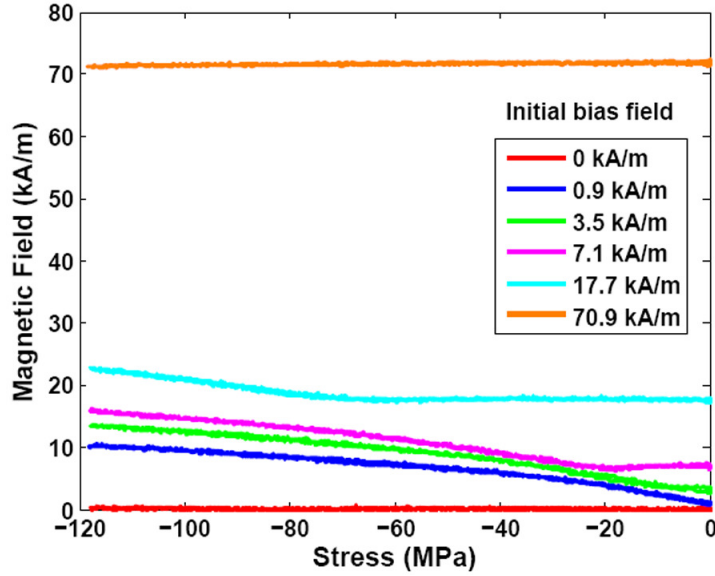
### 2.2.5. Sensor characterization under constant magnetic field

Figure 2.5 shows the different components of the sensor characterization test setup. The sensor characterization involved measurement of the magnetic induction and total strain ( $\varepsilon$ ) of the sample under quasi-static compressive stress from zero to 120 MPa and back to zero at a linear ramp rate of 2 MPa/s while the sample was subjected to DC bias magnetic fields of 0, 1, 1.8, 3.5, 5.3, 7.3, 8.8, 17.8, 35.5 and 71.2 kA/m. The compressive stress cycle was applied using a hydraulic MTS 810 universal testing machine in feedback force-control mode. The compressive force was measured using a load cell. The test sequence comprised of demagnetizing the sample followed by applying the DC bias magnetic field and cycling the stress. At the end of the stress cycle, the magnetic field was turned off. The sensor characterization provided information on material properties such as saturation magnetization ( $M_s$ ), saturation magnetostriction ( $3\lambda_{100}/2$ ), Young's modulus ( $E$ ) and stress sensitivity ( $d^*$ ).



**Figure 2.5. Sensor characterization setup.**

Initially, the DC bias magnetic fields were produced by applying a constant current to the drive coil of the transducer such that the desired magnetic field was obtained when the sample was at zero stress. It was observed that a constant current through the solenoid did not produce a constant magnetic field in the sample during the stress cycle as shown in Figure 2.6.



**Figure 2.6. Magnetic field vs. compressive stress in the  $\text{Fe}_{84}\text{Ga}_{16}$  sample for different constant drive currents which produced the desired initial bias fields at zero stress.**

This behavior can be explained with the help of an equivalent magnetic circuit of the transducer and sample shown in Figure 2.7. The total magneto-motive force ( $MMF_{TOT}$ ) produced by a drive coil is the product of its number of turns ( $N$ ) and current ( $i$ ) flowing through it. The steel housing of the transducer can be modeled as a fixed reluctance ( $R_T$ ). The Galfenol rod can be modeled as a variable reluctance ( $R_S$ ).

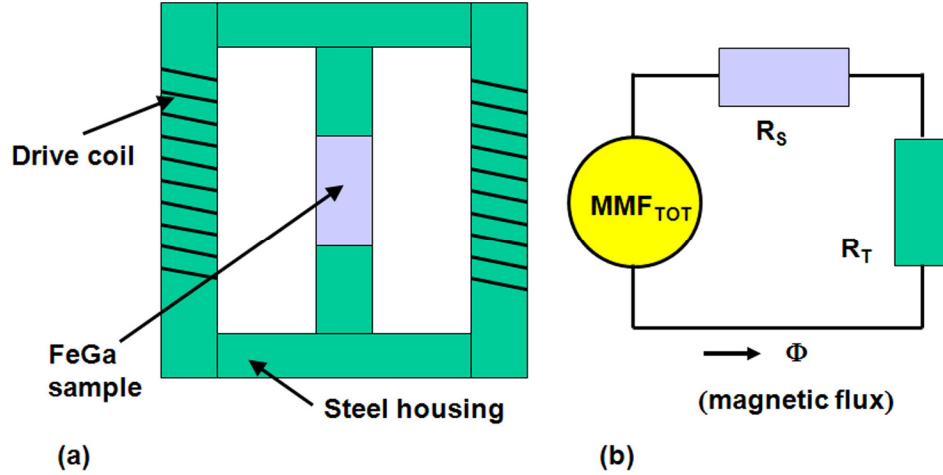


**Figure 2.7. (a) Schematic of the magnetic components in the test setup and (b) its equivalent magnetic circuit.**

The mmf across the Galfenol sample can be obtained from Equation (2.1) using the idea of a voltage-divider circuit.

$$MMF_{FeGa} = MMF_{TOT} \left( \frac{R_S}{R_S + R_T} \right) \quad (2.1)$$

The magnetic field in the sample can be obtained using Ampere's law which takes the form of Equation (2.2) where  $L_{FeGa}$  is the length of the Galfenol sample.

$$H_{FeGa} = \frac{MMF_{FeGa}}{L_{FeGa}} = \frac{Ni}{L_{FeGa}} \left( \frac{R_S}{R_S + R_T} \right) \quad (2.2)$$

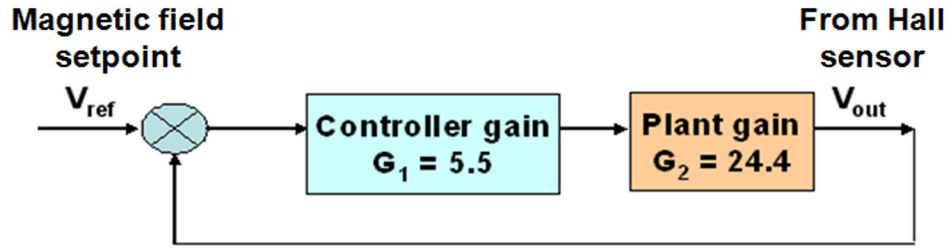
A change in the sample reluctance occurs due to stress-induced change in the permeability of the sample which in turn changes the mmf and internal magnetic field of the sample even for a constant drive current [108] as evident from Equation (2.2).

Figure 2.6 shows that a constant drive current produces the desired magnetic field under zero stress. On application of sufficient compressive stress, the magnetic moments start to rotate away from the direction of stress application which effectively reduces the magnetic permeability of the sample which in turn increases the sample

reluctance while the reluctance of the steel housing remains constant. The increased sample reluctance causes an increase in the mmf dropped across the sample for a constant input mmf across the drive coil [108]. A higher mmf across the sample increases the magnetic field in the sample as can be observed in Figure 2.6.

Note that the sample length ( $L_{FeGa}$ ) and cross-section area also change due to the strain in the material but these changes are on the order of 0.1 % compared to about a 100 times change in the permeability which dominates the change in  $R_S$ . An idea about the relative magnitude of changes in these quantities can be obtained from the results shown in Sections 2.4 and 2.5.

In order to overcome this problem, a feedback controller [108] was used to measure the response from the Hall-effect sensor and adjust the current in the drive coil to maintain a constant magnetic field in the sample throughout the stress cycle. The reference voltage ( $V_{ref}$ ) in the controller was set as the Hall sensor output at the desired magnetic field and was compared with the actual Hall sensor output ( $V_{out}$ ) during the stress cycle. The controller algorithm used a proportional gain of 5.5. A small differential gain of 0.5 was used to decrease overshoot from the setpoint. The controller response at 10 Hz was sufficient to keep the magnetic field constant for the given stress rate and data acquisition rate. Figure 2.8 shows the block diagram of the feedback control system which was used to obtain the desired magnetic field within 4 % accuracy. The plant gain includes the amplifier gain (15 V/V), Hall sensor sensitivity ( $3.23 \times 10^{-5}$  Vm/A), current gain (0.59 A/V) and drive coil parameter (16100 turns/m). Although the controller was used during the stress cycle, it had to be disconnected during the demagnetization sequence.



**Figure 2.8. Block diagram of feedback controller system used to maintain a constant magnetic field in the sample during a quasi-static stress cycle.**

Figure 2.9 shows that when the feedback controller was used to control the drive current, a constant magnetic field condition could be obtained during the entire quasi-static compressive stress cycle. Unable to maintain a constant magnetic field would result in an under-estimate of both stress sensitivity and compliance of the material. In the absence of such a controller, the characterization results would be dependent on the transducer magnetic circuit and hence would undermine the proper understanding of the magnetostrictive material being characterized.

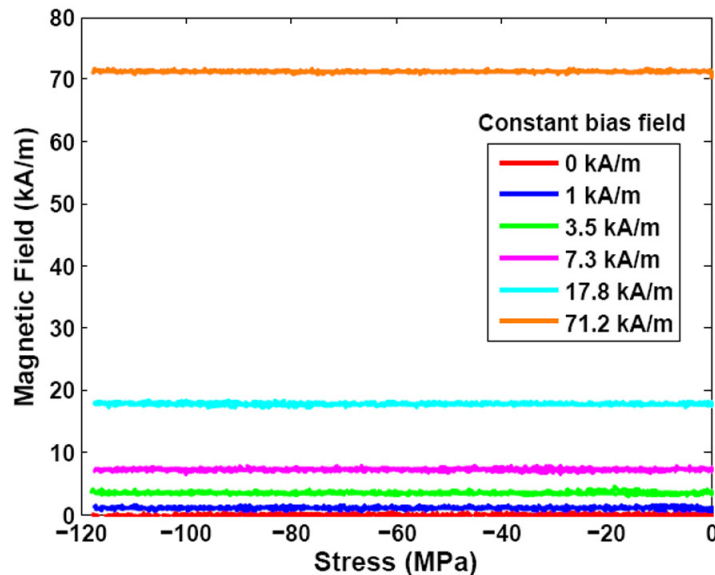


**Figure 2.9. Magnetic field vs. compressive stress in the  $\text{Fe}_{84}\text{Ga}_{16}$  sample with the feedback controller operational.**

### 2.3. Energy-based non-linear constitutive magnetomechanical model

The modeling approach used in this chapter was originally used by Armstrong [153] to model the actuation in Terfenol-D and was later adapted to both model the actuator response and predict the sensor behavior of single crystal and polycrystalline Galfenol subjected to axial stress [111]. In this work, the model is used to predict the magnetomechanical response of a single crystal rod along its  $\langle 100 \rangle$  longitudinal axis. Section 2.3.1 will discuss the energy formulation and Section 2.3.2 will outline the probabilistic approach of modeling the bulk magnetization and magnetostriction. A qualitative comparison with other appropriate models is also presented.

#### 2.3.1. Energy formulation

The energy terms which affect both strain and magnetization in a material were introduced in Sections 1.3 and 1.4. These terms are; exchange energy, magnetocrystalline anisotropy energy, magnetostatic energy, elastic energy, magnetoelastic energy, Zeeman energy and mechanical workdone.

Since, in this work we are only interested in modeling the magnetization and strain response of a bulk material, we can ignore the effect of exchange energy. The exchange energy is non-zero only within the domain walls and the volume of domains walls is only a small fraction of a bulk sample. Hence the omission of the exchange energy can be a practical assumption for this purpose. Note that the exchange energy should not be neglected while modeling the material at smaller length (e.g. thin films or nanostructures) scales where its effect becomes more predominant. Similarly, the magnetostatic energy may also be omitted from the energy formulation if we model a material which has been characterized in a closed

magnetic circuit such that its demagnetization factor is zero. This assumption is also fairly true as the transducer used for material characterization in this work provides a closed magnetic flux path.

With these assumptions, the change in the Gibb's free energy for a quasi-static, isothermal and reversible process can be expressed as the sum of changes in the magnetocrystalline anisotropy energy, magnetoelastic energy, elastic energy, Zeeman energy and mechanical workdone. Note that this energy formulation assumes that the magnetomechanical process takes place for quasi-static stress and magnetic field which for all practical purposes remain constant while the strain and magnetization in the material is perturbed. Mathematically, stress and magnetic field are the independent variables whereas strain and magnetization are the dependent variables. It was shown in Section 1.4 that minimization of the Gibb's free energy with respect to strain yields two significant results.

The first of these results states that the equilibrium strain in the material is the sum of a purely mechanical strain and a magnetoelastic strain. The mechanical strain depends only on the mechanical stress and the stiffness constants of the material. The magnetoelastic strain depends on the magnetization, i.e. the orientation of the magnetic moments and also on the spontaneous magnetostriction that arises due to the spin-orbit coupling. Note that the stiffness constants mentioned here should be evaluated under the condition such that no magnetic moment rotation can take place.

The second result from the energy minimization with respect to strain showed that the substitution of the equilibrium strains in the free energy yields a stress-induced anisotropy energy ( $E_\sigma$ ) and a 4<sup>th</sup> order magnetostrictive anisotropy ( $\Delta K$ ).

From here onwards we will denote the sum of the magnetostrictive anisotropy ( $\Delta K$ ) and the 4<sup>th</sup> order magnetocrystalline anisotropy ( $K_1$ ) as the net 4<sup>th</sup> order magnetocrystalline anisotropy ( $K_1$ ). This is a practical nomenclature because these two parameters cannot be experimentally distinguished from each other, i.e. experimentally measured values of  $K_1$  also includes  $\Delta K$  [169] unless each and every magnetic moment in the material can be clamped [170].

In this work we use the saturation magnetization ( $M_s$ ), the magnetostrictive constant ( $\lambda_{100}$ ) and the 4<sup>th</sup> and 6<sup>th</sup> order anisotropy constants ( $K_1$  and  $K_2$  respectively) to calculate the Zeeman, stress-induced anisotropy and magnetocrystalline anisotropy energies per unit volume due to a stress ( $\sigma$ ) and a magnetic field ( $H$ ) applied along the [100] direction as shown in Equations (2.3), (2.4) and (2.5) respectively.

$$E_H = -\mu_o M_s H \alpha_1 \quad (2.3)$$

$$E_\sigma = -\frac{3}{2} \lambda_{100} \sigma \alpha_1^2 \quad (2.4)$$

$$E_{an} = K_1 (\alpha_1^2 \alpha_2^2 + \alpha_2^2 \alpha_3^2 + \alpha_3^2 \alpha_1^2) + K_2 (\alpha_1^2 \alpha_2^2 \alpha_3^2) \quad (2.5)$$

The stress-induced anisotropy energy [58, 159, 169, 170] has been erroneously called the magnetoelastic energy in several works [111, 153]. The difference between these two energy terms has been explained in details in Section 1.4. It is also ascertained that ignoring the effect of the 6<sup>th</sup> order magnetocrystalline anisotropy constant  $K_2$  as done in prior work [153, 171] can severely change the magnetization and magnetostriction response to magnetic field, particularly at intermediate magnetic fields when the material is not saturated and all of the direction

cosines ( $\alpha_1, \alpha_2, \alpha_3$ ) of magnetization are non-zero. Hence appropriate estimates of  $K_2$  are used in this work.

The free energy ( $E_{TOT}$ ) of the system corresponding to different orientations in 3D space can be expressed in terms of their direction cosines ( $\alpha_1, \alpha_2, \alpha_3$ ) as shown in Equation (2.6).

$$E_{TOT}(\varphi, \theta) = E_H + E_\sigma + E_{an} \quad (2.6)$$

The direction cosines can be expressed in terms of the azimuthal angle ( $\varphi$ ) and polar angle ( $\theta$ ) such that  $\alpha_1 = \sin \theta \cos \varphi$ ,  $\alpha_2 = \sin \theta \sin \varphi$  and  $\alpha_3 = \cos \theta$ . It should be noted that Equation (2.6) is only appropriate for a single crystal but has been often used for modeling polycrystalline material [128, 159, 171] without taking into consideration the fact that the different orientations of the grains in a polycrystalline materials cannot be accounted for by using only one set of magnetization direction cosines in a global coordinate system. An appropriate method for adapting this energy formulation for polycrystalline materials by incorporating the volume fraction of grains with different orientations has been shown by Atulasimha *et al.* [111].

### 2.3.2. Modeling of constitutive behavior

Zhang and Chen [164] have shown that if the exchange and magnetostatic energy terms are not ignored then the Landau-Lifshitz-Gilbert equation can be used to predict the bulk magnetization and magnetostriction response as functions of stress and magnetic field. Although this technique can provide accurate results without imposing assumptions on the energy terms, it is computationally intensive, particularly for implementation in 3D.

A computationally efficient homogenized energy technique was successfully implemented by Smith [158] and Evans and Dapino [159]. This technique is useful for modeling hysteresis and minor loops but is limited by the consideration of only two [158] or six [159] energy minima in the material and require additional parameters compared to Armstrong's approach [153]. Moreover, these models [158, 159] assume that the bulk magnetization and magnetostriction is affected by thermal relaxation and incorporates that using Boltzmann statistics. Boltzmann statistics is only applicable to a large number of non-interacting particles and hence may not be appropriate in ferromagnetic materials as the magnetic moments interact with each other through the exchange coupling. Even if the idea of non-interacting particles is applied to domains instead of the magnetic moments, it is known that the number of domains in a bulk material diminishes rapidly at high magnetic fields and hence the assumption of "large number" which is associated with Boltzmann statistics will not hold true under most operating conditions.

On the other hand, Armstrong [153] modeled the bulk response of the material using a phenomenological probabilistic approach. Although the probabilistic approach takes the form of Boltzmann distribution, it should be noted that this is purely a phenomenological approach which does not use any postulate of Boltzmann statistics. Furthermore, the only justification for using it in place of the LLG equation (which includes exchange and magnetostatic energy terms) is because it provides a computationally efficient method for calculating the bulk response. In this work, we will use the anhysteretic modeling technique which is deemed suitable for Galfenol as Fe-Ga alloys exhibit negligible hysteresis.

In order to develop an expression for the bulk magnetization and magnetostriction, it is necessary to understand the following probabilistic approach. Let us assume that a bulk magnetic material is composed of a number of non-interacting magnetization units. The fraction of these units at a state  $(i, j)$ , which is defined by the orientation  $(\varphi_i, \theta_j)$  of these units, may be denoted by  $p_{ij}$ . From the physics of ferromagnetism, we know that a larger number of magnetic moments would align along a direction of lower energy. Since  $p_{ij}$  is proportional to the number of magnetic moments and inversely proportional to  $E_{TOT}(\varphi_i, \theta_j)$ , a probability density function given by Equation (2.7) can be used to express  $p_{ij}$  as a function of  $E_{TOT}(\varphi_i, \theta_j)$ . The choice of an exponential distribution in Equation (2.7) is made to avoid a singularity at  $E_{TOT} = 0$ .

$$p_{ij}(\varphi_i, \theta_j) = N_m \exp\left[\frac{-E_{TOT}(\varphi_i, \theta_j)}{\Omega}\right] \quad (2.7)$$

Here  $N_m$  is a normalizing factor which can be calculated from Equation (2.8) from the definition of a probability density function and  $\Omega$  is an empirical scaling factor. It is assumed that the energy is distributed in a sphere of unit radius.

$$N_m = \frac{1}{\int_{\varphi=0}^{2\pi} \int_{\theta=0}^{\pi} \exp\left(\frac{-E_{TOT}}{\Omega}\right) |\sin \theta| d\theta d\varphi} \quad (2.8)$$

Let us assume  $Q(\varphi, \theta)$  is a distributed physical quantity. The expected value  $\langle Q \rangle$  can be obtained from Equation (2.9).

$$\langle Q \rangle = \frac{\int_{\varphi=0}^{2\pi} \int_{\theta=0}^{\pi} Q(\varphi, \theta) \exp\left(\frac{-E_{TOT}}{\Omega}\right) |\sin \theta| d\theta d\varphi}{\int_{\varphi=0}^{2\pi} \int_{\theta=0}^{\pi} \exp\left(\frac{-E_{TOT}}{\Omega}\right) |\sin \theta| d\theta d\varphi} \quad (2.9)$$

In order to calculate the magnetization along [100], we substitute  $Q(\varphi, \theta)$  with  $M_{[100]}$  ( $= M_s \alpha_1$ ) in Equation (2.9) and convert the definite integrals to finite summations which gives us Equation (2.10). An optimum value of  $\Delta\varphi = \Delta\theta = 5^\circ$  is used for all cases to get converged solutions in reasonable computation time.

$$M = \frac{\sum_{\varphi=0}^{2\pi} \sum_{\theta=0}^{\pi} M_s \alpha_1 |\sin \theta| \Delta\theta \Delta\varphi \exp\left(\frac{-E_{TOT}}{\Omega}\right)}{\sum_{\varphi=0}^{2\pi} \sum_{\theta=0}^{\pi} |\sin \theta| \Delta\theta \Delta\varphi \exp\left(\frac{-E_{TOT}}{\Omega}\right)} \quad (2.10)$$

The magnetic induction is calculated using Equation (2.11).

$$B = \mu_o (M + H) \quad (2.11)$$

The same hypothesis can be extended to calculate the magnetostriction along [100] using Equation (2.12).

$$\lambda = \frac{\sum_{\varphi=0}^{2\pi} \sum_{\theta=0}^{\pi} \frac{3}{2} \lambda_{100} \left( \alpha_1^2 - \frac{1}{3} \right) |\sin \theta| \Delta\theta \Delta\varphi \exp\left(\frac{-E_{TOT}}{\Omega}\right)}{\sum_{\varphi=0}^{2\pi} \sum_{\theta=0}^{\pi} |\sin \theta| \Delta\theta \Delta\varphi \exp\left(\frac{-E_{TOT}}{\Omega}\right)} \quad (2.12)$$

The total strain can be described by Equation (2.13) where  $E_S$  is the purely mechanical Young's modulus of the material and is also known as the modulus at magnetic saturation. This is the modulus measured when all the magnetic moments are oriented either parallel or anti-parallel.

$$\varepsilon = \frac{\sigma}{E_S} + \lambda \quad (2.13)$$

Although model parameters such as  $M_s$  and  $\lambda_{100}$  can be easily obtained from the magnetomechanical actuator characterization described earlier, the parameters  $K_1$ ,  $K_2$ , and  $\Omega$  have to be obtained empirically in order to get the best fit of the experimental characterization curves. Experimentally measured values of  $K_1$  and  $K_2$

for quenched iron-gallium alloys [118] are used as a starting estimate for determining these empirical values. A detailed study of the effect of the model parameters on the model prediction can be found in the work of Atulasimha *et al.* [156]. The model parameters used for the different samples in this chapter are shown in Table 2.2.

**Table 2.2. Model parameters used in energy-based model.**

Parameters	Fe <sub>84</sub> Ga <sub>16</sub>	Fe <sub>82.5</sub> Ga <sub>17.5</sub>	Fe <sub>81</sub> Ga <sub>19</sub>
M <sub>s</sub> (kA/m)	1456	1420	1321
λ <sub>100</sub> (με)	165	210	212
K <sub>1</sub> (kJ/m <sup>3</sup> )	13	16	17.5
K <sub>2</sub> (kJ/m <sup>3</sup> )	-90	-90	0
Ω (J/m <sup>3</sup> )	600	630	707
E <sub>S</sub> (GPa)	76	65	59

#### 2.4. Model validation

This section presents the experimental results obtained from the actuator and sensor characterization of Fe<sub>84</sub>Ga<sub>16</sub>. The trends are explained using the energy terms discussed earlier. Model simulations of the actuation and sensing behavior are presented and a statistical method is developed to estimate the error in model simulations.

##### 2.4.1. Model fitting of actuator behavior

Figure 2.10 shows the magnetic induction in Fe<sub>84</sub>Ga<sub>16</sub> as a function of the quasi-static magnetic field at different compressive pre-stresses acting on the sample. The saturation magnetization of the sample was calculated to be 1445 ± 43 kA/m. It

was observed that the higher the compressive stress acting on the material, the higher is the magnetic field required to produce the same magnitude of magnetic induction as a result of which a higher magnetic field is required to saturate the material.

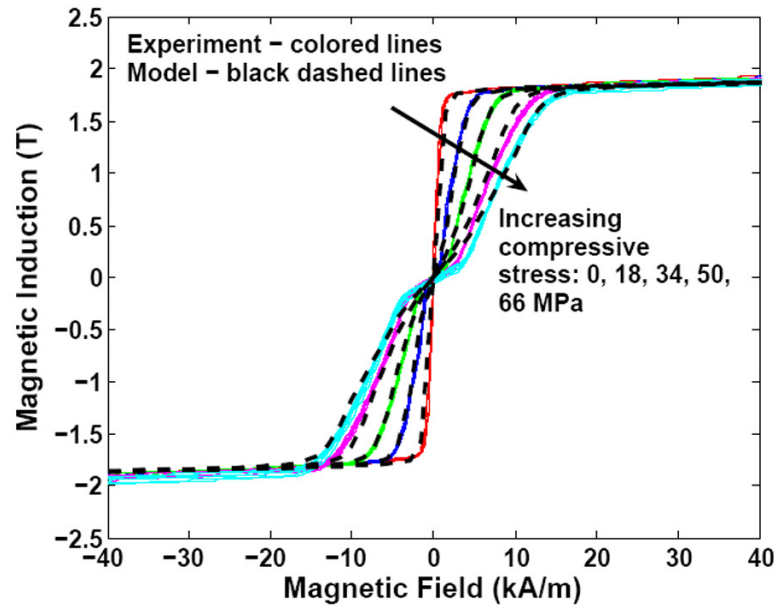


**Figure 2.10. Energy-based model prediction (dashed lines) and experimental (solid lines) magnetic induction ( $B$ ) vs. magnetic field ( $H$ ) at different compressive pre-stresses ( $\sigma$ ) in the  $\text{Fe}_{84}\text{Ga}_{16}$  sample.**

Although in the absence of stress, the equivalent  $\langle 100 \rangle$  directions have minimum energy in a magnetic material with cubic anisotropy, it can be hypothesized that if the compressive stress applied along the  $[100]$  crystal direction is high enough to overcome the magnetocrystalline anisotropy energy, then all the magnetic moments end up aligning perpendicular to the direction of stress and hence the  $[100]$  direction does not remain an easy axis. Under such a pre-stressed condition, when a small magnetic field is applied along  $[100]$ , the magnetic moments lying in the  $[010]$  and  $[001]$  energy wells start rotating away from  $[010]$  or  $[001]$  but do not align along  $[100]$  as it still remains a high energy direction. A net magnetic induction is still

measured along [100] due to the sum of the component of the local magnetizations directed along [100] as the magnetic moments precess around the [010] or [001] energy wells. On increasing the magnetic field to a critical value, an energy well is created along [100] which is marked by the sudden change in the slope of the B-H curve. This condition is described as the "burst region" in B-H curves. This critical value of magnetic field increases with increasing compressive pre-stress. On further increasing the magnetic field, more and more magnetic moments align along [100] as it becomes an absolute minimum energy direction. As the energy well along [100] grows deeper, the energy wells along [010] and [001] get shallower and finally these wells along [010] and [001] disappear. At this stage, all the magnetic moments align along [100] marking the onset of saturation which is denoted by the knee of the B-H curve.

Figure 2.11 shows the strain in  $\text{Fe}_{84}\text{Ga}_{16}$  as a function of the quasi-static magnetic field at different compressive pre-stresses acting on the sample. In order to compare the magnetoelastic strains only due to the magnetic field at different constant pre-stresses, the strains obtained only due to the pre-stress in the absence of a magnetic field were zeroed in Figure 2.11.

The saturation magnetostriction of the sample was calculated to be  $242 \pm 7 \mu\epsilon$  by recording the maximum strain due to magnetic field obtained at non-zero pre-stresses. In the absence of a pre-stress, the magnetic moments in the sample are assumed to be distributed equally along all easy or minimum energy directions. Hence a magnetic field applied along [100] can only rotate those magnetic moments

which are initially aligned along [010] or [001] towards [100] thereby producing the magnetostriction.

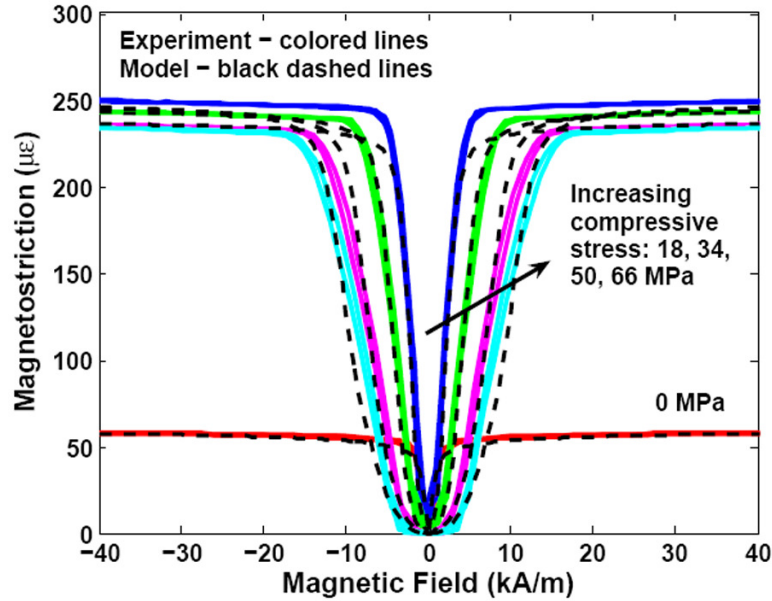


**Figure 2.11. Energy-based model prediction (dashed lines) and experimental (solid lines) magnetostriction ( $\lambda$ ) vs. magnetic field ( $H$ ) at different compressive pre-stresses ( $\sigma$ ) in the  $\text{Fe}_{84}\text{Ga}_{16}$  sample.**

When a sufficient compressive stress is applied along [100], the magnetic moments rotate away from [100] and align along [010] or [001]. When a magnetic field is applied along [100] of the pre-stressed sample, it is able to rotate much larger number of moments from [010] and [001] to [100] thereby yielding higher magnetostriction. It was ensured that the minimum compressive stress (18 MPa) applied during the experiment was high enough to orient all magnetic moments perpendicular to [100].

Similar to the magnetization behavior, it was observed that the higher the compressive stress acting on the material, the higher is the magnetic field required to produce the same magnetostriction as a result of which a higher magnetic field is

required to saturate the material. Also, for each compressive pre-stress, the  $\lambda$ -H curves have a region of very low slope until the magnetic field is high enough to overcome the magnetocrystalline and stress-induced anisotropy energy. The higher the pre-stress, the higher was the critical magnetic field required to initiate this “burst region.” This critical magnetic field for each pre-stress was found to be the same at which the slope of the B-H curve changes abruptly.

**Table 2.3. Estimation of magnetoelastic strain in Fe<sub>84</sub>Ga<sub>16</sub> at different pre-stresses and zero magnetic field.**

<b>Pre-stress</b> <b>[<math>\sigma_0</math> - MPa]</b>	<b>Measured pre-</b> <b>strain [<math>\epsilon_0</math> - <math>\mu\epsilon</math>]</b>	<b>Pure mechanical</b> <b>strain [<math>\sigma/E_S</math> - <math>\mu\epsilon</math>]</b>	<b>Magnetoelastic strain</b> <b>[<math>\lambda(\sigma = \sigma_0, H = 0)</math> - <math>\mu\epsilon</math>]</b>
0	0	0	0
-18	-440	-237	-203
-34	-658	-447	-211
-50	-906	-658	-248
-66	-1065	-868	-197

Table 2.3 shows that the difference between the pre-strains and the purely mechanical strain at a given pre-stress yields the increase in useful magnetostriction which is manifested as an increase in saturation magnetostriction on saturating the sample by applying a magnetic field at that pre-stress. The purely mechanical strain was calculated using  $E_S = 76$  GPa. The value of  $\lambda(\sigma = \sigma_0, H = 0)$  was calculated to be  $-215 \pm 23 \mu\epsilon$  using Equation (2.13). Note that this value is roughly the difference between the saturation magnetostriction at zero pre-stress and at higher pre-stresses

shown in Figure 2.11. This analysis confirms that the pre-stress produces a negative magnetoelastic strain which is regained as the additional useful magnetostriction on application of magnetic field.

Figure 2.12 shows the change in the azimuthal position of the energy minima as the sample, which is originally in a demagnetized state under a constant pre-stress, is saturated by increasing the magnetic field. Figure 2.12 can be compared to Figure 1.17 which showed the 3D energy distribution in a demagnetized pre-stressed sample subjected to increasing magnetic fields upto saturation.

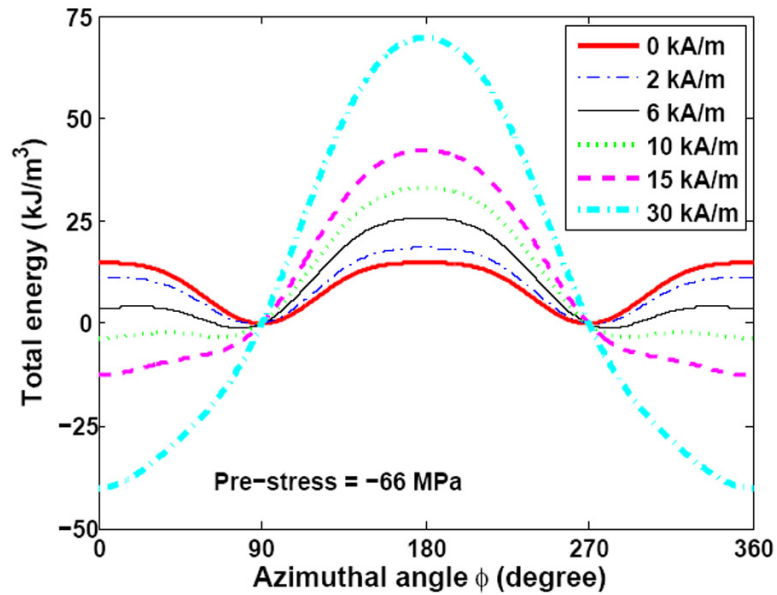


**Figure 2.12. Arbitrary total energy  $[E_{TOT}(\sigma,H)]$  vs. azimuthal angle ( $\phi$ ) of the magnetization direction at a constant pre-stress of -66 MPa and for magnetic field from 0 (demagnetized) to 30 kA/m (saturated). The energy map is plotted at a polar angle ( $\theta$ ) of  $90^\circ$ , i.e. in the azimuthal plane.**

#### 2.4.2. Model prediction of sensor behavior

Figure 2.13 shows the magnetic induction in  $\text{Fe}_{84}\text{Ga}_{16}$  as a function of the quasi-static compressive stress at different constant bias magnetic fields acting on the sample. The saturation magnetization of the sample was calculated to be  $1430 \pm 50$  kA/m. At zero magnetic field, stress has no effect on the net magnetization or magnetic induction because the magnetic domains rearrange in such a way that the magnetization in the domains end up forming closure loops to ensure that there is no stray magnetic field coming out of the material. Hence it is not possible to perform magnetostrictive sensing in the absence of a bias magnetic field.

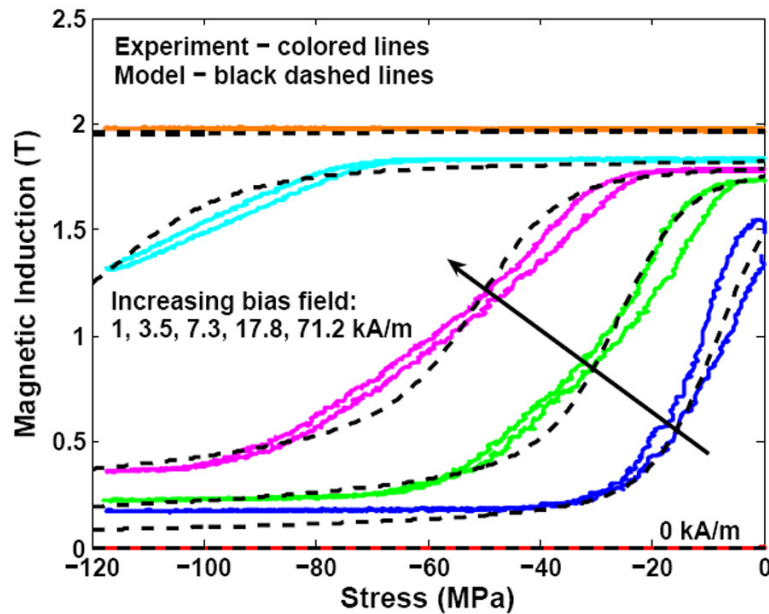


**Figure 2.13. Energy-based model prediction (dashed lines) and experimental (solid lines) magnetic induction ( $B$ ) vs. compressive stress ( $\sigma$ ) at different DC bias magnetic fields ( $H$ ) in the  $\text{Fe}_{84}\text{Ga}_{16}$  sample.**

On application of a bias magnetic field along [100], magnetic moments orient along the direction of the magnetic field and a net magnetic induction is observed at zero stress. If the bias magnetic field is high enough to align all the magnetic

moments along the direction of magnetic field then the material is said to be saturated at zero stress. On application of a compressive stress, the stress-induced anisotropy energy has to work to overcome the Zeeman and magnetocrystalline anisotropy energies during which no magnetic moments rotate. This region is denoted by the horizontal part of the curves close to zero stress in Figure 2.13 (clearly visible for bias fields  $\geq 7.3$  kA/m). On increasing the magnitude of stress, once the stress-induced anisotropy energy overcomes the Zeeman and magnetocrystalline anisotropy energies, the magnetic moments start to rotate away from the direction of magnetic field. This region is denoted by the downward sloping part of the  $B$ - $\sigma$  curves for bias fields between 1 and 17.8 kA/m.

Figure 2.13 also shows that beyond a certain critical value of compressive stress, the value of  $B$  attains saturation. The higher the bias magnetic field, the higher is the stress required to attain saturation. The reason for obtaining a non-zero value of  $B$  at saturation is due to the fact that under the influence of both stress and magnetic field used in this study, the absolute energy minimum does not occur at  $90^\circ$  from the direction of stress application but is usually at some azimuthal angle less than  $90^\circ$  thereby having a component of  $B$  along the direction of field/stress. For a given value of high compressive stress, the higher the bias magnetic field, the more the deviation of the magnetization vector from  $90^\circ$  and hence the higher the value of saturation  $B$ . For a given bias field, it is theoretically possible to apply a stress which can produce the energy minimum at  $90^\circ$  but the magnitude of the stress required to attain this state would be on the order of several GPa which is much higher than the strength of the material and hence for all practical purposes we can expect to see a residual  $B$  at high

stresses. This hypothesis was validated using the energy-based model by finding the azimuthal angle corresponding to the deepest energy well for different combinations of high compressive stress and magnetic fields as shown later in Figure 2.15.

Figure 2.14 shows the strain in  $\text{Fe}_{84}\text{Ga}_{16}$  as a function of the quasi-static compressive stress at different constant bias magnetic fields acting on the sample. At zero magnetic field, there is no strain in the sample at zero stress. On increasing the applied stress, a non-linear elastic region is observed which corresponds to additional magnetoelastic strain due to magnetic moment rotation superimposed on the elastic strain. Beyond a critical compressive stress ( $\sim 15$  MPa), all the magnetic moments align along the equilibrium direction and hence a linear  $\varepsilon$ - $\sigma$  curve is observed.

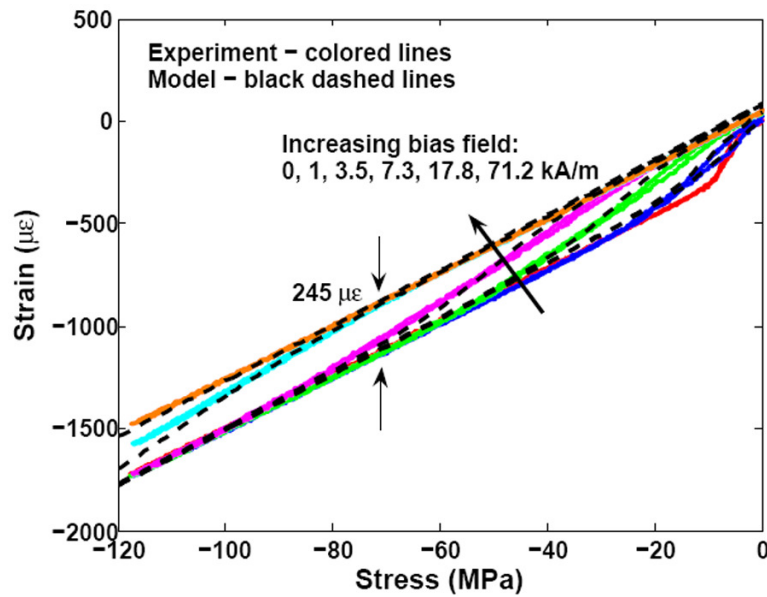


**Figure 2.14. Energy-based model prediction (dashed lines) and experimental (solid lines) strain ( $\varepsilon$ ) vs. compressive stress ( $\sigma$ ) at different DC bias magnetic fields ( $H$ ) in the  $\text{Fe}_{84}\text{Ga}_{16}$  sample.**

On application of a bias magnetic field, the material exhibits a magnetoelastic strain even at zero stress. On increasing the compressive stress, a linear  $\varepsilon$ - $\sigma$  curve is

seen until the stress-induced anisotropy overcomes the Zeeman energy and the magnetic moments start to rotate away from the field/stress direction. The magnetic moment rotation is exhibited by a non-linear region in the  $\epsilon$ - $\sigma$  curve which becomes linear once again at high stresses once all the magnetic moments have aligned along the equilibrium direction. The higher the bias magnetic field, the higher the compressive stress required to rotate the magnetic moments and hence the non-linearity in the  $\epsilon$ - $\sigma$  curves gets shifted towards higher compressive stresses at higher bias magnetic fields. The stress range used for the experiment was not sufficient to overcome the Zeeman energy due to 71 kA/m and hence the magnetic moments in the sample remain aligned along the direction of magnetic field throughout the stress cycle at this bias field. The Young's modulus of the sample at magnetic saturation or "hard modulus" was calculated to be  $76 \pm 5$  GPa. It was observed that the Young's modulus can change as a function of stress as well as magnetic field due to additional strain arising from magnetic moment rotation. This phenomenon is known as Delta-E effect and will be discussed in Section 2.5.

Figure 2.14 shows that the difference in strain at zero stress between zero and saturating bias magnetic fields is around  $60 \mu\epsilon$  which is equal to the value of maximum magnetostriction that can be observed at zero pre-stress in Figure 2.11. Also, the difference in strain at high stresses between zero and saturating bias magnetic fields is around  $247 \pm 4 \mu\epsilon$  which is equal to the saturation magnetostriction observed at non-zero pre-stresses in Figure 2.11. It is noteworthy that the magnetization and magnetostriction at saturation obtained from two independent

experiments yielded similar values and hence provided a measure of consistency for the actuator and sensor characterization techniques described in this chapter.

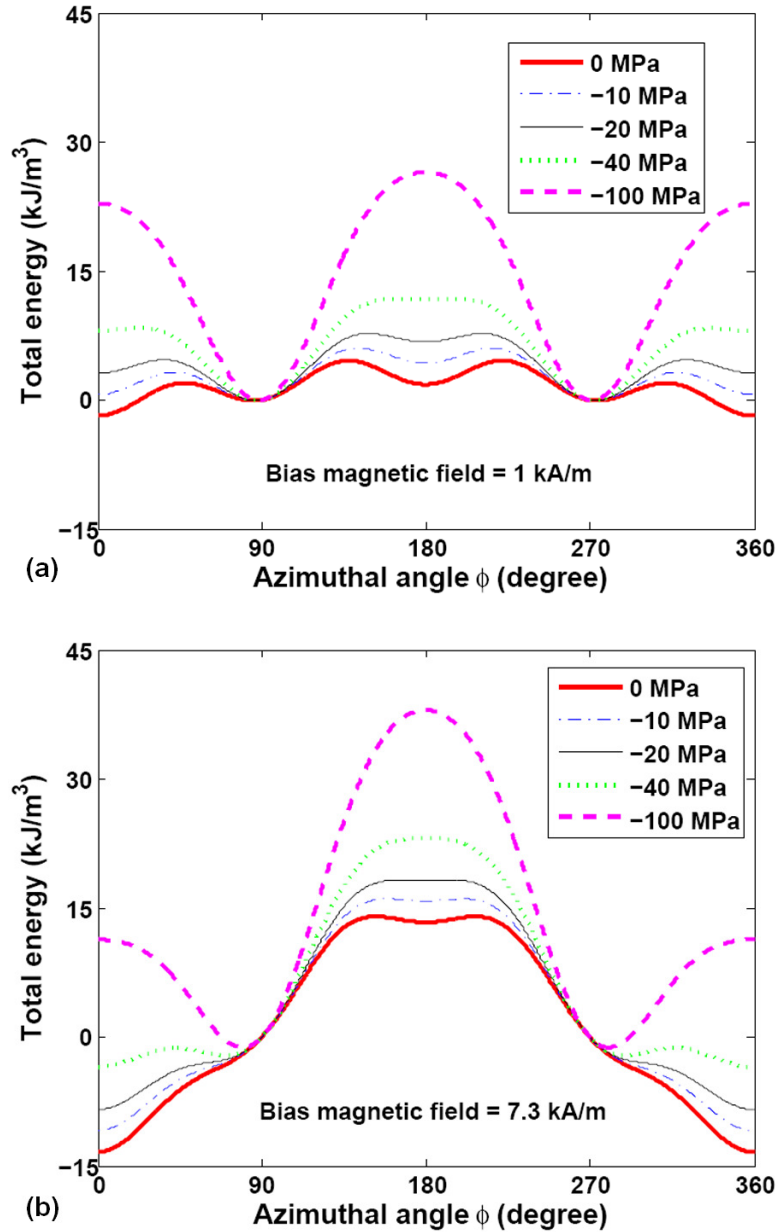


**Figure 2.15. Arbitrary total energy  $[E_{\text{TOT}}(\sigma, H)]$  vs. azimuthal angle ( $\phi$ ) of the magnetization direction at magnetic fields of (a) 1 kA/m and (b) 7.3 kA/m for compressive stresses ranging from 0 to 100 MPa. The energy map is plotted at a polar angle ( $\theta$ ) of  $90^\circ$ , i.e. in the azimuthal plane.**

Figure 2.15(a) shows an energy map at very low magnetic field (1 kA/m) when the material is not saturated at zero stress and Figure 2.15(b) shows the energy map at a magnetic field (7.3 kA/m) when the onset of magnetic saturation is evident at zero stress. The strikingly different energy profiles for the same stresses but at these two different magnetic fields help in the understanding of the sensing behavior of the material by visualizing the azimuthal position and number of energy minima at different operating stress and magnetic field conditions. Figure 2.15 can be compared to Figure 1.16 which showed the 3D energy distribution in a magnetically biased sample subjected to increasing compressive stresses.

#### 2.4.3. Error estimation

In order to use the energy-based model for design purposes, it is important to get an estimate of error between the experimental results and model fit. As the model provides a smooth function while the experimental data does not, in order to compare these two the experimental data was grouped into  $n$  divisions, each with equal number of data points. The mean and standard deviation of the  $i^{\text{th}}$  division is denoted by  $\bar{y}_i$  and  $SD_i$  respectively. The terms  $y_i^{\text{fit}}$  and  $SD_o$  denote the model predicted value for the  $i^{\text{th}}$  division and the standard deviation of the residuals  $(\bar{y}_i - y_i^{\text{fit}})$  respectively. The standardized absolute relative error (*SARE*) given by Equation (2.14) was calculated for the experimental data and model fit to quantify the goodness of the fit.

$$SARE = \frac{1}{n} \sum_n \left| \frac{\text{standardized residual}}{\text{standardized mean}} \right| = \frac{1}{n} \sum_{i=1}^n \left| \frac{(\bar{y}_i - y_i^{\text{fit}}) / SD_o}{\bar{y}_i / SD_i} \right| \quad (2.14)$$

Table 2.4 shows the *SARE* between the model prediction and experimental data for the Fe<sub>84</sub>Ga<sub>16</sub> sample.

**Table 2.4. Error estimates between experimental data and model fit.**

<b>Relationships</b>	B-H	λ-H	B-σ	ε-σ
<b>SARE (%)</b>	2.5	1.1	2.3	8.4

2.5. *Evaluation of stress and magnetic field-dependent material properties*

A set of coupled 1-D linear constitutive relations described by Equations (2.15) and (2.16) can be used to express small changes in strain and magnetic induction in magnetomechanically coupled materials about a given operating point of stress and magnetic field as described in detail in Section 1.6.1.

$$\varepsilon = s\sigma + dH \quad (2.15)$$

$$B = d^* \sigma + \mu H \quad (2.16)$$

Equations (2.15) and (2.16) suggest that the material properties such as permeability ( $\mu$ ), axial strain coefficient ( $d$ ), axial stress sensitivity ( $d^*$ ) and compliance ( $s$ ) or Young's modulus ( $E = 1/s$ ) can be calculated from the slopes of the plots shown in Figures 2.10, 2.11, 2.13 and 2.14 respectively.

Although values for all four of these material properties are generally used as if they are single-valued constants, the purpose of this section is to examine a more suitable assessment of these material properties as suggested in Equations (2.17) and (2.18), which reflect the stress and magnetic field-dependency of these material properties.

$$\varepsilon = s(\sigma, H)\sigma + d(\sigma, H)H \quad (2.17)$$

$$B = d^*(\sigma, H)\sigma + \mu(\sigma, H)H \quad (2.18)$$

### 2.5.1. Experimental method

The material properties were calculated from the experimental B-H,  $\lambda$ -H, B- $\sigma$  and  $\varepsilon$ - $\sigma$  plots using a moving average scheme. This method reduced the large error that can arise if numerical differentiation is performed on experimental data which is not smooth. A window of 0.4 kA/m (for B-H and  $\lambda$ -H) and 1 MPa (for B- $\sigma$  and  $\varepsilon$ - $\sigma$ ) were chosen and a straight line was fitted to all the data points lying inside this window. The slope of the line gave the material properties at the mean value of the field/stress range of that window. The window was moved across the entire range of data to obtain the material properties as functions of magnetic field/stress at different pre-stresses/DC bias magnetic fields respectively.

A limitation on the experimentally obtained data was that all the four magnetomechanical properties could be obtained only for the fifty possible combinations of the five pre-stresses and the ten bias magnetic fields at which the material was characterized.

### 2.5.2. Model simulations

In order to obtain all the material properties as continuous functions of stress and magnetic field, the energy-based model was used to generate B-H,  $\lambda$ -H, B- $\sigma$  and  $\varepsilon$ - $\sigma$  curves for stresses ranging from -150 to 50 MPa at an interval of 1 MPa and magnetic fields ranging from 0 to 100 kA/m at an interval of 0.1 kA/m. The first derivative of these curves obtained by numerical differentiation produced the material properties  $\mu(\sigma, H)$ ,  $d(\sigma, H)$ ,  $d^*(\sigma, H)$  and  $E(\sigma, H)$ .

### 2.5.3. Magnetomechanical properties

The experimental and model simulation of material properties of  $\text{Fe}_{84}\text{Ga}_{16}$  as functions of stress and magnetic field are shown in Figures (2.16) – (2.19). Figures (2.16) – (2.19) show that the model simulations capture the trend in the material properties with varying stress and magnetic field quite well but the model simulations appear to over-predict or under-predict the values of the properties. Such error between the experimentally obtained values and model simulations can be traced back to the fact that the model provides a good fit of the  $B$ - $H$ ,  $\lambda$ - $H$ ,  $B$ - $\sigma$  and  $\varepsilon$ - $\sigma$  curves on an average sense and not at all points on these curves. Any small deviation of the model from the experimental curves would be amplified during the numerical differentiation required to obtain the material properties. Nevertheless, the simulated values are of the same order of magnitude as the experimentally obtained values and for most of the operating region lie within the experimental scatter. Hence the model simulations can be safely assumed to reflect the experimental results. The *SARE* calculated for  $\mu_r$ - $H$ ,  $d$ - $H$ ,  $d^*$ - $\sigma$  and  $E$ - $\sigma$  curves in Figures (2.16) – (2.19) are 7.2 %, 12.4 %, 19.1 % and 28 % respectively.

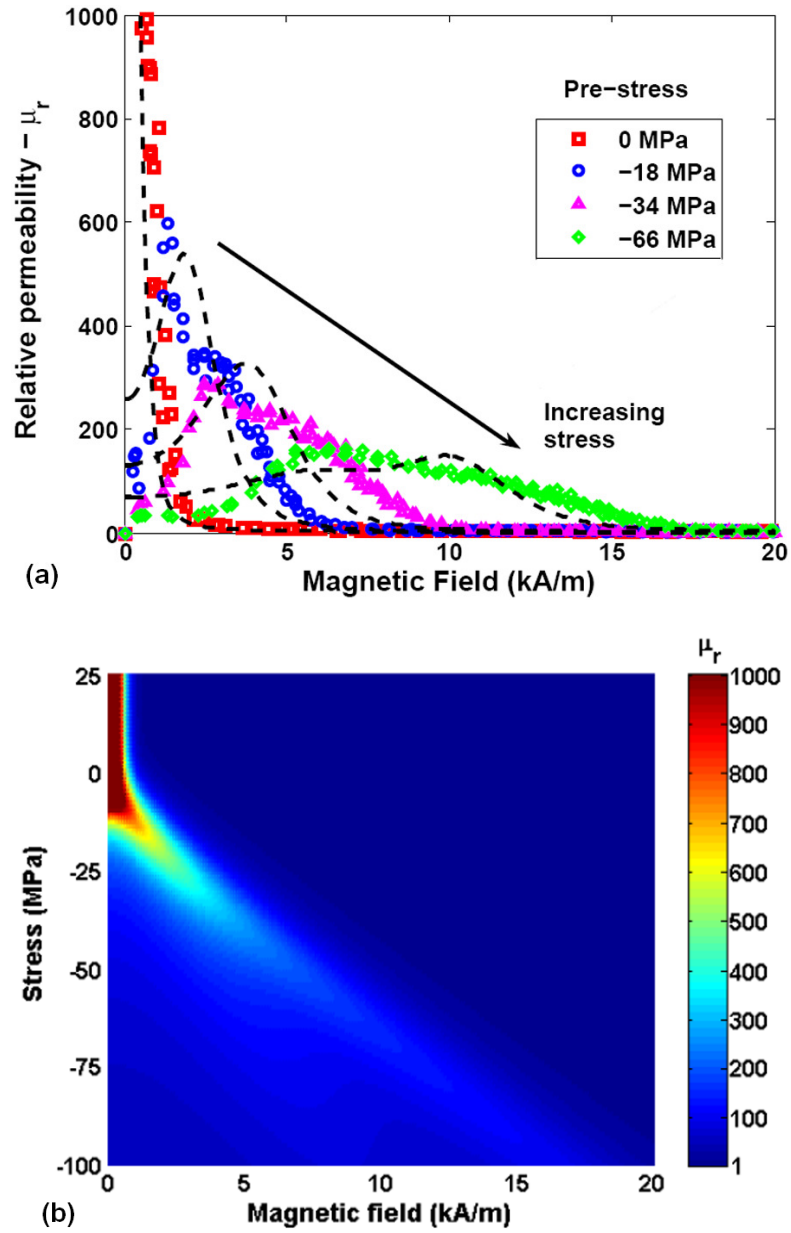


Figure 2.16. (a) Comparison of energy-based model prediction (black dashed lines) and experimental (colored markers) relative permeability ( $\mu_r$ ) in the  $\text{Fe}_{84}\text{Ga}_{16}$  sample. (b) Model simulation of relative permeability as a continuous function of stress and magnetic field -  $\mu_r(\sigma, H)$ , in the  $\text{Fe}_{84}\text{Ga}_{16}$  sample.

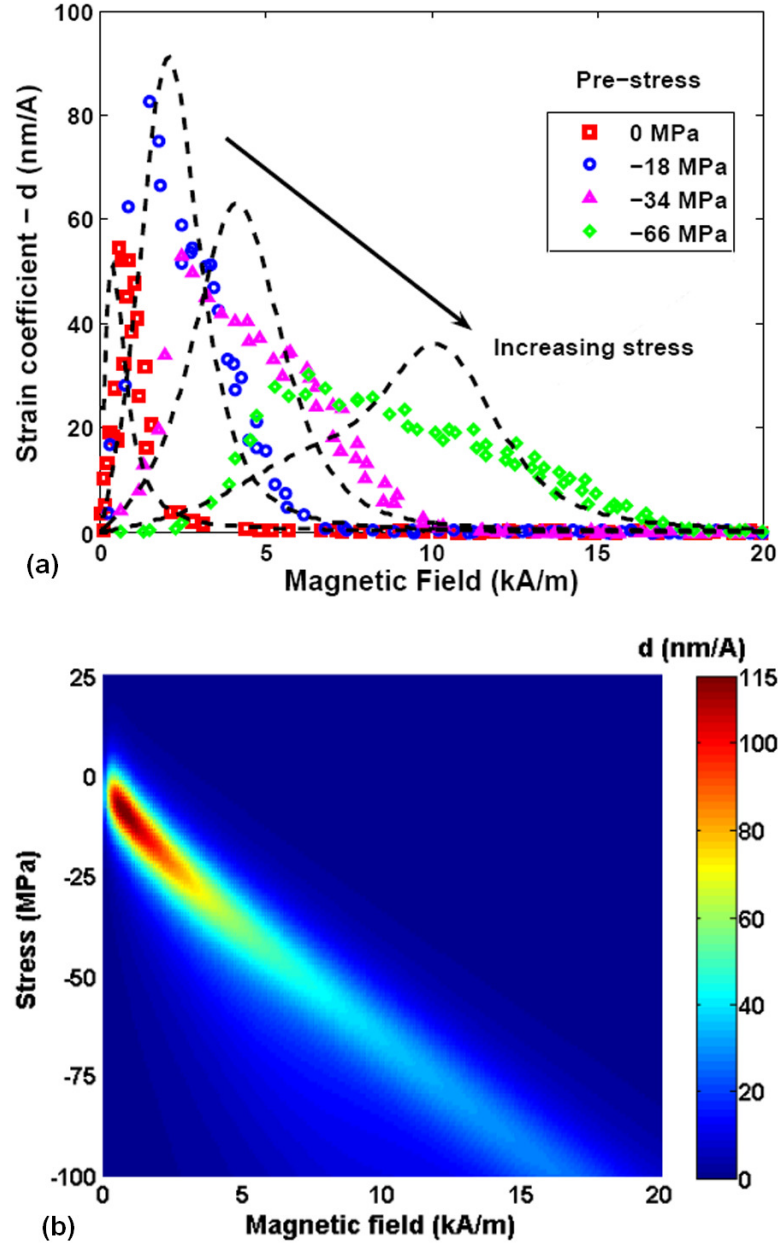


Figure 2.17. (a) Comparison of energy-based model prediction (black dashed lines) and experimental (colored markers) strain coefficient ( $d$ ) in the  $\text{Fe}_{84}\text{Ga}_{16}$  sample. (b) Model simulation of strain coefficient as a continuous function of stress and magnetic field -  $d(\sigma, H)$ , in the  $\text{Fe}_{84}\text{Ga}_{16}$  sample.

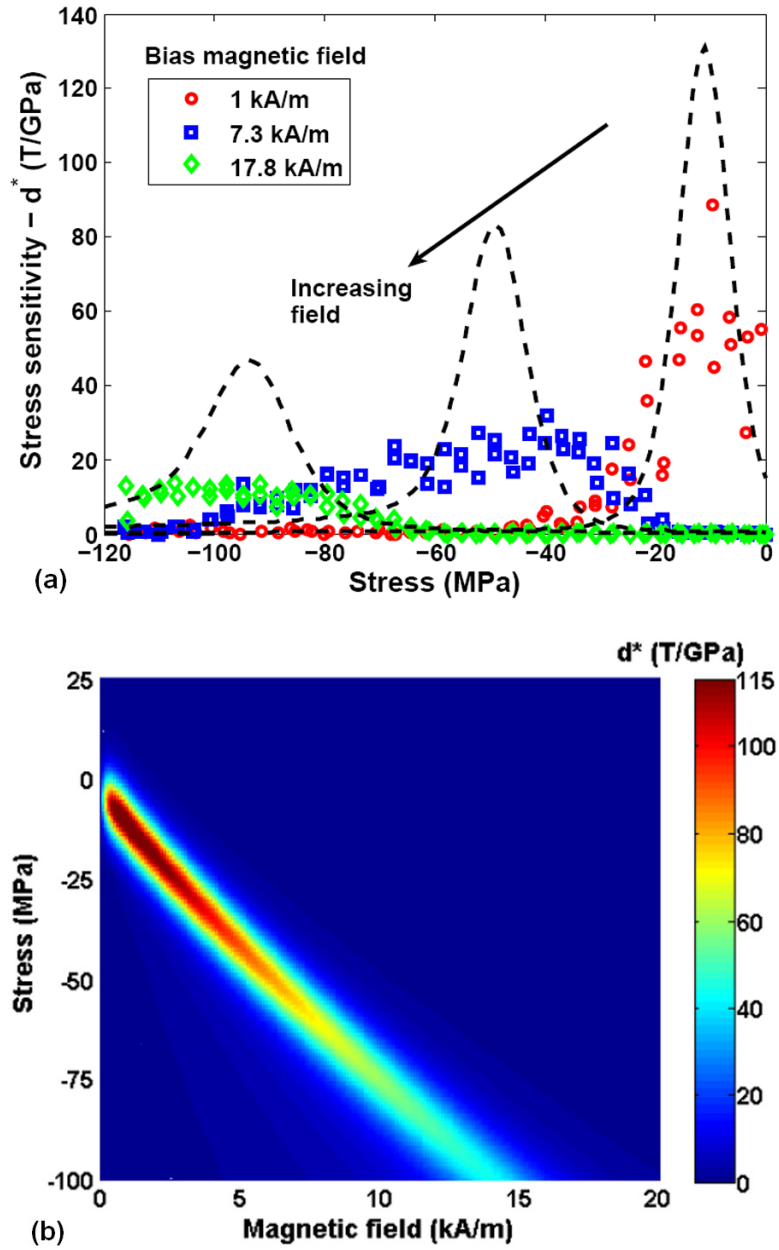


Figure 2.18. (a) Comparison of energy-based model prediction (black dashed lines) and experimental (colored markers) stress sensitivity ( $d^*$ ) in the  $\text{Fe}_{84}\text{Ga}_{16}$  sample. (b) Model simulation of stress sensitivity as a continuous function of stress and magnetic field –  $d^*(\sigma, H)$ , in the  $\text{Fe}_{84}\text{Ga}_{16}$  sample.

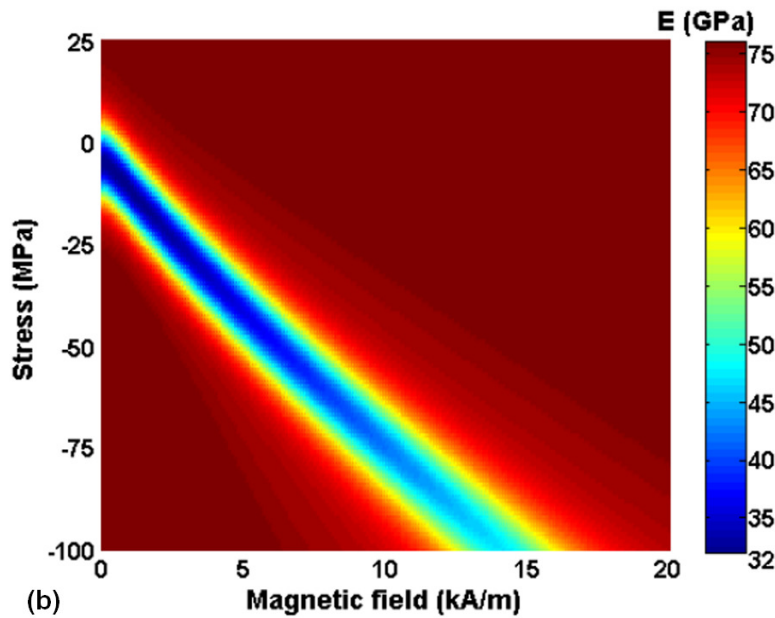
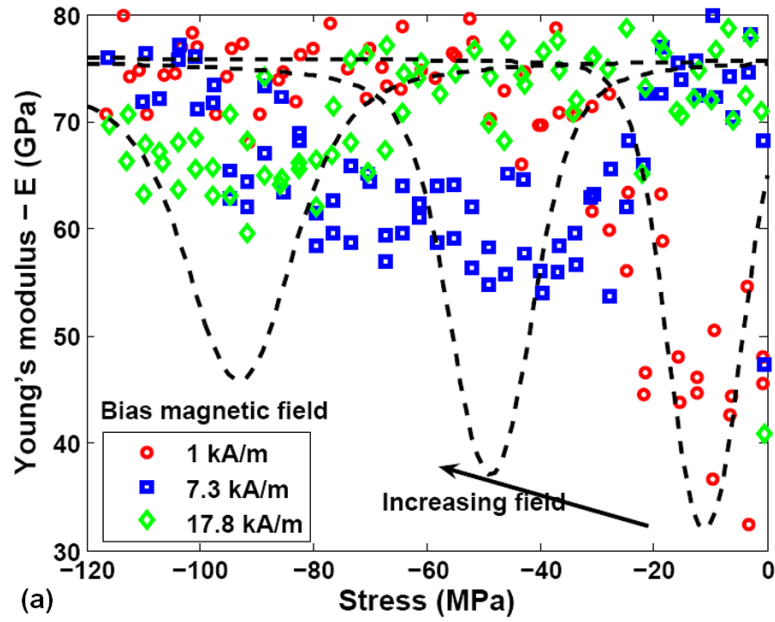


Figure 2.19. (a) Comparison of energy-based model prediction (black dashed lines) and experimental (colored markers) Young's modulus ( $E$ ) in the  $\text{Fe}_{84}\text{Ga}_{16}$  sample. (b) Model simulation of Young's modulus as a continuous function of stress and magnetic field -  $E(\sigma, H)$ , in the  $\text{Fe}_{84}\text{Ga}_{16}$  sample.

#### 2.5.4. Discussion on the trend in material properties

The trend in the material properties can be explained in terms of energy balance in the material. For a given compressive pre-stress, the values of  $\mu_r$ ,  $d$  and  $d^*$  initially increase with increasing magnetic field until they reach a peak value at a critical magnetic field. This peak value indicates a balance of magnetocrystalline anisotropy, stress-induced anisotropy and Zeeman energies such that a small perturbation from this operating point will induce maximum number of magnetic moments to rotate. The higher the pre-stress, the higher is the critical magnetic field required to attain the peak values of the material properties. Beyond this critical magnetic field, the values of  $\mu_r$ ,  $d$  and  $d^*$  decrease with increasing magnetic field.

Similarly if the bias magnetic field is kept constant, the values of  $\mu_r$ ,  $d$  and  $d^*$  initially increase with increasing compressive pre-stress until they reach a peak value at a critical compressive stress which corresponds to the energy balance. The higher the bias magnetic field, the higher is the critical stress required for the energy balance. Beyond this critical stress, the values of  $\mu_r$ ,  $d$  and  $d^*$  decrease with increasing compressive stress.

The dependence of  $E$  on  $\sigma$  and  $H$ , i.e. the Delta-E effect, is somewhat different as can be observed in Figure 2.19. If the bias magnetic field is kept constant and the compressive stress is increased, the Young's modulus initially decreases due to additional magnetoelastic strain produced by magnetic moment rotation. The value of  $E$  reaches a minima when the stress-induced anisotropy energy balances the Zeeman and magnetocrystalline anisotropy energies. On further application of stress,  $E$  increases and asymptotes to a value of 76 GPa which corresponds to the Young's

modulus at saturation ( $E_S$ ). Similar trend is observed at different constant pre-stresses and varying magnetic fields.

A tensile stress collinear to the magnetic field further enhances the anisotropy along that direction and saturates the material at a lower magnetic field than what is required if there were no stress. This is evident in Figure (2.16) – (2.19) from the fact that the variation in magnetomechanical properties under tension is negligible.

There are two special cases that need to be discussed here. The first case deals with quasi-statically changing the magnetic field while no stress is applied to the material which changes the symmetry of the energy map from 4-fold to 1-fold and hence all the magnetic moments orient along one energy minimum thereby producing magnetostriction and exhibiting a non-zero  $d$ . In this case, the magnetic field has to overcome only the magnetocrystalline anisotropy. Hence the peak in strain coefficient ( $d$ ) is observed at very small magnetic field.

In the second case, when the stress is varied quasi-statically in the absence of any magnetic field, the symmetry of the energy map changes from 4-fold to 2-fold which indicates that the magnetic moments are equally likely to reside in both the energy minima thereby not producing any net change in magnetic induction and exhibiting a zero value of  $d^*$  at all stresses while still exhibiting a softening of the Young's modulus due to magnetoelastic strain arising from reorientation of magnetic moments.

Another insight available from Figures 2.17 and 2.18 is that often  $d$  and  $d^*$  are assumed to be equivalent in a small region about an operating point [81]. Figure 2.20 shows the difference between the  $d$  and  $d^*$  values calculated from experimental data

at different operating conditions as shown in Figures 2.17 and 2.18. While much of this plot has values of close to zero, supporting this assumption, it is interesting to note that the discrepancies are larger than the experimental uncertainty and they also show a consistent trend with changing stress and magnetic field. For a given stress, the difference between  $d$  and  $d^*$  appears to increase with an initial increase in magnetic field until this difference reaches a maximum. At higher magnetic fields, this difference decreases to zero. It can be also observed in Figure 2.20, that as the compressive stress is increased in the material, the maxima in the difference between  $d$  and  $d^*$  occurs at a relatively higher magnetic field.

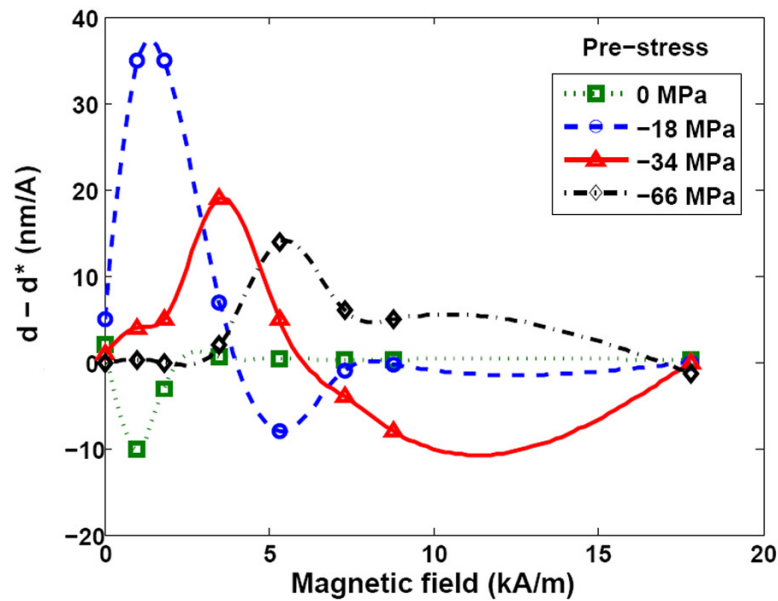


**Figure 2.20.** Difference between  $d$  and  $d^*$  calculated from quasi-static measurements performed on the  $\text{Fe}_{84}\text{Ga}_{16}$  sample at different operating stress and magnetic field conditions.

## 2.6. Energy density

This section presents the experimental and model simulation results obtained from the investigation of the effect of stress, magnetic field and composition on the energy density of Fe-Ga alloys.

The energy density ( $U$ ) of a magnetostrictive material is the magnetoelastic energy that can be stored in a unit volume of the material. Energy density can be calculated as the area under the actuator load line at a given operating magnetic field. The actuator load line is the region in a  $\varepsilon$ - $\sigma$  curve which lies in between the free strain ( $\varepsilon = \lambda$  at  $\sigma = 0$ ) and blocked stress ( $\sigma = \sigma_b$  at  $\varepsilon = 0$ ). In general, if the actuator load line is non-linear then the energy density has to be calculated using numerical integration. A close inspection of the actuator load lines in Figure 2.14 showed that for Galfenol the actuator load lines are highly linear ( $R^2 > 0.99$ ) for all bias magnetic fields. Hence it is reasonable to approximate the blocked stress ( $\sigma_b$ ) as the product of Young's modulus ( $E$ ) and magnetostriction ( $\lambda$ ) for a given pre-stress and operating magnetic field. Therefore the energy density can be obtained by calculating the area under the linear actuator load line using Equation (2.19).

$$U(\sigma, H) = \frac{1}{2} \sigma_b \lambda = \frac{1}{2} E(\sigma, H) \lambda^2(\sigma, H) \quad (2.19)$$

The experimental values of energy density were obtained at 32 unique operating points as shown in Figure 2.21(a). The Young's modulus and magnetostriction at these operating points were obtained by using the scheme explained in Section 2.5. A maximum energy density of  $2.29 \pm 0.09$  kJ/m<sup>3</sup> was calculated for Fe<sub>84</sub>Ga<sub>16</sub> at saturation magnetostriction.

Although the model prediction shown in Figure 2.21(b) matches the trend shown in Figure 2.21(a), the model appears to under-predict the maximum energy density. This behavior of the model can be traced back to the fact that the error between the model and experimental characterization curves is minimized on average but not at all operating points. Moreover, as the energy density is proportional to the square of the magnetostriction, an error in the model fit of the magnetostriction will be amplified in the model prediction of the energy density. An error estimate using Equation (2.14) showed that the *SARE* between the experimental values and model prediction of energy density of  $\text{Fe}_{84}\text{Ga}_{16}$  is 4.7 %.

Figure 2.22 shows the simulated values of energy density of  $\text{Fe}_{82.5}\text{Ga}_{17.5}$  and  $\text{Fe}_{81}\text{Ga}_{19}$  as a continuous function of stress and magnetic field. The maximum energy density of  $\text{Fe}_{82.5}\text{Ga}_{17.5}$  and  $\text{Fe}_{81}\text{Ga}_{19}$  is higher than that of  $\text{Fe}_{84}\text{Ga}_{16}$  owing to their higher saturation magnetostriction. Although  $\text{Fe}_{82.5}\text{Ga}_{17.5}$  and  $\text{Fe}_{81}\text{Ga}_{19}$  have similar saturation magnetostriction,  $\text{Fe}_{82.5}\text{Ga}_{17.5}$  shows a higher value of maximum energy density as it has a higher Young's modulus compared to  $\text{Fe}_{81}\text{Ga}_{19}$ .

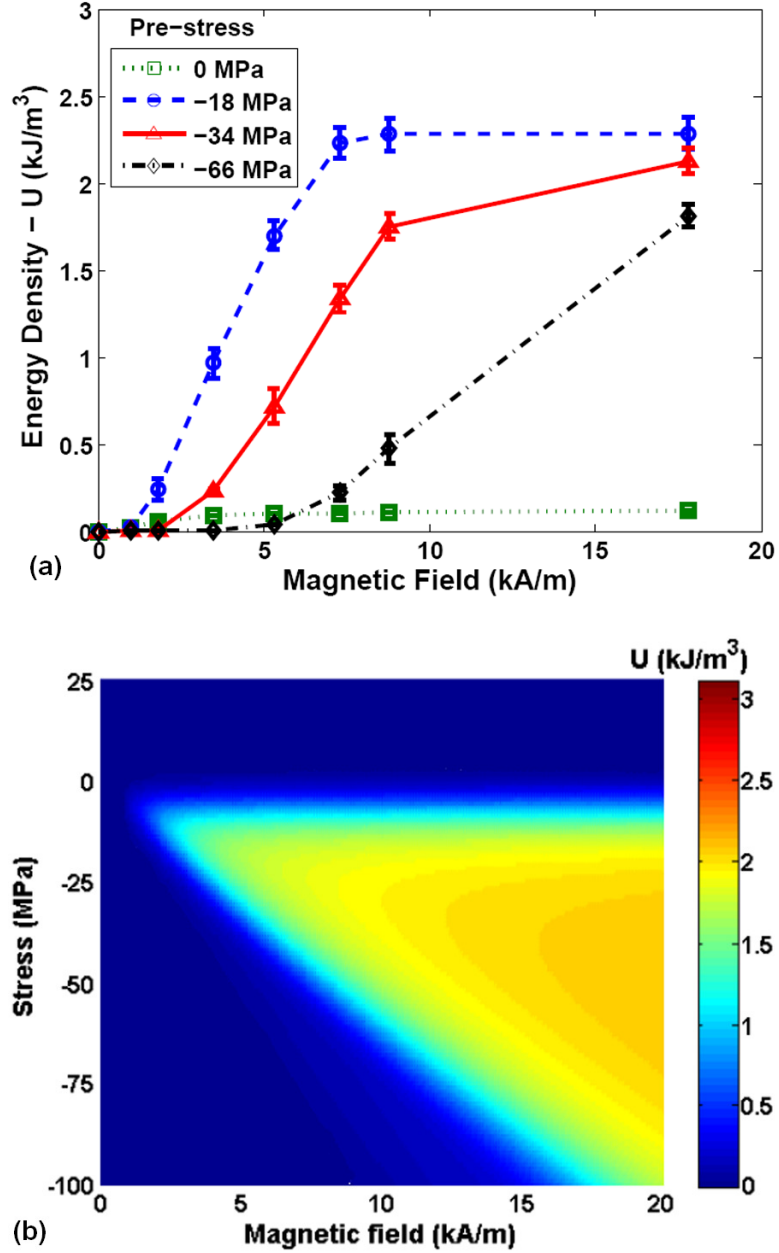


Figure 2.21. (a) Experimental values of energy density ( $U$ ) of Fe<sub>84</sub>Ga<sub>16</sub> at  $\sigma = 0, -18, -34,$  and  $-66$  MPa and  $H = 0, 1, 1.8, 3.5, 5.3, 7.3, 8.8$  and  $17.8$  kA/m. (b) Model simulation of energy density of Fe<sub>84</sub>Ga<sub>16</sub> as a continuous function of magnetic field and stress –  $U(\sigma, H)$ .

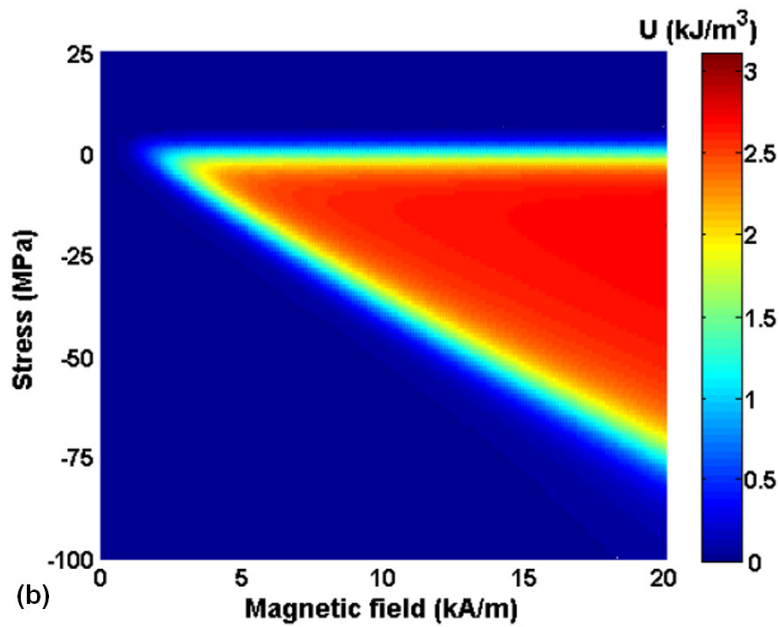
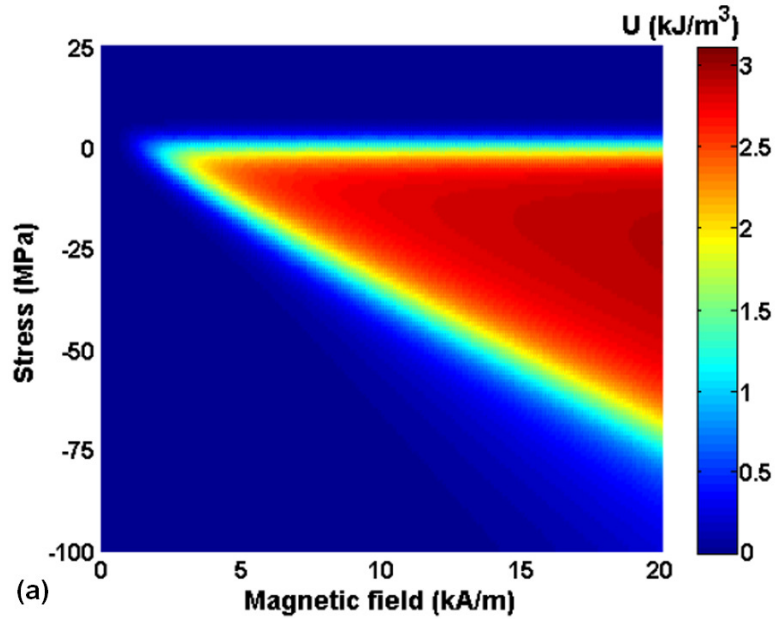


Figure 2.22. Model simulation of energy density of (a)  $\text{Fe}_{82.5}\text{Ga}_{17.5}$  and (b)  $\text{Fe}_{81}\text{Ga}_{19}$  as a continuous function of magnetic field and stress –  $U(\sigma, H)$ .

## 2.7. Magnetomechanical coupling factor

This section presents the experimental and model simulation results obtained from the investigation of the effect of stress, magnetic field and composition on the magnetomechanical coupling factor of Fe-Ga alloys.

The magnetomechanical coupling factor ( $k$ ) is a measure of the transduction efficiency and hence can be defined as the geometric mean of the actuator and sensor efficiencies ( $\eta_a, \eta_s$ ). The actuator efficiency ( $\eta_a$ ) is the ratio of the magnetoelastic work output  $\left( = \frac{1}{2} \sigma \lambda = \frac{1}{2} \sigma dH \right)$  to the magnetic work input  $\left( = \frac{1}{2} BH = \frac{1}{2} \mu H^2 \right)$ . The sensor efficiency ( $\eta_s$ ) is the ratio of the magnetoelastic work output  $\left( = \frac{1}{2} BH = \frac{1}{2} d^* \sigma H \right)$  to the mechanical work input  $\left( = \frac{1}{2} \sigma \varepsilon = \frac{1}{2} \frac{\sigma^2}{E} \right)$ . The coupling factor can be expressed in terms of the material properties as shown in Equation (2.20).

$$k(\sigma, H) = \sqrt{\eta_a \eta_s} = \sqrt{\left( \frac{\frac{1}{2} \sigma dH}{\frac{1}{2} \mu H^2} \right) \left( \frac{\frac{1}{2} d^* \sigma H}{\frac{1}{2} \frac{\sigma^2}{E}} \right)} \quad (2.20)$$

$$= \sqrt{\frac{d(\sigma, H) d^*(\sigma, H) E(\sigma, H)}{\mu(\sigma, H)}}$$

A different derivation of the same coupling factor which can be also obtained from the ratio of magnetoelastic energy to the geometric mean of the magnetic and mechanical energies is shown in Refs. [2, 81].

Prior work by Wun-Fogle *et al.* [171] simulated  $\mu$ ,  $d$  and  $k$  as functions of stress and magnetic field in stress-annealed polycrystalline Galfenol using an energy-

based model. The energy formulation used was restricted to that of single crystal and a value of Young's modulus at constant magnetic induction, calculated at magnetic saturation, was used in the simulation of  $k$  for non-saturated conditions.

In the present work, the experimental capability of maintaining constant magnetic field using a feedback controller is put to advantage in order to obtain stress and magnetic field-dependent Young's modulus values which are used in Equation (2.20) to calculate appropriate values of stress and magnetic field dependent coupling factor from experimental data.

The experimental values of coupling factor were obtained at 32 unique operating points as shown in Figure 2.23(a). The material properties at these operating points were obtained by using the scheme explained earlier. The coupling factor is always zero at zero magnetic field. It can be observed that for each pre-stress, the coupling factor increases with increasing magnetic field, reaches a peak value and then steadily decreases to zero at higher magnetic fields. As the pre-stress is increased, the peak in coupling factor occurs at a higher magnetic field. The highest value of  $k = 0.51 \pm 0.03$  was observed at  $\sigma = -18$  MPa and  $H = 3.5$  kA/m in  $\text{Fe}_{84}\text{Ga}_{16}$ .

The material properties obtained from the energy-based model as continuous functions of stress and magnetic field were used in Equation (2.20) to obtain the coupling factor of  $\text{Fe}_{84}\text{Ga}_{16}$  as shown in Figure 2.23(b). The model confirms the trend in coupling factor observed in the experimental values. It should be noted that an error between the model and the experimental actuator and sensor characterization curves along with the error in the numerical derivatives used to obtain the material properties would affect the calculation of  $k$ . An error estimate using Equation (2.14)

showed that the *SARE* between the experimental values and model prediction of coupling factor of  $\text{Fe}_{84}\text{Ga}_{16}$  is 15.7 %.

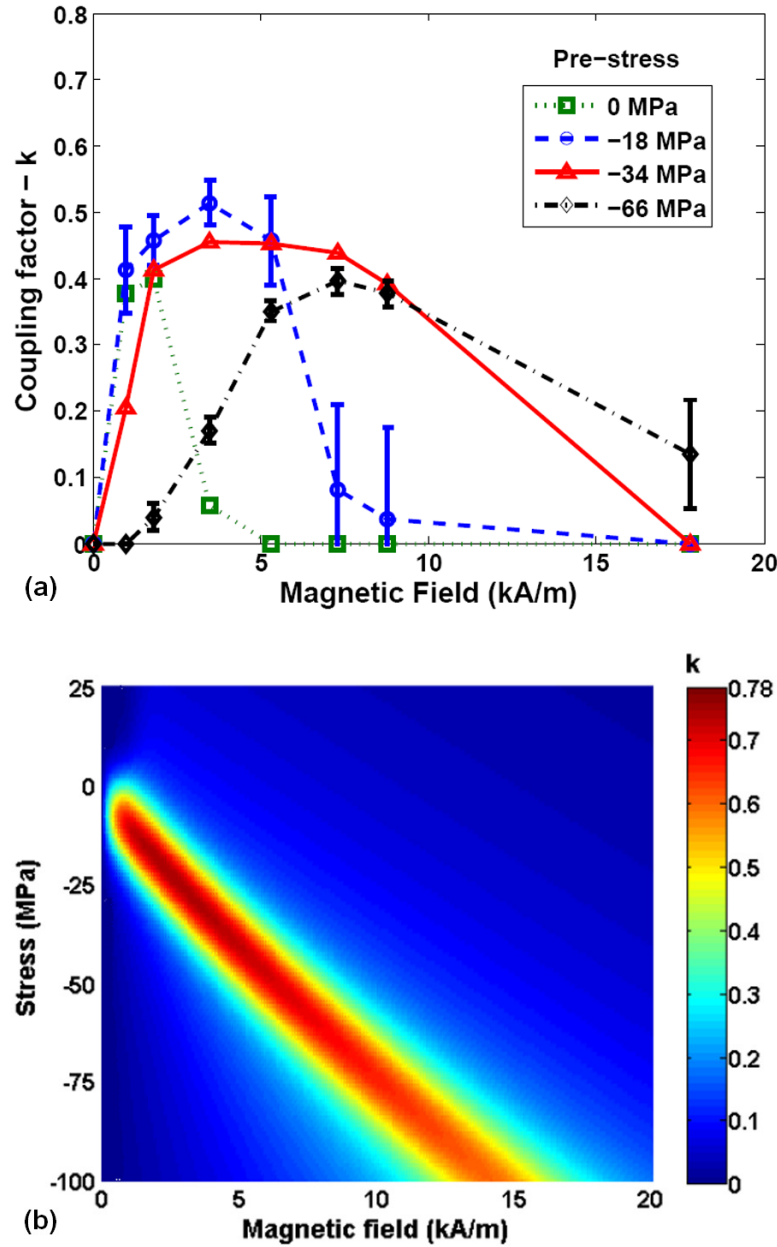


Figure 2.23. (a) Experimental values of coupling factor ( $k$ ) of  $\text{Fe}_{84}\text{Ga}_{16}$  at  $\sigma = 0, -18, -34,$  and  $-66$  MPa and  $H = 0, 1, 1.8, 3.5, 5.3, 7.3, 8.8$  and  $17.8$  kA/m. The error bars are shown only for  $\sigma = -18$  and  $-66$  MPa. (b) Model simulation of coupling factor of  $\text{Fe}_{84}\text{Ga}_{16}$  as a continuous function of magnetic field and stress –  $k(\sigma, H)$ .

The magnetomechanical coupling factor gives a measure of the magnetoelastic workdone by the material for a given magnetic and mechanical work input. The higher the compressive stress acting on the material, the higher is the magnetic field required to obtain the maximum work from the material and hence the coupling factor peaks at higher magnetic field as the pre-stress is increased. The same idea holds true if the magnetic field is kept constant while the stress is varied. Moreover as the stress and magnetic field tend to zero, the coupling factor also tends to zero as no magnetoelastic work is obtained from the material. At the other extreme, the coupling factor can also tend to zero if the magnitude of stress is high enough at a given bias magnetic field or conversely the magnitude of actuating magnetic field is high enough at a given pre-stress such that the material attains saturation and the magnetic moments cannot rotate any further to perform magnetoelastic work. The general trend in variation of  $k$  with stress and magnetic field can be deduced using the energy plots shown in Figures 2.12 and 2.15 as explained below.

The variation in  $k$  depends on the volume fraction of magnetic moments available which can undergo non-180° rotation. Hence the extent of variation in  $k$  depends on the bias magnetic field or pre-stress as that decides the volume fraction of magnetic moments which are available for non-180° rotation and also the energy barrier that needs to be overcome by the stress-induced anisotropy or Zeeman energy respectively in order to rotate the magnetic moments from the direction of one energy minima to another.

The volume fraction of magnetic moments residing in an energy well is proportional to the depth of the energy well. A maxima in  $k$  denotes the operating

condition such that a small perturbation in either the magnetic field or stress results in the rotation of maximum volume fraction of magnetic moments. Such a condition requires availability of shallow energy wells at non-180° intervals which correspond to low stresses and magnetic fields as denoted by  $\sigma = 0, -10$  and  $-20$  MPa curves in Figure 2.15(a).

If the stress-induced anisotropy is significantly higher than the Zeeman energy then there is no possibility of non-180° rotation as there are only two energy wells separated by a 180° interval and hence  $k = 0$  under such conditions, as denoted by  $\sigma = -40$  and  $-100$  MPa curves in Figure 2.15(a). Conversely, if the Zeeman energy is significantly higher than the stress-induced anisotropy then there cannot be any non-180° rotation as there is only one energy well at 0° and hence  $k = 0$  under such conditions, as denoted by  $H = 30$  kA/m curve in Figure 2.12.

In general, the higher the bias magnetic field or pre-stress, the lower the volume fraction of magnetic moments that are available for non-180° rotation and hence, the smaller maxima in  $k$ .

A series of simulations using different combinations of stresses and magnetic fields showed that a maximum coupling factor of  $\sim 0.74$  can be obtained from  $\text{Fe}_{84}\text{Ga}_{16}$  for compressive stresses inbetween 10 to 20 MPa and magnetic fields between 1.5 to 3.5 kA/m.

Figure 2.24 shows the simulated values of coupling factor of  $\text{Fe}_{82.5}\text{Ga}_{17.5}$  and  $\text{Fe}_{81}\text{Ga}_{19}$  as a continuous function of stress and magnetic field. The samples with 16, 17.5 and 19 at. % Ga show maximum coupling factors of higher than 0.7 inspite of the fact that these samples have different magnetomechanical properties. In these

alloys, the permeability at the combination of stresses and magnetic fields where the highest coupling factor is exhibited is about the same. The peak coupling factor remains the same as a decreasing Young's modulus with increasing gallium content (within 16-19 at. %) is compensated for by increasing  $d$  and  $d^*$ .

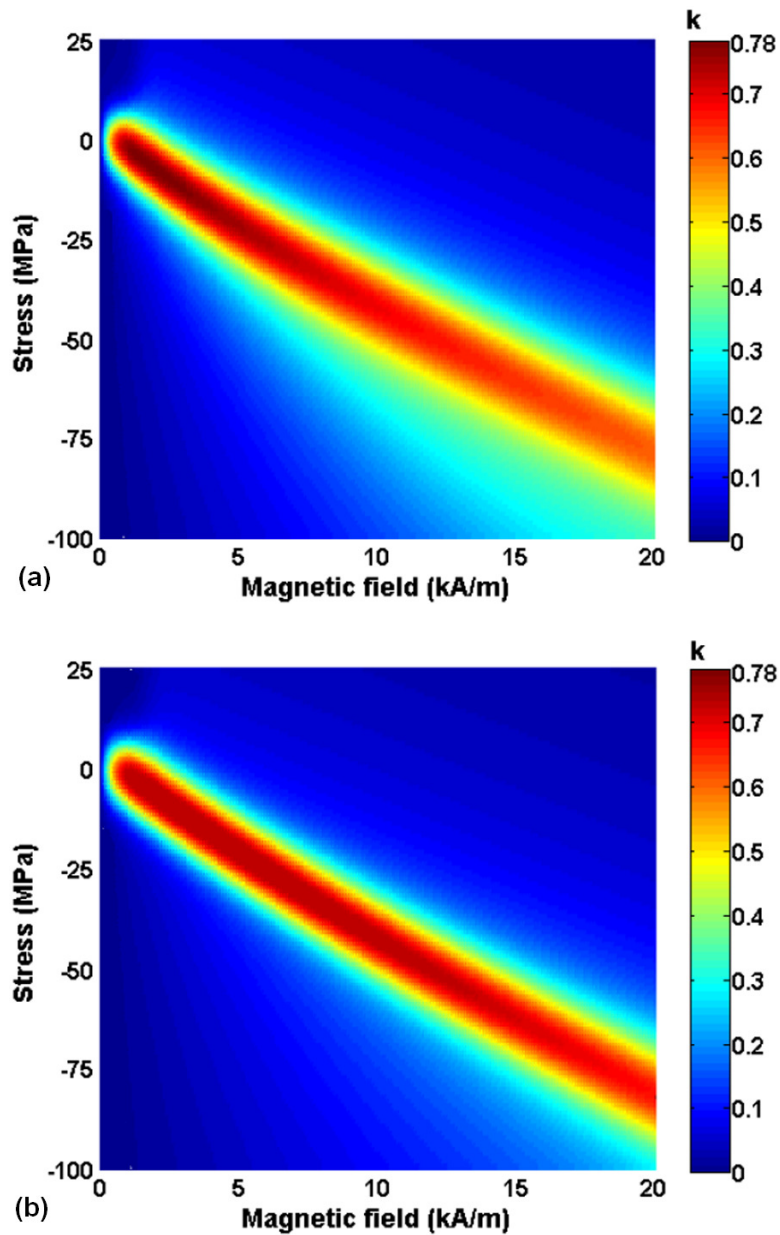


Figure 2.24. Model simulation of coupling factor of (a)  $\text{Fe}_{82.5}\text{Ga}_{17.5}$  and (b)  $\text{Fe}_{81}\text{Ga}_{19}$  as a continuous function of magnetic field and stress  $-k(\sigma, H)$ .

## 2.8. Gage factor

This section presents the experimental and model simulation results obtained from the investigation of the effect of stress, magnetic field and composition on the sensing gage factor of Fe-Ga alloys.

Prior work by Wun-Fogle *et al.* [172] defined a sensing figure of merit ( $F_\mu$ ) analogous to the gage factor of a resistive strain gage by replacing the electrical resistance with magnetic permeability ( $\mu$ ) in the definition of gage factor as shown in Equation (2.21).

$$F_\mu = \frac{1}{\mu} \frac{\partial \mu}{\partial \varepsilon} \quad (2.21)$$

Since magnetic induction can be directly measured, unlike permeability, in this chapter, we will use the sensing figure of merit or gage factor ( $GF$ ) defined by Datta and Flatau [139] as shown in Equation (2.22).

$$\begin{aligned} GF(\sigma, H) &= \frac{1}{B} \frac{\partial B}{\partial \varepsilon} = \frac{1}{B} \frac{\partial B}{\partial \sigma} \frac{\partial \sigma}{\partial \varepsilon} \\ &= \frac{d^*(\sigma, H) E(\sigma, H)}{B(\sigma, H)} \end{aligned} \quad (2.22)$$

The dimensionless gage factor defined by Equation (2.22) satisfies the physical conditions that  $GF$  cannot be defined when  $B = 0$ , i.e. if the material is not exposed to a bias magnetic field and also the fact that  $GF = 0$  when the material saturates and  $d^* = 0$ . As  $d^*$  and  $E$  are always positive, the sign of  $GF$  is the same as the sign of  $B$ . The sign of  $B$  simply shows the direction along which the bias magnetic field has been applied and can be arbitrarily set to be positive as the B-H curves in the 1<sup>st</sup> and 3<sup>rd</sup> quadrants are the reflection of each other about the origin as is evident

from Figure 2.10. Furthermore, Equation (2.22) is flexible enough to accommodate both strain and stress sensing which is evident from the expression shown here.

The experimental values of gage factor were obtained at 20 unique operating points as shown in Figure 2.25(a). The material properties at these operating points were obtained by using the scheme explained earlier. It can be observed that for each bias magnetic field, the gage factor increases with increasing compressive stress, reaches a peak value and then steadily decreases at higher stresses. As the bias magnetic field is increased, the peak in gage factor occurs at a higher compressive stress. The highest value of  $GF = 7000 \pm 1470$  was observed for  $\sigma = -34$  MPa and  $H = 1$  kA/m in  $\text{Fe}_{84}\text{Ga}_{16}$ .

The material properties obtained from the energy-based model as continuous functions of stress and magnetic field were used in Equation (2.22) to obtain the gage factor of  $\text{Fe}_{84}\text{Ga}_{16}$  as shown in Figure 2.25(b). The model aids in the identification of a trend in the gage factor.

A notable difference between the experimental and simulated value of  $GF$  is observed beyond saturation. The experimentally calculated values of  $GF$  at very high stresses are exactly zero because experimental  $d^*$  is exactly equal to zero beyond saturation. The model predicts a small non-zero value of  $GF$  at very high stresses due to its exponential nature as evident from Equations (2.10) and (2.12) and suggests that  $GF$  tends to zero as the compressive stress tends to infinity. An error estimate using Equation (2.14) showed that the *SARE* between the experimental values and model prediction of gage factor of  $\text{Fe}_{84}\text{Ga}_{16}$  is 11 %.

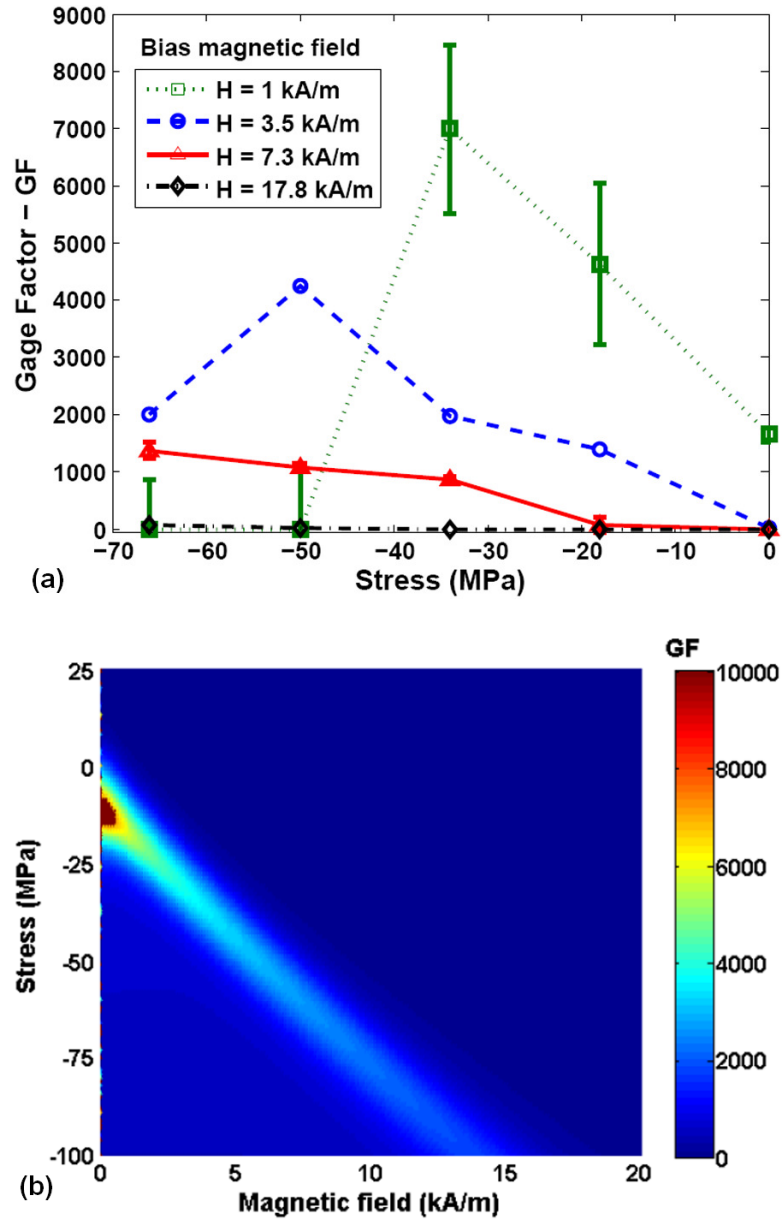
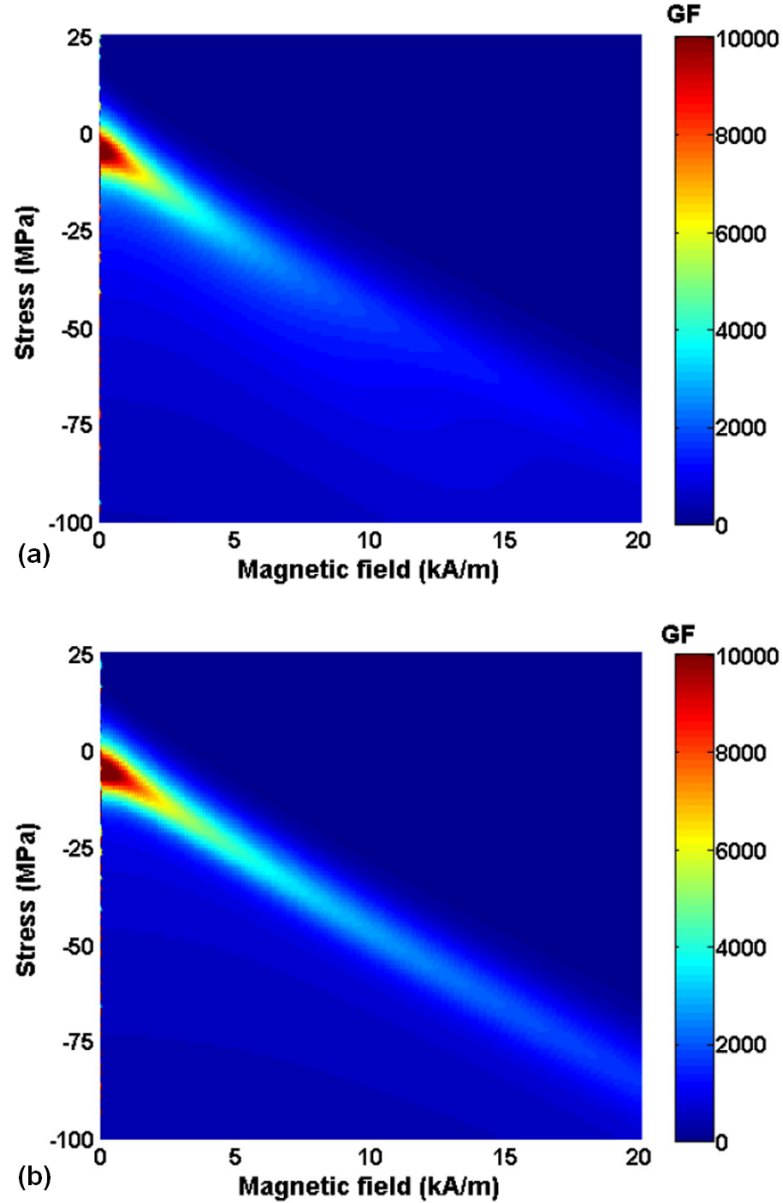


Figure 2.25. (a) Experimental values of gage factor ( $GF$ ) of  $Fe_{84}Ga_{16}$  at  $\sigma = 0, -18, -34, -50$  and  $-66$  MPa and  $H = 1, 3.5, 7.3$  and  $17.8$  kA/m. For visual clarity, the error bars are shown only for the cases when  $H = 1$  and  $7.3$  kA/m. (b) Model simulation of gage factor of  $Fe_{84}Ga_{16}$  as a continuous function of stress and magnetic field –  $GF(\sigma, H)$ .



**Figure 2.26. Model simulation of gage factor of (a)  $\text{Fe}_{82.5}\text{Ga}_{17.5}$  and (b)  $\text{Fe}_{81}\text{Ga}_{19}$  as a continuous function of stress and magnetic field –  $GF(\sigma,H)$ .**

A series of simulations using different combinations of stresses and magnetic fields showed that gage factor greater than 7000 can be obtained from  $\text{Fe}_{84}\text{Ga}_{16}$  for compressive stresses inbetween 5 to 15 MPa and magnetic fields less than 0.5 kA/m. Figure 2.26 shows the simulated values of sensing gage factor of  $\text{Fe}_{82.5}\text{Ga}_{17.5}$  and

$\text{Fe}_{81}\text{Ga}_{19}$  as a continuous function of stress and magnetic field. The highest  $GF$  amongst all the compositions is shown by  $\text{Fe}_{82.5}\text{Ga}_{17.5}$ . The peak values of  $GF$  are slightly lower for both  $\text{Fe}_{84}\text{Ga}_{16}$  and  $\text{Fe}_{81}\text{Ga}_{19}$ . This is because the difference in  $d^*$  between these compositions is more than their difference in Young's modulus and hence the value of  $d^*$  influences  $GF$  more significantly. These results imply that energy harvesting using Galfenol would require very low bias magnetic fields and small compressive pre-stresses for most optimum performance. These results also support the empirical observations made by Staley and Flatau [173].

## 2.9. Evaluation of clamped material properties

This section will present calculated and simulated values of two material properties which are seldom discussed. These are the Young's modulus ( $E^B$ ) at constant magnetic induction and the relative permeability ( $\mu^{\epsilon}$ ) at constant strain. Based on the rigorous mathematical interpretation of the linear constitutive equations presented in Section 1.6.1, it can be said that  $E^B$  is the magnetically clamped modulus when a change in strain in the material can be expressed in terms of small changes in independent variables stress and magnetic induction (instead of magnetic field). Similarly,  $\mu^{\epsilon}$  is the mechanically clamped relative permeability when a change in magnetic induction in the material can be expressed in terms of small changes in independent variables strain (instead of stress) and magnetic field.

### 2.9.1. Young's modulus at constant magnetic induction

From prior discussion, it is apparent that when a stress is applied to a magnetostrictive material in the presence of an external (applied) magnetic field, both

internal magnetic field ( $H$ ) and magnetic induction ( $B$ ) changes in the material. The internal magnetic field changes due to a change in the reluctance of the sample which occurs as the permeability of the sample changes as a function of stress. It was shown in Section 2.2 that the internal magnetic field had to be kept constant using a feedback controller in order to obtain stress-strain data at constant magnetic fields in the material which in turn was used to calculate the Young's modulus as a function of stress and magnetic field in the material.

The magnetic induction changes due to reorientation of magnetic moments along energy minima created as a result of the effect of superposition of both magnetic field and stress. It has been shown [81] that the Young's modulus at a given stress and magnetic induction in a material can be different from the Young's modulus at a given stress and magnetic field which produces the same magnetic induction, depending on whether the magnetic field or magnetic induction is held constant when the stress is quasi-statically changed in the material. The modulus at constant induction ( $E^B$ ) can be obtained from a process where both stress and magnetic field are simultaneously adjusted so as to ensure that  $B$  remains constant as stress changes. Alternatively,  $E^B$  can also be obtained by combining Equations (2.15), (2.16) and (2.20) and eliminating  $H$  which gives the relationship shown in Equation (2.23) [81].

$$E^B(\sigma, B) = \frac{E^H(\sigma, H)}{1 - k^2(\sigma, H)} \quad (2.23)$$

Figure 2.27 shows the calculated and model simulation values of Young's modulus as a function of stress and magnetic induction in  $\text{Fe}_{84}\text{Ga}_{16}$ . The values of the modulus at constant magnetic field ( $E^H$ ) and the magnetomechanical coupling factor

(k) were obtained from the results shown in Sections 2.5 and 2.7.

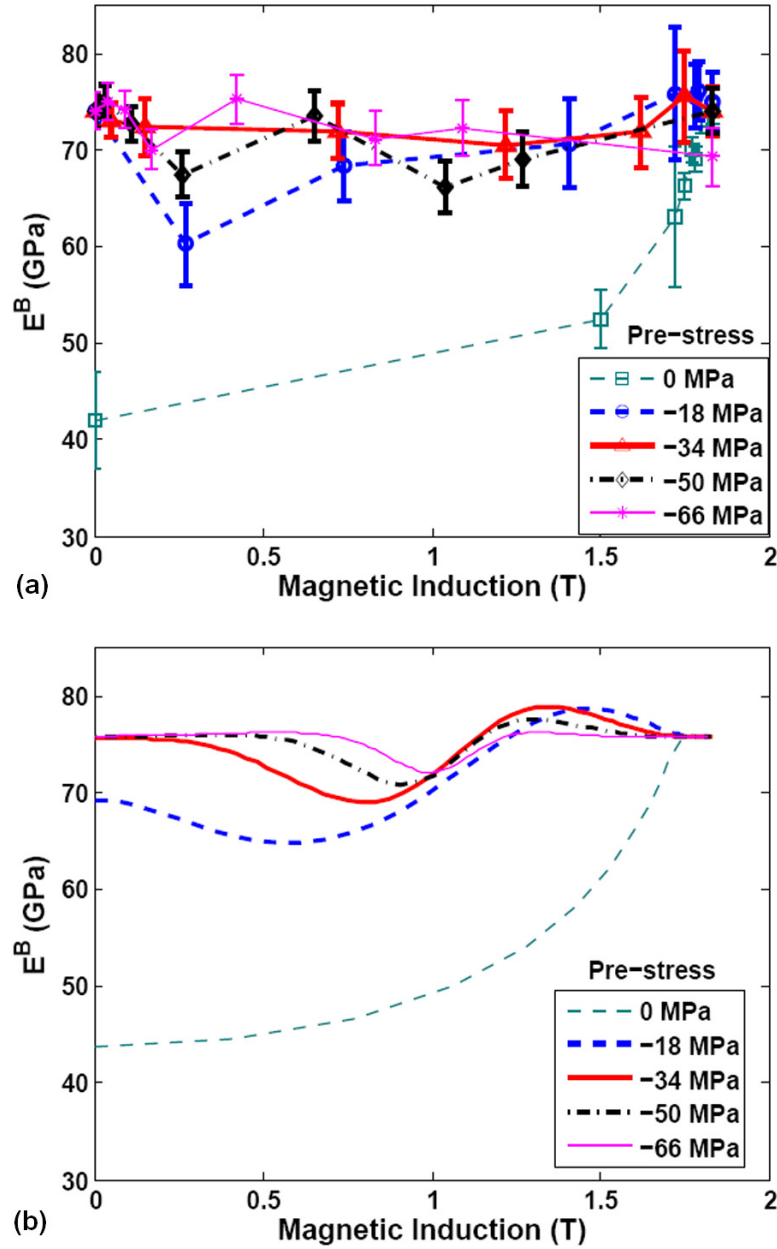


**Figure 2.27. (a) Calculated values of Young's modulus ( $E^B$ ) under iso-induction conditions in Fe<sub>84</sub>Ga<sub>16</sub> as a discrete function of stress and magnetic induction. (b) Model simulation of  $E^B(\sigma, B)$  in Fe<sub>84</sub>Ga<sub>16</sub> as a function of magnetic induction and stress.**

It should be noted that the values of both  $E^H$  and  $E^B \rightarrow E_a$  at  $H = 0$  and  $B = 0$

respectively and as  $\sigma \rightarrow 0$ , where  $E_a$  is the modulus of the material in a demagnetized state. For both these scenarios, the stress-induced anisotropy has to work only against the magnetocrystalline anisotropy in order to rotate the magnetic moments. Theoretically  $E_a$  can be assumed to be a material constant but only if the material is perfectly demagnetized at the beginning of the magnetomechanical transduction process so that an equal number of magnetic moments are oriented along each of the six different easy axes in the material prior to the transduction. Since this initial condition cannot be ensured in a practical process, sample history determines the experimental value of  $E_a$ , which most likely will be somewhat different than its theoretical value.

At  $B = 0$ , as stress increases, the magnetic moments rotate along the two possible directions which are parallel (if the stress is tensile) or perpendicular (if the stress is compressive) to the direction of stress until the material saturates at stresses high enough to change the cubic symmetry of the total energy in the material to a tetragonal one. At these high stresses,  $E^B = E_s$ . At  $\sigma = 0$ ,  $E^B$  monotonically increases with  $B$  until all magnetic moments are oriented along the same direction when  $E^B = E_s$ . The variation in  $E^B$  at other intermediate values of  $B$  and  $\sigma$  can be explained using the energy-based hypothesis presented earlier. Most importantly, it should be noted that  $E^B = E_s$ , only if the material is saturated, i.e., when there is only one energy minimum as shown by the  $H = 30$  kA/m curve in Figure 2.12 or two energy minima which are  $180^\circ$  apart from each other as shown by the  $\sigma = -100$  MPa curve in Figure 2.15.

### 2.9.2. Permeability at constant strain

Analogous to the modulus at constant induction, it can be shown [81] that the relative permeability at a given strain and magnetic field in the material will be different from the relative permeability at a given stress and magnetic field which produces the same strain, depending on whether the stress or strain is held constant when the magnetic field is quasi-statically changed in the material. The permeability at constant strain ( $\mu^\varepsilon$ ) can be obtained from a process where both stress and magnetic field are simultaneously adjusted so as to ensure that  $\varepsilon$  remains constant as magnetic field changes. Alternatively,  $\mu^\varepsilon$  can also be obtained by combining Equations (2.15), (2.16) and (2.20) and eliminating  $\sigma$  which gives the relationship shown in Equation (2.24) [81].

$$\mu^\varepsilon(\varepsilon, H) = [1 - k^2(\sigma, H)] \mu^\sigma(\sigma, H) \quad (2.24)$$

Figure 2.28 shows the calculated and model simulation values of relative permeability as a function of strain and magnetic field in  $\text{Fe}_{84}\text{Ga}_{16}$ . The values of the permeability at constant stress ( $\mu^\sigma$ ) and the magnetomechanical coupling factor ( $k$ ) were obtained from the results shown in Sections 2.5 and 2.6.

The trend shown by  $\mu^\varepsilon$  in Figure 2.28 can be once again explained using the energy-balance approach. Note that a relative permeability of one denotes that the material has saturated. It should also be noted that under iso-strain conditions, magnetic field in the material induces stress as the material cannot expand freely. This stress can be used to calculate the stress-induced anisotropy in the material.

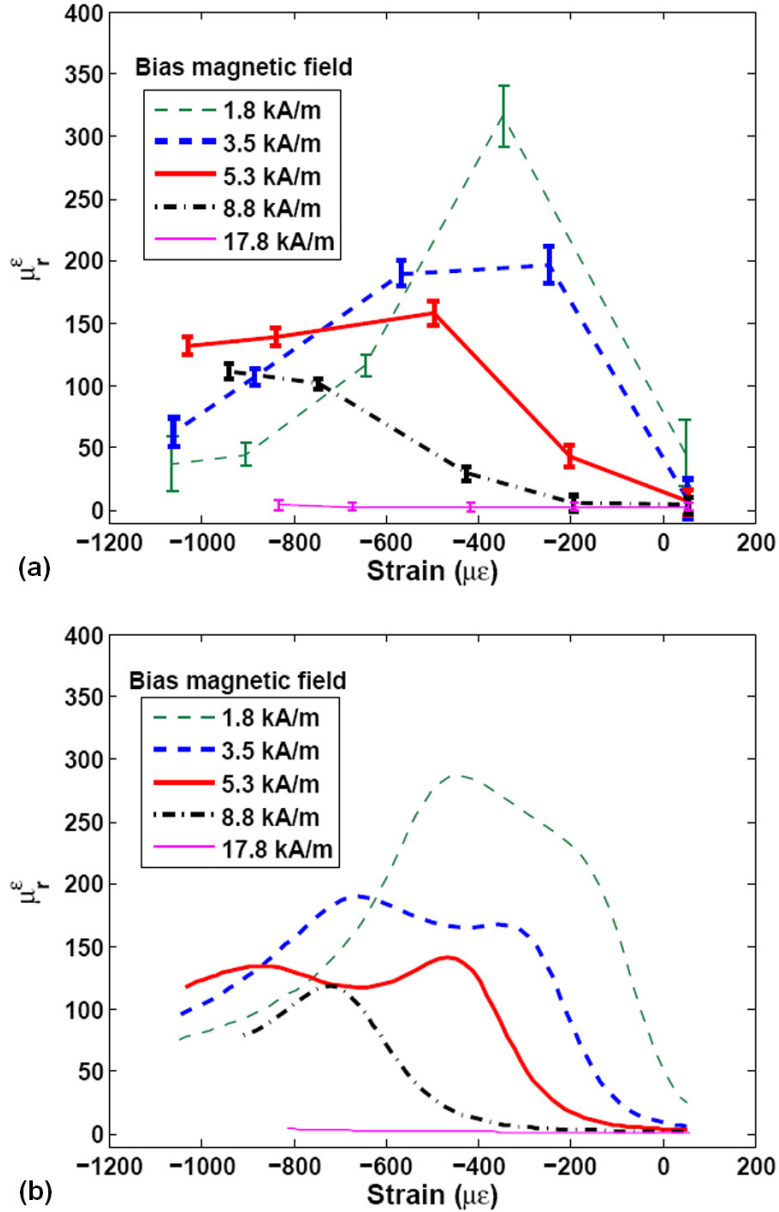


**Figure 2.28.** (a) Calculated values of relative permeability ( $\mu^\varepsilon$ ) under iso-strain conditions in  $\text{Fe}_{84}\text{Ga}_{16}$  as a discrete function of magnetic field and strain. (b) Model simulation of  $\mu^\varepsilon(\varepsilon,H)$  in  $\text{Fe}_{84}\text{Ga}_{16}$  as a function of strain and magnetic field.

When the material is in a state of tensile strain, a small magnetic field collinear to the strain direction can be sufficient to orient the magnetic moments along strain/field direction thereby saturating the material. Hence, when the material

has constant tensile pre-strain, increasing magnetic fields monotonically decrease permeability. If the material has a constant compressive pre-strain, increasing magnetic fields initially decrease the permeability upto a critical magnetic field which balances the stress-induced anisotropy energy. Beyond this magnetic field, increasing magnetic fields result in decreasing permeability. This trend is analogous to the behavior observed in Figure 2.16.

### 2.10. Summary

In this work, single crystal  $\text{Fe}_{84}\text{Ga}_{16}$ ,  $\text{Fe}_{82.5}\text{Ga}_{17.5}$  and  $\text{Fe}_{81}\text{Ga}_{19}$  were studied as magnetostrictive actuators and sensors along the  $\langle 100 \rangle$  crystal direction under different quasi-static stress and magnetic field conditions. Analysis of the experimental data showed that the permeability, strain coefficient, stress sensitivity, Young's modulus, energy density, magnetomechanical coupling factor and sensing gage factor vary significantly based on the stress, magnetic field and gallium content in Fe-Ga alloys.

An energy-based model was used to obtain non-linear fit of both the actuator and sensor characteristics of the samples. It was shown that for a given alloy composition, a set of model parameters obtained from experimental actuator characterization can also be used to predict the sensing behavior. The model was further used to generate the material properties and actuator and sensor figures of merit as continuous functions of stress and magnetic field in the material which were compared with experimentally obtained values at discrete operating stresses and magnetic fields. The model can be a valuable tool to learn about the magnetostrictive material's non-linear response under varying operating stress and magnetic field

without performing time-consuming extensive experimental characterization. Moreover, the material properties obtained from the model can be used for design of magnetostrictive actuators, sensors and energy harvesting devices.

This study can be used to set some general guidelines for using magnetostrictive iron-gallium alloys in actuator and sensor applications. A critical compressive pre-stress ( $\approx K_1/6\lambda_{100}$ ) is required to obtain the maximum saturation magnetostriction for actuator applications. The magnitude of the pre-stress depends on the magnetocrystalline anisotropy and magnetostriction and hence depends on the alloy composition.

It is desirable to operate the material at saturation in order to obtain maximum free strain, blocked stress and energy density as an actuator although the coupling factor for such an operating condition is zero. The peak values of the energy density for different alloy compositions are listed in Table 2.5.

The higher the compressive pre-stress, the higher is the critical magnetic field  $\left( \approx \frac{K_1 - 6\lambda_{100}\sigma}{4\mu_o M_s} \right)$  at which the “burst region” in B-H and  $\lambda$ -H curves is observed. The “burst region” describes the condition when magnetic moments from other easy axes start flipping towards the direction of easy axis closest to the applied magnetic field.

For sensing applications, an increasing bias magnetic field increases the operating stress range but decreases the stress sensitivity. Moreover, if the bias magnetic field is high enough ( $\approx K_1/4\mu_o M_s$ ) to saturate the material at zero stress,

then a critical stress  $\left( \approx \frac{K_1 - 4\mu_o M_s H}{6\lambda_{100}} \right)$  is required below which the sensor cannot be operated.

Hence there is no single operating point for magnetostrictive materials which can give the best performance under all conditions. A suitable pre-stress or bias magnetic field should be chosen based on the operating conditions of an actuator or sensor respectively. In order to operate the material under the optimal condition in a changing environment, a feedback controller can be used to vary the pre-stress or bias magnetic field in actuators and sensors respectively.

**Table 2.5. Effect of composition on the simulated maximum values of actuator and sensor figures of merit.**

<b>Figure of merit</b>	<b>Fe<sub>84</sub>Ga<sub>16</sub></b>	<b>Fe<sub>82.5</sub>Ga<sub>17.5</sub></b>	<b>Fe<sub>81</sub>Ga<sub>19</sub></b>
<b>Energy density (kJ/m<sup>3</sup>)</b>	2.1	3.1	2.8
<b>Magnetomechanical coupling factor</b>	0.74	0.78	0.73
<b>Sensing gage factor</b>	7000	9000	8250

For all compositions, the highest values of coupling factor and gage factor which are listed in Table 2.5 were observed for operating compressive stresses lower than 20 MPa and below magnetic field of 5 kA/m. This observation confirms that to achieve maximum transduction from magnetic to mechanical energy or vice versa the initial orientation of the magnetic moments should be such that a small perturbation in the total energy of the system produced by a change in stress or magnetic field would rotate maximum number of magnetic moments. It was found that the highest

energy density, magnetomechanical coupling and sensing gage factor were exhibited by  $\text{Fe}_{82.5}\text{Ga}_{17.5}$  thereby making it the ideal alloy composition for both actuation and sensing applications. In general, the criteria for a good actuator can be used in vibration control and shape morphing applications whereas the criteria for a good sensor can be used in structural health monitoring and energy harvesting applications.

## Chapter 3: Experimental studies on Galfenol beam as a sensor in bending

As a structural magnetostrictive alloy, Galfenol can be expected to be used in applications involving bending [137]. In this chapter, we will investigate the magnetomechanical transduction in a bending Galfenol member. The challenges related to existing characterization techniques involving bending is discussed to motivate a technique [174] which uses a four-point bending. It is expected that the experimental approach described in this chapter will be useful for evaluating the sensing performance of any structural magnetostrictive material. The experimental results are analyzed using an energy-based approach. Before describing the details of experimental characterization in bending, it is necessary to understand the mechanics of a bending beam.

### 3.1. *Classical beam theory*

Structural members subjected to transverse loads and operating in flexural mode are known as beams. For the purpose of this chapter, we will consider the Euler-Bernoulli assumptions of the Classical Beam Theory which are as follows [175].

1. The cross-section of the beam has a longitudinal plane of symmetry known as the neutral plane.
2. The resultant of the transversely applied loads lies in the longitudinal plane of symmetry.

3. Plane sections originally perpendicular to the longitudinal axis of the beam remain plane and perpendicular to the longitudinal axis after bending.
4. In the deformed beam, the planes of cross-sections have a common intersection, that is, any line originally parallel to the longitudinal axis of the beam becomes an arc of a circle described by the radius of curvature.

These assumptions are applicable to a beam whose length is 8-10 times more than both its width and its thickness.

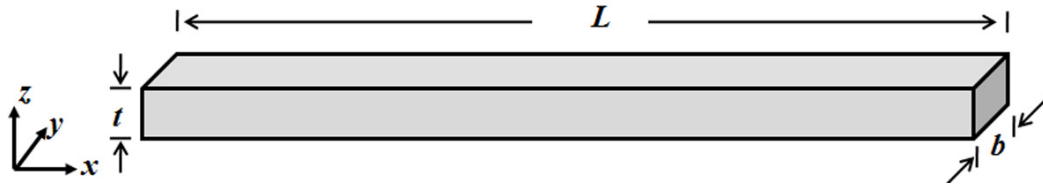


**Figure 3.1. An Euler-Bernoulli beam in a Cartesian coordinate system.**

Let us assume a beam with length ( $L$ ) along the  $x$ -direction and thickness ( $t$ ) along the  $z$ -direction as shown in Figure 3.1, is subjected to a bending force. If the transverse displacement ( $w$ ) along the  $z$ -direction after the bending deformation is much smaller than the beam thickness, then the axial displacement ( $u$ ) along the  $x$ -direction can be expressed using Equation (3.1).

$$u = -z \frac{dw}{dx} \quad (3.1)$$

The axial strain ( $\epsilon_x$ ) can be expressed using Equation (3.2)

$$\epsilon_x = \frac{du}{dx} = -z \frac{d^2w}{dx^2} \quad (3.2)$$

Using Equation (3.2) along with the constitutive equation ( $\sigma_x = E\epsilon_x$ ) for elastic material (where  $E$  is the Young's modulus of the beam material), a moment balance

about the  $y$ -axis would yield Equation (3.3) which describes the relationship between bending moment ( $M$ ), stress and beam dimensions.

$$\sigma_x = -z \frac{M}{I} \quad (3.3)$$

In Equation (3.3),  $I$  is the 2<sup>nd</sup> moment of area which can be calculated from Equation (3.4) for a beam with a uniform rectangular cross-section as shown in Figure 3.1.

$$I = \int_{y=-\frac{b}{2}}^{y=+\frac{b}{2}} \int_{z=-\frac{t}{2}}^{z=+\frac{t}{2}} z^2 dz dy = \frac{1}{12} bt^3 \quad (3.4)$$

Equations (3.2) and (3.3) imply that the stress and strain at a beam cross-section varies along the thickness for a given bending moment. This variation is shown in Figure 3.2.

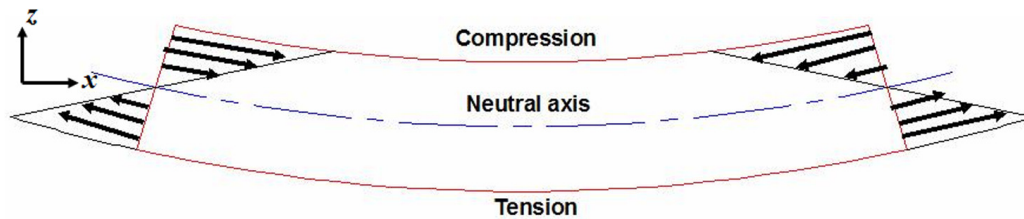


**Figure 3.2. A bending beam with compressive and tensile strain/stress above and below the neutral axis respectively.**

Figure 3.2 shows that when a beam is subjected to transverse loading, the deformed beam has opposite states of strain and stress on opposite sides of a plane which is known as the neutral axis in the two-dimensional representation of the beam. The spatial variation in strain and stress even for a constant bending moment makes characterization under bending distinctly different from characterization of a rod under constant axial force that was described in Chapter 2. An intuitive question that might arise is that whether the opposing stress states produce a net zero change in

magnetic induction when a magnetostrictive beam is subjected to bending in the presence of a bias magnetic field.

### 3.2. *Motivation and scope of this work*

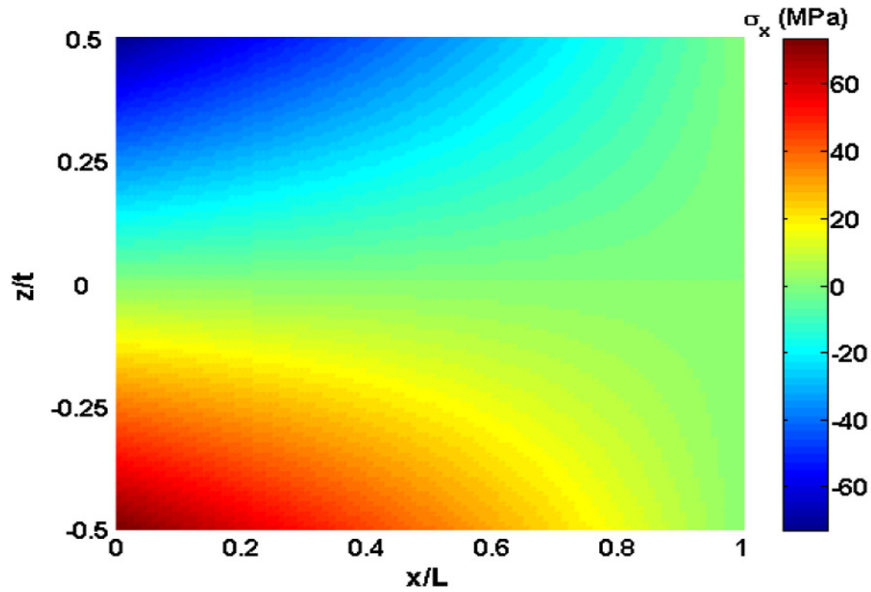
The question posed at the end of the previous section motivates the study of the distribution of stress and magnetic induction along the thickness of a magnetostrictive beam which is fixed at  $x = 0$  and free at  $x = L$ . A beam with these boundary conditions is also known as a cantilevered beam. Cantilevered beams are often used for bending characterization [137].

The stress at a given point in a cantilevered beam subjected to a transverse tip loading ( $F$ ) can be described using Equation (3.5) which can be obtained by substituting  $M = F(L - x)$  in Equation (3.3).

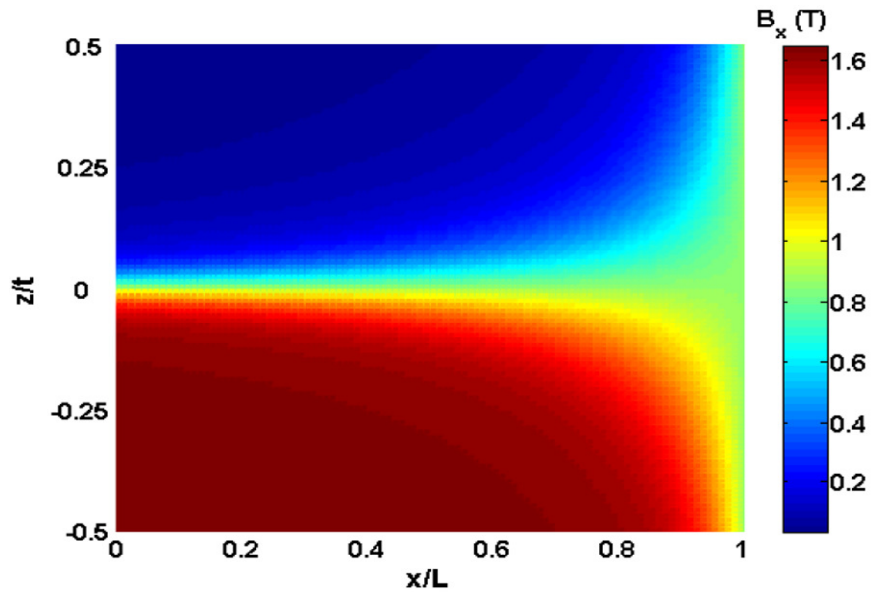
$$\sigma_x(x, z) = -z \frac{F(L - x)}{I} = -\frac{12FL}{bt^2} \left( \frac{z}{t} \right) \left( 1 - \frac{x}{L} \right) \quad (3.5)$$

Figure 3.3 shows the stress distribution along the span and thickness of a cantilevered beam calculated using Equation (3.5). The simulation results are expressed in terms of non-dimensionalized length ( $x/L$ ) and thickness ( $z/t$ ). The parameters used in this calculation are  $F = 2$  N,  $L = 25$  mm,  $b = t = 1.6$  mm.

Using this stress distribution in the energy-based model described in Chapter 2, the magnetic induction distribution in a  $\text{Fe}_{84}\text{Ga}_{16}$  beam can be simulated as shown in Figure 3.4. Note that  $B$  varies significantly along the span as well as thickness of the beam. A GMR or Hall-effect sensor placed on the surface of the beam would measure a value proportional to  $B$  at the location of the sensor. A pick-up coil wrapped around the beam would measure a thickness-averaged  $B$ .



**Figure 3.3. Stress ( $\sigma_x$ ) distribution in a cantilevered beam.**



**Figure 3.4. Magnetic induction ( $B_x$ ) distribution in a cantilevered  $\text{Fe}_{84}\text{Ga}_{16}$  beam for a bias magnetic field of 0.5 kA/m.**

Figure 3.5 shows the simulation results of thickness-averaged  $B$  along the span of the same cantilevered beam subjected to a 2 N tip loading, for different bias magnetic fields. For the purpose of these simulations, we assumed that the bias field is uniform inside the beam. These simulation results show that the thickness-averaged

$B$  measured by a pick-up coil may vary significantly along the beam span and hence the measurement of  $B$  will be affected by the length and position of the pick-up coil.

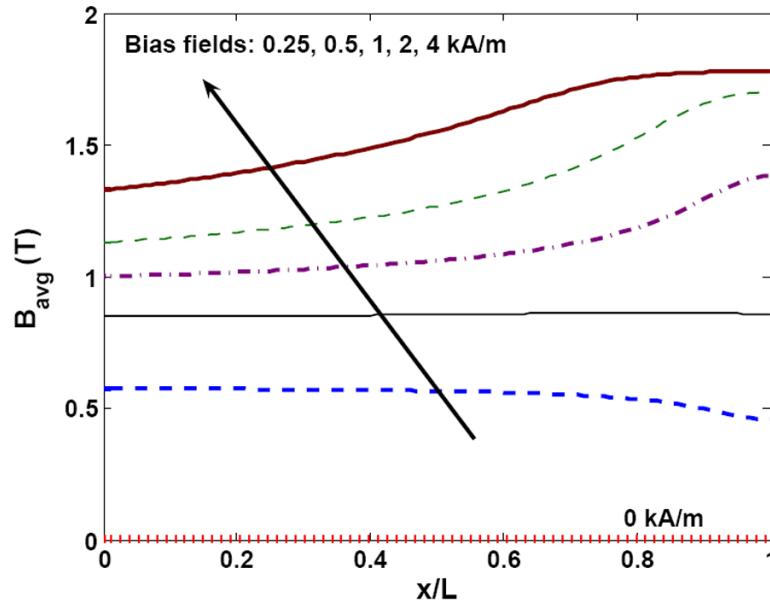


**Figure 3.5. Thickness-averaged magnetic induction along the span of a cantilevered  $\text{Fe}_{84}\text{Ga}_{16}$  beam for bias magnetic fields of 0, 0.25, 0.5, 1, 2, 4 kA/m.**

These challenges related to characterization of cantilevered magnetostrictive beam can introduce significant variation in the experimental results and hence motivates the development of an alternate characterization technique for bending magnetostrictive members. In this chapter, the concept of four-point bending test under magnetic fields will be introduced. The experimental design will be discussed with particular emphasis on the magnetic and mechanical boundary conditions and how that can help in reducing the experimental variability of a magnetostrictive beam characterized as a sensor in bending.

### 3.3. *Design of experiment*

This section will discuss about the design of the magnetomechanical four-point bending experimental setup. The test setup consists of magnetic and mechanical components. The mechanical components were designed based on the guidelines given in ASTM C1161 [176]. The magnetic components were designed to apply different DC bias magnetic fields along the length of the Galfenol beam. The details of the experimental design are discussed as follows.

#### 3.3.1. Mechanical components

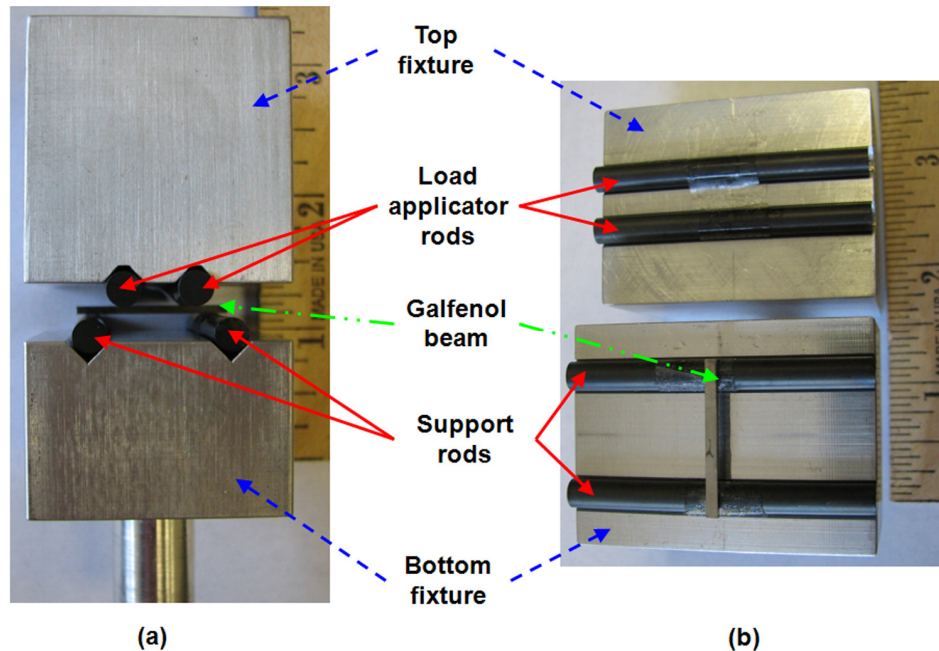


**Figure 3.6. (a) Assembled view and (b) parts view of the mechanical components of the four-point bending test.**

Figure 3.6 shows the mechanical components of the four-point bending test setup. It was ensured that all load-bearing components are non-magnetic so that they

do not interfere with the magnetic flux path. The fixture was made of Aluminum 7075 and the load applicator and support rods were made of silicon carbide.

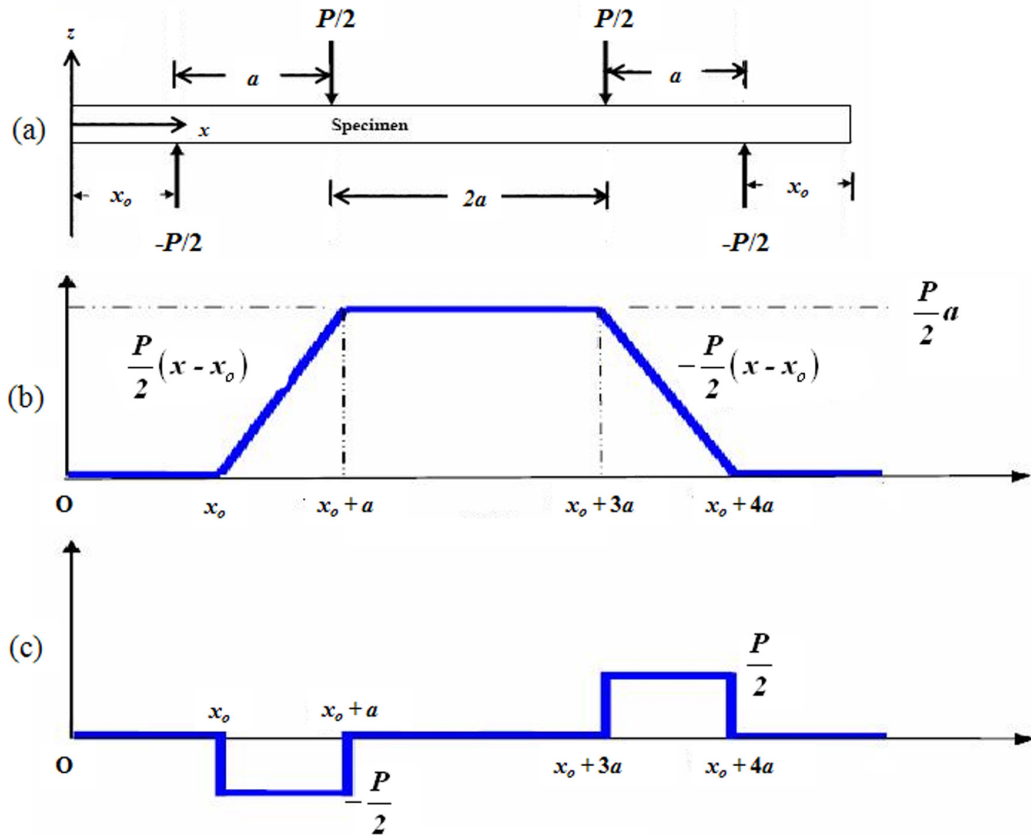


**Figure 3.7. A beam subjected to four-point bending, after Ref.[177]. (a) Free-body diagram showing the applied and resultant forces. (b) Bending moment diagram. (c) Shear force diagram.**

Figure 3.7(a) shows the free-body diagram of the Galfenol beam specimen placed between the top and bottom fixtures. The four silicon carbide rods form line contacts with the beam which can be described by four points as shown in Figure 3.7(a). The two upper rods which are separated by a distance ( $2a$ ) apply equal loads of magnitude ( $P/2$ ). The two lower rods which are separated by a distance ( $4a$ ) provide equal reaction forces of magnitude ( $-P/2$ ).

Figure 3.7(b) shows the bending moment along the beam span. The primary advantage of four-point bending is that it offers a region of constant bending moment between the load applicators. In this region, the stress varies only along the direction of thickness. Hence, if a pick-up coil is wrapped around this region of the beam, it can be expected that the thickness-averaged  $B$  measured by the coil would be independent of the position and length of the coil.

A second advantage of using four-point bending is evident from Figure 3.7(c) which shows the shear force diagram. The shear force diagram implies that in the region between the upper rods, the shear stress ( $\sigma_{xz}$ ) can be expected to be zero. This condition ensures that only one component of stress ( $\sigma_x$ ) is non-zero in the mid-span of the beam and hence the setup can be effectively reduced to a one-dimensional problem. Moreover, the stress-induced changes in magnetic induction in the beam would be only dependent on  $\sigma_x$ .

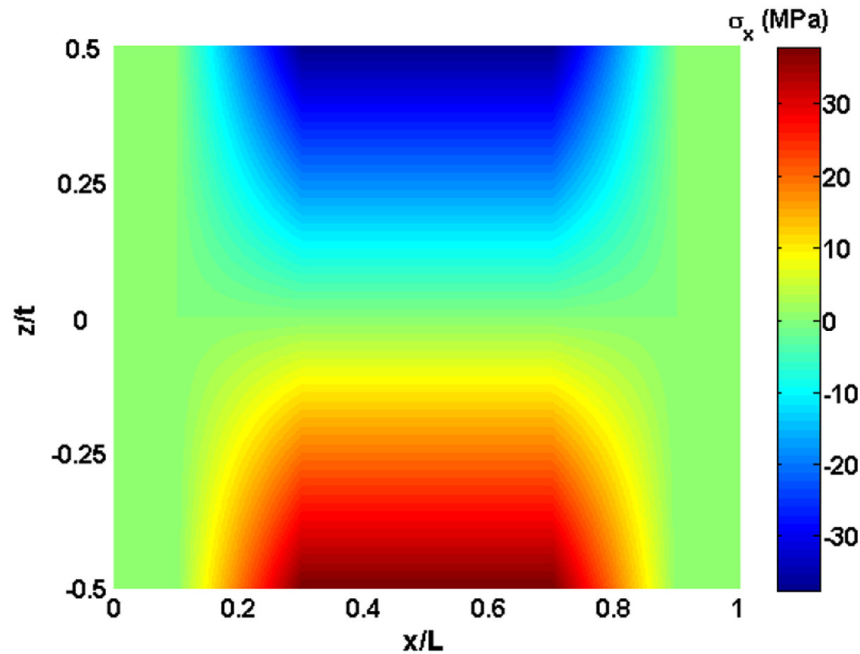


**Figure 3.8. Stress ( $\sigma_x$ ) distribution in a beam subjected to four-point bending.**

Figure 3.8 shows the stress distribution in a beam of length 25-mm and cross-section 2-mm x 2-mm subjected to four-point bending. A force ( $P$ ) of -20 N was used for simulation. As anticipated from Figure 3.7, a region of constant stress can be seen in Figure 3.8 for  $0.3 \leq x/L \leq 0.7$ . A value of  $x_o = 2.5$  mm and  $a = 5$  mm were used in the simulation to be consistent with the actual design.

### 3.3.2. Magnetic components

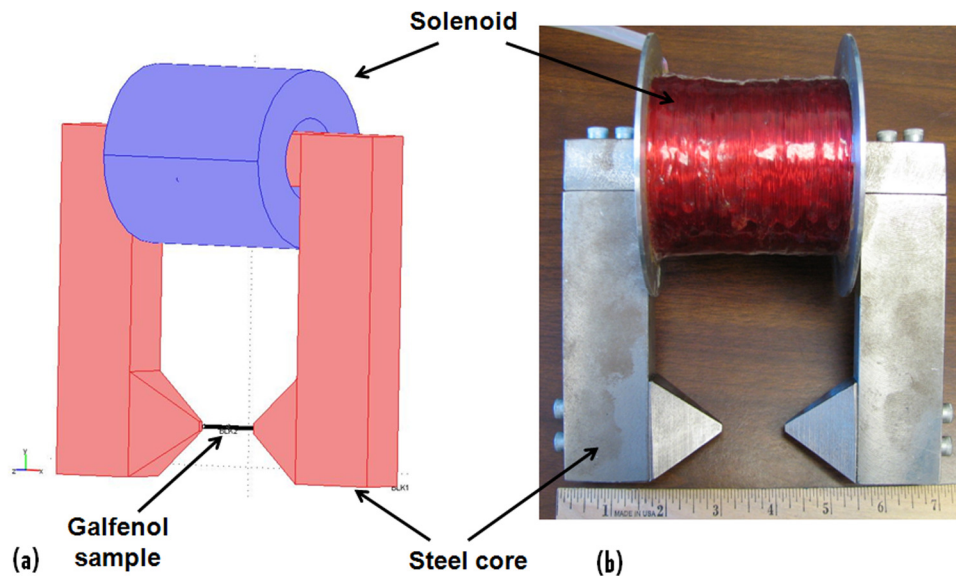


**Figure 3.9. (a) Schematic showing the position of the Galfenol sample in the electromagnet. (b) Photograph of the electromagnet.**

Figure 3.9 shows the electromagnet that was specially designed to apply DC bias magnetic fields to the sample kept inside the four-point bending fixture. Since the sample could not be kept inside a solenoid as that would obstruct the load path, an electromagnet had to be designed which would provide a magnetic flux path. The electromagnet core was made of 1018 steel. The pole pieces were tapered to the cross-section dimensions of the sample in order to maximize flux concentration. The

solenoid was made of insulated copper coil having 2600 turns and it had a length of 8.25 cm. Note that in this setup, the nature of loading prevents the design of a perfectly closed magnetic circuit. Therefore, a finite element analysis was performed to estimate the effectiveness of the magnetic flux path.

A 3D electromagnetic finite element analysis was performed using the AC/DC module in COMSOL Multiphysics 3.4. The “*Magnetostatics*” formulation used vector - quadratic elements. The magnetic boundary value problem is solved by COMSOL using the governing Equation (3.6) where  $\mathbf{A}$  is a vector potential and  $\mathbf{J}$  is the current density in the coil. Note that Equation (3.6) is a special form of the Maxwell’s equations described in Section 1.3.4. The current density is the current flowing through per unit area perpendicular to the flow of current. In this case, the relevant area is the length of the solenoid times the thickness of the conducting wires in the solenoid.

$$\nabla \times \left[ \frac{1}{\mu_o \mu_r} (\nabla \times \mathbf{A}) \right] = \mathbf{J} \quad (3.6)$$

The relation between  $\mathbf{B}$  and  $\mathbf{A}$  is described by Equation (3.7). The potential  $\mathbf{A}$  is chosen to be a vector in order to satisfy the subsidiary condition given by the Gauss’s law ( $\nabla \cdot \mathbf{B} = 0$ ). The constitutive relation is given by Equation (3.8).

$$\mathbf{B} = \nabla \times \mathbf{A} \quad (3.7)$$

$$\mathbf{H} = \frac{1}{\mu_o \mu_r} \mathbf{B} \quad (3.8)$$

For simulation purposes, relative permeability of  $10^4$  and 1 were assigned to steel and copper coil respectively. The relative permeability of Galfenol was obtained as a function of  $B$  at zero stress from the simulated data created in Chapter 2. A

rectangular parallelepiped air domain with relative permeability of one and of roughly three times the size of the electromagnet along each of the  $x$ ,  $y$  and  $z$ -directions was defined to ensure that the flux leakage is accurately estimated. A boundary condition of magnetic insulation was assigned to the boundaries of the air domain. This boundary condition ensures that the magnetic field has only tangential component at the boundary of the air domain.

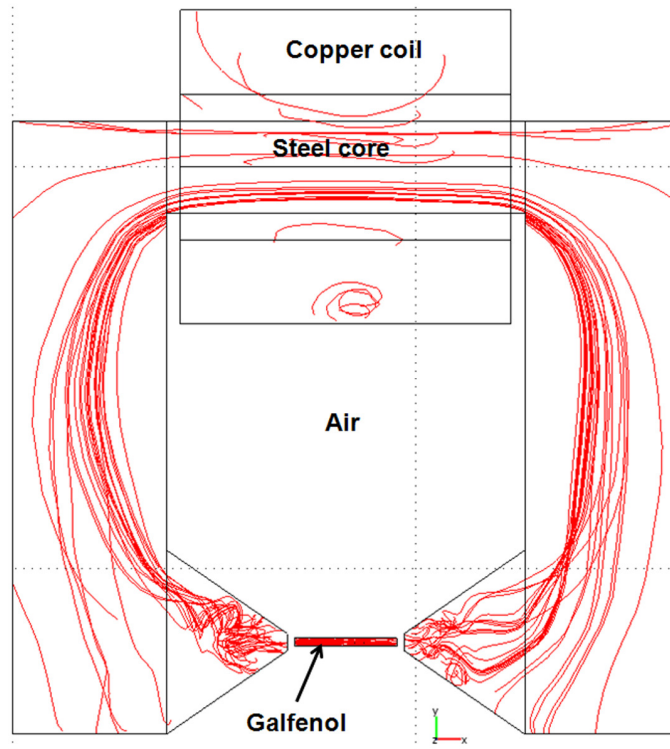


**Figure 3.10. Flow of magnetic flux lines in the experimental setup. The flux lines in air are suppressed for visual clarity.**

Figure 3.10 shows the simulated magnetic flux lines for  $\mathbf{J} = 0\hat{i} - \frac{J_o z}{\sqrt{y^2 + z^2}}\hat{j} + \frac{J_o y}{\sqrt{y^2 + z^2}}\hat{k}$  where  $J_o = 3.95 \times 10^6 \text{ A/m}^2$ . Note that the centerline of the solenoid is aligned with the global  $x$ -axis, i.e., it passes through  $y = 0$  and  $z = 0$ . It can be seen in Figure 3.10 that the flux lines flow through the steel electromagnet

core and concentrate in the Galfenol sample that is placed between the electromagnet pole pieces. The simulation also showed that in general the flux leakage is more predominant at edges and corners.

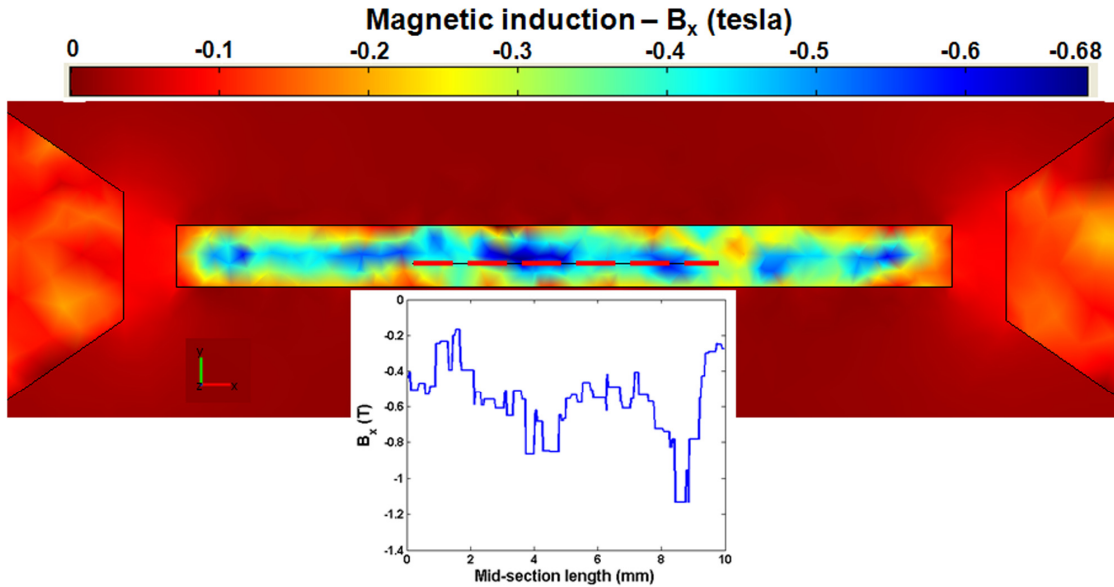


**Figure 3.11. Spatial distribution of  $B_x$  in the Galfenol beam. The plot shows the variation in  $B_x$  along the section of the beam between the two upper rods. This section is indicated by the red dashed line.**

Figure 3.11 shows the simulated distribution of magnetic induction in the beam placed between the electromagnet pole pieces. A line plot of the variation of  $B_x$  between the load application points showed that  $B_x$  can vary at most by 35 % in this region. Considering that the nature of the experiment prevents a perfectly closed magnetic circuit, the estimation of the variation in magnetic induction is important to understand the variation in bias field for a constant current applied through the solenoid.

### 3.4. *Magnetomechanical four-point bending test*

This section describes the Galfenol sample used for the experiment and the test procedure of the magnetomechanical four-point bending test.

#### 3.4.1. Sample description

The rectangular parallelepiped single crystal Galfenol beam sample shown in Figure 3.12 was obtained from the same ingot described in Chapter 2 from which the  $\text{Fe}_{84}\text{Ga}_{16}$  rod was obtained. An EDS analysis of this Galfenol beam showed a composition of  $81.2 \pm 0.7$  atomic % iron and  $18.8 \pm 0.7$  atomic % gallium. The compositional gradient in the ingot can be attributed to the growth and processing technique.



**Figure 3.12. Single crystal Galfenol ( $\text{Fe}_{81}\text{Ga}_{19}$ ) beam sample used in magnetomechanical four-point bending test.**

The Galfenol beam measured 25 mm x 2 mm x 2 mm and its length, width and thickness were oriented along the crystallographic  $\langle 100 \rangle$  directions. The size of the Galfenol beam corresponded to smallest dimensions prescribed in ASTM C1161 [176]. A larger sample could not be obtained owing to the restriction imposed by the size of the iron-gallium ingot.

### 3.4.2. Test procedure

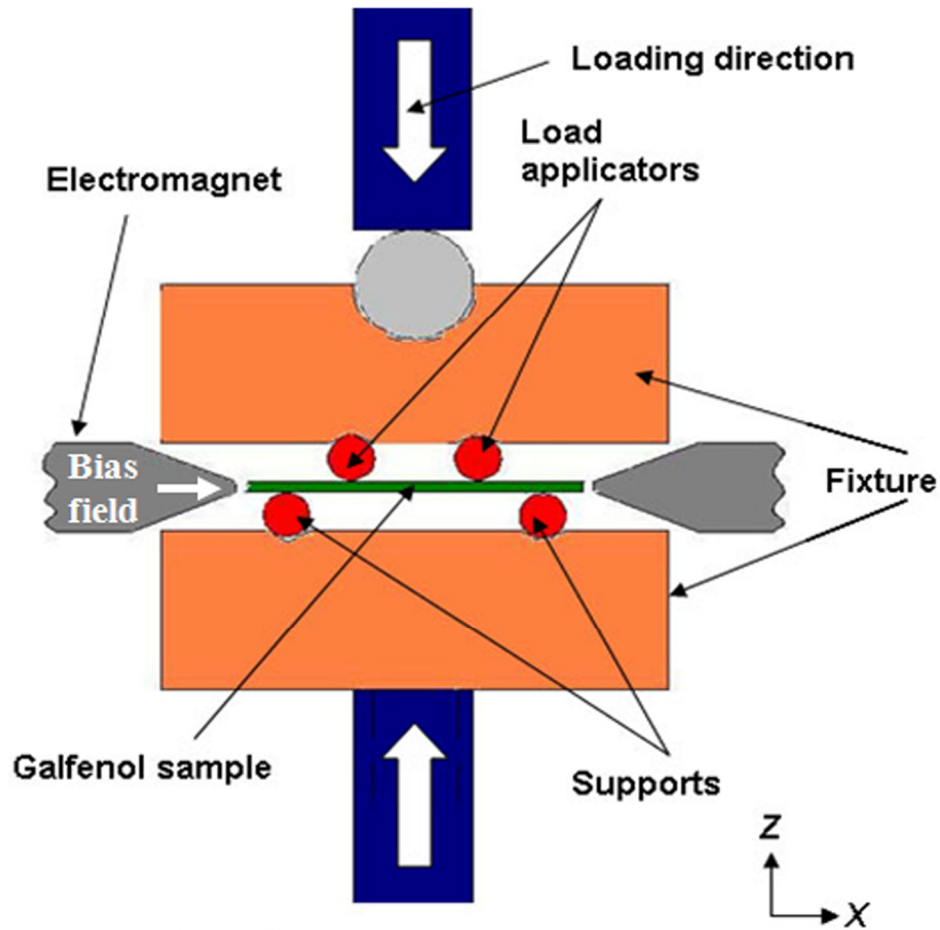


**Figure 3.13. Schematic of the magnetomechanical four-point bending test setup.**

Figure 3.13 shows the assembled test setup. The mechanical fixture was mounted on a hydraulic MTS 810 universal testing machine. A silicon carbide ball that was used to transfer load from the MTS machine to the mechanical fixture provided a point contact in order to ensure that only axial force is exerted on the Galfenol beam. The electromagnet was clamped on two sides and placed in the same horizontal plane as the sample so as to apply magnetic field along the length of the sample. The DC bias magnetic field was applied by passing a constant current through the solenoid. The load was quasi-statically cycled once from 0 to 40 N at a

ramp rate of 2 mm/min. At the end of the load cycle, the constant current in the solenoid was switched off. Before each test, the sample was demagnetized over 167 cycles using a 1 Hz sinusoidal field which underwent a 5 % geometric decay every 1.5 cycles from an initial amplitude of 15 kA/m. The procedure was repeated for applied magnetic fields of 0,  $1.35 \pm 0$ ,  $1.99 \pm 0$ ,  $2.71 \pm 0$ ,  $7.52 \pm 0.33$  and  $11.01 \pm 0.12$  kA/m which were obtained by passing currents of 0, 0.05, 0.15, 0.25, 1 and 1.75 ampere through the solenoid.

Note that these applied magnetic fields were measured in air by placing a hand-held gaussmeter (F. W. Bell Model 5080) in between the pole pieces of the electromagnet for different constant current in the solenoid. In this experiment, the bias magnetic field in the sample could not be maintained during the loading cycle using the feedback controller described in Chapter 2 because of the lack of closed magnetic circuit. Moreover, the stress distribution in the Galfenol beam creates a spatial distribution of the magnetic field in the beam unlike in the Galfenol rod described in Chapter 2, where a uniform stress-state in the entire rod ensured a uniform change in reluctance and magnetic field in the Galfenol sample.

A pick-up coil with 100 turns wrapped around the sample and connected to an integrating fluxmeter measured the thickness-averaged magnetic induction along the beam span between the load applicators.

### 3.5. *Results and discussion*

This section describes the results obtained from the magnetomechanical four-point bending test and attempts to explain the trends using a qualitative energy-based approach.

In Chapter 2, stress could be used as an independent input parameter in the characterization as it was uniform in the rod-shaped sample for a given axial force. For a given transverse force, a stress distribution occurs along the thickness and length of the beam. The physical quantity that remains constant along the thickness at a given beam section is the bending moment. However, the same bending moment can produce a different stress distribution based on the cross-section dimensions of the beam. Hence, in this chapter, the parameter ( $M_{xt} = M/bt^2$ ) is introduced to replace the use of stress as an input parameter in characterization involving bending. Note that  $M_{xt}$  has the dimension of stress and the magnitude of stress due to pure bending at any point along the beam thickness is bounded by  $0 \leq |\sigma_x| \leq 6M_{xt}$ .

### 3.5.1. Sensor characterization in bending

Figure 3.14 shows the thickness-averaged magnetic induction ( $B_x$ ) measured by the pick-up coil placed in the mid-section of the beam in between the load application points. The maximum induction that could be observed in the Galfenol sample was limited to ~0.5 T because of the following reason. An applied magnetic field of 7.52 kA/m was sufficient to saturate the electromagnet steel core and hence any additional current through the solenoid did not significantly increase the flux through the electromagnet. Although the electromagnet was useful for concentrating the magnetic flux into the Galfenol sample, the lack of a perfectly closed magnetic circuit caused significant flux leakage and could generate a magnetic induction of only 0.5 T in the Galfenol sample while the electromagnet core got saturated.

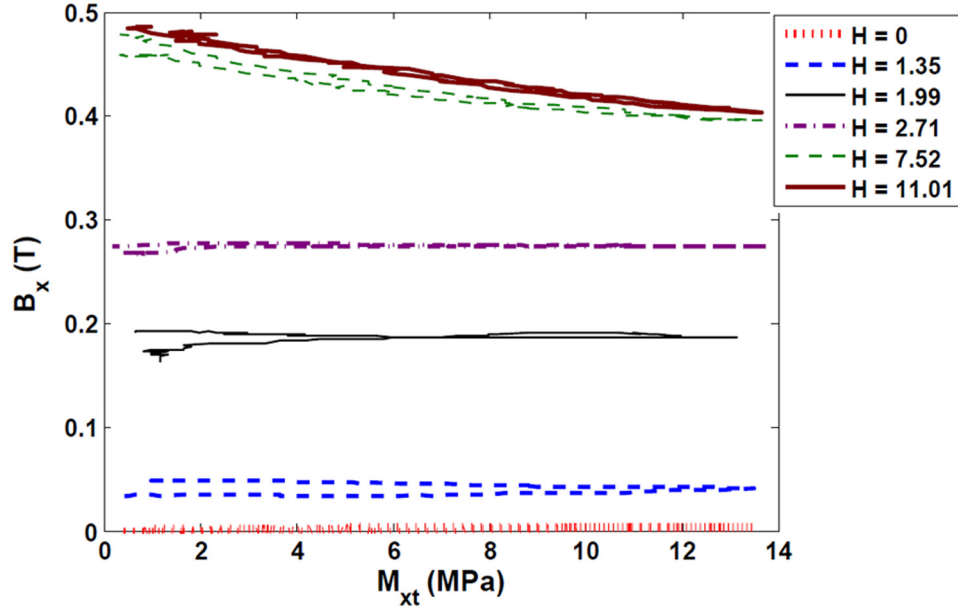


**Figure 3.14. Thickness-averaged magnetic induction ( $B_x$ ) as a function of  $M_{xt}$  at applied bias magnetic fields of 0, 1.35, 1.99, 2.71, 7.52 and 11.01 kA/m.**

At a given non-zero magnetic bias field ( $H$ ), Galfenol is expected to show an increase in  $B$  under tension and a decrease in  $B$  under compression. If the effect of tension and compression due to bending on  $B$  were equal then  $B$  should remain constant at all  $M_{xt}$ . Such behavior is observed at zero and low  $H$  (upto 2.71 kA/m). At higher  $H$  (7.52 and 11.01 kA/m), the magnetic moments are mostly aligned in the direction of  $H$  and hence a tensile stress collinear to  $H$  does not contribute to any change in  $B$  and the magnetic response is dominated by compressive stress. This is evident from the decrease in  $B$ . If  $M_{xt}$  is increased to a critical value, the magnetic moments in the compressive region of the sample are all aligned perpendicular to  $H$ . Beyond this  $M_{xt}$ , no stress induced change in magnetic moment orientation takes place thereby leading to a steady value of  $B$ .

### 3.5.2. Discussion on experimental trends

The trends shown in the magnetomechanical four-point bending test can be explained in terms of the total energy per unit volume of the Galfenol beam. The total energy considered here is the sum of the magnetocrystalline anisotropy, stress-induced anisotropy and Zeeman energies.

The thickness-averaged  $B$  can be deduced using the principle of superposition. The net  $B$  measured by the pick-up coil can be assumed to be the average of the  $B$  below the neutral axis of the Galfenol beam which is in tension and the  $B$  above the neutral axis of the beam which is in compression. The  $B$  below and above the neutral axis will be proportional to the volume fraction of magnetic moments and their orientation in these regions respectively. This information can be qualitatively deduced from the energy maps shown in Figures 3.15 and 3.16.

Note that the magnetic fields used for simulation are internal magnetic fields in Galfenol and not the applied magnetic field. Moreover, a lumped parameter approach is used in demarcating regions with compressive and tensile stresses in the beam instead of using a detailed profile of the stress variation along the beam thickness. These assumptions are acceptable as we are only interested in understanding the physics of the behavior qualitatively. A more rigorous modeling technique for bending magnetostrictive beams will be developed in Chapter 5.

Figure 3.15(a) shows the four equal energy minima in Galfenol in the absence of stress and magnetic field owing to its cubic magnetocrystalline anisotropy. Figure 3.15(b) shows that when a small bias magnetic field is applied, say along  $0^\circ$ , only a small fraction of the magnetic moments which were earlier oriented along  $90^\circ$ ,  $180^\circ$

and  $270^\circ$  rotate towards  $0^\circ$  as the energy wells along  $90^\circ$ ,  $180^\circ$  and  $270^\circ$  still continue to exist.

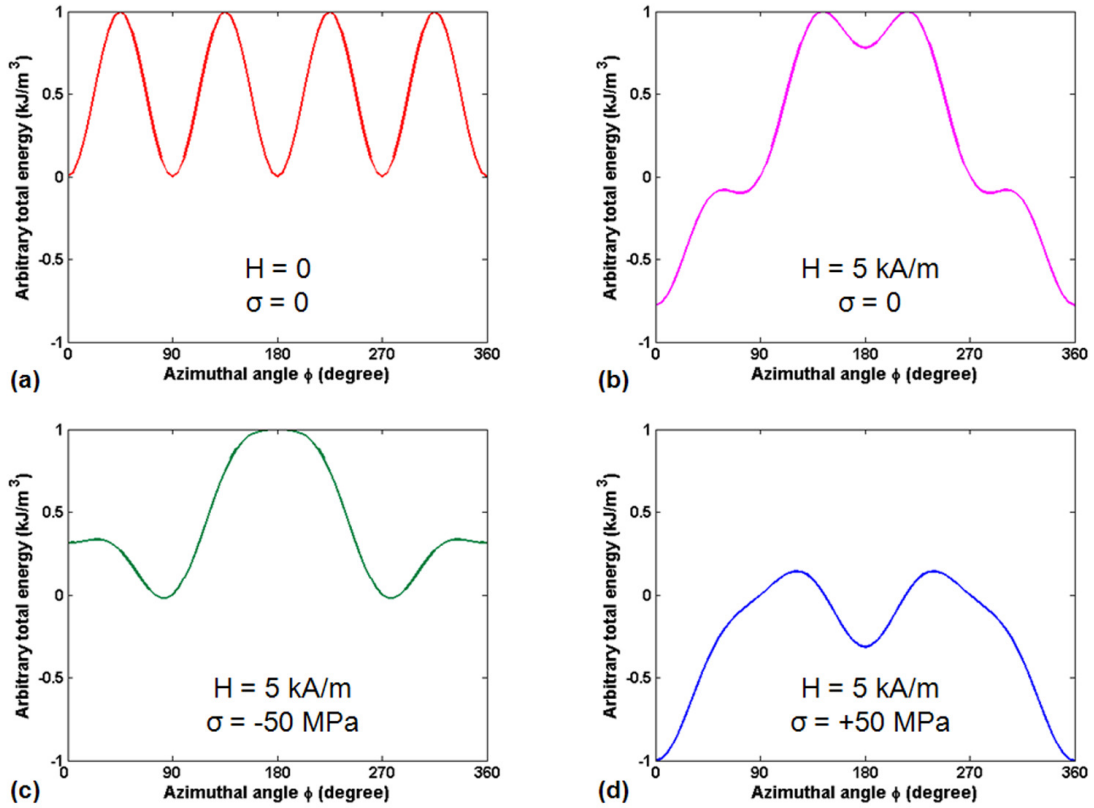


**Figure 3.15. Total energy distribution,  $E_{TOT}(\sigma, H)$ , in the azimuthal plane (a) in a demagnetized and un-stressed sample, (b) after applying a low bias magnetic field, (c) in the region above neutral axis after bending and (d) in the region below neutral axis after bending.**

When the Galfenol sample undergoes bending in presence of a small bias field, the parts of it which are in compression and tension have the energy distribution as shown in Figure 3.15(c) and Figure 3.15(d) respectively. The compressive stress rotates the magnetic moments lying above the neutral axis of the beam from  $0^\circ$  and  $180^\circ$  toward  $90^\circ$  and  $270^\circ$ . The tensile stress rotates the magnetic moments lying below the neutral axis of the beam from  $90^\circ$  and  $270^\circ$  toward  $0^\circ$  and  $180^\circ$ . As a net

effect, there is an insignificant change in thickness-averaged  $B$  before and after bending in the presence of a small bias magnetic field.

Figure 3.16(a) shows the four equal energy minima in Galfenol in the absence of stress and magnetic field owing to its cubic magnetocrystalline anisotropy. Figure 3.16(b) shows that when a large bias magnetic field is applied along  $0^\circ$ , most of the magnetic moments which were earlier oriented along  $90^\circ$ ,  $180^\circ$  and  $270^\circ$  rotate towards  $0^\circ$ .

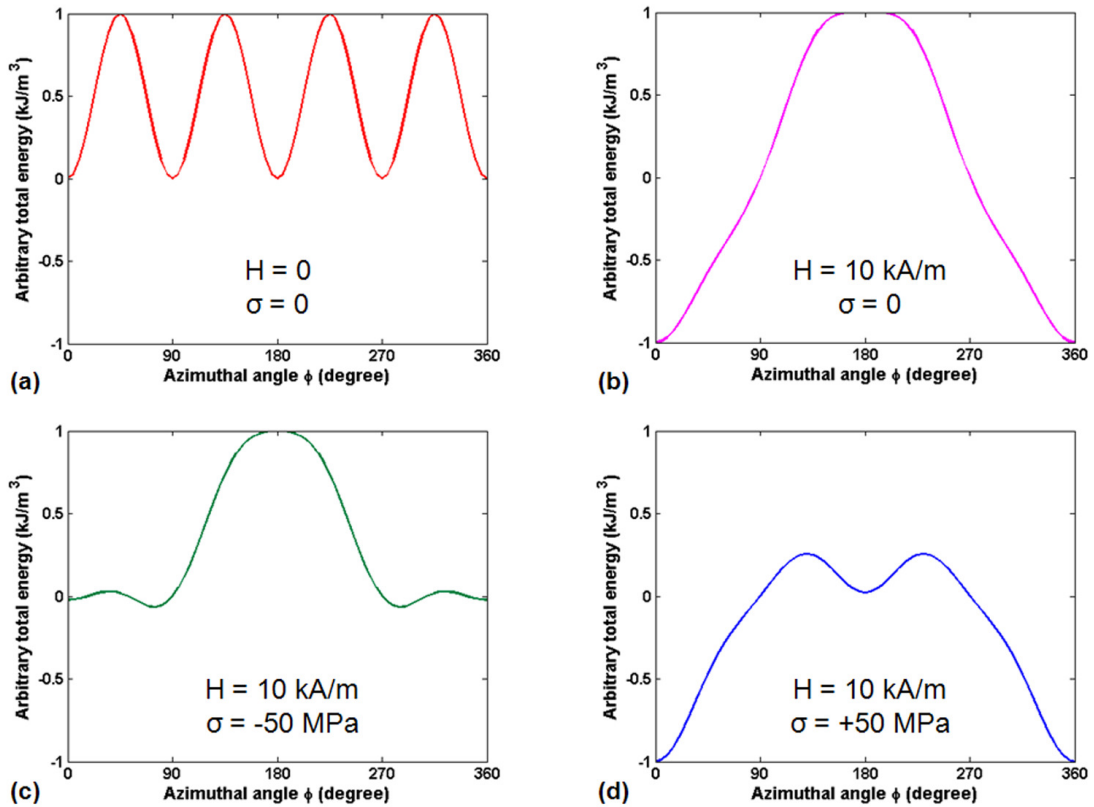


**Figure 3.16. Total energy distribution,  $E_{TOT}(\sigma, H)$ , in the azimuthal plane (a) in a demagnetized and un-stressed sample, (b) after applying a high bias magnetic field, (c) in the region above neutral axis after bending and (d) in the region below neutral axis after bending.**

When the Galfenol sample undergoes bending in presence of the large bias field, the parts of it which are in compression and tension have the energy distribution as shown in Figure 3.16(c) and Figure 3.16(d) respectively. The compressive stress rotates some of the magnetic moments lying above the neutral axis of the beam from  $0^\circ$  toward  $90^\circ$  and  $270^\circ$ . The tensile stress can rotate the magnetic moments lying below the neutral axis of the beam to either  $0^\circ$  or  $180^\circ$ . Since most of the magnetic moments are already oriented along  $0^\circ$  under the influence of a large bias field, the tensile stress has no effect. As a result, the effect of compressive stress in the upper half of the beam dominates over the effect of tensile stress in the beam's lower half, and a net change in thickness-averaged  $B$  is observed before and after bending in the presence of a large bias magnetic field.

### 3.6. Summary

In this chapter, the use of a magnetostrictive beam as a sensing element was introduced. Existing characterization technique which uses cantilevered beam was reviewed. It was shown that the continuous span-wise variation of bending moment (and stress) makes it experimentally challenging to evaluate the sensing performance of a cantilevered magnetostrictive beam.

The concept of a magnetomechanical four-point bending test was introduced as an alternate characterization technique. The main advantage of this technique is that it produces a region of constant bending moment along the span of the beam in-between the two loading points. A prototype fixture was designed, built and used to test a single crystal  $\text{Fe}_{81}\text{Ga}_{19}$  beam at different applied bias magnetic fields. Challenges related to application of bias field in bending sensor due to lack of a

closed magnetic circuit were discussed. The experimental results were analyzed using the energy terms introduced in Chapter 1.

In conclusion, it can be said that magnetostrictive sensing can be performed in bending even when both tensile and compressive stresses are developed in the material. The sensing is primarily due to the dominating effect of compression over tension. A critical bias magnetic field is required below which the magnetostrictive sensing cannot be observed under bending.

## Chapter 4: Experimental studies on laminated Galfenol-Aluminum composite

Active materials are often integrated with passive structural materials in laminated composites which can be used as smart structures. The simplest laminated active composite is a bi-layered structure with an active and a passive layer. Such a bi-layered structure which has one active layer is also known as a unimorph. A unimorph can work as the fundamental element of bending-based smart structure. This type of smart structure undergoes actuation due to the strain induced by the active layer. The unimorph configuration can be also used for sensing mechanical quantities. For example, a force applied to the unimorph would produce a stress in the active layer thereby changing its properties which in turn can be measured and correlated to the applied force.

In this chapter, we will investigate the actuation and sensing behavior of laminated Galfenol-Aluminum composite beams such as the one shown in Figure 4.1. The concept of induced-strain actuation in composite beams comprising of active and passive lamina will be introduced. Applications of Galfenol-based laminated composites and motivation to study their design and performance criteria will be stated. The design of experimental setup and challenges related to measurement techniques will be discussed which will be followed by the interpretation of the actuator and sensor characterization results from the tests performed on the Galfenol-Aluminum unimorphs.

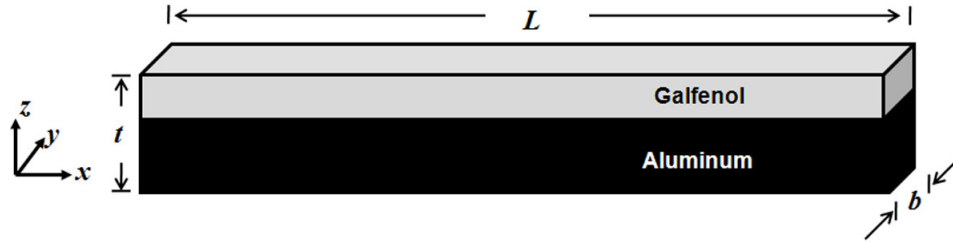


**Figure 4.1. A Galfenol-Aluminum laminated composite beam.**

4.1. Classical laminated beam theory with induced-strain actuation

The Euler-Bernoulli beam theory can be used [1] for structural analysis of laminated beams with the following assumptions.

1. The bond layer between the laminae is infinitesimally small and there is no flaw or gap in the bond layer.
2. There is no shear deformation in the bond layer, i.e. the laminae cannot slip relative to each other.
3. The bond layer has infinite stiffness and hence the composite beam behaves like a single lamina with integrated properties.

Section 3.1 presented the relevant mathematical expressions required for modeling pure bending but in general a composite beam may undergo both extension and bending. Therefore, the axial displacement along  $x$ -direction may be expressed using Equation (4.1) where  $u^o$  is the extensional displacement of the mid-plane of the composite beam and the other terms are the same as described in Section 3.1.

$$u = u^o - z \frac{dw}{dx} \quad (4.1)$$

Similarly the total axial strain ( $\varepsilon_x$ ) can be expressed using Equation (4.2) where  $\varepsilon^o$  is the mid-plane strain and  $\kappa$  is the curvature about the  $y$ -axis. Note that a non-zero mid-

plane strain indicates that the neutral axis (where  $\varepsilon_x = 0$ ) of the composite beam will not coincide with its mid-plane.

$$\varepsilon_x = \frac{\partial u}{\partial x} = \varepsilon^o - z \frac{d^2 w}{dx^2} = \varepsilon^o - z\kappa \quad (4.2)$$

Let us assume that a composite beam with  $NL$  number of laminae is subjected to a force ( $F$ ) along the  $x$ -direction and a bending moment ( $M$ ) about the  $y$ -axis. If  $\sigma_x$  is the axial stress developed in the beam, then a force-balance along the  $x$ -axis and moment-balance about the  $y$ -axis would yield Equations (4.3) and (4.4).

$$F = \int_{-t/2}^{t/2} \sigma_x b dz = \sum_{k=1}^{NL} \int_{h_k}^{h_{k+1}} \sigma_x b dz \quad (4.3)$$

$$M = - \int_{-t/2}^{t/2} \sigma_x b z dz = - \sum_{k=1}^{NL} \int_{h_k}^{h_{k+1}} \sigma_x b z dz \quad (4.4)$$

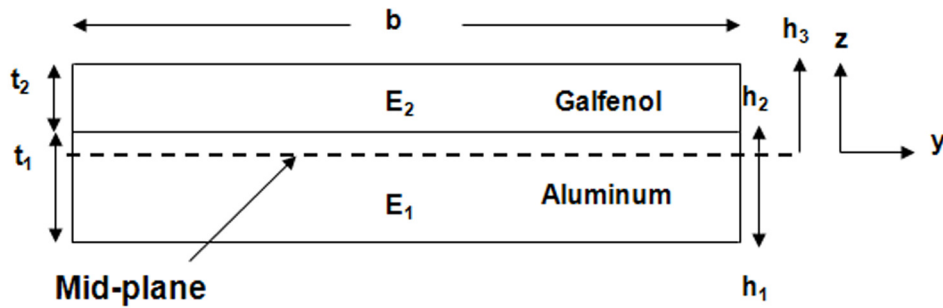


**Figure 4.2. Cross-section of Galfenol-Aluminum unimorph showing the different parameters required to calculate the composite stiffness terms.**

Here  $h_k$  is the distance of the edge of each lamina from the mid-plane as shown in Figure 4.2. Note that the mid-plane is considered as the plane where  $z = 0$ . For an active material with free strain ( $\lambda$ ), the 1D Hooke's law can be written as shown in Equation (4.5) where  $E$  is the Young's modulus.

$$\sigma_x = E(\varepsilon_x - \lambda) = E(\varepsilon^o - z\kappa - \lambda) \quad (4.5)$$

Substituting Equation (4.5) in Equations (4.3) and (4.4) and integrating over the thickness of each lamina, the force and moment balance in the beam can be expressed in terms of Equations (4.6) and (4.7) respectively. It is assumed that the Young's modulus and width of each lamina do not vary across the thickness of each lamina.

$$F = \sum_{k=1}^{NL} E_k b_k \left[ (h_{k+1} - h_k) \varepsilon^o - \frac{1}{2} (h_{k+1}^2 - h_k^2) \kappa - (h_{k+1} - h_k) \lambda_k \right] \quad (4.6)$$

$$M = \sum_{k=1}^{NL} E_k b_k \left[ -\frac{1}{2} (h_{k+1}^2 - h_k^2) \varepsilon^o + \frac{1}{3} (h_{k+1}^3 - h_k^3) \kappa + \frac{1}{2} (h_{k+1}^2 - h_k^2) \lambda_k \right] \quad (4.7)$$

Equations (4.6) and (4.7) can be combined and written as Equation (4.8) which can be used to obtain the mid-plane strain and curvature of the composite beam [1].

$$\begin{bmatrix} EA & -ES \\ -ES & EI \end{bmatrix} \begin{Bmatrix} \varepsilon^o \\ \kappa \end{Bmatrix} = \begin{Bmatrix} F + F_\lambda \\ M + M_\lambda \end{Bmatrix} \quad (4.8)$$

The terms used in Equation (4.8) which are namely the extensional stiffness ( $EA$ ), extension-bending coupling stiffness ( $ES$ ), bending stiffness ( $EI$ ), actuation-induced force ( $F_\lambda$ ) and actuation-induced moment ( $M_\lambda$ ) can be obtained from Equations (4.6) and (4.7) as shown in Equations (4.9) – (4.13).

$$EA = \sum_{k=1}^{NL} E_k b_k (h_{k+1} - h_k) \quad (4.9)$$

$$ES = \frac{1}{2} \sum_{k=1}^{NL} E_k b_k (h_{k+1}^2 - h_k^2) \quad (4.10)$$

$$EI = \frac{1}{3} \sum_{k=1}^{NL} E_k b_k (h_{k+1}^3 - h_k^3) \quad (4.11)$$

$$F_\lambda = \sum_{k=1}^{NL} E_k b_k \lambda_k (h_{k+1} - h_k) \quad (4.12)$$

$$M_{\lambda} = -\frac{1}{2} \sum_{k=1}^{NL} E_k b_k \lambda_k (h_{k+1}^2 - h_k^2) \quad (4.13)$$

Equation (4.8) signifies that the axial and bending displacements can be coupled in a laminated composite beam and the active strain in any of the laminae produces both extensional force and bending moment which deform the active composite beam. This theory can be applied to analyze the Galfenol-Aluminum unimorphs that will be used in this chapter.

#### 4.2. Motivation and scope of this work

Several works have shown the application of Galfenol-based unimorphs where a Galfenol lamina was attached to other materials [132, 136, 178]. However, no experimental work or theoretical estimation have been done that help in understanding the effect of composite stiffness and operating conditions on the actuation and sensing performance of such unimorphs. In this chapter, experiments will be designed and performed based on the theory discussed in Section 4.1 to study the effect of stiffness and operating conditions on the performance of active unimorphs.

The unimorphs will be comprised of a Galfenol layer of constant thickness and an Aluminum layer of a thickness that will be varied to alter the stiffness of the different unimorphs. The effect of operating condition will be evaluated by performing experiments at different magnetic fields and mechanical loading conditions.

Actuator characterization is expected to provide information on optimal stiffness, magnetic field and mechanical loading criteria that would produce

maximum bending displacement in the unimorph. The sensor characterization is expected to provide information on the effect of unimorph stiffness, bias magnetic field and mechanical loads on several sensing parameters which will be defined. The results of these characterizations are expected to provide design criteria for smart structures using Galfenol unimorphs that can produce maximum output under different operating conditions.

#### 4.3. Description of experiment

This section describes the Galfenol and Aluminum samples that were used to make the unimorphs. The choice of thickness of the different Aluminum samples is justified using the theory described in Section 4.1. The test setups used for characterizing the unimorphs as actuator and sensor are described. The magnetic and mechanical aspects of the experimental setup are analyzed separately in Sections 4.4 and 4.5 to provide a deeper insight into the effect of both of these aspects in the experiment design.

##### 4.3.1. Description and characterization of Galfenol lamina

The rectangular parallelepiped single crystal Galfenol lamina sample shown in Figure 4.3 was obtained from the same ingot described in Chapter 2 from which the  $\text{Fe}_{84}\text{Ga}_{16}$  rod and the  $\text{Fe}_{81}\text{Ga}_{19}$  beam were obtained. An EDS analysis of this Galfenol lamina showed a composition of  $81.8 \pm 0.7$  atomic % iron and  $18.2 \pm 0.7$  atomic % gallium. The composition stated here is based on an average of EDS data obtained at five equi-spaced points along the length of the Galfenol sample.



**Figure 4.3. Single crystal Galfenol ( $\text{Fe}_{82}\text{Ga}_{18}$ ) sample used in the unimorphs.**

The Galfenol lamina measured 25 mm x 8.4 mm x 1.86 mm and its length, width and thickness were oriented along the crystallographic  $\langle 100 \rangle$  directions. A larger sample could not be obtained owing to the restriction imposed by the size of the iron-gallium ingot.

Based on the theory discussed in Section 4.1, it is evident that in order to design the unimorphs, it is necessary to obtain a measure of the magnetostriction of the Galfenol lamina. However, the transducer setup described in Chapter 2 could not be used to characterize this Galfenol sample due to its non-cylindrical shape. Therefore, an 82–mm long and 35–mm diameter solenoid with ~2800 turns was used to apply the magnetic field.

The Galfenol lamina was placed inside the solenoid along the center of the long axis and was subjected to a cyclic quasi-static magnetic field with an amplitude of 65 kA/m at a frequency of 0.01 Hz. Prior to the application of the quasi-static magnetic field, the Galfenol sample was demagnetized over 167 cycles using a 1 Hz sinusoidal magnetic field which underwent a 5 % geometric decay every 1.5 cycles from an initial amplitude of 80 kA/m.

Note that all magnetic field values mentioned in this chapter were measured in air using a hand-held gaussmeter. Hence these values correspond to those of the applied magnetic fields. The Hall-effect sensor could not be used to estimate a single-valued internal magnetic field in Galfenol due to the absence of a closed magnetic circuit which caused flux leakage and spatial magnetic field variation as will be shown later using finite element analysis.

The strain ( $\lambda_{||}$ ) along the length of the Galfenol lamina which was placed parallel to the direction of applied magnetic field was measured using a Vishay CEA-13-500UW-120 resistive strain gage. A maximum free strain of  $226 \pm 5 \mu\epsilon$  was observed as shown in Figure 4.4.

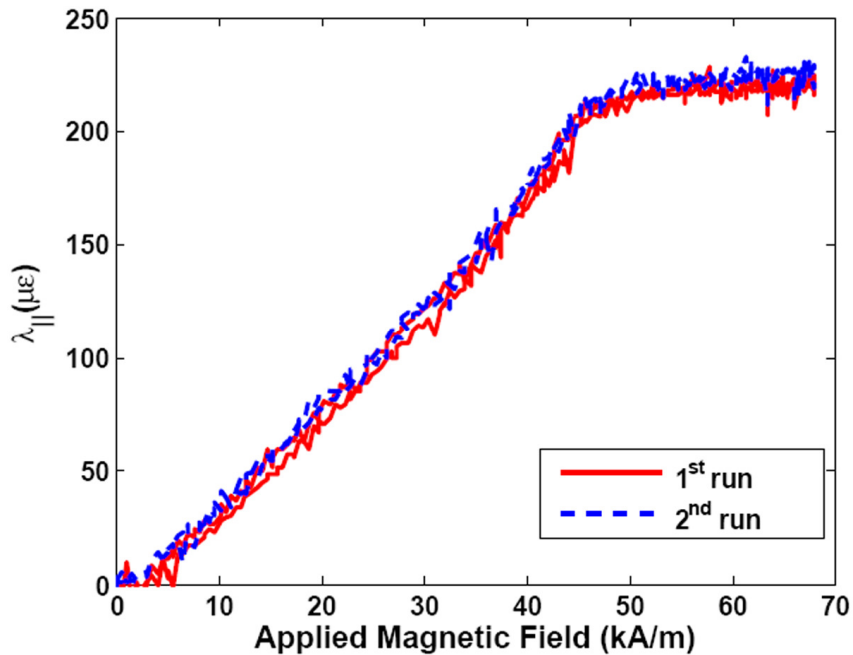


**Figure 4.4.** Free strain ( $\lambda_{||}$ ) vs. applied magnetic field in the single crystal Galfenol ( $\text{Fe}_{82}\text{Ga}_{18}$ ) sample.

#### 4.3.2. Choice of thickness of Aluminum laminae

In order to study the effect of composite stiffness on the out-of-plane tip displacement ( $w_{TIP}$ ) of cantilevered unimorphs, Aluminum laminae of different thickness ( $t_1$ ) were chosen. For small out-of-plane tip displacement such that the curvature ( $\kappa \approx \partial^2 w / \partial x^2$ ) is independent of the position,  $w_{TIP}$  ( $= w$  at  $x = L_1$ ) can be obtained from the curvature and lengths of the Aluminum ( $L_1$ ) and Galfenol ( $L_2$ ) layers using Equation (4.14).

$$w_{TIP} = \frac{\kappa}{2} L_2^2 + \kappa L_2 (L_1 - L_2) \quad \text{for } L_2 \leq L_1 \quad (4.14)$$

From Equation (4.2) and Figure 4.2, it can be deduced that the curvature can be obtained from the difference of strains on the surfaces of the passive and active layers divided by the thickness ( $t$ ) of the composite beam as shown in Equation (4.15).

$$\kappa = \frac{\epsilon_x^{PASSIVE} - \epsilon_x^{ACTIVE}}{t} \quad (4.15)$$

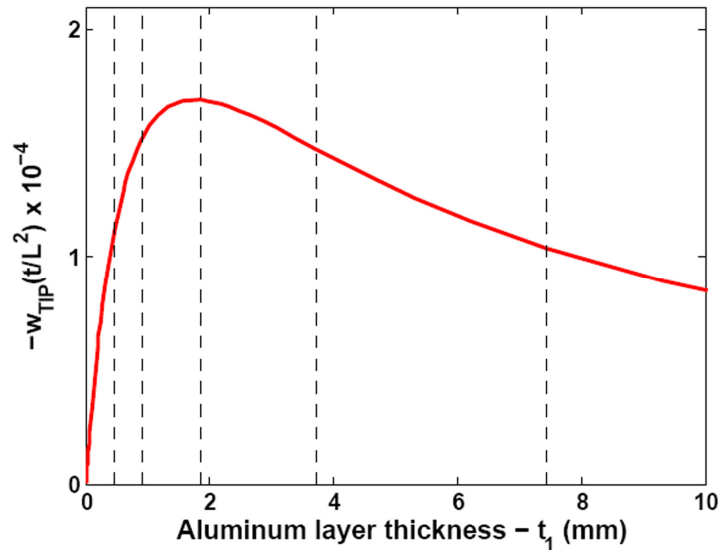


**Figure 4.5. Normalized tip displacement of cantilevered Galfenol-Aluminum unimorph vs. Aluminum layer thickness. Assumed  $L_1 = L_2 = L$ .**

The normalized tip displacement ( $w_{TIP}/L^2$ ) of cantilevered Galfenol-Aluminum unimorphs as a function of the thickness ( $t_1$ ) of the Aluminum layer for a constant Galfenol layer thickness ( $t_2 = 1.86$  mm) and free strain ( $\lambda = 226 \mu\epsilon$ ) is shown in Figure 4.5. The simulation used Young's modulus values of Aluminum as  $E_1 = 70$  GPa and Galfenol as  $E_2 = 63$  GPa. Based on this simulation result, Aluminum laminae of thickness 0.46, 0.91, 1.85, 3.71 and 7.43 mm were obtained using wire EDM for making the Galfenol-Aluminum unimorphs which were expected to show different maximum values of tip displacement. These thickness values are marked by the dashed lines in Figure 4.5. A series of experiments were conducted to evaluate the performance of these unimorphs as actuators and sensors in bending.

#### 4.3.3. Description of no-load actuator characterization

The no-load actuator tests were performed to study the effect of magnetic field on the actuation of the unimorphs having different stiffness. The composite stiffness was varied by using Aluminum layers that were 0.46, 0.91, 1.85, 3.71 and 7.43-mm thick. The same 1.86-mm thick Galfenol lamina was used in all the unimorphs. The Galfenol and Aluminum pieces were laminated using Vishay M-Bond. The Aluminum layers were 35-mm long and 8.4-mm wide. The 10-mm overhang of the Aluminum layer was inserted into a clamping device.

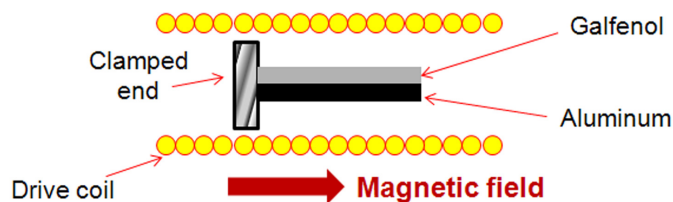


**Figure 4.6. Schematic of the no-load actuator test setup.**

The cantilevered unimorph was placed at the center of the solenoid described earlier and as shown in Figures 4.6 and 4.7. Vishay CEA-13-500UW-120 resistive strain gages attached on the free surfaces of the Galfenol and Aluminum layers were used to measure the strains while the unimorph was subjected to a cyclic quasi-static magnetic field with an amplitude of 65 kA/m at a frequency of 0.01 Hz. The demagnetization sequence described in Section 4.3.1 preceded each test run. The test sequence was repeated four times on each unimorph to ensure consistency in the acquired data.

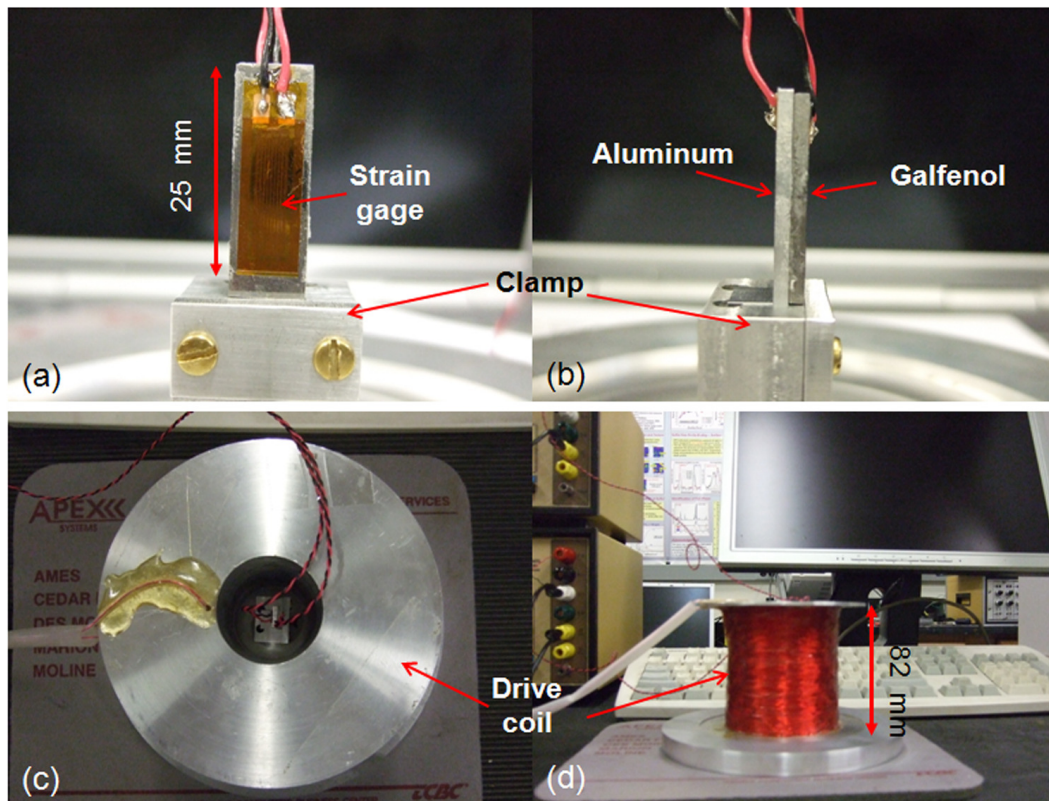


**Figure 4.7. (a) Strain gage bonded on the unimorph surface. (b) Side view of the cantilevered unimorph. (c) End view of the clamped unimorph placed inside the drive coil. (d) Side view of the drive coil.**

At the end of all experiments performed on each unimorph, the Galfenol and Aluminum were delaminated by immersing the composite beam in an acetone bath and subjecting it to ultrasonic shaking for 20 minutes.

#### 4.3.4. Description of pre-load actuator characterization

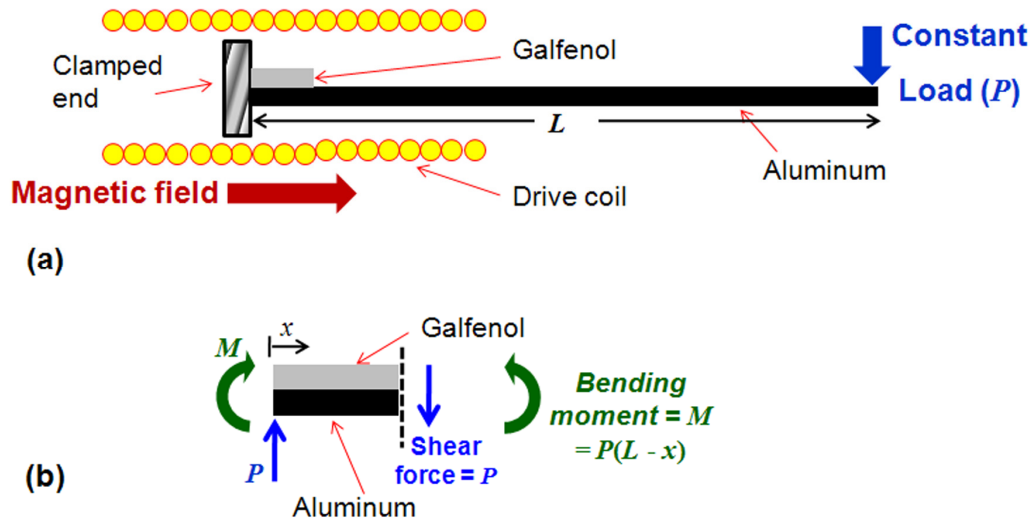


**Figure 4.8. (a) Schematic of the pre-load actuator test setup. (b) Free body diagram of the laminated section showing the shear force and bending moment.**

The pre-load actuator tests were performed to study the effect of magnetic field and mechanical pre-load on the actuation of the unimorphs having different stiffness. A schematic and photograph of the test setup are shown in Figures 4.8 and 4.9 respectively. In order to produce significant bending moments in the Galfenol patch attached near the clamped end by hanging different loads at the free end, a longer Aluminum beam had to be used. All Aluminum beams used for the pre-load tests were 305-mm long out of which 10 mm was inserted in the clamping fixture. In order to avoid bending of the beams due to their own weight, only the stiffer Aluminum beams, with thicknesses of 1.84, 3.70 and 7.43 mm, were used.

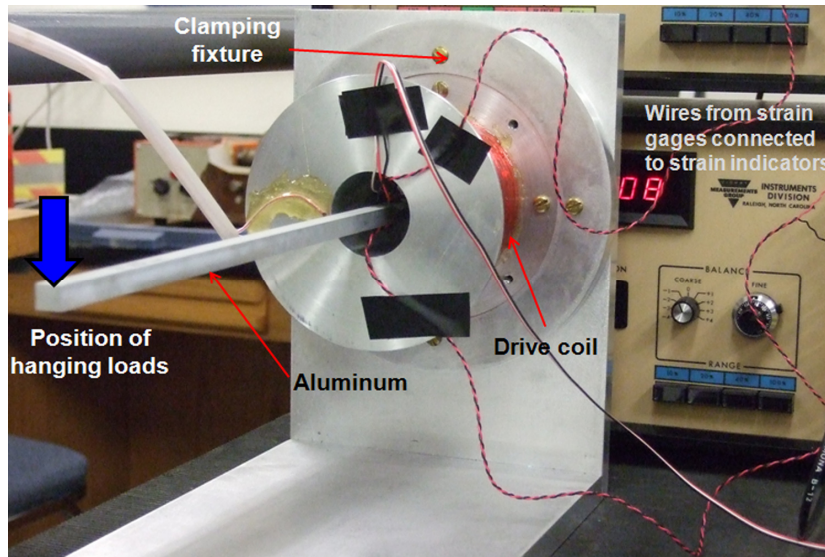


**Figure 4.9. The pre-load actuator test setup.**

Different constant loads ( $P$ ) were applied by hanging precision weights from the free end of the cantilevered beam. After the beam was stabilized, the demagnetization sequence was carried out followed by the quasi-static magnetic field cycle. Strains on the free surfaces of Galfenol and Aluminum near the clamped end were measured using Vishay CEA-13-500UW-120 resistive strain gages. Prior to recording the strain due to the quasi-static cyclic magnetic field as described for the no-load tests, the pre-strain due to the mechanical load was also noted in these tests.

Since the three beams used in the experiment were of different thickness, the same load would produce different stress profile across the thickness of these beams. Hence it would be inaccurate to directly compare the characterization results obtained from the different beams. In order to avoid this problem, a set of different loads were chosen for the different beams such that the parameter  $M_{xt}$  ( $= M/bt^2$ ), introduced in Chapter 3, remains same. The actual loads and the corresponding values of  $M_{xt}$  used in the characterization for the three different beams are shown in Table 4.1. The

bending moment [ $M = P(L-x)$ ] was calculated at the mid-length of the strain gage by substituting  $L = 295$  mm and  $x = 12.7$  mm. Experiments were performed for both positive and negative values of  $M_{xt}$  by laterally inverting the unimorph such that the Galfenol was made the bottom and the top layer respectively. Note that it was not possible to obtain identical values of  $M_{xt}$  for the three cases due to the finite combinations of loads available.

**Table 4.1. Values of actual load ( $P$ ) and  $M_{xt}$  used for the different beams.**

$t = 9.29$ mm		$t = 5.56$ mm		$t = 3.7$ mm	
$P$ (g)	$M_{xt}$ (MPa)	$P$ (g)	$M_{xt}$ (MPa)	$P$ (g)	$M_{xt}$ (MPa)
0	0	0	0	0	0
47	0.18	16	0.17	7	0.17
87	0.33	32	0.34	14	0.33
157	0.60	57	0.61	25	0.6
207	0.79	67	0.71	32	0.77
307	1.17	107	1.14	47	1.13
457	1.74	157	1.67	57	1.37
557	2.12	207	2.2	67	1.61
707	2.69	257	2.73	87	2.09
807	3.07	307	3.26	107	2.57
907	3.45	357	3.80	157	3.77
1140	4.34	407	4.33	207	4.97
1367.5	5.21	507	5.39	-	-

#### 4.3.5. Description of sensor characterization

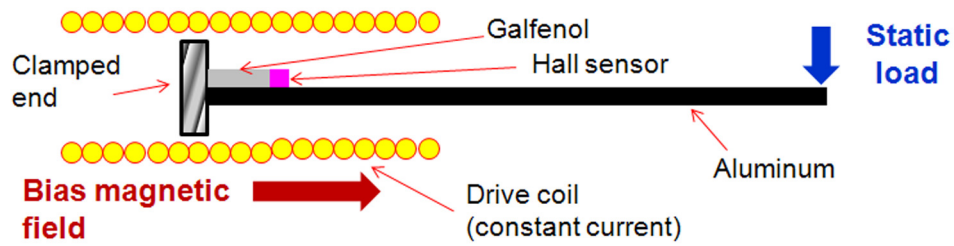


**Figure 4.10. Schematic of the sensor characterization test setup.**

The sensor characterization used the same test setup as described for the pre-load actuator tests except for the fact that an Allegro 1323 linear Hall-effect sensor was attached at one end of the Galfenol layer as shown in Figures 4.10 and 4.11.

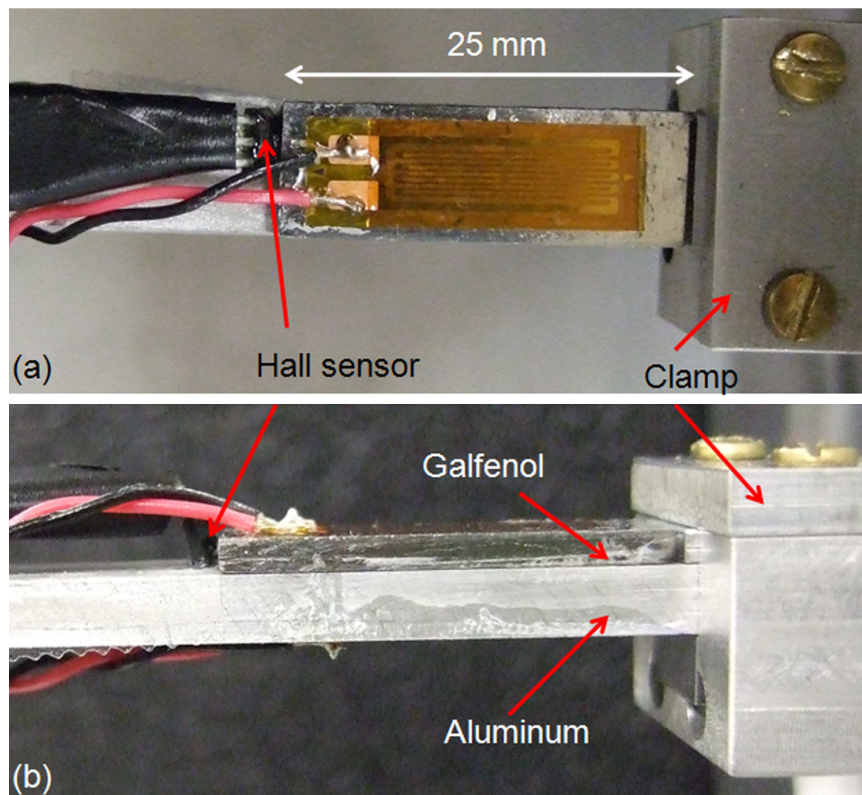


**Figure 4.11. (a) Top view and (b) side view of the cantilevered unimorph showing the position of the Hall-effect sensor.**

The Hall-effect sensor acquired a signal proportional to the change in magnetic induction in the Galfenol patch under the influence of different magnetic fields and bending loads. Note that the Hall sensor measured a signal proportional to  $B$  and not  $H$  because it was placed in such a way that it measured the axial component of the magnetic flux lines emanating from the Galfenol patch. Also note that since there is a spatial variation in  $B$  within the Galfenol layer during bending, the Hall sensor can only measure a signal proportional to  $B$  but not the absolute value of  $B$  as was measured using a pick-up coil in Chapters 2 and 3. Furthermore, as mentioned earlier, the internal magnetic field in Galfenol also varies spatially and hence cannot be maintained using the feedback controller described in Chapter 2. Hence all references to magnetic field would indicate the applied magnetic field, i.e. the magnetic field measured in air at the center of the solenoid for a given drive current.

The sensor characterization was performed in two different ways to measure the consistency in experimental data. In the first method, the Hall sensor data was acquired while the magnetic field was quasi-statically cycled for each of the different loads hanging from the free end of the beam. In the second method, a constant drive current was used to produce a bias applied magnetic field. In the presence of this bias field, the mechanical loads were quasi-statically varied and the change in Hall sensor response was noted. The second method was used for four different bias magnetic fields. The Hall sensor data obtained as a function of magnetic field and  $M_{xt}$  from the two different methods were compared. Note that the first method is analogous to measurement of B-H curves whereas the second method resembles the measurement of B- $\sigma$  curves, both of which were discussed in Chapter 2.

#### 4.4. Magnetic analysis of test setup

In this section, the method of magnetic field application is analyzed using finite element method and an estimate of the spatial distribution of the magnetic flux and the demagnetization effect in the Galfenol lamina is obtained.

##### 4.4.1. Estimation of magnetic flux variation

Since the drive coil is of finite length ( $L_c$ ) and diameter ( $D_c$ ) the magnetic field produced inside it will not be uniform and may not be calculated using Equation (1.3). The relevant analytical formula to calculate the magnetic field along the centerline of the coil is given by Equation (4.16) [63] where  $N$  and  $i$  are the number of turns in the coil and current respectively. Note that  $-L_c/2 \leq x \leq L_c/2$ .

$$H = \frac{Ni}{L_c} \left\{ \frac{L_c + 2x}{2[D_c^2 + (L_c + 2x)^2]^{1/2}} + \frac{L_c - 2x}{2[D_c^2 + (L_c - 2x)^2]^{1/2}} \right\} \quad (4.16)$$

Besides using Equation (4.16), the magnetic field variation along the long axis of the coil was also measured using a hand-held gaussmeter for  $i = 0.5$  A. Furthermore, a 3D electromagnetic finite element analysis was performed using the AC/DC module in COMSOL Multiphysics 3.4. The “*Magnetostatics*” formulation used vector - quadratic elements. The relevant boundary value problem for magnetic FEA was defined in Section 3.3. Comparison of experimental measurements of  $H$  at the center of the solenoid for different  $i$  with the estimated magnetic field from the FEA showed that  $J_o = 9 \times 10^5$  A/m<sup>2</sup> corresponded to  $i = 0.5$  A.

Results from all the three methods of magnetic field estimation are shown in Figure 4.12. It was found that the value of  $H$  at the center of the solenoid

corresponded to the value given by Equation (1.3) and that  $H$  monotonically drops to half of the peak value at the two ends of the solenoid. Figure 4.12 also indicates that it is desirable to place the Galfenol lamina in the central region of the solenoid in order to expose it to maximum magnetic field for a given drive current with minimum spatial variation in the field.

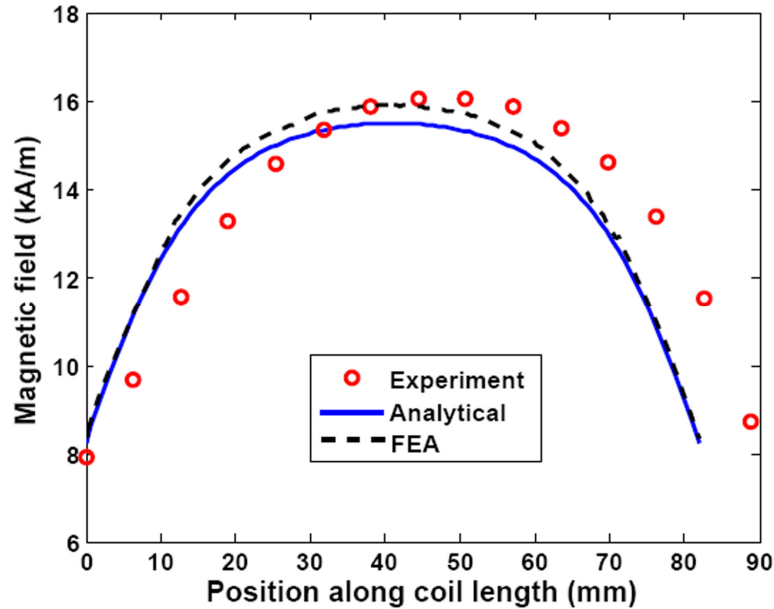


**Figure 4.12. Comparison of measured values of magnetic field in air along the long axis of the solenoid with calculated values from analytical expression and finite element analysis.**

A 3D FEA analysis of the magnetic components in the unimorph actuator and sensor tests that comprised of the drive coil (solenoid), the Galfenol lamina and an air domain surrounding them was also performed. Since the clamps were made of Aluminum ( $\mu_r = 1$ ), they could be considered as a part of the air domain. Figure 4.13 shows these components.

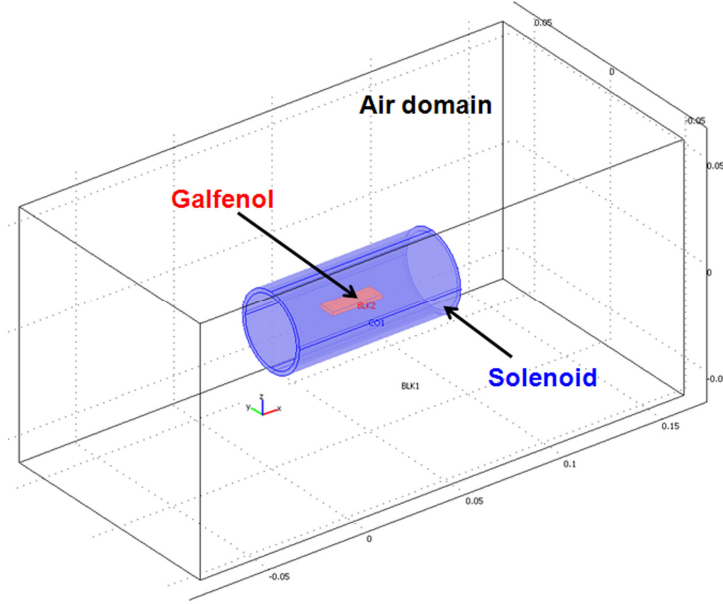


**Figure 4.13. Schematic of the magnetic components of the experimental setup.**

The constitutive B-H relation (at  $\sigma = 0$ ) for Galfenol was obtained from a look-up table generated using the energy-based model described in Chapter 2. The model parameters are shown in Table 4.2. The model parameters were estimated from Figure 4.4 and Table 2.2. For a value of  $B$  calculated in Galfenol, the value of  $H$  was obtained from the look-up table using piecewise-cubic interpolation.

**Table 4.2. Parameters used in the energy-based constitutive model for  $\text{Fe}_{82}\text{Ga}_{18}$ .**

$M_s$ (kA/m)	$\lambda_{100}$ ( $\mu\epsilon$ )	$K_1$ (kJ/m <sup>3</sup> )	$K_2$ (kJ/m <sup>3</sup> )	$\Omega$ (J/m <sup>3</sup> )
1330	220	16.5	-45	200

This analysis was useful to estimate the spatial variation of  $B$  in the Galfenol lamina which in turn was helpful to determine appropriate position for placement of strain gage and Hall-effect sensor on the Galfenol lamina.

As shown in Figure 4.14, the 3D magnetic FEA indicated that most of the magnetic flux lines concentrated through the Galfenol lamina. The flux lines formed closed loops around the solenoid and were found to be axially symmetric.

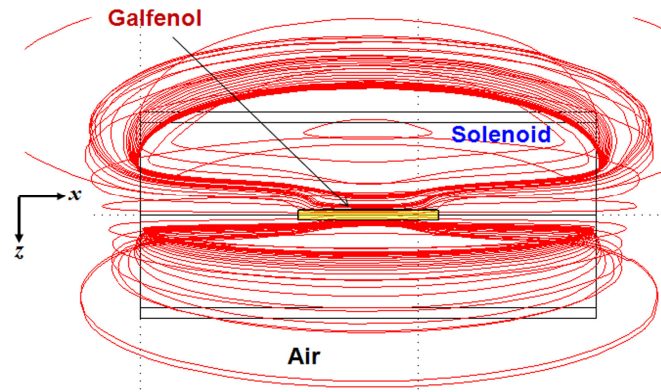


**Figure 4.14. Concentration of magnetic flux lines through Galfenol.**

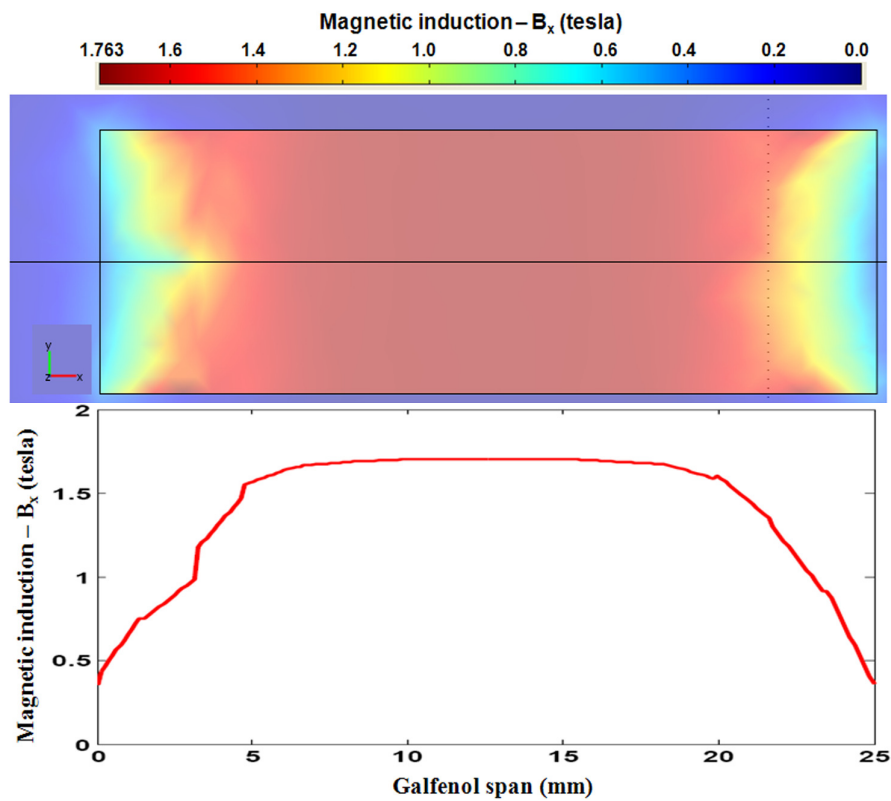


**Figure 4.15. Spatial distribution of  $B_x$  in the x-y plane of the Galfenol lamina and the variation in  $B_x$  along the span of the Galfenol lamina.**

Figure 4.15 shows the spatial variation of the  $x$ -component of  $B$  in the Galfenol lamina for a drive current of 2 A ( $J_o = 3.6 \times 10^6$  A/m<sup>2</sup>). The plotted values were calculated on a plane passing through the mid-thickness of the lamina. Figure 4.15 shows that  $B_x$  does not vary significantly along a 15-mm mid-span in the Galfenol lamina. The uniformity of  $B_x$  in the mid-region of Galfenol makes it the ideal position for placement of strain gage as shown in Figure 4.7. However,  $B_x$  sharply drops off near the two ends along the length of the Galfenol sample and its value reduces by  $\sim 70\%$  from its peak value observed along the mid-span.

The determination of a suitable position for the Hall sensor is somewhat more challenging. Figure 4.16 shows a close-up of the finite element simulation of the magnetic flux lines flowing through and around the Galfenol sample. Ideally, the Hall sensor should be placed perpendicular to the flux lines in order to measure  $B_x$ .

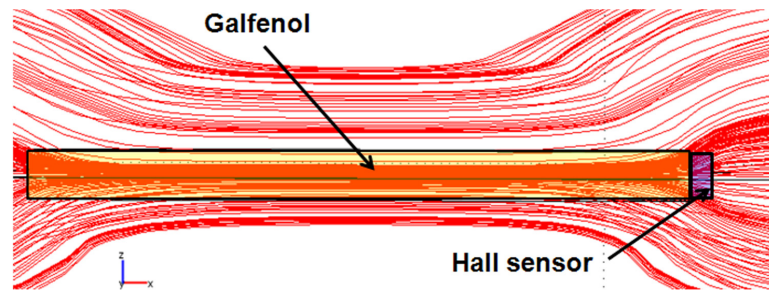


**Figure 4.16. FEA simulation of magnetic flux lines through Hall sensor placed at one end of the Galfenol sample.**

Based on the information from Figure 4.16, the Hall sensor cannot be placed adjacent to the strain gage on the free surface of the Galfenol sample as then it would be tangential to the flux lines. Hence, as shown in Figures 4.11 and 4.16, the only option is to place the Hall sensor at one end of the Galfenol sample.

Figure 4.17 shows the finite element simulation of  $B_x$  along the long axis of the solenoid when a current of 2 A is passed through the coil. An expected increase in  $B_x$  is seen inside the Galfenol sample due to its higher relative permeability compared to that of air. The span-wise variation in  $B_x$  makes the Hall sensor measure a signal which is highly dependent on its position. Moreover, the effect of bond layer and small air gap between the Hall sensor and Galfenol further mitigates the signal and hence the Hall sensor ends up measuring a signal that is proportional to the maximum magnetic induction in Galfenol. Figure 4.17 shows an estimate of the difference between the Hall sensor signal and maximum  $B_x$  in Galfenol. This knowledge is important in order to interpret the sensor characterization results.

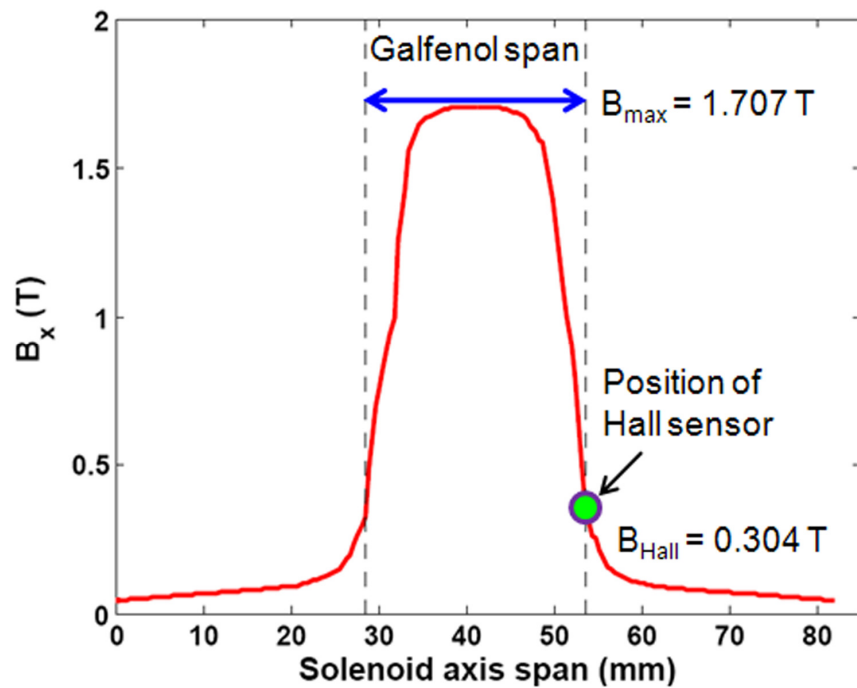


**Figure 4.17. FEA simulation of  $B_x$  along the long axis of the solenoid.**

#### 4.4.2. Estimation of demagnetization

The existence of an open magnetic circuit in the experimental setup motivates the estimation of the demagnetization effect in the Galfenol lamina. For a rectangular prism with dimensions  $a$ ,  $b$  and  $c$  along the  $x$ ,  $y$  and  $z$  axes respectively, the demagnetization factor can be obtained using the analytical expression shown in Equation (4.17) [60].

$$\begin{aligned}
 \pi D_z = & -\frac{b^2 - c^2}{2bc} \ln\left(\frac{\sqrt{a^2 + b^2 + c^2} - a}{\sqrt{a^2 + b^2 + c^2} + a}\right) + \frac{a^2 - c^2}{2ac} \ln\left(\frac{\sqrt{a^2 + b^2 + c^2} - b}{\sqrt{a^2 + b^2 + c^2} + b}\right) + \frac{b}{2c} \ln\left(\frac{\sqrt{a^2 + b^2} + a}{\sqrt{a^2 + b^2} - a}\right) + \frac{a}{2c} \ln\left(\frac{\sqrt{a^2 + b^2} + b}{\sqrt{a^2 + b^2} - b}\right) \\
 & + \frac{c}{2a} \ln\left(\frac{\sqrt{b^2 + c^2} - b}{\sqrt{b^2 + c^2} + b}\right) + \frac{c}{2b} \ln\left(\frac{\sqrt{a^2 + c^2} - a}{\sqrt{a^2 + c^2} + a}\right) + 2 \arctan\left(\frac{ab}{c\sqrt{a^2 + b^2 + c^2}}\right) + \frac{a^3 + b^3 - 2c^3}{3abc} \\
 & + \frac{a^2 + b^2 - 2c^2}{3abc} \sqrt{a^2 + b^2 + c^2} + \frac{c}{ab} (\sqrt{a^2 + c^2} + \sqrt{b^2 + c^2}) - \frac{(a^2 + b^2)^{3/2} + (b^2 + c^2)^{3/2} + (c^2 + a^2)^{3/2}}{3abc}.
 \end{aligned} \tag{4.17}$$

Here  $D_z = N_{zz}$ . The demagnetization factors along the  $x$  and  $y$  directions, i.e.  $N_{xx}$  and  $N_{yy}$ , for a rectangular prism can be calculated using the same formula by applying twice the circular permutation  $c \rightarrow a \rightarrow b \rightarrow c$ . Using this formula, the demagnetization factors calculated for the Galfenol lamina were;  $N_{xx} = 0.062$ ,  $N_{yy} = 0.192$  and  $N_{zz} = 0.746$ .

An alternative method using the energy-based model was also used to estimate the demagnetization factor ( $N_{xx}$ ) for the Galfenol sample. In this method, the energy-based model was used to simulate the magnetostriction shown in Figure 4.4 using the parameters shown in Table 4.2. Equation (1.14) was used to obtain the applied magnetic field from the simulated magnetization and prescribed internal magnetic field values. An initial guess of  $N_{xx} = 0.062$  as obtained from Equation

(4.17) was used. Empirical variation of  $N_{xx}$  about the initial guess showed that  $N_{xx} = 0.035$  provided the best fit with the experimental data as shown in Figure 4.18.

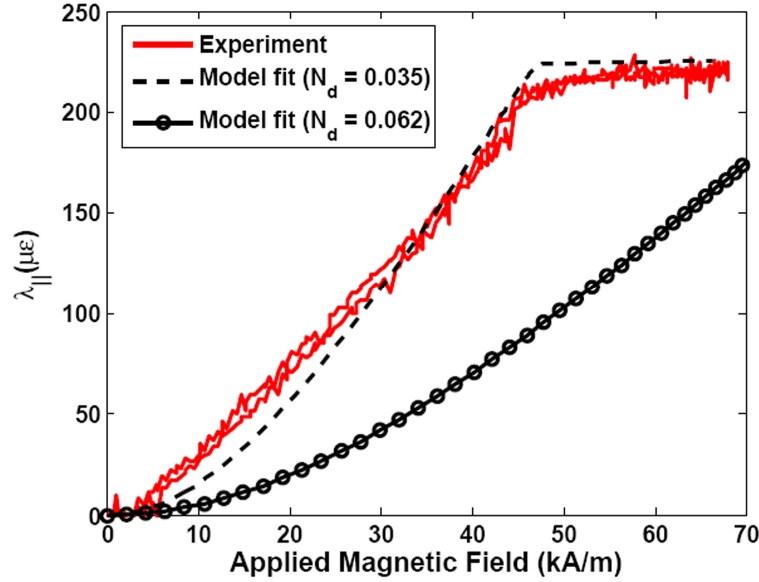


**Figure 4.18. Energy-based model fit of magnetostriction in  $\text{Fe}_{82}\text{Ga}_{18}$  as a function of the applied magnetic field. The demag factor  $N_d = N_{xx}$  in this case.**

A second alternative method for finding the demagnetization factor used the results of the magnetic finite element analysis. Using the subdomain integration option in COMSOL Multiphysics 3.4, the volume-averaged values were calculated for  $B_x$  ( $= 1.4677$  T), internal  $H_x$  ( $= 15.942$  kA/m) and applied  $H_x$  ( $= 63.2$  kA/m) in the Galfenol sample for a drive current of 2 A in the solenoid. Substituting these values in Equation (1.15) yielded a value of  $N_d = N_{xx} = 0.041$ . Note that the estimate of  $N_{xx}$  obtained from the 2<sup>nd</sup> and 3<sup>rd</sup> methods are close to each other as both of them considered the fact that the entire sample was not homogeneously magnetized using empirical and finite element approaches respectively. These estimates of  $N_{xx}$  were significantly different from the one obtained from the analytical expression given by Equation (4.17) which is valid only for a homogeneously magnetized body.

#### 4.5. Mechanical analysis of test setup

In this section, the structural aspects of the experimental setup are analyzed using the finite element method. The objective of this study is to find whether the location of strain gages were appropriate for measuring the desired strain or the strain gages measured an average strain from a large spatial strain distribution. Furthermore, since the aspect ratio of some of the unimorphs did not strictly conform to that suggested in the Euler-Bernoulli beam theory, it was desired to perform a 3D structural analysis using finite element method to find the relative magnitudes of the stress components in both the Galfenol and Aluminum layers.

The 3D structural finite element analysis was performed using the Structural Mechanics module in COMSOL Multiphysics 3.4. The “Solid, Stress-Strain - static” analysis used Lagrange – quadratic elements. The mechanical boundary value problem is solved by COMSOL using the static stress equilibrium Equation (4.18) where  $b_x$ ,  $b_y$  and  $b_z$  are the components of body forces along  $x$ ,  $y$  and  $z$ -directions respectively.

$$\begin{aligned}\frac{\partial \sigma_{xx}}{\partial x} + \frac{\partial \tau_{xy}}{\partial y} + \frac{\partial \tau_{zx}}{\partial z} + b_x &= 0 \\ \frac{\partial \tau_{xy}}{\partial x} + \frac{\partial \sigma_{yy}}{\partial y} + \frac{\partial \tau_{yz}}{\partial z} + b_y &= 0 \\ \frac{\partial \tau_{zx}}{\partial x} + \frac{\partial \tau_{yz}}{\partial y} + \frac{\partial \sigma_{zz}}{\partial z} + b_z &= 0\end{aligned}\tag{4.18}$$

The strain displacement relation for small strains is shown in Equation (4.19).

$$\begin{Bmatrix} \varepsilon_{xx} \\ \varepsilon_{yy} \\ \varepsilon_{zz} \\ \gamma_{yz} \\ \gamma_{zx} \\ \gamma_{xy} \end{Bmatrix} = \begin{Bmatrix} \partial u / \partial x \\ \partial v / \partial y \\ \partial w / \partial z \\ \partial v / \partial z + \partial w / \partial y \\ \partial w / \partial x + \partial u / \partial z \\ \partial u / \partial y + \partial v / \partial x \end{Bmatrix} \quad (4.19)$$

The strain compatibility Equation (4.20) serves as the subsidiary condition.

$$\begin{aligned} \frac{\partial^2 \varepsilon_{xx}}{\partial y^2} + \frac{\partial^2 \varepsilon_{yy}}{\partial x^2} &= \frac{\partial^2 \gamma_{xy}}{\partial x \partial y} \\ \frac{\partial^2 \varepsilon_{yy}}{\partial z^2} + \frac{\partial^2 \varepsilon_{zz}}{\partial y^2} &= \frac{\partial^2 \gamma_{yz}}{\partial y \partial z} \\ \frac{\partial^2 \varepsilon_{zz}}{\partial x^2} + \frac{\partial^2 \varepsilon_{xx}}{\partial z^2} &= \frac{\partial^2 \gamma_{zx}}{\partial z \partial x} \\ \frac{\partial^2 \varepsilon_{xx}}{\partial y \partial z} &= \frac{1}{2} \frac{\partial}{\partial x} \left[ -\frac{\partial \gamma_{yz}}{\partial x} + \frac{\partial \gamma_{zx}}{\partial y} + \frac{\partial \gamma_{xy}}{\partial z} \right] \\ \frac{\partial^2 \varepsilon_{yy}}{\partial z \partial x} &= \frac{1}{2} \frac{\partial}{\partial y} \left[ \frac{\partial \gamma_{yz}}{\partial x} - \frac{\partial \gamma_{zx}}{\partial y} + \frac{\partial \gamma_{xy}}{\partial z} \right] \\ \frac{\partial^2 \varepsilon_{zz}}{\partial x \partial y} &= \frac{1}{2} \frac{\partial}{\partial z} \left[ -\frac{\partial \gamma_{yz}}{\partial x} + \frac{\partial \gamma_{zx}}{\partial y} - \frac{\partial \gamma_{xy}}{\partial z} \right] \end{aligned} \quad (4.20)$$

The stress-strain constitutive relation is described by Equation (4.21) where  $[c]$  is the stiffness matrix and  $\lambda = \{\lambda_{xx} \lambda_{yy} \lambda_{zz} \lambda_{yz} \lambda_{zx} \lambda_{xy}\}^T$  is the free strain vector.

$$\{\sigma\} = [c] [\{\varepsilon\} - \{\lambda\}] \quad (4.21)$$

$$[c] = \frac{E}{(1+\nu)(1-2\nu)} \begin{bmatrix} 1-\nu & \nu & \nu & 0 & 0 & 0 \\ \nu & 1-\nu & \nu & 0 & 0 & 0 \\ \nu & \nu & 1-\nu & 0 & 0 & 0 \\ 0 & 0 & 0 & 1-2\nu & 0 & 0 \\ 0 & 0 & 0 & 0 & 1-2\nu & 0 \\ 0 & 0 & 0 & 0 & 0 & 1-2\nu \end{bmatrix} \quad (4.22)$$

The stiffness matrix for isotropic materials can be obtained from the Young's modulus ( $E$ ) and Poisson's ratio ( $\nu$ ) as shown in Equation (4.22). For modeling

purposes it was considered that  $E_{Al} = 70$  GPa,  $E_{Fe-Ga} = 63$  GPa,  $\nu_{Al} = 0.33$  and  $\nu_{Fe-Ga} = 0.45$  [115]. The free strain in Galfenol was implemented in COMSOL by assigning values of saturation magnetostriction ( $\lambda_{xx} = 220 \times 10^{-6}$   $\lambda_{yy} = -110 \times 10^{-6}$   $\lambda_{zz} = -110 \times 10^{-6}$ ) to the variables ( $\varepsilon_{x,i}$   $\varepsilon_{y,i}$   $\varepsilon_{z,i}$ ) which denote a uniform pre-strain in the material. All shear free strain components were considered to be zero due to the orientation of the single crystal  $Fe_{82}Ga_{18}$  sample being used. For Aluminum, the free strains were set to zero.

The 3D structural FEA was used to simulate three cases. The first case studied the effect of free strain on the unimorph where both Galfenol and Aluminum layers were of same length. This case simulated the no-load actuator tests. The second case studied the effect of free strain on the unimorph when the Aluminum layer was longer than the Galfenol layer. This case simulated the pre-load actuator test setup without any hanging loads. The simulation results from these two cases are discussed in Section 4.5.1. Section 4.5.2 shows the simulation results for the third case where the effect of both free strain and hanging load on the unimorph created for the second case were considered. For all these cases, the clamping of one end of the composite structure was simulated by assigning a “fixed” boundary condition on the faces at one end along the span of both the Galfenol and Aluminum layers whereas all other faces were assigned a “free” boundary condition.

#### 4.5.1. Effect of free strain

The simulation for the first case was performed for the five different Aluminum thicknesses that were used in the experiments. Figure 4.19 shows the simulation result for the 7.43-mm thick Aluminum layer used which represents the

extreme scenario where the 3D effects should be most prominent. It is evident from Figure 4.19 that the strain on the free surfaces of both Galfenol and Aluminum layers are fairly uniform except very close to the clamped end and the tip of the composite beam. The existence of such uniform strain makes these areas suitable for strain gage bonding as shown in Section 4.3.

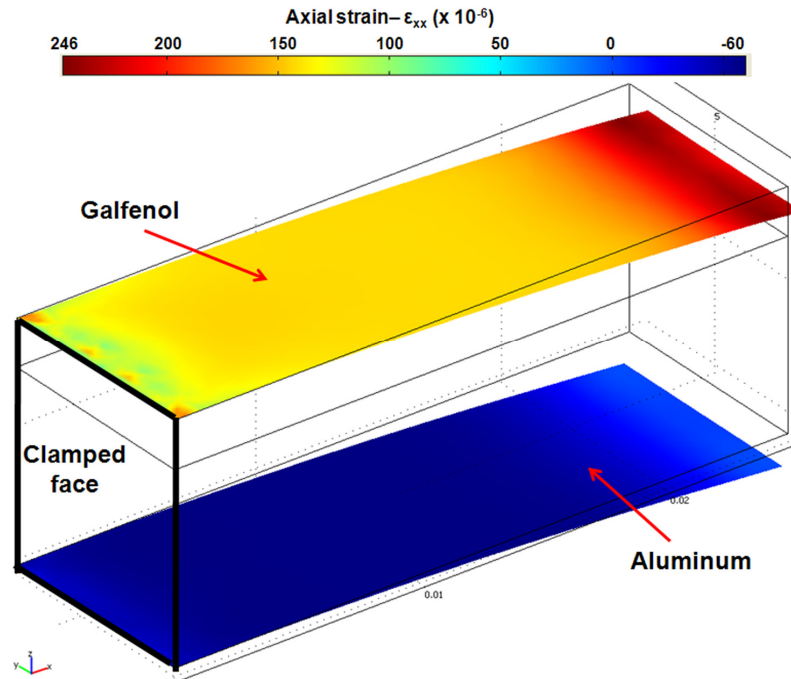


**Figure 4.19. Strain profile ( $\epsilon_{xx}$ ) on free surfaces of Galfenol and Aluminum layers in the unimorph due to a uniform free strain in the Galfenol layer.**

Since the Euler-Bernoulli beam theory is only applicable if the shear-stresses are negligible, it was deemed necessary to find the maximum magnitude of all the stress components in the unimorphs with different thicknesses. In all the five unimorphs, the most dominant stress component was  $\sigma_{xx}$  with a maximum magnitude of 5 MPa. The only other non-zero stress component was  $\sigma_{yy}$  with a maximum magnitude of 1.5 MPa. The 3D FEA showed that a 2D plate-theory type analysis

might be sufficient for modeling these unimorphs. Such a 2D model will be developed and presented in Chapter 5.

In order to further compare the predictions of 1D beam theory and 3D finite element structural models, the normalized tip displacement was calculated using both these models. The 1D analysis used Equations (4.14) and (4.15) whereas the 3D analysis used the actual tip displacement in  $z$ -direction in order to calculate the normalized tip displacement. The simulation results are shown in Table 4.3.

**Table 4.3. Predicted values of normalized tip displacement ( $-w_{TIP}/L^2 \times 10^{-6}$ ) of unimorphs with different Aluminum layer thickness ( $t_1$  in mm) used in no-load actuator tests.**

$t_1$	0.46	0.91	1.85	3.71	7.43
<b>1D</b>	109	149	165	144	101
<b>3D</b>	106	143	160	141	104

The simulated values of normalized tip displacement shown in Table 4.3 corroborates the fact that the aspect ratio of the unimorphs does not have a significant effect and a complete 3D structural analysis may not be necessary to model the unimorphs.

The simulation for the second case was performed for the three different Aluminum thicknesses that were used in the experiments. The strain on the free surfaces of both Galfenol and Aluminum layers in the area where the strain gages were attached were found to be uniform. In all the three unimorphs, the most dominant stress component was  $\sigma_{xx}$  with a maximum magnitude of 5 MPa. The only other non-zero stress component was  $\sigma_{yy}$  with a maximum magnitude of 2MPa. The

normalized out-of-plane tip displacements ( $w_{TIP}/L_2^2$ ) for the unimorphs are shown in Table 4.4.

**Table 4.4. Predicted values of normalized tip displacement ( $-w_{TIP}/L_2^2 \times 10^{-6}$ ) of unimorphs with different Aluminum layer thickness ( $t_1$  in mm) used in pre-load actuator tests.**

$t_1$	1.84	3.70	7.43
<b>1D</b>	3712	3256	2274
<b>3D</b>	3635	3078	2096

The simulated values of normalized out-of-plane tip displacement listed in Table 4.4 shows that even for the thickest unimorph the difference between 1D and 3D predictions is 7.8 % which is within the bounds of experimental uncertainty. Hence the beam theory formulae may be used to analyze the experimental results that will be presented in Sections 4.6 and 4.7.

#### 4.5.2. Effect of free strain and bending load

In these simulations, the hanging load was simulated by assigning an edge load (unit: N/m) at the free end of the beam. The edge load was calculated by dividing the desired force by the width of the beam. Figure 4.20 shows the setup with the position of the load and the clamped end of the beam.

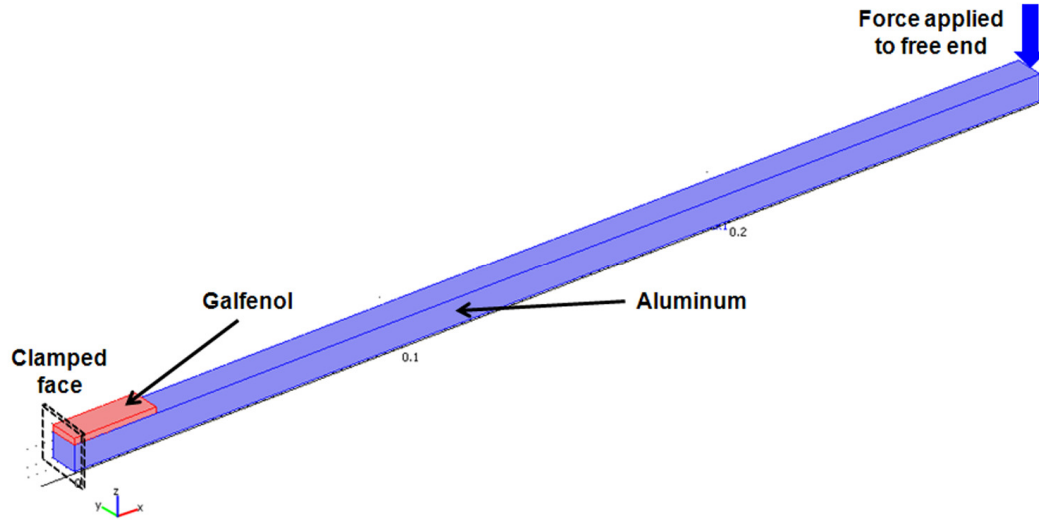


**Figure 4.20. Geometry and boundary conditions used for 3D finite element analysis of pre-load actuator tests.**

In order to evaluate the extreme scenario, the thickest beam ( $t_1 = 7.43$  mm) and highest tip loading (1367.5 g) were considered. Once again the dominant stress component was found to be  $\sigma_{xx}$  having a maximum magnitude of 30 MPa while the same for  $\sigma_{yy}$  was only 2 MPa. All other stress components were found to be negligible. However, this simulation showed a slightly higher variation in strain ( $\epsilon_{xx}$ ) in the region where the strain gages were bonded. Figure 4.21 shows the strain distribution on the free surfaces of Galfenol and Aluminum. A variation of ~ 10 % and 4 % were observed for the Galfenol and Aluminum surfaces respectively in the strain gage region for a load along negative  $z$ -axis. For the same edge load acting along positive  $z$ -axis, the variation in strain on Galfenol and Aluminum surfaces was 26 % and 9 % respectively. A positive edge load produces strain which is of opposite sign to that of the free strain and hence leads to a higher variation in strain.

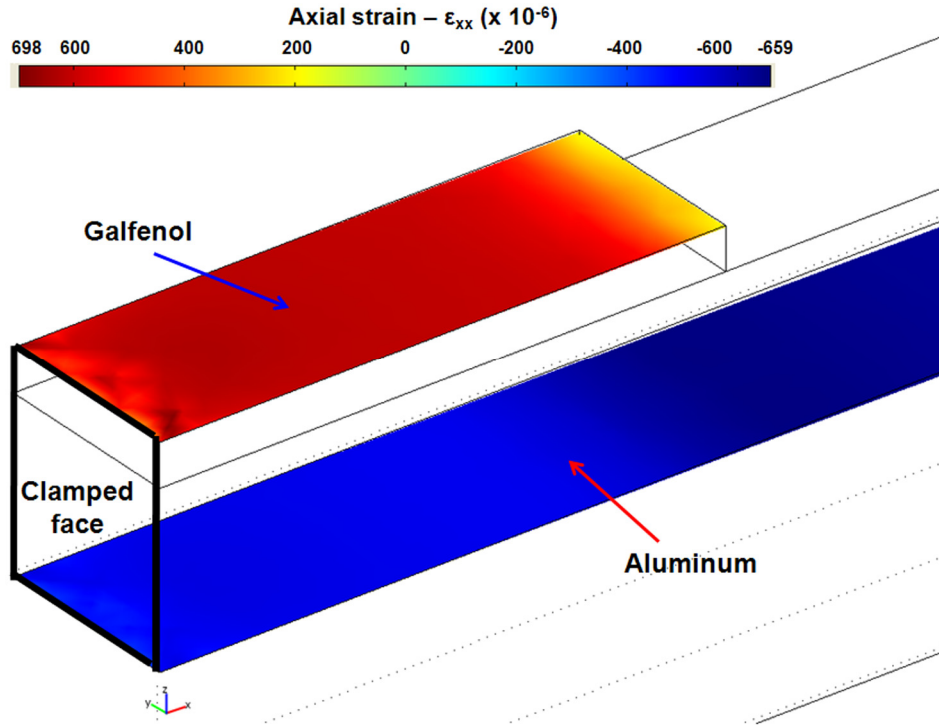


**Figure 4.21. Strain profile ( $\epsilon_{xx}$ ) on free surfaces of Galfenol and Aluminum layers in the unimorph due to a uniform free strain in the Galfenol layer and an edge load (-1595 N/m) at the free end of the Aluminum layer.**

#### 4.6. Actuator characterization results

This section presents the results obtained from the no-load and pre-load actuator tests described in Section 4.3. The magnetic field,  $M_{xt}$  and Aluminum layer thickness in the unimorphs are considered as control parameters and their effect on strain on Galfenol and Aluminum surfaces are shown and analyzed. These strains are used to calculate the tip displacements of the unimorphs which are compared to the model predictions listed in Tables 4.3 and 4.4.

#### 4.6.1. Effect of laminate thickness under no-load condition

The effect of changing the Aluminum layer thickness on the strains observed on the free surfaces of Galfenol and Aluminum layers are shown in Figures 4.22 and 4.23 respectively. The strains are plotted as a function of the applied magnetic field.

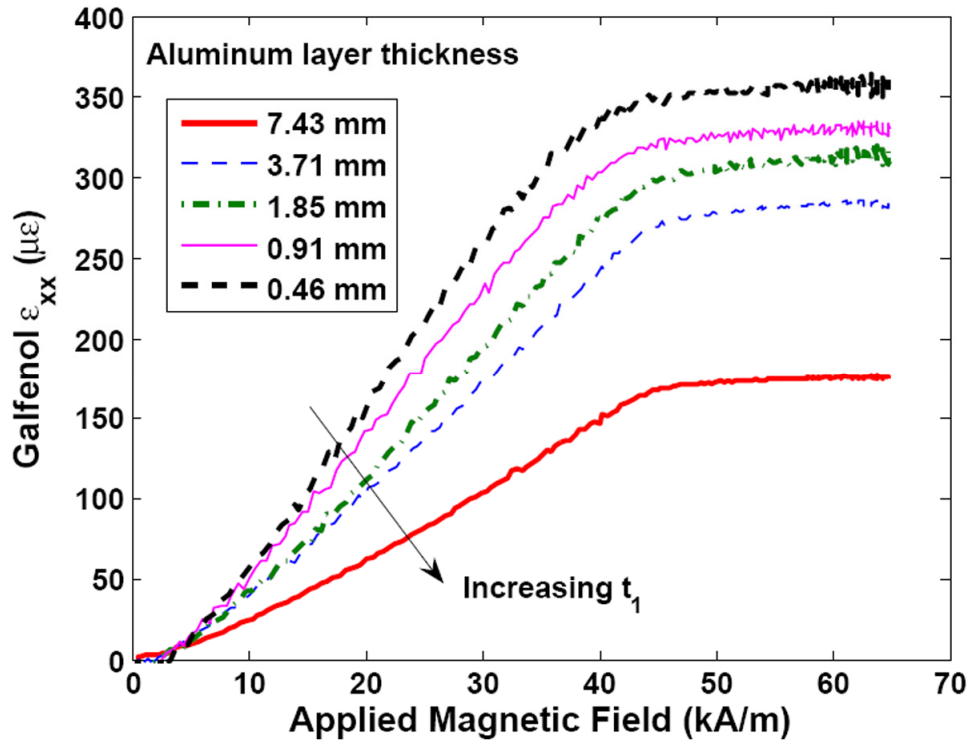


**Figure 4.22. Strain ( $\epsilon_{xx}$ ) measured on the surface of Galfenol as a function of applied magnetic field for unimorphs with different Aluminum layer thickness.**

Figure 4.22 shows that for each unimorph, the strain on Galfenol surface increases monotonically till it saturates at some magnetic field. This behavior is similar to that of the  $\lambda$ -H curve shown earlier. However, the slope of the curve as well as the saturation strain value appeared to increase with decreasing Aluminum layer thickness. A possible explanation for this behavior is that for a given Galfenol layer thickness, a thinner Aluminum layer provides less constraint to the Galfenol layer thereby letting it expand more freely. It should also be noted that for all the

unimorphs except for one (i.e.  $t_1 = 7.43$  mm), the maximum strain on Galfenol surface is higher than saturation magnetostriction of this Galfenol sample. Therefore the strain on the free surface of Galfenol is due to both extension and bending and should not be construed as the free strain of Galfenol.

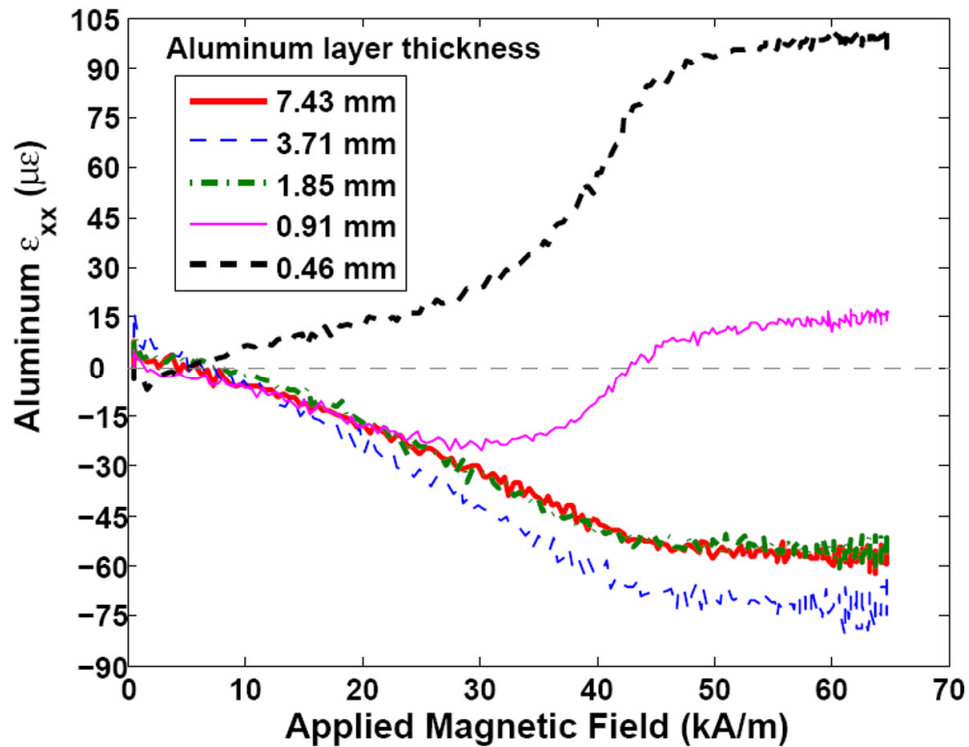


**Figure 4.23. Strain ( $\epsilon_{xx}$ ) measured on the surface of Aluminum as a function of applied magnetic field for unimorphs with different Aluminum layer thickness. Zero-strain is indicated with a grey dashed line.**

Figure 4.23 shows that the behavior of the strain on the Aluminum surface is somewhat different than the strain on the Galfenol surface. In general, for all unimorphs, the magnitude of strain increased with increasing magnetic field until it saturated. However, the monotonic behavior of strain with increasing magnetic field as well as the monotonic behavior of saturation strains with increasing Aluminum layer thickness as shown in Figure 4.22 does not hold true for Figure 4.23.

For  $t_1 = 7.43, 3.71$  and  $1.85$  mm, the strain on Aluminum surface decreases monotonically with increasing magnetic field thereby clearly exhibiting a bending of these unimorphs. For  $t_1 = 0.91$  mm, the strain initially appears to decrease with increasing magnetic field upto  $30$  kA/m beyond which the strain increases with increasing magnetic field and even changes sign at  $43$  kA/m. This behavior indicates that at lower magnetic fields the unimorph predominantly deforms due to bending but at higher magnetic fields ( $> 30$  kA/m), the effect of bending reduces and finally for fields higher than  $43$  kA/m the deformation is dominated by extension which is evident from the same sign of strain on both the Galfenol and Aluminum surfaces. For  $t_1 = 0.46$  mm, the strain on Aluminum surface is positive at all magnetic fields which shows that this unimorph predominantly deforms by extension.

The negative values of saturation strain on the Aluminum surface increases when  $t_1$  is changed from  $7.43$  mm to  $3.71$  mm but decreases on further reducing  $t_1$  to  $1.85$  mm. The saturation strains for  $t_1 = 0.91$  and  $0.46$  mm are positive and are increasing with decreasing  $t_1$ . Note that although the change in  $t_1$  follows a geometric progression, i.e. each being the half of the previous value, no such monotonic behavior can be observed in the saturation strain values for different  $t_1$ . It appears that the saturation strain varies very little for large Aluminum thickness but varies significantly for smaller Aluminum thickness. This behavior is related to the contribution of Aluminum to the integrated stiffness of the composite structure and will be explained in details in Chapter 5 using model simulations.

In order to visualize the extension and bending of each of the unimorphs separately, the strains shown in Figures 4.22 and 4.23 could be used to calculate the

mid-plane strain ( $\varepsilon^o$ ) and normalized tip displacement of the unimorphs based on the beam theory assumptions using Equations (4.23) and (4.24) respectively. Here,  $\varepsilon^{AL}$  and  $\varepsilon^{FEGA}$  are the strains on the Aluminum and Galfenol surfaces respectively.

$$\varepsilon^o = \frac{\varepsilon^{AL} + \varepsilon^{FEGA}}{2} \quad (4.23)$$

$$\frac{w_{TIP}t}{L^2} = \frac{\varepsilon^{AL} - \varepsilon^{FEGA}}{2} \quad (4.24)$$

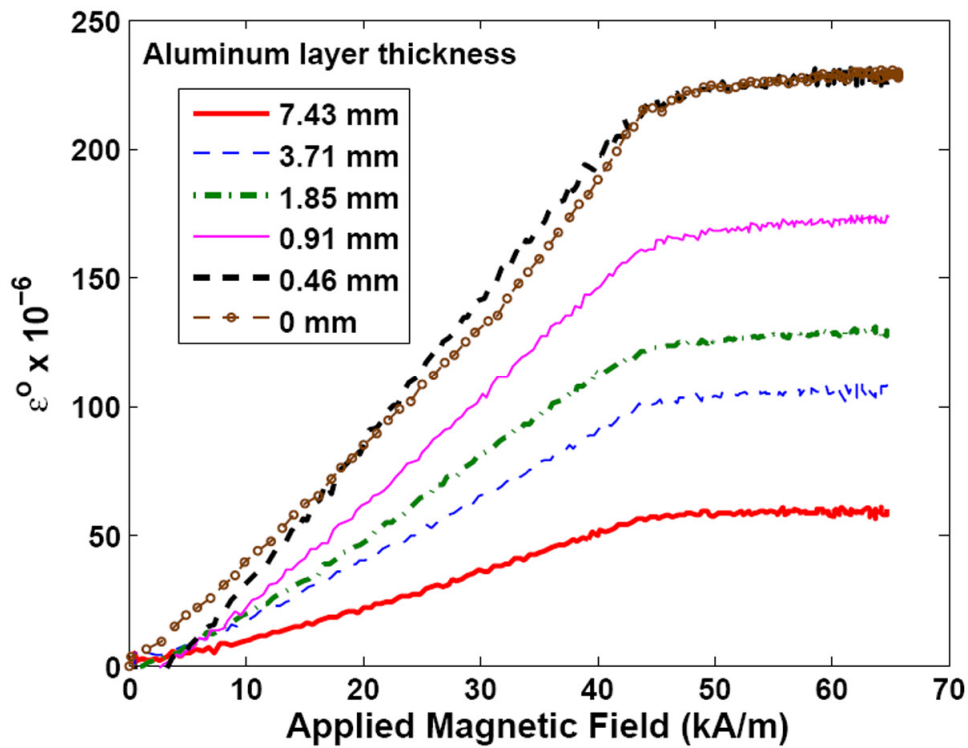


**Figure 4.24. Mid-plane strain ( $\varepsilon^o$ ) as a function of applied magnetic field for unimorphs with different Aluminum layer thickness.**

Figure 4.24 shows the mid-plane strain in the unimorphs as a function of applied magnetic field. For a given Aluminum layer thickness, the mid-plane strain monotonically increases with increasing magnetic field and for a given magnetic field, the mid-plane strain monotonically increases with decreasing Aluminum layer thickness. The unimorph structure tends to extend more freely with decreasing

Aluminum layer thickness as the contribution of Aluminum to the composite stiffness decreases. Hence the mid-plane strain asymptotes to the free strain of the Galfenol layer with decreasing Aluminum layer thickness. The free strain of Galfenol shown in Figure 4.4 is also shown in Figure 4.24 to emphasize this fact.

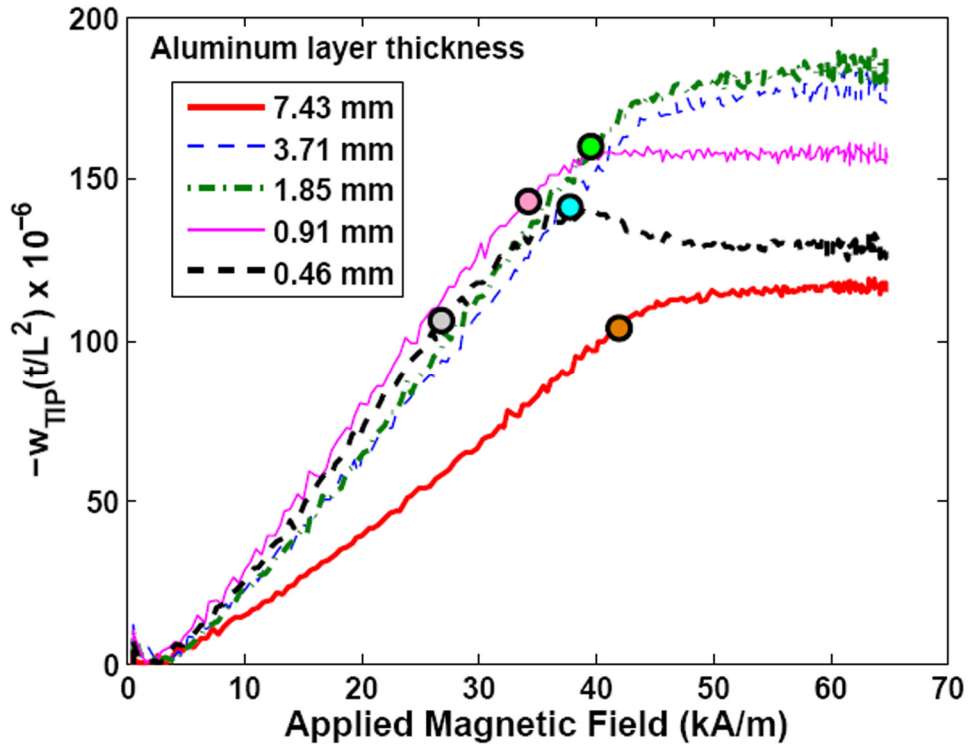


**Figure 4.25. Normalized tip displacement ( $-w_{TIP}/L^2$ ) as a function of applied magnetic field for unimorphs with different Aluminum layer thickness. The circles show the 3D FEA predictions from Table 4.3.**

Figure 4.25 shows the normalized tip displacement in the unimorphs as a function of applied magnetic field. For a given Aluminum layer thickness, the mid-plane strain monotonically increases with increasing magnetic field except for  $t_1 = 0.46$  mm. This apparently anomalous behavior can be explained by combining the information from Figure 4.22 and 4.23 and using them in Equation (4.24). For  $t_1 = 0.46$  mm, the strain on both the Galfenol and Aluminum surfaces are of same signs.

Hence if the rate of change of strain with respect to magnetic field is higher in Galfenol than in Aluminum, the magnitude of normalized tip displacement can decrease with increasing magnetic field. It can be deduced that this effect may be even more prominent for a thinner Aluminum layer.

At magnetically saturated conditions, the normalized tip displacement increases with decreasing values of  $t_1$  upto 1.85 mm. For  $t_1$  smaller than 1.85 mm, normalized tip displacement decreases with decreasing values of  $t_1$ . This trend is consistent with the 1D and 3D simulations shown in Table 4.3. However, the 3D FEA predictions appear to consistently under-predict the saturation values of tip displacement as shown in Figure 4.25 using the circles on each curve.

The under-prediction of experimental results by both 1D and 3D models is possibly due to the omission of the effect of the bond layer between Galfenol and Aluminum layers and any associated imperfection or local delamination in the bond. The bond layer can be modeled as an additional layer between Galfenol and Aluminum in the Euler-Bernoulli composite beam. Using the formulae in Section 4.1, the effect of the bond layer on the normalized tip displacement of the unimorphs can be estimated as a function of the Young's modulus of the cured bond and the bond layer thickness as shown in Figure 4.26. Since the exact value of the Young's modulus of the bond is unknown, the simulation was performed using possible range of values for typical cured cyanoacrylate glue. Moreover, since the thickness of the bond layer can vary in the different unimorphs, the simulation was performed for a range of bond layer thickness. Figure 4.26 shows that normalized tip displacement can increase with increasing bond layer thickness and the bond's Young's modulus

significantly from an ideal condition of a non-existing bond layer. The simulation results of Figure 4.26 provides a possible explanation of the higher saturation values of normalized tip displacement calculated from experiment compared to the values predicted by ideal models which ignored the effect of a bond layer.

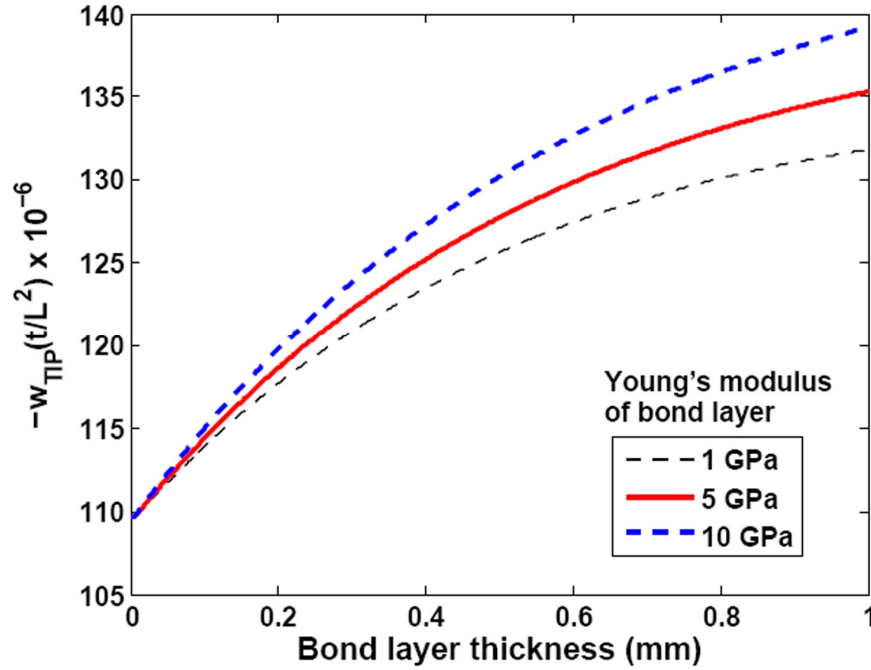


**Figure 4.26. Effect of thickness and Young's modulus of bond layer on normalized tip displacement ( $-w_{TIP}t/L^2$ ) for Galfenol and Aluminum layer thickness of 1.86 and 0.46 mm respectively.**

#### 4.6.2. Effect of bending loads in absence of magnetic field

From the discussion in Section 3.5, we know that the maximum bending stress due to an externally applied bending moment is  $6M_{xt}$ . Figures 4.27 – 4.29 show the measured strain and calculated bending stress ( $6M_{xt}$ ) at the surface of the beam where the strains were measured for the three different unimorphs. These strains were measured in the absence of a magnetic field.

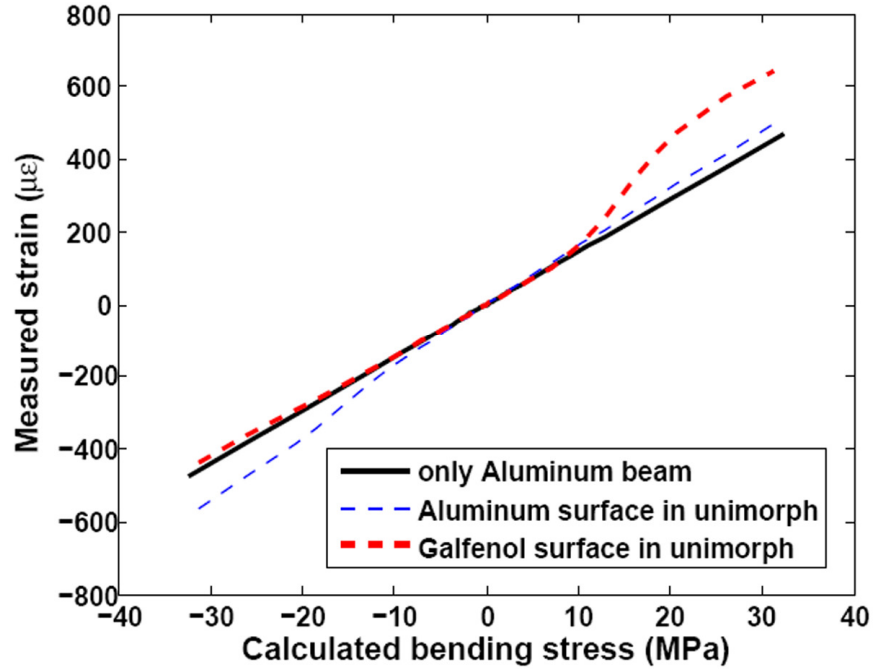


Figure 4.27. Measured strain vs. calculated bending stress ( $= 6M_{xt}$ ) for 7.43-mm thick Aluminum beam and also for the unimorph made with the same.

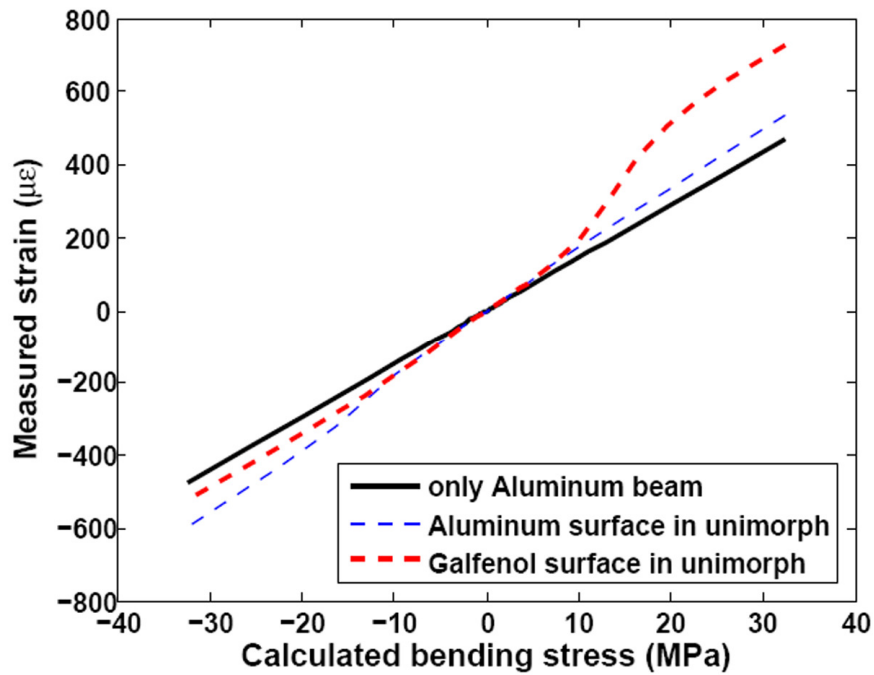
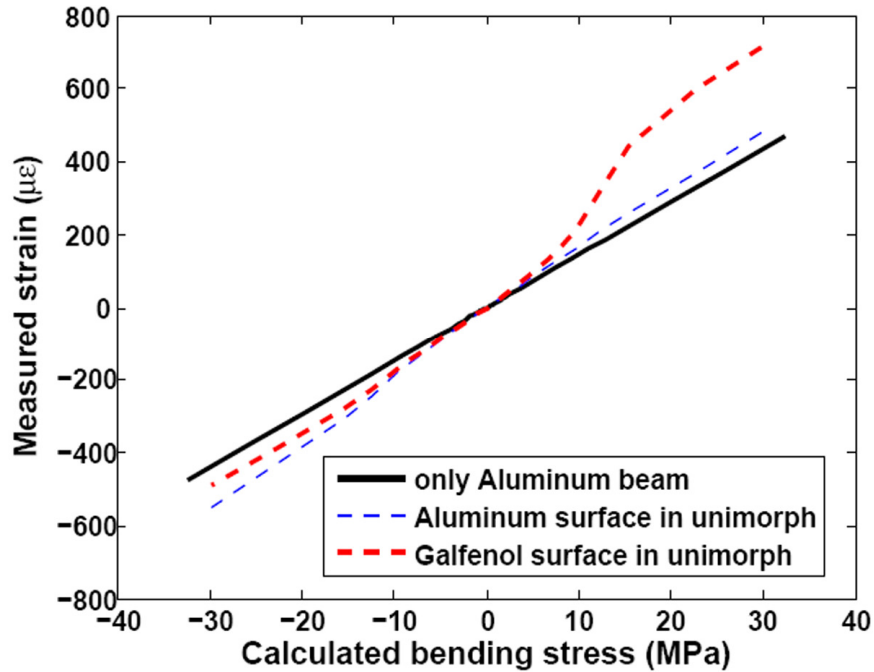


Figure 4.28. Measured strain vs. calculated bending stress ( $= 6M_{xt}$ ) for 3.7-mm thick Aluminum beam and also for the unimorph made with the same.



**Figure 4.29. Measured strain vs. calculated bending stress ( $= 6M_{xt}$ ) for 1.84-mm thick Aluminum beam and also for the unimorph made with the same.**

Additionally, the strains measured on the surface of the Aluminum beams prior to bonding the Galfenol patch are also shown in Figures 4.27 – 4.29. For all cases the stress-strain curve of only the Aluminum beam was perfectly linear and consistently showed a slope of  $68 \pm 1$  GPa which is close the literature value (70 GPa) of Young’s modulus of Aluminum.

The strains measured on the Galfenol surface showed a highly non-linear response even in the absence of a magnetic field due to the stress-induced magnetoelastic strain. However, the Galfenol strain appeared to be locally linear at higher magnitudes of  $M_{xt}$  when the stress developed on the Galfenol surface was sufficient to magnetoelastically saturate the Galfenol lamina at the surface by orienting the magnetic moments near the Galfenol surface either parallel or perpendicular to the strain measurement direction depending on whether the local

stress is tensile or compressive respectively. Note that at other points along the thickness of the Galfenol layer the stress would be lower and hence magnetic moments would still have different orientations.

Another prominent feature of the strain measured on the Galfenol surface is that it increased with decreasing Aluminum layer thickness thereby exhibiting a different slope in the different unimorphs. This shows that the unimorphs do not undergo pure bending even when a bending moment is applied in the absence of magnetic field and hence the strain measured on the Galfenol surface cannot be used to obtain the true Young's modulus of Galfenol from bending measurements. Similarly, the strain measured on the Aluminum surface of the unimorphs were also different than that measured from the pure Aluminum beam for a given  $M_{xt}$ . Moreover, the strain on the Aluminum surface of the unimorph was non-linear due to the effect of non-linear Young's modulus (Delta E effect) of Galfenol which affected the composite stiffness. Note that the apparent Young's modulus of Galfenol varied along its thickness due to the variation of stress and stress-induced magnetoelastic strain thereby making the unimorph a highly non-linear elastic structure. A method of modeling this behavior will be shown in Chapter 5.

In general, the results shown in Figures 4.27 – 4.29 clearly exhibited the integrated mechanical properties in the Galfenol-Aluminum laminated composites which motivate the use of a suitable structural model for predicting the behavior of these unimorphs. The non-linear strains obtained in the absence of a magnetic field also motivates the use of a non-linear constitutive material model instead of a single-

valued free strain to model the actuation in these unimorphs. A modeling approach combining these features will be developed in Chapter 5.

#### 4.6.3. Effect of bending loads in presence of magnetic field

This section shows the effect of variation of all three parameters which have been introduced, on the actuation behavior of unimorphs. These parameters are the applied magnetic field, bending load ( $M_{xt}$ ) and the Aluminum layer thickness. In Figures 4.30 – 4.33, the Aluminum layer thickness is kept constant (1.84 mm) while the effect of changing the applied magnetic field and  $M_{xt}$  is discussed with respect to the strains measured on the free surface of the Galfenol and Aluminum layers. In Figure 4.34, the actuation-induced normalized tip displacement is calculated at magnetic saturation and shown as a function of  $M_{xt}$  and Aluminum layer thickness in the different unimorphs.

Figures 4.30 – 4.33 show that the strain response with respect to the applied magnetic field is analogous to the  $\lambda$ -H curves. This is expected because a higher magnetic field will enhance the magnetostriction in the Galfenol layer thereby increasing the magnitude of strain transferred to the Aluminum layer until the magnetostriction saturates. As expected from Figure 4.23, the strain on Aluminum surface is of opposite sign compared to the strain on Galfenol surface for this combination of Galfenol/Aluminum thickness at all magnetic fields. Also note that Figures 4.30 – 4.33 show the actual strain in order to give a feel of the relative difference between the pre-strain induced due to  $M_{xt}$  in the absence of a magnetic field and the strain due to magnetic actuation while  $M_{xt}$  is kept constant.

Figures 4.30 and 4.31 show that increasingly negative values of  $M_{xt}$  induce increasing tensile pre-stresses in the Galfenol layer thereby reducing the effective free strain that can be obtained from it. Note that a stress gradient still exists along the thickness of the Galfenol layer and hence this scenario is not the same as subjecting a Galfenol rod to uniaxial tension. This gradient of pre-stress in Galfenol creates a gradient of magnetically induced-strain on application of magnetic fields. This complexity cannot be modeled with the existing modeling techniques described earlier which assume a uniform and constant free strain in the active layer of the unimorph. An appropriate modeling technique will be discussed in Chapter 5.

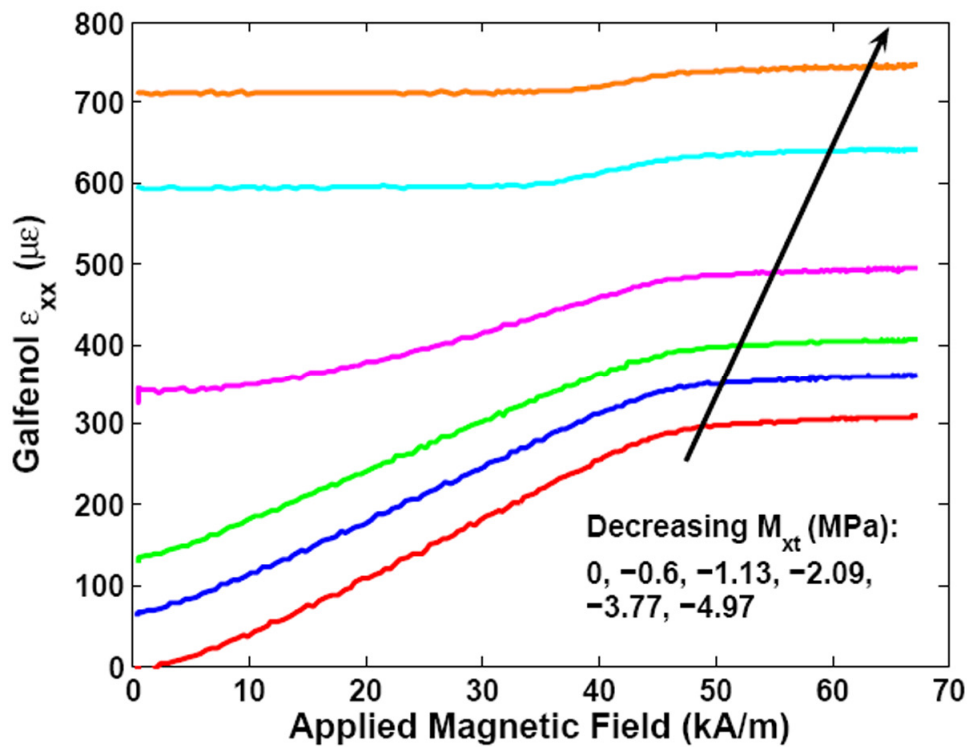


**Figure 4.30. Total strain on Galfenol surface vs. applied magnetic field for different  $M_{xt}$  which produce tension in the Galfenol layer in the unimorph having a 1.84-mm thick Aluminum layer.**

Nevertheless, as a result of reduced free strain due to tensile pre-stresses, the maximum values of magnetic field-induced strain on both Galfenol and Aluminum surfaces reduce with increasingly negative  $M_{xt}$  applied to the unimorph as shown in Figures 4.30 and 4.31. This implies that a device using a Galfenol-based unimorph should ensure that any external forces acting on that device should not create significant tensile stresses in the Galfenol layer which could block the actuation strain.

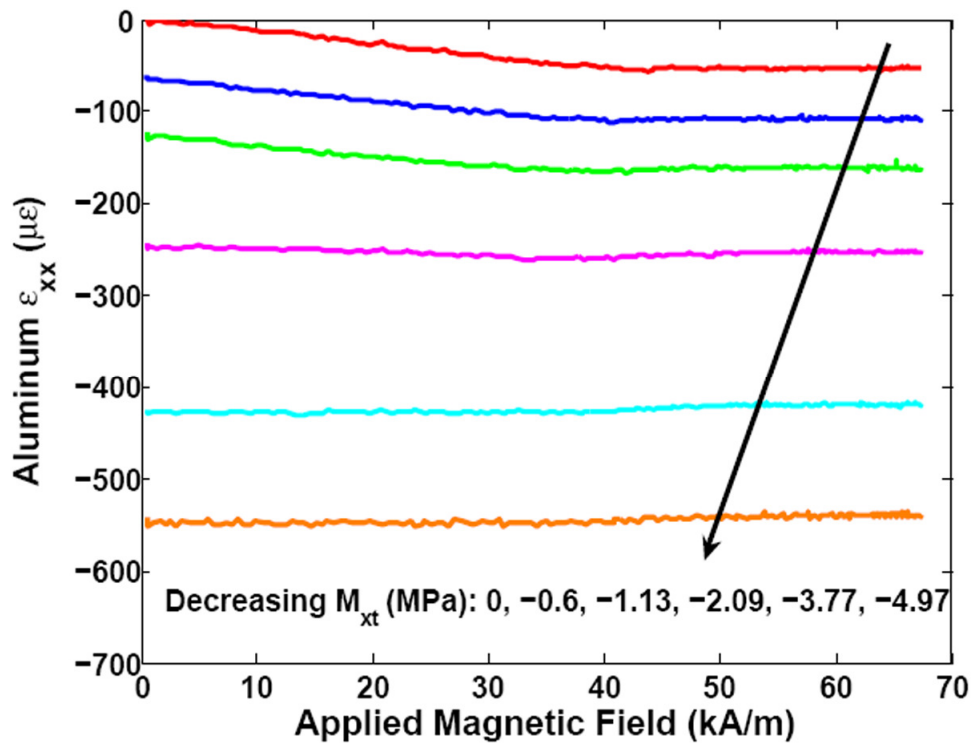


**Figure 4.31. Total strain on Aluminum surface vs. applied magnetic field for different  $M_{xt}$  which produce tension in the Galfenol layer in the unimorph having a 1.84-mm thick Aluminum layer.**

Figures 4.32 and 4.33 show that increasingly positive values of  $M_{xt}$  induce increasing compressive pre-stresses in the Galfenol layer thereby increasing the effective free strain that can be obtained from it. However, the extent of increase in

free strain in Galfenol will depend on the stress distribution along its thickness and hence on the Aluminum layer thickness too. The limiting value of the free strain is  $(3/2)\lambda_{100}$  which can be obtained if the minimum magnitude of compressive stress in Galfenol is sufficient to orient all the magnetic moments perpendicular to the length of the Galfenol sample. Once again, it should be noted that this behavior of the unimorph cannot be modeled by assuming a constant free strain in Galfenol layer. The modeling of this scenario would require the combination of a structural model and a non-linear material constitutive model.

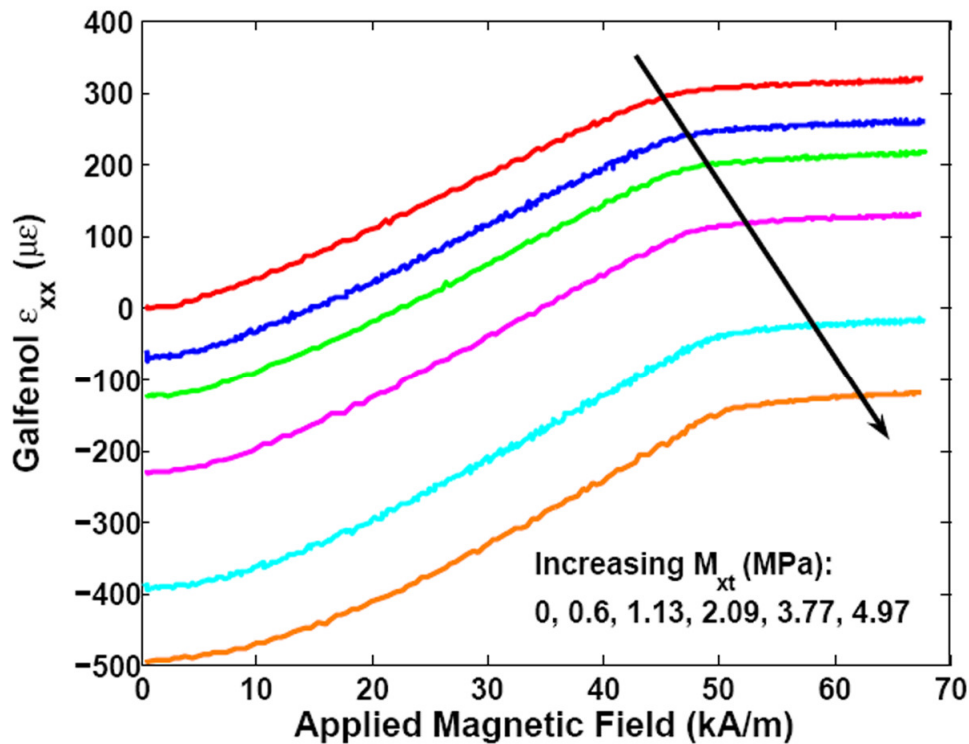


**Figure 4.32. Total strain on Galfenol surface vs. applied magnetic field for different  $M_{xt}$  which produce compression in the Galfenol layer in the unimorph having a 1.84-mm thick Aluminum layer.**

As a result of increased free strain due to compressive pre-stresses, the maximum value of magnetic field-induced strain on both Galfenol and Aluminum

surfaces increases with increasingly positive  $M_{xt}$  applied to the unimorph as shown in Figures 4.32 and 4.33. This implies that a device using a Galfenol-based unimorph may be subjected to external forces that would create significant compressive stresses in the Galfenol layer in order to improve the actuation performance.

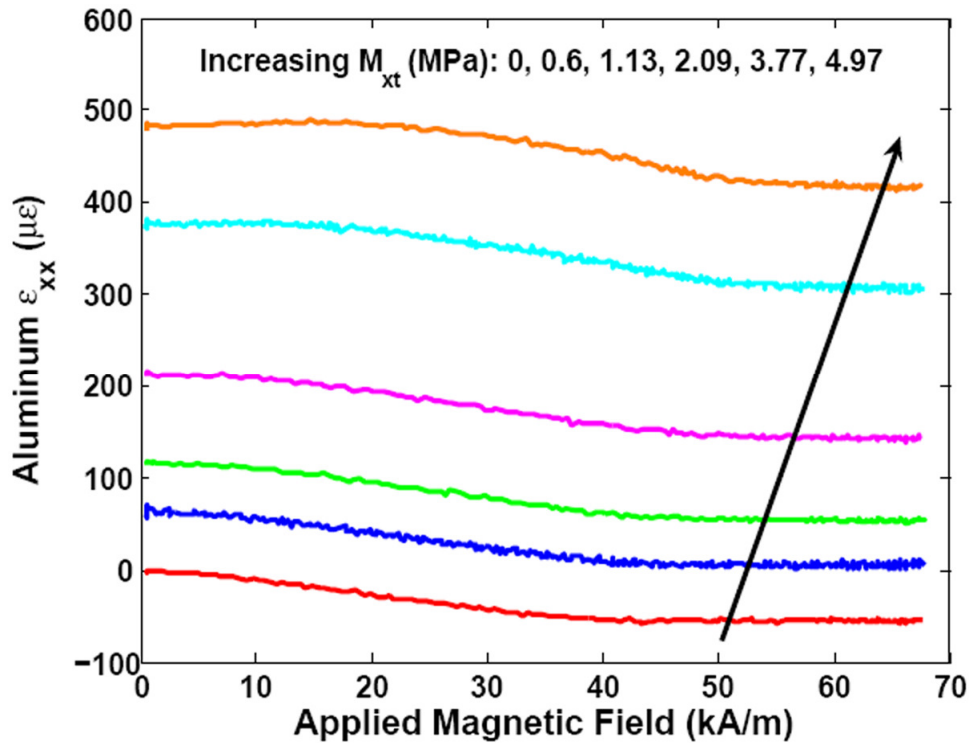


**Figure 4.33. Total strain on Aluminum surface vs. applied magnetic field for different  $M_{xt}$  which produce compression in the Galfenol layer in the unimorph having a 1.84-mm thick Aluminum layer.**

The same analysis repeated on the strains obtained from the Galfenol and Aluminum surfaces in the unimorphs with 3.7 and 7.43-mm thick Aluminum layers showed the same trends with respect to variations in magnetic field and  $M_{xt}$ .

Figure 4.34 shows the actuation-induced normalized tip displacement of the three different unimorphs as a function of  $M_{xt}$ . These values were calculated from the strains observed at magnetic saturation. The tip displacement due to application of  $M_{xt}$

at zero magnetic field was subtracted in order to compare the additional tip displacement only due to magnetic actuation effect. The tip displacement was normalized with respect to the length of the active layer and total thickness of active and passive layers so that the effect of  $M_{xt}$  can be compared. Since in these unimorphs, the active and passive layers are of different lengths, the choice of total thickness of active and passive layers but only the length of active layer for calculating the normalized tip displacement was based on Equations (4.14) and (4.15).

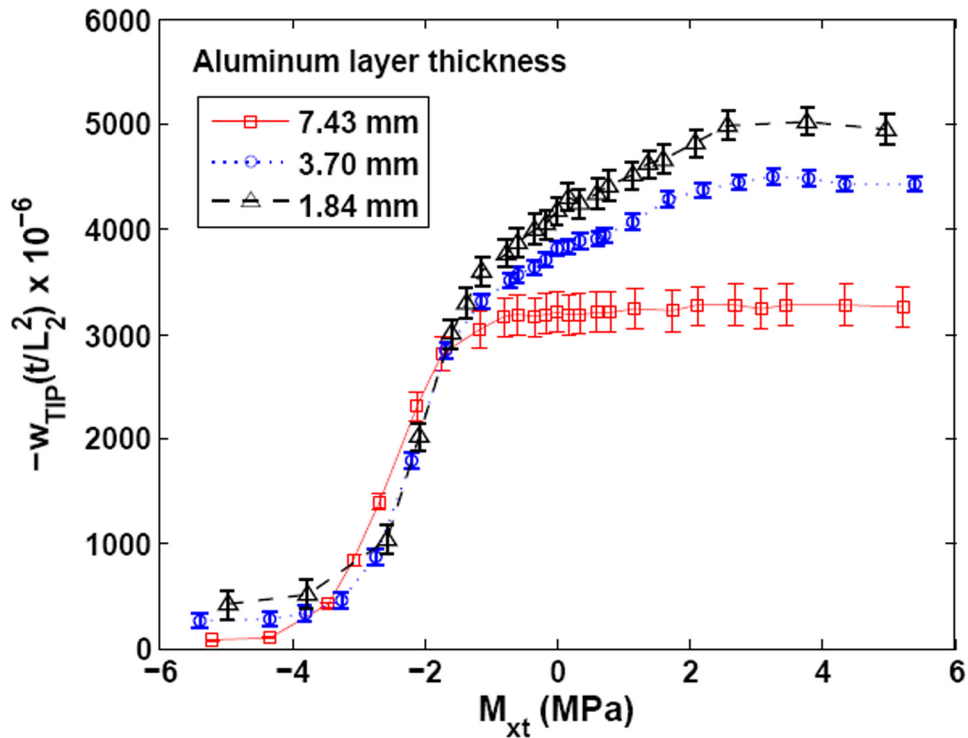


**Figure 4.34.** Actuation-induced normalized tip displacement ( $-w_{TIP}t/L_2^2$ ) vs.  $M_{xt}$  at magnetic saturation for the unimorphs with 7.43, 3.70 and 1.84-mm thick Aluminum layers.

The experimental values at  $M_{xt} = 0$  were compared to the predicted values in Table 4.4. Both the 1D and 3D models predicted the trend and order of magnitude of

the values well. However, they consistently under-predicted the tip displacement values in all three unimorphs probably because they did not account for the bond layer.

Figure 4.34 confirms the observations made from Figures 4.30 – 4.33. A negative  $M_{xt}$  induces tension in Galfenol and reduces its actuation capability whereas a positive  $M_{xt}$  induces compression in Galfenol thereby enhancing its actuation capability. The tip displacement can be reduced to zero by applying a sufficiently negative  $M_{xt}$  which can block the actuation-induced bending moment. On the other hand, there is also a critical value of positive  $M_{xt}$  which is required to obtain the maximum tip displacement. Further increase in  $M_{xt}$  does not increase the tip displacement. Figure 4.34 also shows that the values of both blocking  $M_{xt}$  and critical  $M_{xt}$  are inversely proportional to the Aluminum layer thickness for the three unimorphs on which the experiments were performed. This proportionality indicates that the composite stiffness of the unimorphs plays an important role in determining the actuation performance of the active layer as well as the entire composite structure. Such complex behavior of active structures can only be modeled using a combination of structural and non-linear material constitutive models as mentioned earlier. Such a model can be used for investigation of the actuation performance of unimorphs for a wider range of parameter variation.

#### 4.7. Sensor characterization results

Prior work by Datta and Flatau [139] presented magnetostrictive strain sensing results using two different configurations of Galfenol-based unimorph. These results were obtained at only one bias magnetic field which was provided by a

permanent magnet placed on the Galfenol layer in the unimorph. Such a configuration introduced significant inhomogeneity in the magnetic flux distribution in the Galfenol layer and also restricted the study of the effect of magnetic biasing on the sensing behavior which is known to be an important performance parameter from the discussion in Chapter 2.

The results shown in this section were obtained using a non-contact magnetic biasing mechanism that used a solenoid and hence the sensing behavior could be evaluated at different bias magnetic fields by controlling the current in the solenoid. However, a practical restriction on the measurement was imposed by the range of the Hall sensor which acquired a signal proportional to the magnetic induction in the Galfenol layer. The Hall sensor could measure upto 1000 gauss and hence would saturate at an applied magnetic field of 20-25 kA/m depending on the applied  $M_{xt}$ .

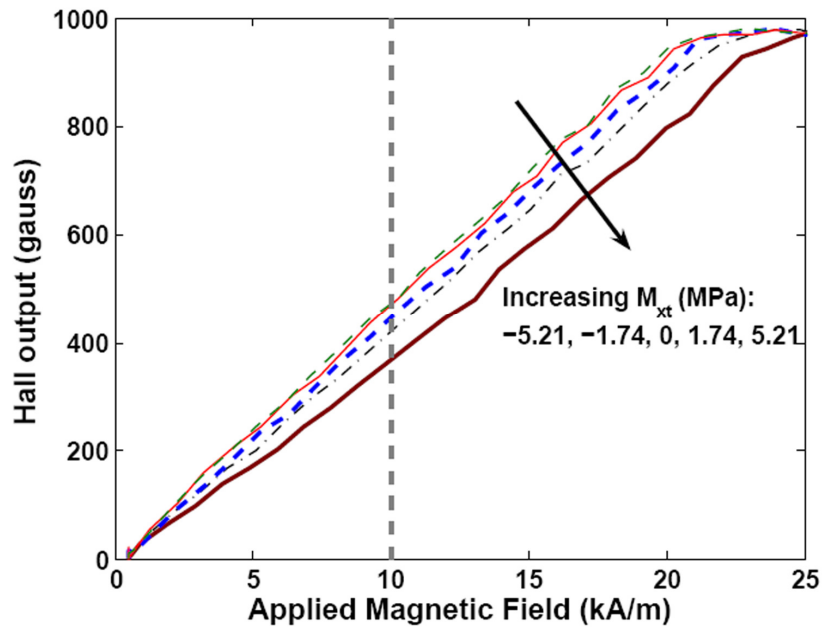
A commercially available Hall sensor with higher range would exhibit a lower sensitivity to change in magnetic induction and hence it would not be able to measure change in magnetic induction due to small changes in  $M_{xt}$ . This trade-off between range and sensitivity in a Hall sensor is not avoidable and hence it is advisable to choose an appropriate Hall sensor which can operate within the desired range with an acceptable sensitivity for any magnetostrictive sensing application.

#### 4.7.1. Self-consistency in sensor data

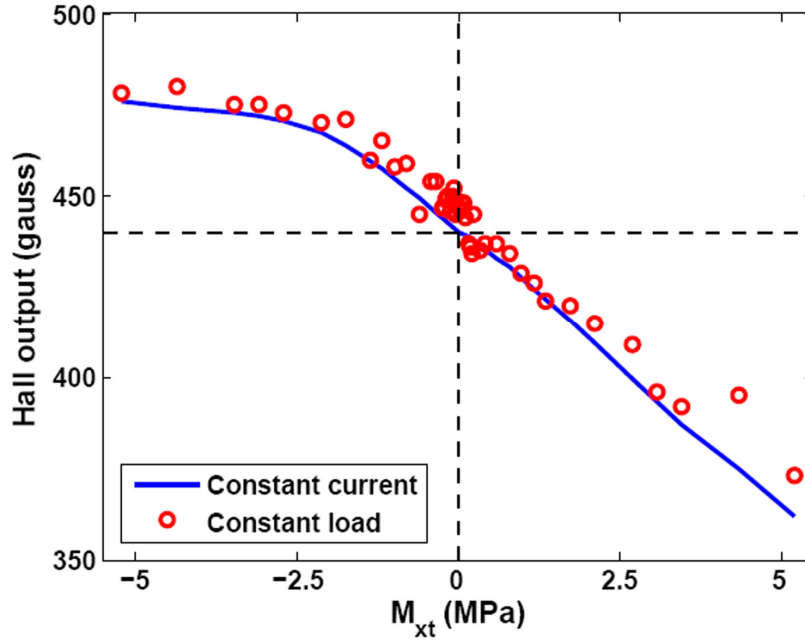
It was shown in Chapter 2 that  $B(\sigma, H)$  is a state function for quasi-static changes in  $\sigma$  and  $H$ . Based on this premise, the unimorph sensor characterization was performed using two different methods as described in Section 4.3 in order to verify the consistency in the Hall sensor data ( $B_{Hall}$ ).

Figure 4.35 shows a typical plot obtained from the first method where the  $B_{Hall}$  was acquired for quasi-statically varying  $H_{app}$  at different constant  $M_{xt}$ . Using this plot, it is possible to find  $B_{Hall}$  at different  $M_{xt}$  at a constant  $H_{app}$  as shown by the vertical grey dashed line on Figure 4.35. These data points can be plotted as  $B_{Hall}$  vs.  $M_{xt}$  at constant  $H_{app}$  as shown in Figure 4.36 by the circles for  $H_{app} = 10$  kA/m.

In the second method, the  $H_{app}$  was kept constant by passing a constant current through the solenoid while the tip loading was varied to obtain different  $M_{xt}$  and correspondingly different values of  $B_{Hall}$ . The  $B_{Hall}$  vs.  $M_{xt}$  data obtained from the second method is shown by the solid line in Figure 4.36. A comparison of the data obtained from the two different methods clearly shows that the sensor characterization data was self-consistent.



**Figure 4.35. Hall sensor output vs. applied magnetic field obtained at constant  $M_{xt}$  of -5.21, -1.74, 0, 1.74 and 5.21 MPa from the unimorph with 7.43-mm thick Aluminum layer.**



**Figure 4.36. Hall sensor output vs.  $M_{xt}$  obtained at a constant applied magnetic field of 10 kA/m from the unimorph with 7.43-mm thick Aluminum layer.**

#### 4.7.2. Effect of bias magnetic fields

Figure 4.37 shows  $B_{Hall}$  vs.  $M_{xt}$  at  $H_{app}$  of 4.6, 9.8, 14.7 and 19.2 kA/m obtained from the unimorph with 1.84-mm thick Aluminum layer. Such sensor characterization curves obtained from other unimorphs were qualitatively similar. Therefore, the effect of bias magnetic field and  $M_{xt}$  on the sensing behavior will be discussed using the representative plots shown in Figure 4.37. The labels “tension” and “compression” denote the dominant stress state in the Galfenol patch due to the applied  $M_{xt}$ . Also note that the subplots in Figure 4.37 have different maximum and minimum values of  $B_{Hall}$  on their y-axis but the range is same (100 G) in all the subplots.

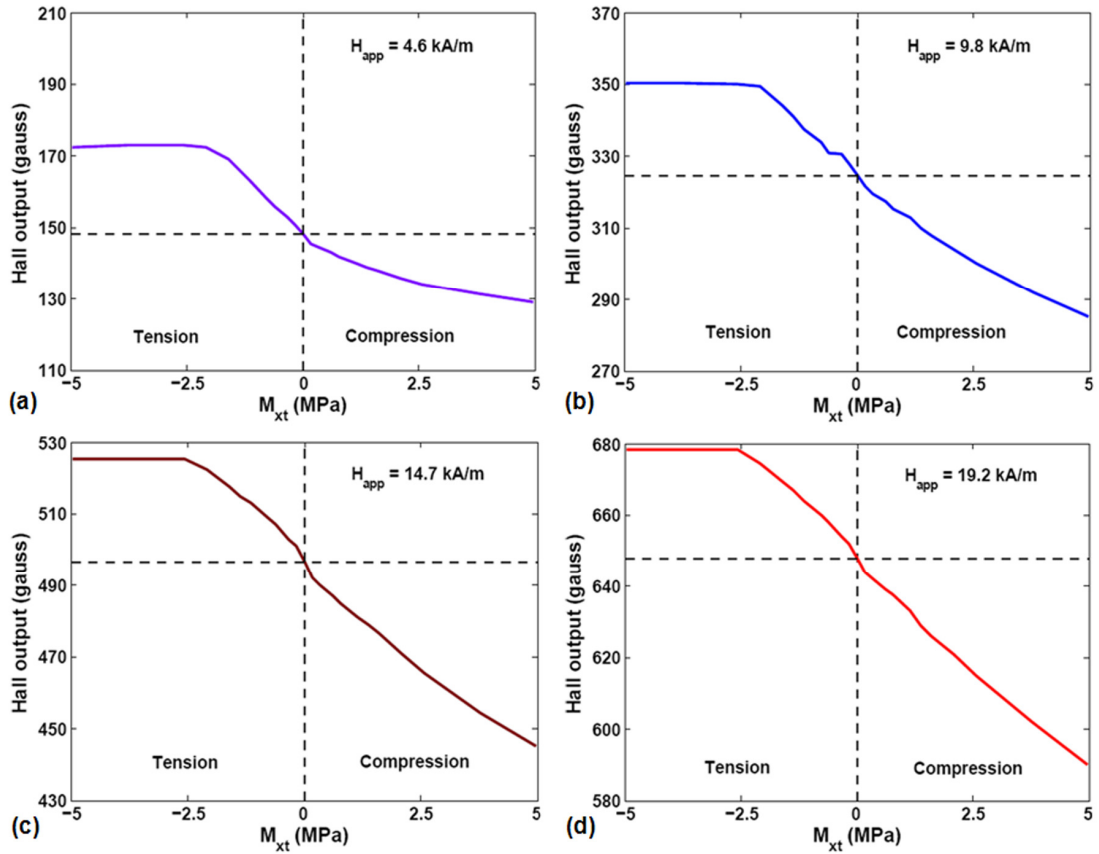


**Figure 4.37. Hall sensor output vs.  $M_{xt}$  at bias applied magnetic fields of (a) 4.6 kA/m, (b) 9.8 kA/m, (c) 14.7 kA/m and (d) 19.2 kA/m in the unimorph with 1.84-mm thick Aluminum layer.**

Figure 4.37 shows that at a given bias applied magnetic field, the material saturates at a relatively small magnitude of  $M_{xt}$  ( $\leq 2.5$  MPa) if the Galfenol patch is in tension. Note that both bias field and tension acting together favor the orientation of magnetic moments along the length of the Galfenol patch thereby saturating Galfenol. Saturation of  $B_{Hall}$  is not observed if the Galfenol is in compression unless the bias field is very small (4.6 kA/m) such that relatively small compressive stresses which can be produced by  $M_{xt} \leq 5$  MPa is sufficient to rotate most magnetic moments perpendicular to the length of the Galfenol patch. Note that the characteristic curve

shown in the lower right quadrant of Figure 4.37 is analogous to the  $B$ - $\sigma$  curves obtained under compression which were shown in Chapter 2 whereas the curves in upper left quadrant is analogous to  $B$ - $\sigma$  curves under tension.

Although the aforementioned analogy is helpful to relate the bending behavior with the axial sensing behavior, it should be noted that since the internal magnetic field could not be kept constant under bending, the sensing behavior is highly influenced by the shape anisotropy and the stress distribution in the Galfenol patch both of which affect the internal field for a constant applied magnetic field. Keeping these factors in view, the features shown by the curves in Figure 4.37 could be explained more accurately.

For example, it is logical to assume that as the bias field would increase, Galfenol would saturate in tension at a lower value of  $M_{xt}$ . However, Figure 4.37 shows that although the applied magnetic field is changed by a factor of four, the saturation in tension always takes place close to  $M_{xt} = 2.5$  MPa. This behavior can be explained by the reasoning that for a given applied magnetic field, an increasing tensile stress decreases the internal magnetic field (as explained in Chapter 2) and a smaller fraction of magnetic moments orient along the length of the Galfenol patch than it would be expected. Hence the sensing range in tension is increased by a compensating reduction in the internal magnetic field.

Similarly, the internal magnetic field in Galfenol would increase for increasing compressive stresses thereby reducing the range as well as sensitivity of the Galfenol sensor under compression. However, this phenomenon can be put to advantage for designing a Galfenol-based bending sensor which requires equal range

of operation in tension and compression. Since the internal field depends on the demagnetization factor, applied field and stress, an iterative design and experimental approach could be used to find suitable dimensions and bias applied magnetic field that could be used to operate the Galfenol sensor in the desired stress range. Since such an iterative design procedure can be time consuming and costly, it is desired to develop a modeling technique for a magnetostrictive sensor in bending which can be used to simulate sensing behavior in order to choose such design parameters. Such a modeling technique will be shown in Chapter 5.

#### 4.7.3. Analysis of sensor parameters

It is required to define certain parameters [179] in order to gain more useful information from sensor characterization curves. These parameters are useful for sensor design and for comparing sensor performance under different conditions.

*Sensitivity* is the ratio of change in the output signal ( $B_{Hall}$ ) to change in input signal ( $M_{xt}$ ). This can be obtained from the slope of the best fit straight line to the  $B_{Hall}$  vs.  $M_{xt}$  plot. It can be expressed in T/GPa which is also the unit for stress sensitivity ( $d^*$ ) under axial loading. Note that the sensitivity listed in Table 4.5 is significantly lower than the values of  $d^*$  shown in Chapter 2. This indicates that the device sensitivity will always be significantly lower than the sensitivity of the active material.

Table 4.5 indicates that in all the unimorphs, the device sensitivity is higher when Galfenol is in compression (i.e. positive  $M_{xt}$ ) except for the lowest bias field (4.6 kA/m). Also, the sensitivity increased with increasing bias fields for both positive and negative  $M_{xt}$ . The effect of unimorph thickness could not be clearly

distinguished due to small variations in Hall sensor position between one unimorph and another.

**Table 4.5. Effect of bias applied magnetic field ( $H_{app}$  in kA/m), nature of  $M_{xt}$  (negative/positive) and Aluminum layer thickness ( $t_1$  in mm) on sensitivity (T/GPa) of Galfenol-Aluminum unimorphs.**

$H_{app}$	4.6		9.8		14.7		19.2	
$M_{xt}$	-	+	-	+	-	+	-	+
$t_1 = 7.43$	0.47	0.79	0.69	1.54	0.81	1.87	0.89	2.01
$t_1 = 3.70$	0.48	0.47	0.55	1.01	0.59	1.25	0.64	1.36
$t_1 = 1.84$	0.52	0.37	0.56	0.79	0.59	1.02	0.64	1.16

*Operating range* is the range of input for which the sensor can give a proportional (preferably linear) output. No comment can be made about the entire operating range of the unimorph sensors since the operating range of the Hall sensor used in the experiments did not allow the measurement of magnetic signal upto saturation. However, it can be said that for the bias fields at which the experiments were performed, the unimorphs showed a linear sensing response for  $-2.5 \text{ MPa} \leq M_{xt} \leq 5 \text{ MPa}$ . Note that in dynamic applications, the range of frequency within which the sensor can work needs to be defined too.

*Resolution ( $Rn_{dev}$ )* of a magnetostrictive sensing device is the smallest change in input which produces a measurable change in the output. This parameter depends on the sensitivity of the Hall sensor ( $S_{Hall} \approx 2.5 \text{ mV/gauss}$ ), the sensitivity ( $\partial B_{Hall}/\partial M_{xt}$ ) of the magnetostrictive sensing device and the resolution ( $Rn_{meas} = 0.25 \text{ mV}$ ) of the voltage measuring device which measures the output of the Hall sensor.

The resolution of the magnetostrictive sensing device can be expressed using Equation (4.25).

$$Rn_{dev} = \frac{Rn_{meas}}{S_{Hall} (\partial B_{Hall} / \partial M_{xt})} \quad (4.25)$$

Table 4.6 lists the sensing resolution of the unimorph sensors under different bias fields and loading conditions. In general, the resolution was better when the Galfenol patch was in compression. The resolution showed nominal improvement with increasing bias fields.

**Table 4.6. Effect of bias applied magnetic field ( $H_{app}$  in kA/m), nature of  $M_{xt}$  (negative/positive) and Aluminum layer thickness ( $t_1$  in mm) on sensing resolution ( $\times 10^3$  Pa) of Galfenol-Aluminum unimorphs.**

$H_{app}$	4.6		9.8		14.7		19.2	
$M_{xt}$	-	+	-	+	-	+	-	+
$t_1 = 7.43$	21	13	14	6	12	5	11	5
$t_1 = 3.70$	20	21	18	10	16	8	15	7
$t_1 = 1.84$	19	26	17	12	16	10	15	8

*Accuracy* is the ratio of maximum error of output to the full scale output expressed as a percentage. The highest value of standard deviation for any data point, which was  $\sim 2$  gauss, was considered as the maximum error. The full scale output is the difference between the values of  $B_{Hall}$  corresponding to the maximum and minimum values of  $M_{xt}$ . In these experiments, the accuracy was between 1.3 – 4.6 %.

*Linearity* is the maximum deviation of experimental data points from best straight line fit between output and input. A straight line can be fitted to the  $B_{Hall}$  vs.

$M_{xt}$  plot and the correlation coefficient ( $R^2$ ) can be considered as the measure of linearity. Table 4.7 lists the values of  $R^2$  obtained from the straight line fits of the sensor characterization data. As expected from previous analyses, the values in Table 4.7 also confirm that higher bias fields and compressive stresses in Galfenol produced more linear sensing response from the unimorphs.

**Table 4.7. Effect of bias applied magnetic field ( $H_{app}$  in kA/m), nature of  $M_{xt}$  (negative/positive) and Aluminum layer thickness ( $t_1$  in mm) on correlation coefficient ( $R^2$ ) of Galfenol-Aluminum unimorphs.**

$H_{app}$	4.6		9.8		14.7		19.2	
$M_{xt}$	-	+	-	+	-	+	-	+
$t_1 = 7.43$	0.818	0.993	0.873	0.999	0.870	0.999	0.861	0.999
$t_1 = 3.70$	0.788	0.972	0.810	0.996	0.809	0.999	0.824	0.999
$t_1 = 1.84$	0.713	0.935	0.774	0.987	0.781	0.992	0.798	0.999

*Hysteresis* is the change in output for the same input applied cyclically. The standard deviation in  $B_{Hall}$  obtained for each value of strain gives a measure of the hysteresis. The hysteresis in the data was extremely small ( $\leq 2$  G) under the operating conditions of the experiments.

*Offset* is the value of output for zero input. This is the signal ( $B_o$ ) obtained from the Hall sensor when a bias magnetic field is applied in the absence of a mechanical loading. Table 4.8 lists the Hall sensor offset values under different bias applied magnetic fields for the different unimorphs. Note that for the same  $H_{app}$ , a different  $B_o$  could be measured based on small misalignment or variation in the position of Hall sensor which can occur during bonding.

**Table 4.8. Offset ( $B_o$  in gauss) in Hall sensor output for different bias applied magnetic fields ( $H_{app}$  in kA/m) in the Galfenol-Aluminum unimorphs with Aluminum layer thickness ( $t_1$  in mm).**

$H_{app}$	4.6	9.8	14.7	19.2
$t_1 = 7.43$	208	440	666.25	867.5
$t_1 = 3.70$	142.75	311	475	620
$t_1 = 1.84$	148.25	324.5	496.5	647.75

*Noise* is a measure of the clarity of the signal. Noise can be introduced due to drift in measuring instruments, harmonics of the frequency at which the power line operates, or even faulty electrical or mechanical connections. Most of it can be taken care by applying simple signal conditioning on the output signal. Since all experiments were performed under quasi-static conditions, the electronically acquired data displayed a 60 Hz noise due to the power line. Hence appropriate filtering and averaging was performed on the raw data.

*Operating conditions* include environmental factors for which the calibration of a device is valid. All material properties are temperature dependent and phase transformations take place at certain temperatures. Humidity and pH values of the operating environment affect corrosion rate. Dynamic conditions can lead to fatigue. Hence it is necessary to have the knowledge of operating conditions. All experiments on the unimorphs were performed at room temperature ( $\sim 20 \pm 1$  °C) under quasi-static conditions. The solenoid was surrounded by ice-packs to avoid any significant local temperature variation due to Joule heating. The temperature in air inside the solenoid was measured using a commercial thermometer.

*Figure of merit* (FM) is a dimensionless number which defines the performance of the magnetostrictive sensing device. An experimental figure of merit based on Equation (2.20) can be defined for a bending sensor as shown in Equation (4.26). Here  $|\Delta M_{xt}|$  is the absolute value of operating range for which the sensitivity has been calculated. Note that Equation (4.26) includes the effect of device sensitivity, operating range and magnetic bias condition and hence can be considered as a comprehensive measure of the device performance.

$$FM = \frac{|\Delta M_{xt}|}{B_o} \left. \frac{\partial B_{Hall}}{\partial M_{xt}} \right|_{H=H_{app}} \quad (4.26)$$

**Table 4.9. Effect of bias applied magnetic field ( $H_{app}$  in kA/m), nature of  $M_{xt}$  (negative/positive) and Aluminum layer thickness ( $t_1$  in mm) on figure of merit (FM) of Galfenol-Aluminum unimorphs.**

$H_{app}$	4.6		9.8		14.7		19.2	
$M_{xt}$	-	+	-	+	-	+	-	+
$t_1 = 7.43$	0.11	0.20	0.08	0.19	0.06	0.15	0.05	0.13
$t_1 = 3.70$	0.18	0.17	0.10	0.17	0.06	0.14	0.05	0.12
$t_1 = 1.84$	0.18	0.12	0.09	0.12	0.06	0.10	0.05	0.09

Table 4.9 lists the values of *FM* obtained from the unimorphs under different bias fields and loading conditions. These values reiterate earlier observations which showed that better sensing performance could be obtained at higher bias field and if the Galfenol was under compression. The *FM* values also showed that for the lowest bias field (4.6 kA/m) the sensing performance under tension and compression were similar.

From the analysis of gage factors of Galfenol in Chapter 2, it is known that the sensitivity of Galfenol peaks at small values of magnetic bias and compressive stress. Since all the unimorphs showed improvement of sensing performance with increasing bias applied magnetic field, it can be deduced that for all these applied magnetic fields, the internal magnetic fields in Galfenol were possibly less than or equal to the bias magnetic field where the peak in gage factor was observed in Chapter 2.

#### 4.8. Summary

In this chapter, the concept of a magnetostrictive laminated composite was introduced. A unimorph with an active magnetostrictive layer and a passive structural layer was identified as the simplest active composite which could be used in bending applications both as an actuator and as a sensor. The composite stiffness, mechanical load and magnetic field were identified as the key parameters that influence the performance of magnetostrictive laminated composites.

Galfenol-Aluminum unimorphs were built based on design criteria set by beam theory with induced-strain actuation. These unimorphs were characterized as actuators and sensors which can work in bending mode. The effect of unimorph stiffness, mechanical pre-load and actuating magnetic field on the actuator performance was studied. The out-of-plane tip displacement of the unimorphs normalized with respect to the composite thickness and length of active layer was chosen as the performance parameter for actuation. Similarly, the effect of unimorph stiffness, bias magnetic field and nature of mechanical loading on the sensor performance was also studied. Several performance parameters for sensing were defined and calculated.

A number of challenges related to experimental characterization were analyzed and discussed. Some of these challenges, such as the effect of bond layer on stiffness matching condition dealt with the structural aspect of the unimorphs whereas other issues such as demagnetization and magnetic flux variation dealt with the magnetic aspect of these magnetostrictive composites. Challenges related to measurement and interpretation of magnetic signal for sensing purposes using commercial magnetic field sensors was also discussed.

The experimental studies revealed the presence of coupling between the magnetic circuit of the device, the structural design of the setup and the magnetomechanical response of the active material. The experimental results showed consistent trends which had to be explained using a combination of theories discussed so far. A suitable modeling technique for magnetostrictive laminated composites would be one that can be used to simulate the actuation and sensing behavior for a wider range of parameter variation which could not be performed in the experimental studies. Chapter 5 will present such a coupled modeling technique.

## Chapter 5: Modeling of magnetostrictive laminated composite

In this chapter, a generalized modeling approach is described for a magnetostrictive device which is then used to develop a magnetomechanical plate model (MMPM) to predict the strain, stress and magnetic induction in laminated structures with magnetostrictive and non-magnetic layers.

The MMPM is used to perform simulation studies of a unimorph structure having a magnetostrictive Galfenol layer attached to different non-magnetic passive layers. The actuation response from the patch is obtained for in-plane axial magnetic field acting on the unimorph. The MMPM is used to predict the normalized tip displacement due to induced-strain actuation in cantilevered unimorph beams and the results are compared with existing modeling techniques.

The model is used to study the effect of tensile and compressive axial forces, and bending moments on the actuation and sensing response of the unimorph at different magnetic fields. A study is also performed to understand the effect of total thickness of the structure, the ratio of the active/passive layer thickness and the effect of the mechanical properties of different passive materials on the actuator and sensor performance.

Finally, the MMPM is used to model the actuation and sensing response of the unimorphs discussed in Chapter 4. The results demonstrate that the model captures the non-linearity in the magnetomechanical process and the different structural couplings in a magnetostrictive laminated composite.

### 5.1. Background and scope of this work

Several researchers have attempted to address the challenges involved in modeling the actuation and sensing behavior of magnetostrictive composites using different approaches. Klokhholm [180] developed an analytical expression to find the magnetostriction constant of a magnetostrictive thin film attached to a non-magnetic substrate from the measured displacement of the free end of a cantilevered composite beam. Another analytical expression for the same scenario was obtained by du Tremolet de Lacheisserie *et al.* [181] which differed from Klokhholm's formula by a factor of  $(1 - \nu)/(1 + \nu)$ . Assuming a Poisson's ratio of  $\nu = 0.33$ , for a given cantilever tip displacement; Lacheisserie's formula would predict a magnetostriction which is nearly half of what Klokhholm's formula would predict. In a later work, Klokhholm *et al.* [182] validated their formula with experimental results from thin film measurements. A tacit assumption in both these approaches was that the film thickness is negligible compared to the substrate thickness and hence the structure undergoes pure mechanical bending due to a "bending moment" arising from the constraint imposed by the passive substrate on the free strain of the active layer.

This limitation in the model was addressed in other analytical approaches [183] using beam theory and shell theory to account for both expansional and bending strains due to induced-strain actuation of a composite beam but these approaches did not account for the effect of magnetic field and stress on the magnetostrictive layer. In a later work [184], an improved analytical model was obtained using energy minimization methods, which was shown to be valid for all active/passive layer thickness ratios. However, the omission of the magnetocrystalline anisotropy energy

which indicates the preference of magnetic moment orientation along particular directions called easy axes made this model only suitable to handle only isotropic saturation magnetostriction in amorphous magnetostrictive materials. Moreover, Guerrero's model [184] does not account for the change in magnetostriction or magnetic induction in the active layer due to the stress developed in the active material as a result of the deformation of the composite structure due to induced-strain actuation.

Wun-Fogle *et al.* [185] used a planar magnetization rotation model for predicting the sensing performance of an amorphous magnetostrictive material adhered to an Aluminum beam subjected to various loading conditions. This approach is well suited for one-dimensional prediction of the magnetostrictive response in the regime where magnetization rotation takes place. The scheme used for calculating the magnetostriction is suitable for prediction along the magnetic easy axis provided all the magnetic moments in the material are initially aligned perpendicular to this axis. Their model included the magnetomechanical interactions unlike the other models discussed, but the structural interaction with the Aluminum beam and its effect on the performance of the magnetostrictive material was not taken into account.

Structural interactions between the active and passive layers of a magnetostrictive composite were addressed in a finite element approach [186]. However, this work used constant magnetomechanical properties of the active layer thereby ignoring the effect of stress developed due to structural deformation of the active layer on its magnetomechanical properties.

In order to overcome these limitations, a magnetomechanical plate model (MMPM) is developed in this chapter by combining an energy-based constitutive magnetostrictive model with the classical laminated plate theory and a lumped parameter magnetic model. Although the results shown in this chapter are relevant for quasi-static mechanical stress and magnetic field application, the model algorithm can be used in a dynamic setting too. The model described here is two-dimensional in nature and can be used to analyze laminated structures in which active magnetostrictive layers actuate the structures.

This model offers the following advantages. The energy-based constitutive magnetostrictive model offers the flexibility of applying stress and magnetic field in any direction in 3D space and the resulting non-linear magnetization and magnetostriction can also be predicted along any direction. The plate theory accounts for Poisson's effect and other types of mechanical coupling such as extension-bending coupling. The lumped parameter magnetic model accounts for demagnetization and helps in calculating the internal magnetic field for a given applied magnetic field. Most importantly, a recursive algorithm used in this work accounts for the change in magnetostriction and internal magnetic field in the active layer due to the stress developed in it as a result of the deformation of the composite structure due to induced-strain actuation and application of external forces.

## 5.2. *Model formulation*

This section will describe a generalized coupled modeling approach for magnetostrictive devices using a recursive algorithm. In order to use this technique in laminated magnetostrictive composites, a constitutive magnetostrictive model, the

classical laminated plate theory and a lumped parameter magnetic model will be introduced. Finally, a specific algorithm for combining these theories to develop the MPPM will be described.

### 5.2.1. Magnetostrictive device modeling approach

Physics-based modeling of a magnetostrictive actuation or sensing device requires the modeling of three mutually dependent problems. These three problems are namely the structural analysis of the device, the magnetic analysis of the device and modeling the constitutive behavior of the active material which is at the core of the device. The flow diagram of such a modeling approach is shown in Figure 5.1.

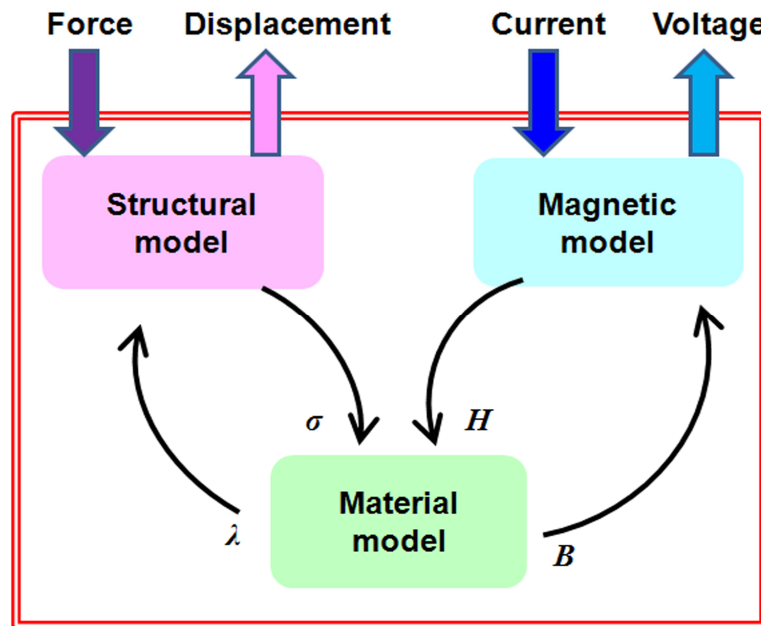


**Figure 5.1. Flow diagram of device-level model.**

The structural analysis of the device is performed by solving the mechanical boundary value problem. The structural model accounts for the effect of an external force (axial and shear forces, bending moment and torque) acting on the device and predicts the displacement (in and out-of-plane displacements and twist) of the device.

It also calculates the stress in the magnetostrictive material in the device. The structural analysis can be performed using lumped parameter force-balance approach (zero-dimension), beam theory (1D), plate theory (2D) or finite element method (3D). The general mechanical boundary value problem has been discussed in Chapter 4.

The magnetic analysis is performed by solving the magnetic boundary value problem. The magnetic model accounts for the effect of an external applied magnetizing source (current in a solenoid or remnant magnetization in a permanent magnet) on the device and predicts the corresponding magnetic quantities (magnetization, magnetic induction and magnetic flux). It also considers the entire device as a magnetic circuit and hence can predict the magnetic field in any of the components of this circuit. The magnetic model is necessary to account for demagnetization effect. The magnetic analysis can be performed using lumped parameters, simple magnetic circuits or finite element methods. The general magnetic boundary value problem has been discussed in Chapters 3 and 4.

Once the stress and magnetic field in the magnetostrictive material are known by solving the mechanical and magnetic boundary value problems, the material constitutive model can be used to predict the magnetization (or magnetic induction) and magnetostriction in the active material. The coupled linear constitutive equations and several non-linear phenomenological and energy-based models described in Chapters 1 and 2 can be used for this purpose.

Most device level [2, 81] models use a combination of two out of the three analyses mentioned above. For example, magnetostrictive actuator models use a magnetic circuit to calculate magnetic field from drive current and uses this magnetic

field value in a constitutive model to calculate the magnetostriction in the active material. Other types of actuator models consider the magnetostriction to be a known and constant value and use that value in a structural model to calculate deformation or force induced by the active material. Conversely, sensor models assume a known and constant value of bias magnetic field in the material. The stress in the material is calculated from a structural model without taking into consideration any actuation effect caused by the bias magnetic field. The stress and bias magnetic field values are used in a constitutive model to calculate the magnetic induction in the material.

Mudivarthi *et al.* [166] developed a bi-directionally coupled magnetoelastic model (BCMEM) approach which used a recursive solution of all of the three problems. Hence there was no distinction made between actuation and sensing effect as both cases required solving the mechanical and magnetic boundary value problems using a non-linear constitutive material model for the magnetostrictive material. Whereas other models consider stress and magnetic field as the fundamental independent inputs, this approach considered them to be mutually dependent. The model was validated against experimental data obtained from Galfenol-based unimorph strain sensor [139].

It was evident from the discussion of the experimental results in Chapter 4 that stress and magnetic field cannot be considered as independent inputs in magnetostrictive composites. In an actuation scenario, the magnetostriction produced by an applied magnetic field deforms the composite and produces stress in the active material. The stress changes the permeability of the material and therefore the internal magnetic field also changes. The development of stress and change in internal

magnetic field as a result of actuation affects the magnetostriction which in turn changes the actuation stress in the material. Therefore this problem can be accurately solved only by using a recursive approach. In a sensing scenario, the stress produced by an external mechanical force changes the permeability and internal magnetic field for a given bias applied magnetic field. Furthermore, the internal magnetic field also produces magnetostriction which also deforms the structure thereby producing additional stress in the material. This stress once again leads to change in the internal magnetic field thereby making the problem a recursive one.

In this chapter, the recursive approach is applied to model the actuation and sensing behavior of magnetostrictive laminated composites. Since the preliminary analysis in Chapter 4 showed that a 2D structural model would be sufficient to analyze the unimorphs, the classical laminated plate theory was deemed to be an ideal candidate for the structural model. As the magnetic field in the experiment was applied only in one direction using a solenoid, a lumped parameter magnetic model was deemed sufficient to analyze this scenario. Similarly, the energy-based magnetostrictive model which was used in Chapter 2, was considered a good choice for modeling the non-linear constitutive behavior of Galfenol in magnetostrictive composites. These modeling components will be described in details in Sections 5.2.2 – 5.2.4. Finally, Section 5.2.5 will present the algorithm for combining these models into a recursive algorithm that can be used as a coupled magnetomechanical plate model (MMPM) for predicting the actuation and sensing behavior of magnetostrictive laminated composites.

### 5.2.2. Energy-based constitutive magnetostrictive model

The energy-based constitutive magnetostrictive model [153] described in Chapter 2 is presented here in its 3D form. The model uses the saturation magnetization ( $M_s$ ), the magnetostrictive constants ( $\lambda_{100}$ ,  $\lambda_{111}$ ) and the 4<sup>th</sup> and 6<sup>th</sup> order magnetocrystalline anisotropy constants ( $K_1$ ,  $K_2$ ) to calculate the Zeeman, stress-induced anisotropy and magnetocrystalline anisotropy energies per unit volume due to a magnetic field ( $H$ ) applied along the direction cosines ( $\beta_1$ ,  $\beta_2$ ,  $\beta_3$ ) and a stress ( $\sigma$ ) applied along the direction cosines ( $\gamma_1$ ,  $\gamma_2$ ,  $\gamma_3$ ) as shown in Equations (5.1), (5.2) and (5.3) respectively.

$$E_H = -\mu_o M_s H (\alpha_1 \beta_1 + \alpha_2 \beta_2 + \alpha_3 \beta_3) \quad (5.1)$$

$$E_\sigma = -\frac{3}{2} \lambda_{100} \sigma (\alpha_1^2 \gamma_1^2 + \alpha_2^2 \gamma_2^2 + \alpha_3^2 \gamma_3^2) - 3 \lambda_{111} \sigma (\alpha_1 \alpha_2 \gamma_1 \gamma_2 + \alpha_2 \alpha_3 \gamma_2 \gamma_3 + \alpha_3 \alpha_1 \gamma_3 \gamma_1) \quad (5.2)$$

$$E_{an} = K_1 (\alpha_1^2 \alpha_2^2 + \alpha_2^2 \alpha_3^2 + \alpha_3^2 \alpha_1^2) + K_2 (\alpha_1^2 \alpha_2^2 \alpha_3^2) \quad (5.3)$$

However, in a 3D scenario, the stress-induced anisotropy energy cannot be calculated using Equation (5.2) which shows only one magnitude of stress and one set of direction cosines. In order to include the effect of all the components of a stress tensor, the eigen-value problem shown in Equation (5.4) should be solved to get the principal stresses ( $\sigma_j$ ) and a set of direction cosines ( $\gamma_{1j}$ ,  $\gamma_{2j}$ ,  $\gamma_{3j}$ ) for each principal stress and these values should be used as shown in Equation (5.5) to calculate the total stress-induced anisotropy energy for a 3D case.

$$\begin{bmatrix} \sigma_{xx} & \tau_{xy} & \tau_{xz} \\ \tau_{xy} & \sigma_{yy} & \tau_{yz} \\ \tau_{xz} & \tau_{yz} & \sigma_{zz} \end{bmatrix} \begin{Bmatrix} \gamma_1 \\ \gamma_2 \\ \gamma_3 \end{Bmatrix} = \sigma \begin{Bmatrix} \gamma_1 \\ \gamma_2 \\ \gamma_3 \end{Bmatrix} \quad (5.4)$$

$$E_{\sigma} = -\frac{3}{2} \lambda_{100} \sum_{j=1}^3 \sigma_j (\alpha_1^2 \gamma_{1j}^2 + \alpha_2^2 \gamma_{2j}^2 + \alpha_3^2 \gamma_{3j}^2) - 3 \lambda_{111} \sum_{j=1}^3 \sigma_j (\alpha_1 \alpha_2 \gamma_{1j} \gamma_{2j} + \alpha_2 \alpha_3 \gamma_{2j} \gamma_{3j} + \alpha_3 \alpha_1 \gamma_{3j} \gamma_{1j}) \quad (5.5)$$

The total energy ( $E_{TOT}$ ) of the system corresponding to different orientations of the magnetic moments with direction cosines ( $\alpha_1, \alpha_2, \alpha_3$ ) is shown in Equation (5.6). The direction cosines can be expressed in terms of the azimuthal angle ( $\varphi$ ) and polar angle ( $\theta$ ) such that  $\alpha_1 = \sin \theta \cos \varphi$ ,  $\alpha_2 = \sin \theta \sin \varphi$  and  $\alpha_3 = \cos \theta$ .

$$E_{TOT}(\varphi, \theta) = E_H + E_{\sigma} + E_{an} \quad (5.6)$$

The magnetization components are calculated using Equation (5.7).

$$\mathbf{M} = \begin{Bmatrix} M_1 \\ M_2 \\ M_3 \end{Bmatrix} = \frac{\sum_{\varphi=0}^{2\pi} \sum_{\theta=0}^{\pi} M_s \begin{Bmatrix} \alpha_1 \\ \alpha_2 \\ \alpha_3 \end{Bmatrix} |\sin \theta| \Delta \theta \Delta \varphi e^{\frac{-E_{TOT}}{\Omega}}}{\sum_{\varphi=0}^{2\pi} \sum_{\theta=0}^{\pi} |\sin \theta| \Delta \theta \Delta \varphi e^{\frac{-E_{TOT}}{\Omega}}} \quad (5.7)$$

The magnetic induction is calculated using Equation (5.8).

$$\mathbf{B} = \mu_o (\mathbf{M} + \mathbf{H}) \quad (5.8)$$

The magnetostriction components are calculated using Equation (5.9).

$$\begin{Bmatrix} \lambda_{11} \\ \lambda_{22} \\ \lambda_{33} \\ \lambda_{23} \\ \lambda_{31} \\ \lambda_{12} \end{Bmatrix} = \frac{\sum_{\varphi=0}^{2\pi} \sum_{\theta=0}^{\pi} \begin{Bmatrix} \frac{3}{2} \lambda_{100} (\alpha_1^2 - 1/3) \\ \frac{3}{2} \lambda_{100} (\alpha_2^2 - 1/3) \\ \frac{3}{2} \lambda_{100} (\alpha_3^2 - 1/3) \\ 3 \lambda_{111} \alpha_2 \alpha_3 \\ 3 \lambda_{111} \alpha_3 \alpha_1 \\ 3 \lambda_{111} \alpha_1 \alpha_2 \end{Bmatrix} |\sin \theta| \Delta \theta \Delta \varphi e^{\frac{-E_{TOT}}{\Omega}}}{\sum_{\varphi=0}^{2\pi} \sum_{\theta=0}^{\pi} |\sin \theta| \Delta \theta \Delta \varphi e^{\frac{-E_{TOT}}{\Omega}}} \quad (5.9)$$

The model parameters used to simulate the non-linear magnetomechanical behavior of  $\text{Fe}_{82}\text{Ga}_{18}$  are shown in Table 5.1. The model parameters were estimated from Figure 4.4 and Table 2.2.

**Table 5.1. Parameters used in the energy-based constitutive model.**

$M_s$ (kA/m)	$\lambda_{100}$ ( $\mu\epsilon$ )	$\lambda_{111}$ ( $\mu\epsilon$ )	$K_1$ (kJ/m <sup>3</sup> )	$K_2$ (kJ/m <sup>3</sup> )	$\Omega$ (J/m <sup>3</sup> )
1330	220	-13	16.5	-45	200

### 5.2.3. Classical laminated plate theory

While the energy-based constitutive model is sufficient to predict the actuation and sensing behavior in a magnetostrictive material along a given direction, it needs to be coupled with a structural model to address actuation leading to or sensing due to extension/contraction, shear, twist and anticlastic or synclastic bending. The bending can be anticlastic or synclastic depending on opposite or similar signs of the curvatures along the  $x$  and  $y$ -directions which are denoted by  $\kappa_x$  and  $\kappa_y$ , respectively. The classical laminated plate theory was found to be suitable for modeling 2D laminated structures with active magnetostrictive layers and passive structural layers. A typically deformed unimorph exhibiting anticlastic bending under the influence of magnetic fields and/or mechanical forces is shown in Figure 5.2.

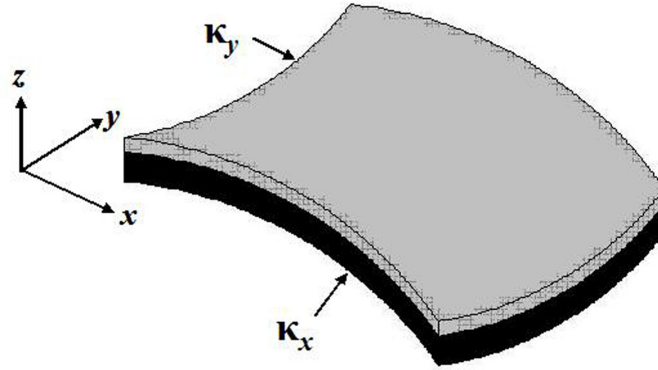


**Figure 5.2. Schematic of a deformed unimorph. The grey and black patches are the active and passive layers respectively.**

In the MMPM, plate theory is used to determine the magnitudes as well as the directions of stresses in the magnetostrictive layers and in turn these are used in the energy-based constitutive model and therefore the magnetostriction becomes a function of axial/shear forces and/or bending/twisting moments.

To apply CLPT [187] to the laminated structure, it is assumed that there is perfect bonding between the layers. Additionally, each lamina has to satisfy the Kirchhoff-Love thin-plate assumptions. Plates are assumed to be in a state of plane stress ( $\sigma_z = 0$ ) under the influence of in-plane forces. A plate subjected to bending or twisting moments will produce out-of-plane displacement which should be small compared to the plate thickness. Planes normal to the neutral plane always remain normal to it ( $\gamma_{yz} = \gamma_{xz} = 0$ ) and are also unstretched along the plate's thickness ( $\varepsilon_z = 0$ ).

This formulation leads to what appears to be a contradictory assumption, i.e., both plane stress ( $\sigma_z = 0$ ) and plane strain ( $\varepsilon_z = 0$ ). This assumption was discussed and explained by Bhaskar *et al.* [188] who showed it to be appropriate for thin plates. Hence the non-zero values of  $\varepsilon_z$  calculated by earlier models [181, 184] violate the formulation of models which are based on the assumption of thin plates.

As shown in Equation (5.10), CLPT can be used to find the mid-plane axial and shear strains  $\{\boldsymbol{\varepsilon}^o\} = \{\boldsymbol{\varepsilon}_x^o \quad \boldsymbol{\varepsilon}_y^o \quad \boldsymbol{\gamma}_{xy}^o\}^T$  and bending and twisting curvatures  $\{\boldsymbol{\kappa}\} = \{\boldsymbol{\kappa}_x \quad \boldsymbol{\kappa}_y \quad \boldsymbol{\kappa}_{xy}\}^T$  of a laminated structure with  $NL$  layers using the structural stiffness and forces acting on it.

$$\begin{bmatrix} [A] & -[B] \\ -[B] & [D] \end{bmatrix} \begin{Bmatrix} \{\boldsymbol{\varepsilon}^o\} \\ \{\boldsymbol{\kappa}\} \end{Bmatrix} = \begin{Bmatrix} \{N\} + \{N_\lambda\} \\ \{M\} + \{M_\lambda\} \end{Bmatrix} \quad (5.10)$$

The extensional  $[A]$ , coupling  $[B]$  and bending  $[D]$  stiffnesses of the structure can be calculated from Equations (5.11), (5.12) and (5.13) respectively. The mechanical and actuating forces  $\{N\}$  and  $\{N_\lambda\}$  and moments  $\{M\}$  and  $\{M_\lambda\}$  per unit length, are explained in detail later.

$$A_{ij} = \sum_{k=1}^{NL} (Q_{ij})_k (h_{k+1} - h_k) \quad (5.11)$$

$$B_{ij} = \frac{1}{2} \sum_{k=1}^{NL} (Q_{ij})_k (h_{k+1}^2 - h_k^2) \quad (5.12)$$

$$D_{ij} = \frac{1}{3} \sum_{k=1}^{NL} (Q_{ij})_k (h_{k+1}^3 - h_k^3) \quad (5.13)$$

Here  $i, j = 1, 2$  and  $6$  for plane stress condition and  $h_k$  is the distance of the  $k^{\text{th}}$  layer from the mid-plane ( $z = 0$ ). The reduced stiffness matrix  $[Q]$  of a material under plane stress and having a cubic symmetry is given by Equation (5.14).

$$[Q] = \begin{bmatrix} \frac{E}{1-\nu^2} & \frac{\nu E}{1-\nu^2} & 0 \\ \frac{\nu E}{1-\nu^2} & \frac{E}{1-\nu^2} & 0 \\ 0 & 0 & G \end{bmatrix} \quad (5.14)$$

The mechanical properties of the different passive materials used in the model simulations are shown in Table 5.2. For an isotropic material, the shear modulus is given by  $G = \frac{E}{2(1+\nu)}$ . Single crystal Galfenol ( $\text{Fe}_{82}\text{Ga}_{18}$ ) is not isotropic but has a cubic symmetry and hence its Young's modulus ( $E = 63$  GPa) and Poisson's ratio ( $\nu = 0.45$ ) are the same along any of the equivalent  $\langle 100 \rangle$  directions and  $G = 128$  GPa [115].

**Table 5.2. Mechanical properties of different passive materials [189].**

Material	Aluminum	Silicon	Alumina
E (GPa)	70	165	530
$\nu$	0.33	0.22	0.24

The stiffness matrix of the laminated unimorph structure is shown below.

$$\begin{bmatrix} A_{11} & A_{12} & 0 & -B_{11} & -B_{12} & 0 \\ A_{12} & A_{11} & 0 & -B_{12} & -B_{11} & 0 \\ 0 & 0 & A_{66} & 0 & 0 & -B_{66} \\ -B_{11} & -B_{12} & 0 & D_{11} & D_{12} & 0 \\ -B_{12} & -B_{11} & 0 & D_{12} & D_{11} & 0 \\ 0 & 0 & -B_{66} & 0 & 0 & D_{66} \end{bmatrix}$$

The terms  $A_{11}$ ,  $D_{11}$  and  $D_{66}$  are the standard extensional, bending and torsional stiffness respectively. The numerical values of stiffness terms with subscripts 11 and 22 are equal and those with subscripts 12 and 21 are also equal as the materials are assumed to be either cubic or isotropic. The non-zero value of  $A_{12}$  indicates the extension-contraction coupling in the  $x$ - $y$  direction due to Poisson's effect. A non-zero  $B_{11}$  (or  $B_{22}$ ) indicates an extension-bending coupling in the same direction as the loading whereas  $B_{12}$  indicates an extension-bending coupling between orthogonal

directions. The presence of the  $B_{66}$  term indicates a shear-twist coupling in the laminated structure. The  $D_{12}$  indicates a coupling between the curvatures  $\kappa_x$  and  $\kappa_y$  due to bending along the  $x$  and  $y$ -directions respectively.

The mechanical axial and shear forces and bending and twisting moments per unit length acting on the laminated structure are given by the vectors  $\{N\}$  and  $\{M\}$  respectively. The actuation forces and moments per unit length due to magnetostriction can be calculated from Equations (5.15) and (5.16) respectively [1].

$$\{N_\lambda\} = \sum_{k=1}^{NL} [Q]_k \{\lambda\}_k (h_{k+1} - h_k) \quad (5.15)$$

$$\{M_\lambda\} = -\frac{1}{2} \sum_{k=1}^L [Q]_k \{\lambda\}_k (h_{k+1}^2 - h_k^2) \quad (5.16)$$

Figure 5.3 illustrates the symbols used in this work for describing the in-plane forces and moments per unit length acting on a thin plate.

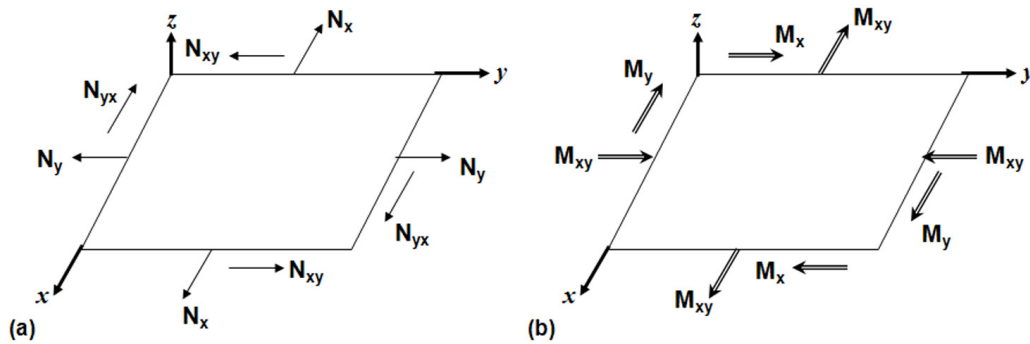


**Figure 5.3. (a) Forces per unit length ( $N$ ) acting on a thin plate. The arrows indicate the direction of the forces. Tensile force is considered positive. (b) Moments per unit length ( $M$ ) acting on a thin plate. The arrows indicate the axis about which the moments are applied. Anti-clockwise moment is considered positive.**

For comparison between laminates of different thickness, the parameters such as force per unit cross-section ( $N_{xt} = N_x/t$ ) or normalized moments ( $M_{xt} = M_x/t^2$ ) are more appropriate and hence will be often used in this chapter.

The strains and stresses at any point  $z$  (lying in the  $k^{\text{th}}$  layer) along the thickness of the structure can be calculated from Equations (5.17) and (5.18) respectively.

$$\{\boldsymbol{\varepsilon}\} = \{\boldsymbol{\varepsilon}^o\} - z\{\boldsymbol{\kappa}\} \quad (5.17)$$

$$\{\boldsymbol{\sigma}\} = [\boldsymbol{Q}]_k (\{\boldsymbol{\varepsilon}\} - \{\boldsymbol{\lambda}\}_k) \quad (5.18)$$

#### 5.2.4. Lumped parameter magnetic model

While the energy-based magnetostrictive model can predict the actuation and sensing behavior in a magnetostrictive material for a given internal magnetic field in the material, it needs to be coupled with a magnetic model to calculate the internal magnetic field corresponding to a measurable applied magnetic field. For magnetic fields applied along one direction, a lumped parameter model can be used to calculate the internal field from the applied field by using the relative permeability ( $\mu_r$ ) and demagnetization factor ( $N_d$ ) of the magnetostrictive material in Equation (5.19).

$$H_{in} = \frac{H_{app}}{1 - N_d + N_d \mu_r(\boldsymbol{\sigma}, H_{in})} \quad (5.19)$$

Note that for the same applied field, a change in the stress state of the material will change the permeability thereby changing the internal field. This can be readily implemented by considering stress and magnetic field-dependent permeability as shown in Chapter 2. The use of a variable permeability in Equation (5.19) makes it a recursive equation.

Figure 5.4 shows the effect of demagnetization factor on the internal magnetic field for different applied magnetic fields. Note that the plot is shown in log scale to account for the large difference between applied and internal fields at higher values of demagnetization factor.

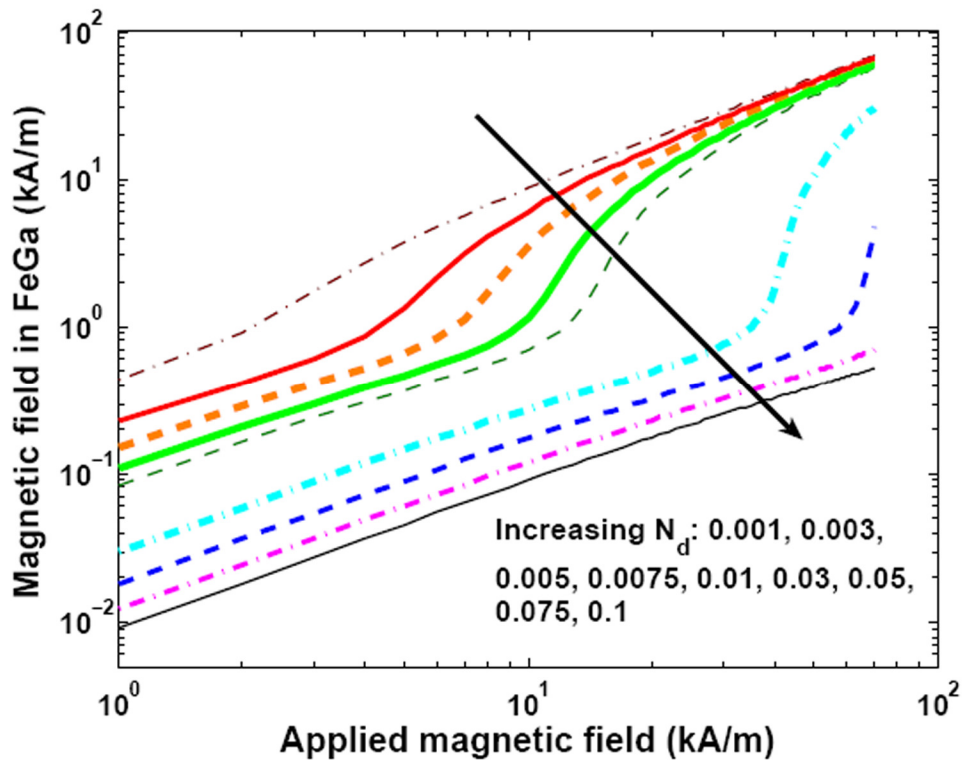


**Figure 5.4. Effect of demagnetization factor on internal magnetic field for a given applied magnetic field.**

Although a lumped parameter approach is not suitable for obtaining spatial variation in magnetic quantities in the magnetostrictive material, however it can be computationally efficient for modeling along one direction using an average demagnetization factor calculated based on an average of the magnetic field distribution in the material as shown in Chapter 4.

### 5.2.5. Algorithm of Magnetomechanical Plate Model

The energy-based constitutive model was combined with the CLPT and lumped parameter magnetic model to develop a magnetomechanical plate model (MMPM). The input and output parameters of these models were coupled using the recursive algorithm shown in Figure 5.5.

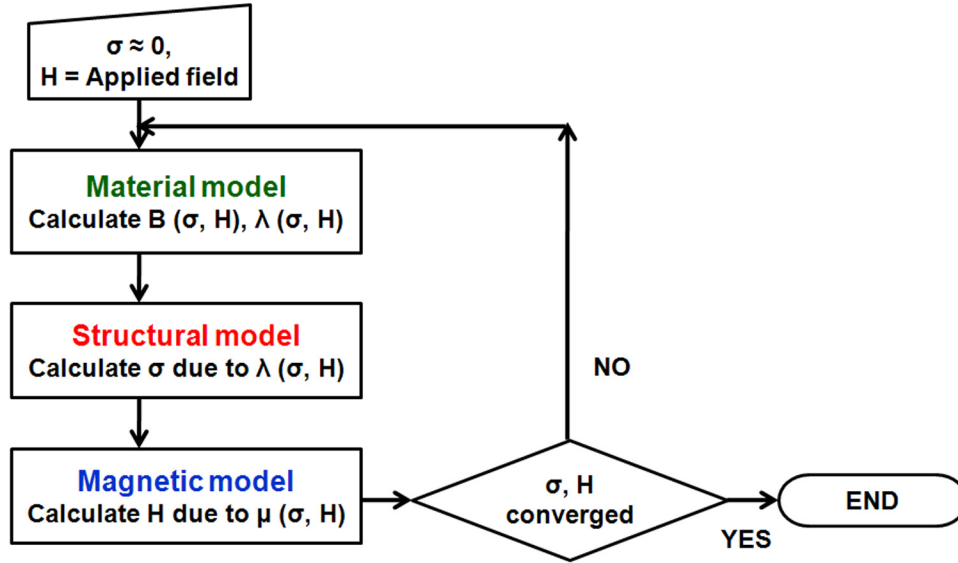


**Figure 5.5. Recursive algorithm used for coupling the material, structural and magnetic model in the magnetomechanical plate model.**

The applied magnetic field along the  $x$ -direction ( $H_x$ ) and an initial guess of small non-zero (to ensure convergence) stress were used in the energy-based constitutive model to obtain the magnetostriction ( $\lambda_x = \lambda_{11}$ ,  $\lambda_y = \lambda_{22}$  and  $\lambda_{xy} = \lambda_{12}$ ) and magnetic induction ( $B_x = B_1$ ). The magnetic induction was used to calculate the permeability. The magnetostriction values were used to calculate  $\{N_\lambda\}$  and  $\{M_\lambda\}$ . These values along with values of initial mechanical forces ( $N_x$ ,  $N_y$  or  $N_{xy}$ ) were used in the CLPT to calculate the mid-plane strains and curvatures. The values of  $\{\varepsilon^o\}$  and  $\{\kappa\}$  obtained were used to find the strains and stresses on the free surfaces of the

active and passive layers using Equations (5.17) and (5.18). The magnetic model was used to calculate the internal magnetic field using Equation (5.19). The stresses ( $\sigma_x$ ,  $\sigma_y$  and  $\tau_{xy}$ ) on the Galfenol layer and the internal magnetic field were used to update the value of the stress-induced anisotropy and Zeeman energy respectively in the energy-based model to obtain new magnetostriction and magnetic induction values which were used to recalculate the strains and stresses using CLPT and internal magnetic field using magnetic model. The process was repeated until the calculated stress and internal magnetic field on the Galfenol patch converged to within 0.1 % deviation.

The advantage of using the MPPM is illustrated using Figures 5.6 and 5.7. The results shown in these figures were obtained using an MPPM simulation on a Galfenol-Aluminum unimorph where both the materials were of equal length (25 mm) and width (8.4 mm). The thickness of the Galfenol and Aluminum layers were 1.86 mm and 3.7 mm respectively.

Figure 5.6 shows the internal vs. applied magnetic field in the Galfenol layer calculated using a demagnetization factor of 0.035. The “no coupling” curve was obtained by using permeability values in Equation (5.19) which were obtained at the required internal magnetic field but at zero stress. The MPPM simulation considered the stress developed in the Galfenol layer which altered the permeability and hence affected the calculated values of internal magnetic field.

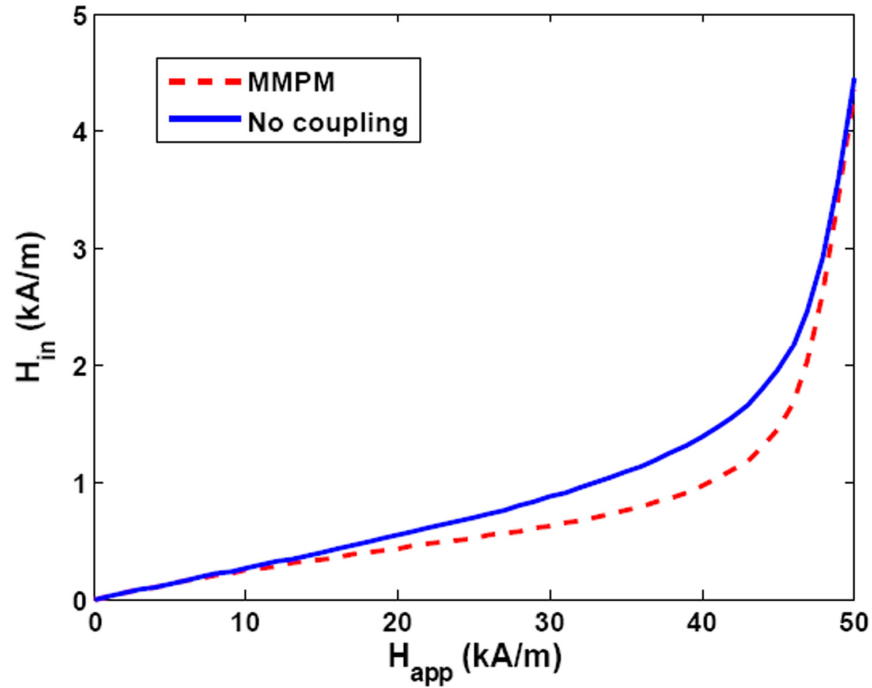


Figure 5.6. Internal vs. applied magnetic field calculated in Galfenol layer of a Galfenol-Aluminum unimorph. The Galfenol layer was assigned an  $N_d = 0.035$ .

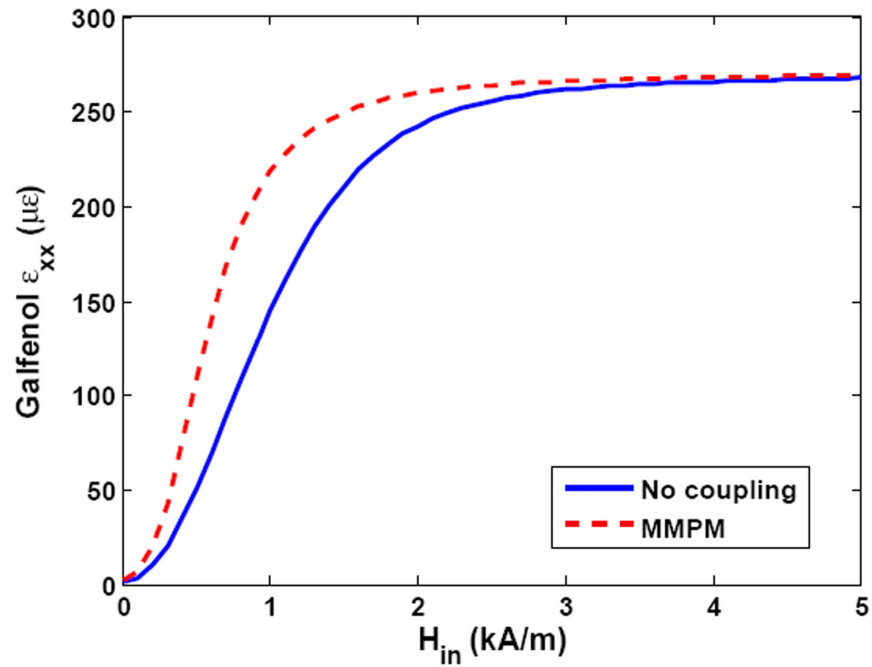


Figure 5.7. Strain on Galfenol surface vs. internal magnetic field in a Galfenol-Aluminum unimorph.

Figure 5.7 shows the strain calculated on the free surface of the Galfenol layer in the unimorph as a function of the internal magnetic field. The difference between the “no coupling” and MMPM curves are caused by the fact that MMPM modifies the free strain in Galfenol based on both its stress and internal magnetic field states whereas the “no coupling” curve considers only the internal magnetic field which is also calculated erroneously as shown in Figure 5.6 if the coupling is not considered.

These results motivate the use of the MMPM for design and analysis of Galfenol-based unimorph actuators and sensors.

### 5.3. *Model simulation results*

In this section, the coupled model (MMPM) is used to simulate the actuation and sensing behavior of Galfenol-based unimorphs. In Section 5.3.1, the out-of-plane tip displacement of cantilevered unimorphs obtained from MMPM is compared with the same obtained from other models in order to highlight the difference in their prediction capabilities.

From the perspective of actuator design, the primary interest lies in studying the strain and stress in Galfenol as a function of the magnetic field and how much of that strain and stress is transferred to the substrate leading to extension and bending of the composite structure. It is also of interest to know stiffness-matching criteria and effect of pre-loads on the actuation performance. Sections 5.3.2 and 5.3.3 will present simulation results showing the effect of magnetic field and axial pre-load on the structure, the effect of varying the ratio of active to passive layer thickness and the effect of mechanical properties of the passive layer on the actuator performance.

From the perspective of sensor design, the primary interest lies in studying the change in magnetic induction in Galfenol as a function of the applied force or bending moment. Section 5.3.4 will present simulation results showing the effect of bias applied magnetic fields and tensile and compressive extensional forces on the sensor performance.

Finally in Section 5.3.5, the MMPM simulations are compared with the experimental results obtained from the actuator and sensor characterization described in Chapter 4.

### 5.3.1. Comparison with existing models

The analytical formulae used by Lacheisserie [181], Klokhholm [182] and Guerrero [184] were used to find the normalized tip displacement ( $\Delta t/L^2$ ) of a cantilevered Galfenol-Aluminum unimorph as a function of the thickness ratio ( $t_r$ ). Here  $t$  is the thickness of the composite beam,  $L$  is its length and thickness ratio ( $t_r$ ) is the ratio of the thicknesses of the active and passive layers. The net tip displacement ( $\Delta$ ) is the difference between out-of-plane tip displacements ( $w_{TIP}$ ) obtained when the magnetic field is parallel and perpendicular to the length of the beam respectively. For either of the magnetic field conditions, the tip displacement ( $w_{TIP}$ ) of the cantilevered unimorph can be obtained from Equation (5.20). Here  $\kappa_x$ , which is the beam's curvature along the  $x$ -direction, can be obtained from the axial strains on the surfaces of the active and passive layers of the unimorph as shown in Equation (5.21).

$$w_{TIP} = \frac{\kappa_x}{2} L^2 \quad (5.20)$$

$$\kappa_x = \frac{\epsilon_x^{PASSIVE} - \epsilon_x^{ACTIVE}}{t} \quad (5.21)$$

The results obtained from the other models are compared with that obtained from the MPPM for an applied magnetic field ( $H_{app} = 65$  kA/m) along the  $x$ -direction in Figure 5.8. Both Lacheisserie and Klokhholm predict an infinite increase in the tip displacement with an increasing thickness ratio. The displacement predicted by Klokhholm's model is  $(1 - \nu)/(1 + \nu)$  times that of Lacheisserie's prediction. Both Guerrero's model and MPPM predict that the magnitude of normalized tip displacement increases initially with an increase in the thickness ratio and reaches a maximum when the strain due to bending is maximum. Further increase in  $t_r$  decreases  $\Delta$  as the unimorph extends freely at increasingly higher  $t_r$ .

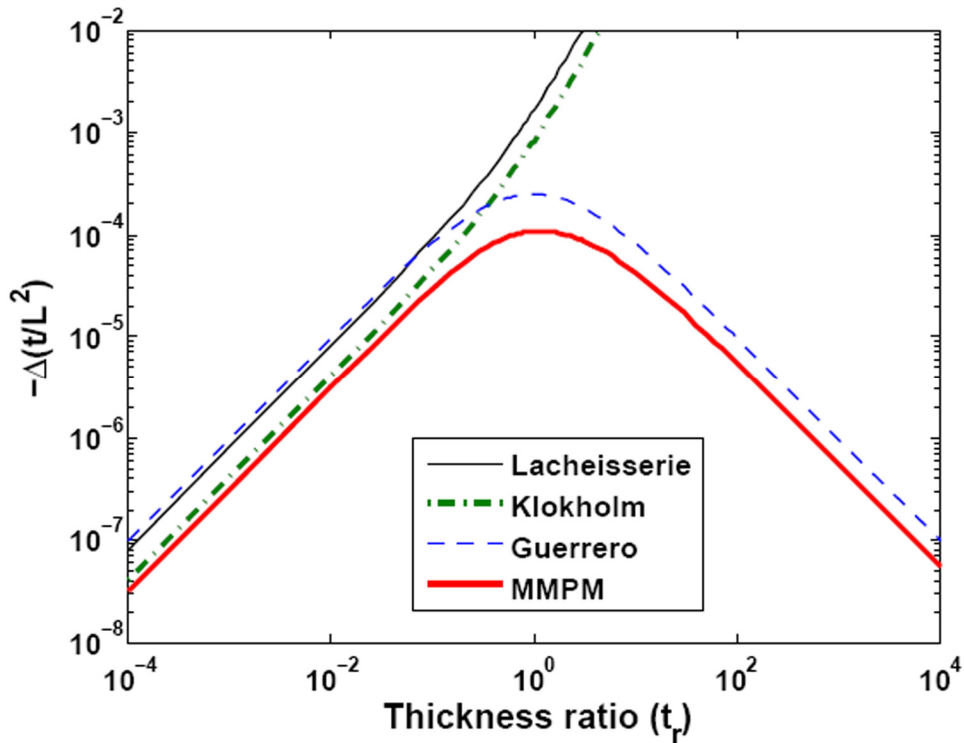


**Figure 5.8. Normalized out-of-plane tip displacement ( $\Delta t/L^2$ ) vs. thickness ratio ( $t_r$ ) of a cantilevered Galfenol-Aluminum unimorph obtained at an applied magnetic field ( $H_{app} = 65$  kA/m). The Galfenol layer was assigned an  $N_d = 0.035$ .**

**Table 5.3. Comparison of normalized tip displacement of cantilevered Galfenol-Aluminum unimorph as predicted by models proposed by Lacheisserie [181], Klokhholm [180], Guerrero [184] and the MMPM.**

<b><math>t_r</math></b>	<b>0.0001</b>	<b>0.01</b>	<b>1</b>	<b>100</b>	<b>10000</b>
<b>Lacheisserie</b>	$8.17 \times 10^{-8}$	$8.25 \times 10^{-6}$	$16 \times 10^{-4}$	8.25	$8.17 \times 10^4$
<b>Klokhholm</b>	$4.12 \times 10^{-8}$	$4.16 \times 10^{-6}$	$8.23 \times 10^{-4}$	4.16	$4.12 \times 10^4$
<b>Guerrero</b>	$9.95 \times 10^{-8}$	$9.76 \times 10^{-6}$	$2.48 \times 10^{-4}$	$9.65 \times 10^{-6}$	$9.84 \times 10^{-8}$
<b>MMPM</b>	$3.20 \times 10^{-8}$	$3.17 \times 10^{-6}$	$1.08 \times 10^{-4}$	$5.48 \times 10^{-6}$	$5.65 \times 10^{-8}$

Table 5.3 lists the values of the normalized tip displacement at certain thickness ratios as predicted by the earlier models and compares them with the values predicted by MMPM at the same thickness ratios. For the purpose of comparison, same material properties and saturation magnetostriction value for Galfenol were used in all the models. The results of MMPM were evaluated at  $H_{app} = 65$  kA/m which is sufficient to saturate Galfenol as evident from the experimental results shown in Chapter 4. Guerrero's model and MMPM predict similar tip displacement only at high thickness ratio when the stress developed in the Galfenol patch is negligible and does not affect the magnetostriction. If the stress developed in the Galfenol patch is significant, as in the cases with low  $t_r$ , and induces anisotropy so as to oppose the magnetic field-induced anisotropy, the magnetostriction will change as a function of the stress developed in Galfenol which in turn will affect the tip displacement and the stress developed in the Galfenol patch. Since the recursive scheme explained in Section 5.2.5 takes care of this coupled behavior, the MMPM

provides a more flexible and accurate framework for modeling the response of magnetostrictive composites at any magnetic field and thickness ratio.

### 5.3.2. Effect of actuating magnetic field and pre-load

In order to study the effect of magnetic field and axial pre-load, a unimorph structure of thickness ( $t = 3.7$  mm) having single crystal Galfenol ( $\text{Fe}_{82}\text{Ga}_{18}$ ) attached to Aluminum such that  $t_r = 0.5$  was used for simulation purposes. The formulation is independent of the actual length and width of the structure as the values of stiffness and forces were defined for unit length and width. Since it is easy to measure the strain in a laminated structure by placing strain gages on the free surfaces of the structure, which in turn can be used to calculate the curvature and tip displacement of the structure, the results presented here refer to the values calculated at the free surfaces of the Galfenol and Aluminum layers. For all cases, the Galfenol layer was assigned a demagnetization factor of 0.035 along the  $x$ -direction.

The strains ( $\varepsilon_x$  and  $\varepsilon_y$ ) and stresses ( $\sigma_x$  and  $\sigma_y$ ) in Galfenol and Aluminum along the  $x$  and  $y$ -directions as functions of the applied magnetic field along the  $x$ -direction are shown in Figures 5.9 and 5.10 respectively. These figures show the results when there are no external mechanical forces or moments acting on the structure. As Galfenol exhibits positive magnetostriction, a magnetic field applied along the  $x$ -direction extends the free surface of the Galfenol layer along the  $x$ -direction but the material contracts along the  $y$ -direction. An increasing magnitude of strain is observed along both the  $x$  and  $y$ -directions on the free surface of the Galfenol layer with increasing magnetic field until the material saturates at high fields.

The maximum change in strain ( $\Delta\varepsilon_x$ ) in Galfenol due to applied magnetic field was found to be 208  $\mu\varepsilon$ . On actuation, the structure shows a negative curvature ( $\kappa_x$ ) along the  $x$ -axis and positive curvature ( $\kappa_y$ ) along the  $y$ -axis which make both the strain and stress in Aluminum compressive along the  $x$ -direction and tensile along the  $y$ -direction. In order to calculate the stress in the Galfenol layer, the free-strain ( $\lambda$ ) has to be subtracted from the total strain as indicated in Equation (5.18). Since the Galfenol layer is constrained by the Aluminum layer due to the bonding, the total strain on its free surface is less than the free strain. This leads to the development of a small compressive stress along the  $x$ -direction and small tensile stress along the  $y$ -direction on the free surface of Galfenol.

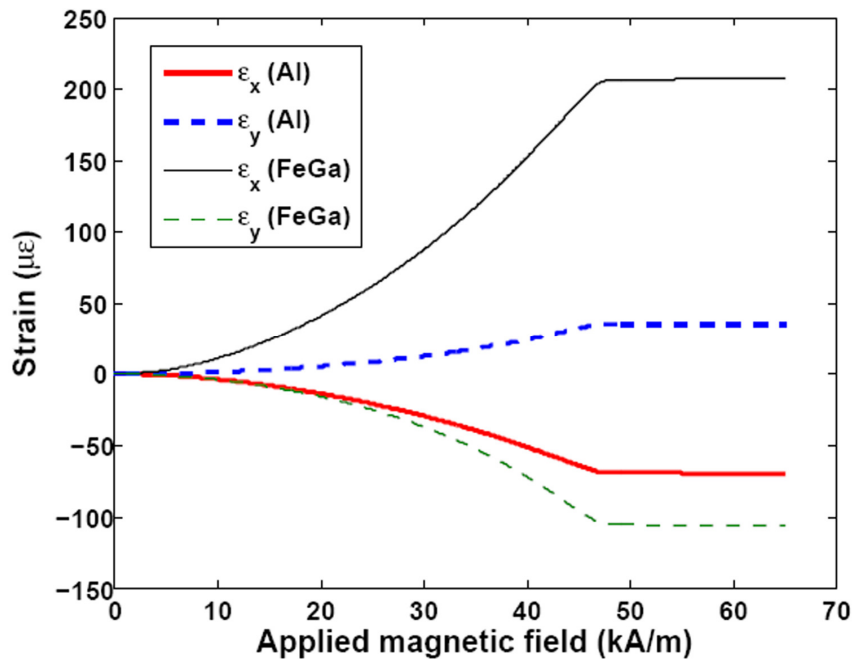


**Figure 5.9. Strains ( $\varepsilon_x$  and  $\varepsilon_y$ ) on the surfaces of Galfenol and Aluminum layers vs. applied magnetic field ( $H_x$ ) for  $N_{xt} = 0$ .**

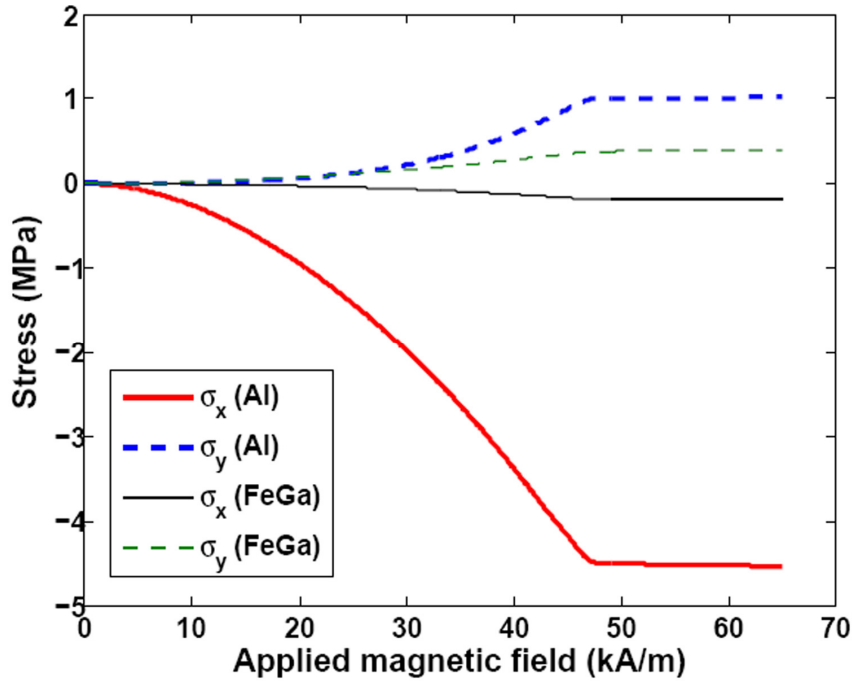


**Figure 5.10. Stresses ( $\sigma_x$  and  $\sigma_y$ ) on the surfaces of Galfenol and Aluminum layers vs. applied magnetic field ( $H_x$ ) for  $N_{xt} = 0$ .**

A compressive pre-stress applied to Galfenol along the same direction as the magnetic field is expected to provide an initial alignment to the magnetic moments perpendicular to the field direction and produce a corresponding decrease in initial length in this direction due to the stress-induced magnetoelastic strain in addition to the mechanical strain. In the presence of a magnetic field, the magnetic moments align themselves along the field direction recovering the pre-stress induced magnetostriction and thereby yielding a higher net actuation strain. A different scenario arises when a tensile pre-stress is applied to Galfenol along the same direction as the magnetic field. A tensile stress is expected to initially align the magnetic moments parallel to the field direction and produce a corresponding increase in initial length in this direction due to the stress-induced magnetostriction in addition to the mechanical strain. In the presence of a magnetic field the remaining

magnetic moments align themselves along the field direction thereby yielding a smaller actuation strain.

It is evident from Equation (5.18) that it is not possible to apply a constant pre-stress to the laminated structure but it is possible to apply a constant initial force per unit cross-section. Hence a simulation was run to find out the effect of constant initial force per unit cross-section on the Galfenol-Aluminum laminated structure. It was assumed that the structure was subjected to a constant initial force per unit cross-section ( $N_{xt}$ ) and the actuation response from the structure was obtained as the applied magnetic field was varied from 0 to 65 kA/m.

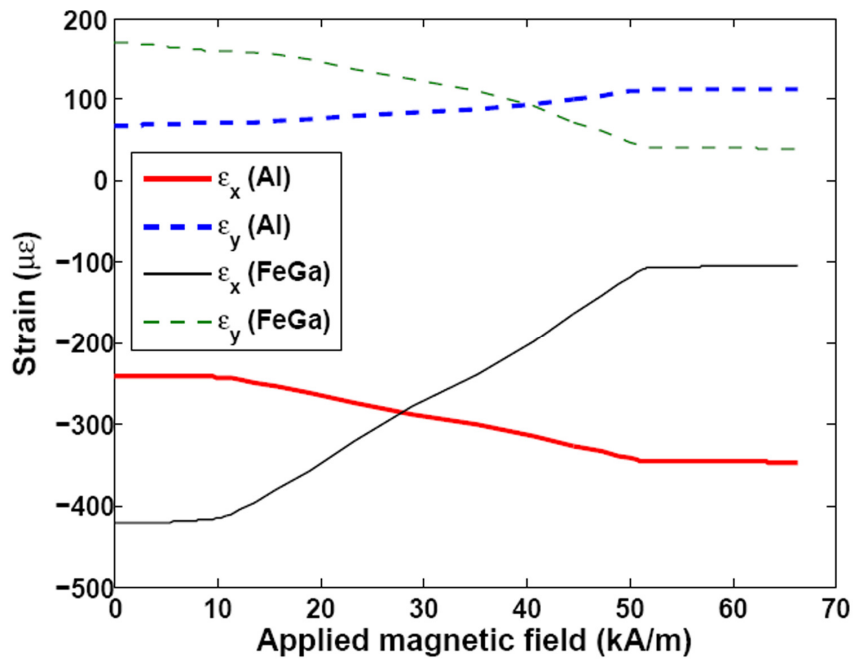


**Figure 5.11. Strains ( $\epsilon_x$  and  $\epsilon_y$ ) on the surfaces of Galfenol and Aluminum layers vs. applied magnetic field ( $H_x$ ) for  $N_{xt} = -20$  MPa.**

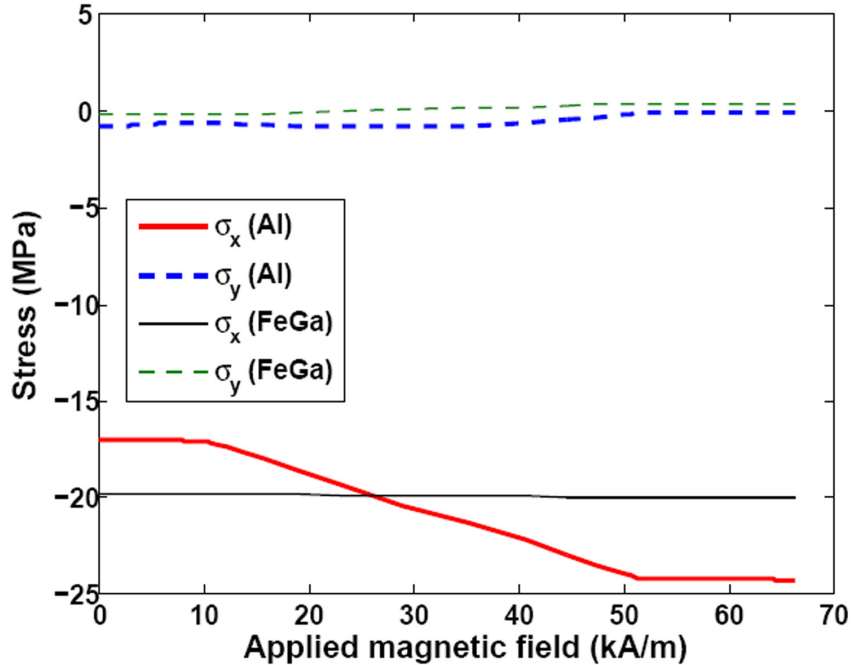


**Figure 5.12. Stresses ( $\sigma_x$  and  $\sigma_y$ ) on the surfaces of Galfenol and Aluminum layers vs. applied magnetic field ( $H_x$ ) for  $N_{xt} = -20$  MPa.**

The variations in strains ( $\varepsilon_x$  and  $\varepsilon_y$ ) and stresses ( $\sigma_x$  and  $\sigma_y$ ) on the free surfaces of Galfenol and Aluminum layers as functions of the applied magnetic field for an axial compressive initial force per unit cross-section of  $N_{xt} = -20$  MPa are shown in Figures 5.11 and 5.12 respectively. The compressive  $N_{xt}$  imparts an initial negative strain ( $\varepsilon_x$ ) and stress ( $\sigma_x$ ) in the structure which are different at the free surfaces of the two materials. If there were no extension-bending coupling in the structure, then  $N_{xt}$  would have produced the same pre-strain in both the materials. Additionally if the Young's modulus and Poisson's ratio of both the materials were the same then the initial stress would also have been the same.

The maximum change in strain ( $\Delta\varepsilon_x$ ) in Galfenol due to applied magnetic field increased to  $318 \mu\varepsilon$  thereby increasing the strain in the Aluminum surface. The simulation supported the idea that higher actuation strain can be obtained by

introducing a compressive initial force per unit cross-section. It is also evident from Figure 5.12 that the change in  $\sigma_x$  and  $\sigma_y$  in Galfenol and  $\sigma_y$  in Aluminum is insignificant compared to the change in  $\sigma_x$  in Aluminum due to actuation.

A simulation was also carried out to find the effect of a tensile initial force per unit cross-section of  $N_{xt} = +20$  MPa on the actuation response. The tensile pre-load imparts an initial positive strain ( $\epsilon_x$ ) and stress ( $\sigma_x$ ) in the structure which are different in the two materials due to the difference in the mechanical properties of Galfenol and Aluminum and the inherent extension-bending coupling in the structure. The maximum change in strain ( $\Delta\epsilon_x$ ) in Galfenol reduced to  $1.33 \mu\epsilon$  thereby reducing the strain in the Aluminum surface to almost zero. The simulation supported the idea that lower actuation strain is obtained by introducing a tensile initial force per unit cross-section. It was also found that application of  $+/-N_y$  and  $H_x$  was analogous to the application of  $-/+N_x$  and  $H_x$ . The effect of application of  $+/-M_x$  and  $-/+M_y$  were similar. The simulation effect of  $M_x$  will be shown in Section 5.3.5.

The shear strain ( $\gamma_{xy}$ ) and stress ( $\tau_{xy}$ ) in both Galfenol and Aluminum were zero as  $\kappa_{xy} = 0$  for all the scenarios presented above due to the absence of any shear force or twisting moment acting on the structure and also because of the absence of any structural coupling in the unimorph between the extension/shear, bending/shear, extension/torsion and bending/torsion modes. The lack of these structural couplings in the unimorph also resulted in no effect on strains and stresses along the  $x$  and  $y$ -directions due to application of  $N_{xy}$  and  $H_x$ . The effect of  $M_{xy}$  is analogous that of  $N_{xy}$  for strains and stresses along the  $x$  and  $y$ -directions.

Model simulations showed that shear strain could be created by applying a combination of  $H_x$  and  $H_y$  even in the absence of any external mechanical forces. The shear strain is produced due to the existence of a non-zero  $\lambda_{xy}$  under the influence of two mutually perpendicular magnetic fields or a magnetic field directed in a way such that it has two non-zero mutually perpendicular components. Figures 5.13 and 5.14 show the shear strains on the free surfaces of Galfenol and Aluminum layers respectively. The values of magnetic field shown in Figures 5.13 and 5.14 are the internal magnetic fields. For a given  $H_y$ , the maximum shear strain is obtained when  $H_x = H_y$ . Since the value of shear strain depends on  $N_{xy}$  and  $M_{xy}$ , the maximum shear strain that can be obtained is limited by the magnetostriction of the Galfenol layer and the properties of the laminate.

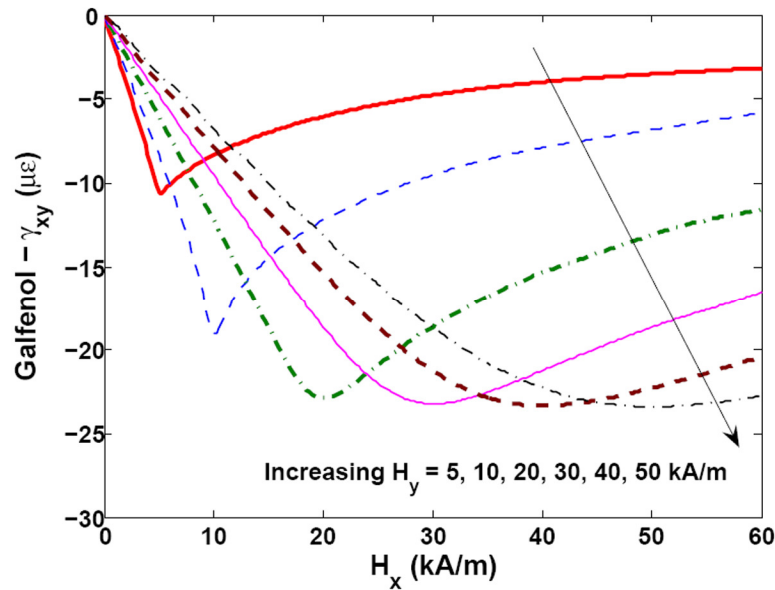


**Figure 5.13. Shear strain ( $\gamma_{xy}$ ) on Galfenol surface vs. internal magnetic field along the  $x$ -direction ( $H_x$ ) at different values of internal magnetic field along the  $y$ -direction  $H_y$ .**

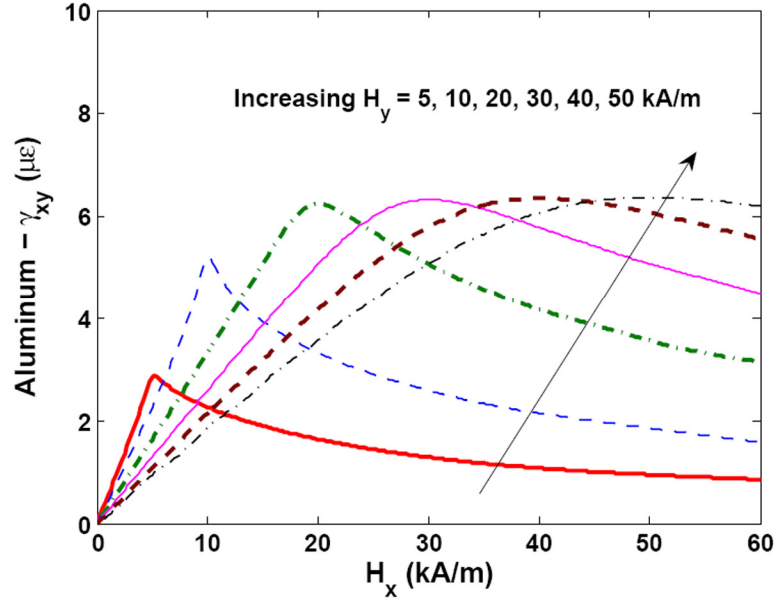


**Figure 5.14. Shear strain ( $\gamma_{xy}$ ) on Aluminum surface vs. internal magnetic field along the  $x$ -direction ( $H_x$ ) at different values of internal magnetic field along the  $y$ -direction  $H_y$ .**

A dimensionless parameter, “percentage strain transfer” defined by Equation (5.22) was used to analyze the actuation behavior as a function of different thickness ratios ( $t_r$ ) and stiffness ratios ( $Q_r$ ) of the laminated structure.

$$ST_i(t_r, Q_r) = \frac{\Delta \varepsilon_i(\text{free surface of passive layer})}{\Delta \varepsilon_i(\text{free surface of active layer})} \times 100 \quad (5.22)$$

In Equation (5.22),  $Q_r$  is the ratio of the stiffness  $[E/(1-\nu^2)]$  of the active layer to that of the passive layer and  $\Delta \varepsilon_i$  is the change in strain measured along the direction  $i$  in the material due to a magnetic field.

Table 5.4 shows the maximum change in strain along the  $x$  and  $y$ -directions in both Galfenol (Fe-Ga) and Aluminum (Al) under different conditions of initial force per unit cross-section and the corresponding  $ST_i$ . The initial  $\varepsilon_x$  and  $\varepsilon_y$  denote the pre-

strain in the material only due to the initial force at zero magnetic field. The change in strain is calculated between applied magnetic fields of  $H_x = 0$  and  $H_x = 65$  kA/m.

**Table 5.4. Induced strain ( $\Delta\varepsilon$ ) and percentage strain transfer (ST) from Galfenol to Aluminum ( $t_r = 0.5$ ,  $Q_r = 1.05$ ) under different  $N_{xt}$ .**

	Initial $\varepsilon_x$ ( $\mu\varepsilon$ )	$\Delta\varepsilon_x$ ( $\mu\varepsilon$ )	ST <sub>x</sub>	Initial $\varepsilon_y$ ( $\mu\varepsilon$ )	$\Delta\varepsilon_y$ ( $\mu\varepsilon$ )	ST <sub>y</sub>
$N_{xt} = 0$						
Fe-Ga	0	208	-34	0	-106	-34
Al	0	-70		0	36	
$N_{xt} = -20$ MPa						
Fe-Ga	-422	318	-34	171	-131	-34
Al	-240	-107		68	44	
$N_{xt} = +20$ MPa						
Fe-Ga	527	1.33	-34	-242	-0.64	-34
Al	205	-0.45		-44	0.22	

The simulation results showed that in general the strain variation with field follows the same trend in both the active and passive layers and the  $ST_i$  varies by less than 1 % with initial mechanical force and measurement direction. The data shown in Table 5.4 confirms the significant effect of axial initial force per unit cross-section on actuation strain in both the active and passive materials in a unimorph.

Table 5.5 shows the maximum change in stress ( $\Delta\sigma$ ) along the  $x$  and  $y$ -directions in both Aluminum and Galfenol under different conditions of initial force per unit cross-section acting on the laminated structure. The initial  $\sigma_x$  and  $\sigma_y$  denote the pre-stress on the free surfaces of the laminated structure only due to the initial

force at zero magnetic field. The change in stress is calculated between applied magnetic fields of  $H_x = 0$  and  $H_x = 65$  kA/m.

**Table 5.5. Actuation stresses in Galfenol and Aluminum ( $t_r = 0.5$ ,  $Q_r = 1.05$ ) under different initial  $N_{xt}$ .**

	Initial $\sigma_x$ (MPa)	$\Delta\sigma_x$ (MPa)	Initial $\sigma_y$ (MPa)	$\Delta\sigma_y$ (MPa)
$N_{xt} = 0$				
Fe-Ga	0	-0.18	0	0.39
Al	0	-4.53	0	1.02
$N_{xt} = -20$ MPa				
Fe-Ga	-20	-0.22	-0.25	0.59
Al	-17	-7.20	-0.85	0.72
$N_{xt} = 20$ MPa				
Fe-Ga	20	-0.001	0.45	0.003
Al	15	-0.03	1.83	0.005

It should be noted that the magnitude of change in stress ( $\Delta\sigma_x$  or  $\Delta\sigma_y$ ) is always larger in the passive layer than in the active layer. The large change in stress in the passive layer develops due to the actuation effect while the small change in stress in the Galfenol layer develops as it is constrained by the passive layer. In the absence of any constraint, the free strain in the Galfenol layer would not have produced any stress in it.

### 5.3.3. Effect of laminate thickness and stiffness

Based on the results shown in Section 5.3.2,  $ST_i$  was deemed as a suitable parameter to evaluate the performance of unimorph actuator as a function of the

thickness of the unimorph structure as well as the ratio of the thicknesses of the active and passive layers. Section 5.3.3 shows simulation results which were obtained by using passive layers of Aluminum ( $Q_r = 1.05$ ), Silicon ( $Q_r = 0.46$ ) and Alumina ( $Q_r = 0.14$ ) in the unimorph along with the Galfenol layer. For each combination of active and passive layers, the total thickness of the unimorph was varied from 0.1 to 100 mm and for each of these unimorph thicknesses,  $t_r$  was varied from  $10^{-4}$  to  $10^4$  in order to simulate structures of different thicknesses with very thick passive material and very thick active material respectively. Strain ( $\varepsilon_x$ ) and stress ( $\sigma_x$ ) on free surfaces of Galfenol and passive layers as well as the  $ST_x$  were calculated at an internal magnetic field  $H_x = 20$  kA/m and in the absence of any external mechanical pre-loads.

The results showed that the strains, stresses and % strain transfer are functions of the mechanical properties of the passive and active layers and  $t_r$  but they are independent of the total thickness of the structure. On actuation, the unimorph exhibits both mid-plane strains and curvatures. Along any direction ( $x$  or  $y$ ), the curvature is proportional to the inverse of the total thickness and the mid-plane strain is independent of the total thickness. The distance ( $z$ ) from the mid-plane of the structure to the plane where the strains and stresses are being calculated can be expressed as a fraction of the total thickness of the structure. Hence the strains and stresses at the free surfaces of the structure calculated using Equations (5.17) and (5.18), and the  $ST_i$  are independent of the total thickness of the structure.

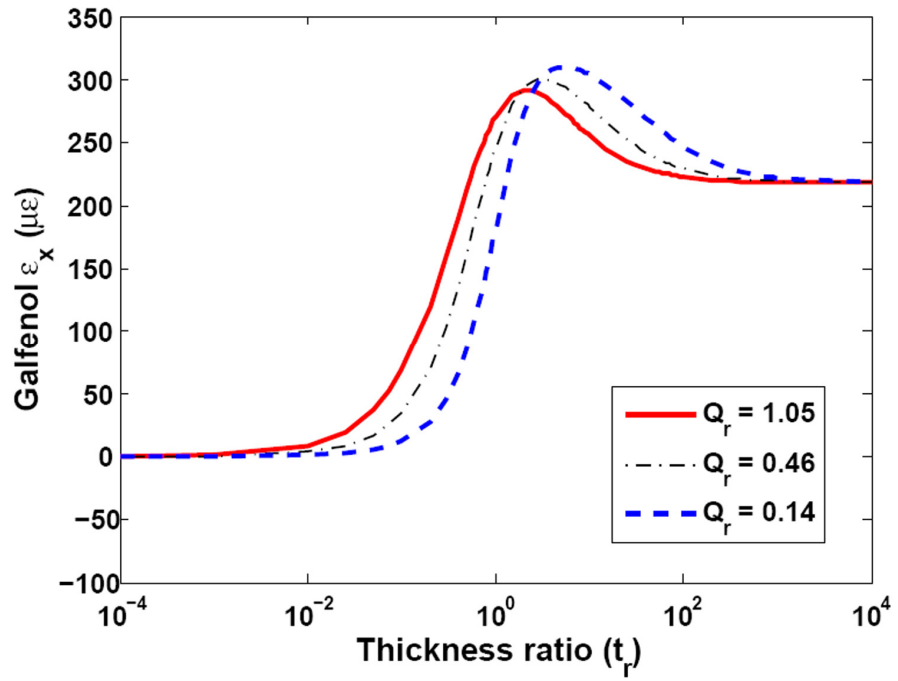


Figure 5.15. Effect of thickness ratio ( $t_r$ ) on the strain ( $\varepsilon_x$ ) on Galfenol surface for different stiffness ratios ( $Q_r$ ).

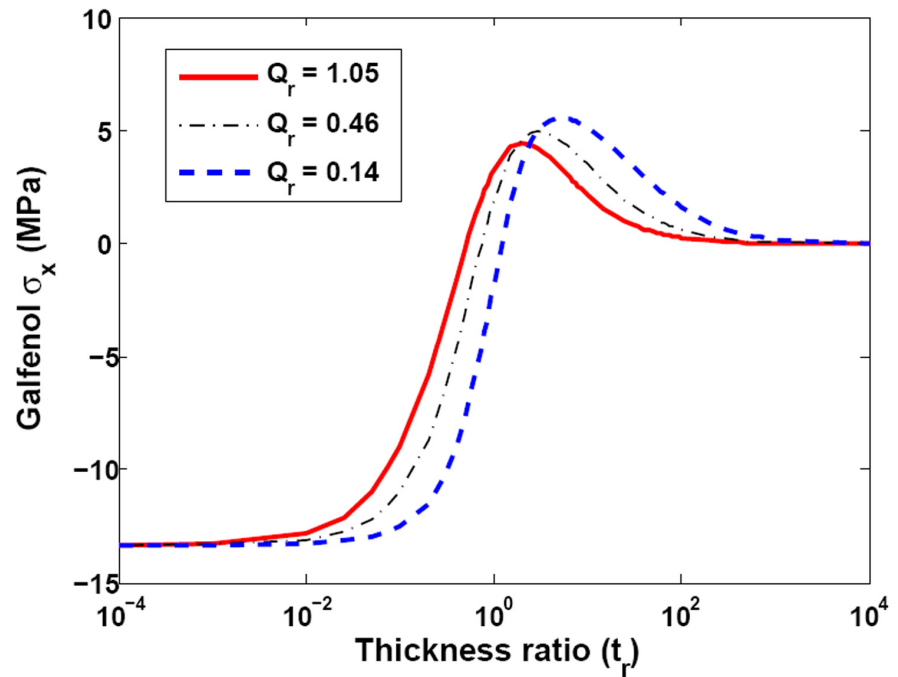


Figure 5.16. Effect of thickness ratio ( $t_r$ ) on the stress ( $\sigma_x$ ) on Galfenol surface for different stiffness ratios ( $Q_r$ ).

Figure 5.15 shows the strain along the  $x$ -direction ( $\varepsilon_x$ ) on the free surface of the Galfenol layer as a function of the thickness ratio ( $t_r$ ) for different stiffness ratios. The strain is always tensile, peaking at some  $t_r = t_{rc}$  for each stiffness ratio, and dropping slightly for higher values of  $t_r$  to approach a constant value. For  $t_r < t_{rc}$ , the strain decreases rapidly with decreasing  $t_r$ . This behavior is related to the constraint imposed by the thick passive layer on the thin active layer. For  $t_r > t_{rc}$ , the strain on free surface of the Galfenol layer is higher for stiffer passive layers. At high  $t_r$ , the strain approaches the free strain of the active material. As shown in Figure 5.15, the strain at  $t_r = t_{rc}$  is higher than the free strain of the active material, owing to the superposition of maximum bending strain with extensional strain. The behavior of the active layer under actuation induced bending is counter-intuitive when contrasted with that of pure mechanical bending.

Figure 5.16 shows the stress ( $\sigma_x$ ) on the free surface of the Galfenol layer as a function of the thickness ratio for different stiffness ratios. The stress is compressive at low  $t_r$  due to the constraint imposed on the thin active layer by a thicker passive layer. On increasing  $t_r$ , the stress becomes zero at a point when the summation of bending and extensional strain in the Galfenol layer equals its free strain. Beyond this value of  $t_r$ , the stress becomes tensile and keeps increasing till it peaks at  $t_r = t_{rc}$ . For  $t_r > t_{rc}$ , the stress decreases on increasing  $t_r$  and approaches zero as the active material strains freely at high  $t_r$ .

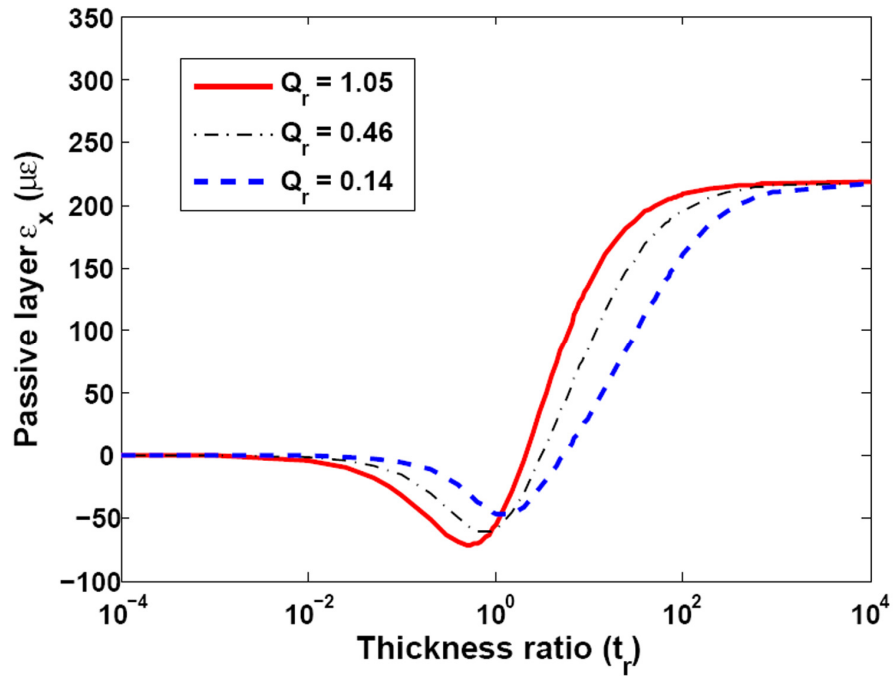


Figure 5.17. Effect of thickness ratio ( $t_r$ ) on the strain ( $\epsilon_x$ ) on passive layer surface for different stiffness ratios ( $Q_r$ ).

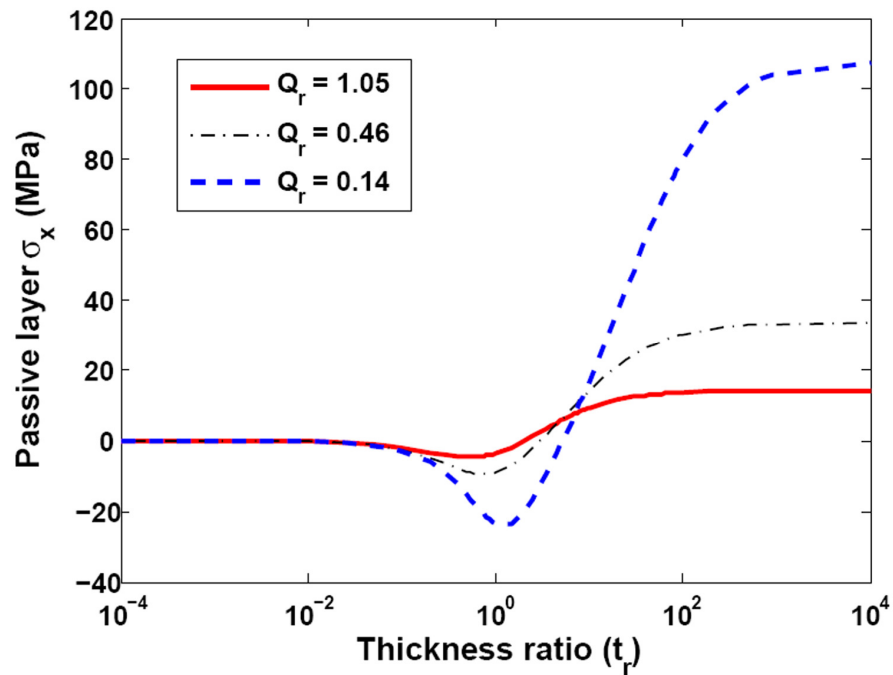


Figure 5.18. Effect of thickness ratio ( $t_r$ ) on the stress ( $\sigma_x$ ) on passive layer surface for different stiffness ratios ( $Q_r$ ).

Figures 5.17 and 5.18 show the strain ( $\varepsilon_x$ ) and stress ( $\sigma_x$ ) respectively on the free surface of the different passive layers used in the unimorph as a function of the thickness ratio. The strain and stress are compressive for  $t_r < t_{rc}$  and tensile for  $t_r > t_{rc}$ . The strain and stress attain the maximum magnitude under compression at a  $t_r$  which corresponds to the state of zero stress on the free surface of the Galfenol layer as shown in Figure 5.16. Below this value of  $t_r$ , the magnitude of strain and stress decreases with decreasing  $t_r$  and approaches zero at very small  $t_r$  due to very low actuation force. For  $t_r > t_{rc}$ , as the passive layer becomes thinner and offers less resistance to deformation due to actuation, the strain on its free surface approaches to the free strain of the active material and hence the strains in the different passive layers become independent of  $Q_r$ . The stress always depends on  $Q_r$  and hence for a given value of strain, a stiffer passive layer develops a greater stress.

A visual comparison of Figures 5.15 and 5.17 shows that the strains on the opposite free surfaces of the unimorph can be tensile under induced-strain actuation unlike in pure mechanical bending where the strains on the opposite surfaces of a beam/plate are of opposite nature. Comparison of Figures 5.16 and 5.18 shows that the stress-states on the free surfaces of the unimorph can be both tensile or compressive unlike in pure mechanical bending.

The physical significance of the parameter  $ST_i$  is evident from Figure 5.19 which shows  $ST_x$  as a function of  $t_r$  for the Galfenol layer attached to different passive layers. A negative  $ST_i$  indicates that the strain on opposite surfaces of the structure are of opposite signs and hence bending is the predominant mode of deformation while a positive  $ST_i$  indicates that the strain on opposite surfaces of the structure are of similar

nature (can be both tensile or compressive) and hence the deformation is dominated by extension or contraction.

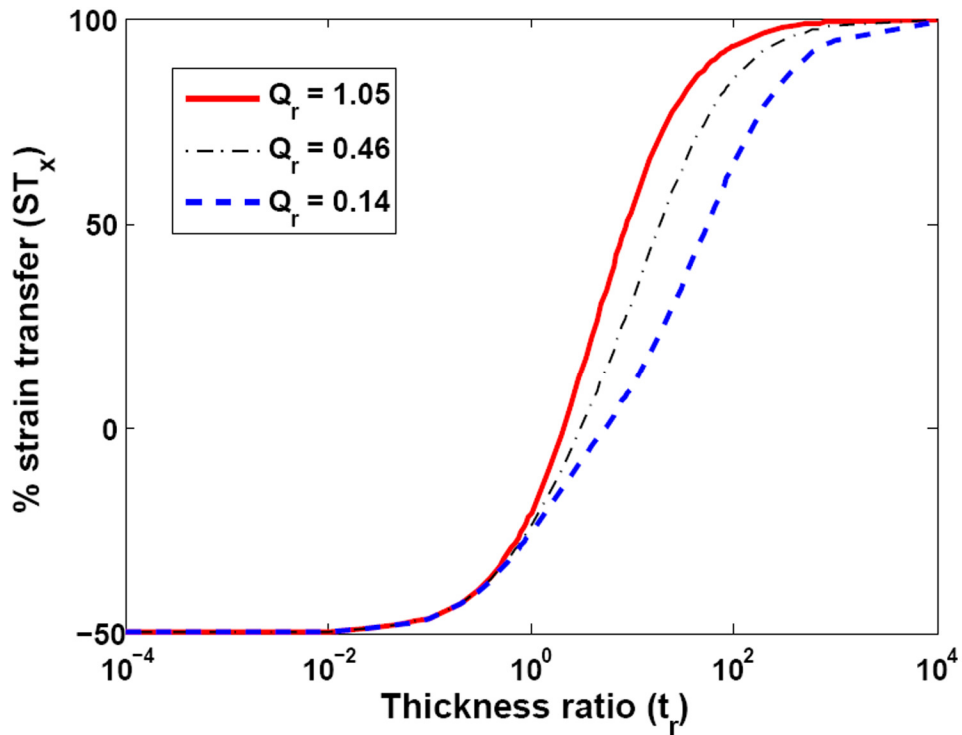


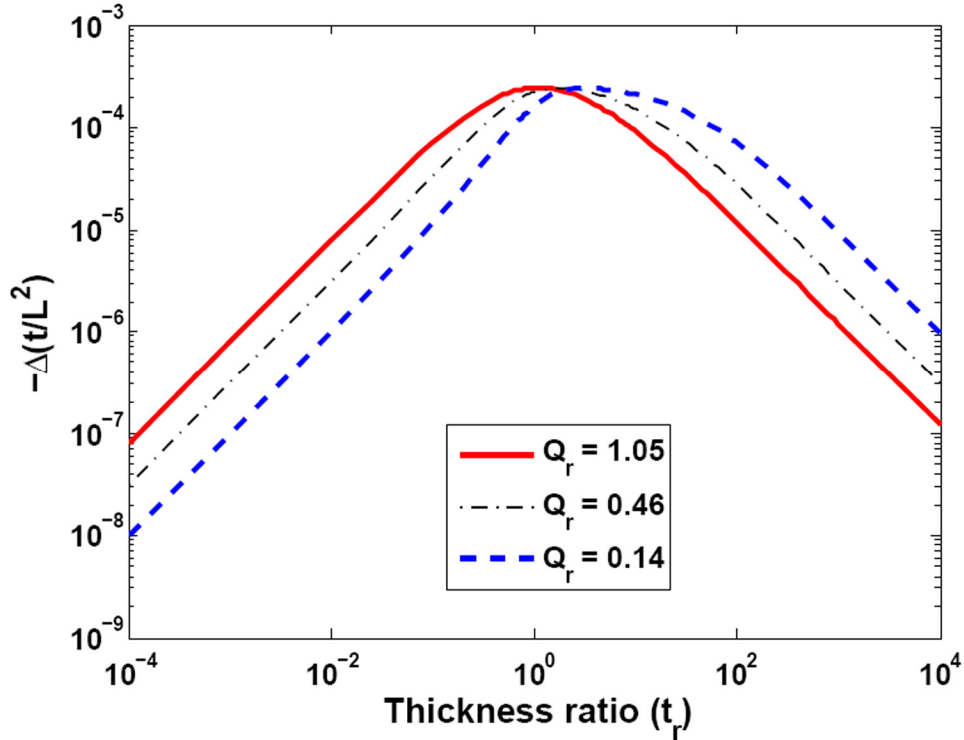
**Figure 5.19.** Effect of thickness ratio ( $t_r$ ) on the % strain transfer ( $ST_x$ ) along the  $x$ -direction for different stiffness ratios ( $Q_r$ ).

A critical thickness ratio ( $t_{rc}$ ) can be defined to denote the situation when  $ST_i = 0$ . As  $t_r$  increases above  $t_{rc}$ , extension dominates the deformation of the structure. Figure 5.19 also shows the expected result that as  $t_r$  tends to infinity, the passive layer vanishes thereby exhibiting 100 % strain transfer due to pure extension. As  $t_r$  decreases below  $t_{rc}$ , bending starts to dominate the structural deformation. Although the theory formulated here shows that there will be no induced strain for  $t_r = 0$  as there will be no actuation, the theory also suggests that as the thickness of the active layer tends to zero (say in case of a thin film), the strain transferred from the free surface of the active layer to the free surface of the passive layer approaches -50 %.

It is interesting to note that for  $t_r < 0.5$ ,  $ST_x$  appears to be independent of  $Q_r$ . For small values of  $t_r$ , the active layer becomes thin enough such that its mechanical properties do not affect the stiffness of the composite structure and it merely provides a surface force on the passive layer. Under these conditions, the strain is both due to extension and bending and it can be assumed that there is no strain/stress gradient across the thickness of the active layer. It should be noted that the  $t_{rc}$  observed in Figure 5.19 is the same  $t_{rc}$  which corresponds to the maximum strain (Figure 5.15) and maximum stress (Figure 5.16) in the active layer.

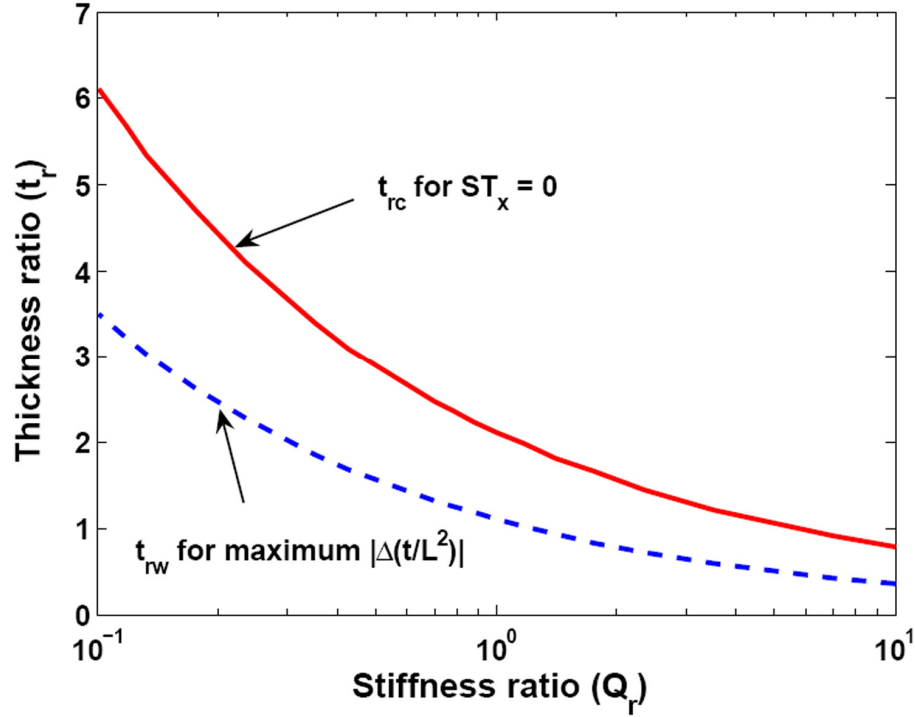
It should be noted that the maximum strain due to bending is different from the total strain which is due to the superposition of bending and extension. Since the out-of-plane tip displacement depends only on the component of strain due to bending, this necessitates the introduction of the new parameter  $t_{rw}$  to denote the thickness ratio for a given active/passive layer combination which produces the maximum tip displacement.

Figure 5.20 shows the normalized out-of-plane tip displacement of unimorph cantilevers with Galfenol attached on different passive layers. For all cases, it can be observed that a peak in the tip displacement occurs at some thickness ratio ( $t_r = t_{rw}$ ). For  $t_r < t_{rw}$ , the actuation moment ( $M_\lambda$ ) shown in Equation (5.16) decreases due to an effective decrease in active layer thickness thereby reducing the out-of-plane tip displacement. For  $t_r > t_{rw}$ , the actuation moment ( $M_\lambda$ ) decreases while increasing the extensional actuation force ( $N_\lambda$ ) shown in Equation (5.15) thereby extending the entire structure at high  $t_r$ .



**Figure 5.20. Effect of thickness ratio ( $t_r$ ) on the normalized out-of-plane tip displacement of a cantilevered unimorph beam for different stiffness ratios ( $Q_r$ ).**

The thickness ratio  $t_{rw}$  can be used to get an estimate of the optimum thickness ratio required to produce maximum tip displacement of the actuator for a given combination of active/passive layers. For the chosen parameters for Galfenol the magnitude of the maximum normalized tip displacement was found to be  $2.45 \times 10^{-4}$ . This value depends on the properties of the active layer only, so for a given active layer the same tip displacement can be obtained by varying the thickness for different passive layers. For the Galfenol active layer, the  $t_{rw}$  obtained from Figure 5.20 for Al, Si and  $\text{Al}_2\text{O}_3$  passive layers were 1.10, 1.77 and 3.14 respectively.



**Figure 5.21. Critical thickness ratio ( $t_{rc}$ ) and thickness ratio ( $t_{rw}$ ) for maximum tip displacement as a function of stiffness ratio ( $Q_r$ ).**

Figure 5.21 shows  $t_{rc}$  and  $t_{rw}$  as functions of the stiffness ratio ( $Q_r$ ) varying from 0.1 to 10 which covers a wide range of stiffness values for all practical purposes. Both  $t_{rc}$  and  $t_{rw}$  decreases roughly as the square root of  $Q_r$ .

The critical thickness ratio ( $t_{rc}$ ) denotes the condition when the stiffness of the passive layer is just enough to counter the actuation force so that there is neither any extension nor any bending at the free surface of the passive layer and hence  $ST_i = 0$ . As  $t_{rc}$  denotes the thickness ratio which produces the maximum stress on the free surface of the Galfenol patch, this configuration would also lead to maximum stress-induced change in magnetization in the Galfenol layer thereby producing the highest sensitivity to change in stress at a constant magnetic field. Hence  $t_{rc}$  is the most desirable configuration for sensing purposes.

For the Galfenol active layer, the  $t_{rc}$  obtained from Figure 5.19 for Al, Si and  $\text{Al}_2\text{O}_3$  substrates were 2.11, 3.13 and 5.38 respectively. It was observed that for a given active material (like Galfenol), the Young's modulus of the passive materials affects the  $t_{rc}$  more strongly than the Poisson's ratio. Hence for simulation purposes, Poisson's ratio was considered to be 0.33 for all cases shown in Figure 5.21. A change in  $\nu$  by 50 % for Si and 37.5 % for  $\text{Al}_2\text{O}_3$  produced a difference in  $t_{rc}$  by only 1 % and 0.6 % respectively.

#### 5.3.4. Effect of applied force and bias magnetic field

The results presented in this subsection were obtained from the simulation of a unimorph structure having a single crystal Galfenol ( $\text{Fe}_{82}\text{Ga}_{18}$ ) layer attached to an Aluminum layer such that  $t_r = 0.5$ . The results presented here refer to the values calculated at the free surface of the Galfenol patch.

Figure 5.22 shows the magnetic induction along the  $x$ -direction ( $B_x$ ) as a function of the axial force per unit cross-section applied along the  $x$ -axis ( $N_{xt}$ ) and the bias applied magnetic field ( $H_x$ ) in the same direction. A positive  $N_{xt}$  extends (and also causes bending due to coupling). The value of  $B_x$  at zero force indicates the induction due to bias field.

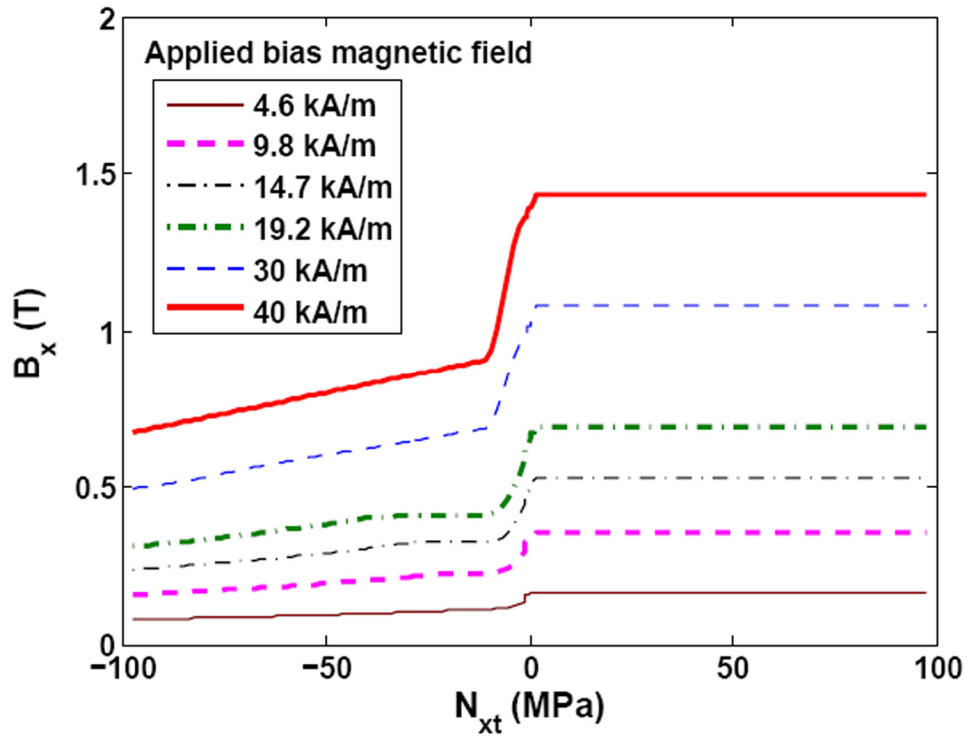


**Figure 5.22. Effect of axial force per unit cross-section along the  $x$ -direction ( $N_{xt}$ ) on the magnetic induction ( $B_x$ ) at different bias applied magnetic fields ( $H_x$ ).**

It was shown in Chapter 2, that if the internal magnetic field can be kept constant then the sensing range would increase with increasing bias field but the sensor operating region would shift towards compressive stresses. Note that in Figure 5.22 the internal magnetic field also changes when  $N_{xt}$  is changed at a given applied magnetic field. A positively increasing  $N_{xt}$  induces tensile stress in Galfenol thereby reducing the internal magnetic field while a negatively increasing  $N_{xt}$  increases the internal magnetic field. Therefore, the stress and internal magnetic field developed for a given  $N_{xt}$  and applied magnetic field produces opposing effects on the magnetic induction of Galfenol. As a result of this, the sensitivity is reduced compared to the material's sensitivity ( $d^*$ ) under all operating conditions.

This coupled behavior between stress and internal magnetic field also affects the operating range in a way contrary to that discussed in Chapter 2. Since a positively increasing  $N_{xt}$  increases the tensile stress but reduces the internal field, a higher operating range can be obtained in tension. Whereas a negatively increasing  $N_{xt}$  increases the compressive stress which reduces  $B_x$  but also increases internal field which contributes to increase in the value of  $B_x$ . As a result, the operating range in compression is reduced compared to a hypothetical case of constant internal magnetic field. In general, an increase in the bias applied magnetic field increases the operating range both along positive and negative  $N_{xt}$  and not only along negative  $N_{xt}$  as it would happen if the internal magnetic field were kept constant. The simulation results showed that in bending it is possible to use Galfenol as a sensor in tension even at higher bias magnetic field.

For all bias applied magnetic fields, a distinctively linear sensor operating region is observed at small values of tensile and compressive force but if the tensile/compressive force is increased beyond a critical value (depending on the bias magnetic field),  $B_x$  appears to saturate. This behavior can be explained by the following reasoning. The linear region denotes the operating conditions which favor the maximum rotation of magnetic moments due to small perturbations in stress or magnetic field as discussed in Chapter 2. Since tension collinear to the magnetic field favors alignment of magnetic moments along the field/stress direction, a small value of tension produces sufficient stress-induced anisotropy which along with the Zeeman energy is able to orient most magnetic moments along the field/stress direction. Note

that tension does not significantly increase the value of  $B_x$  as it also orients some magnetic moments towards  $180^\circ$  from the direction of bias field.

The saturation behavior under compression is significantly different. For any given bias magnetic field, the value of  $B_x$  under compression appears to approach zero induction, as the stress-induced anisotropy works against the Zeeman energy to orient the magnetic moments away from the field/stress direction. For a small bias field, it may be possible to achieve zero induction by applying a significant amount of compressive force. However, if the bias field is high enough to almost saturate the material, then the stress required to counteract the Zeeman energy may be higher than the strength of the material and hence under all practical conditions a residual  $B_x$  would exist in the material. This behavior would also lead to a “second” linear operating region in the unimorph sensor but one with a significantly reduced sensitivity.

#### 5.3.5. Comparison of experimental data and model prediction

In order to appreciate the usefulness of the MMPM model, it is imperative to compare the model predictions with certain baseline experimental results which can highlight the effectiveness of the model with respect to its prediction capability for different input parameter variation. This subsection will compare MMPM simulation results with the experimental results obtained from Chapter 4.

Table 5.6 lists the experimental values of strain on Galfenol and Aluminum surfaces, the calculated values of mid-plane strain and normalized tip displacement and the % strain transfer in the unimorphs with different thickness ratios used in the no-load actuator tests in Chapter 4. Corresponding to each experimental value, the

MMPM prediction is also listed. All values were measured or calculated at an applied magnetic field of 65 kA/m when the Galfenol layer was saturated. The model predictions are of the same order of magnitude as the experimental values and also exhibit similar trends in variations of strains and other output parameters for the variation in the input parameter of thickness ratio.

**Table 5.6. Comparison of MMPM prediction with experimental data obtained from the different unimorphs at  $H_{app} = 65$  kA/m from the no-load actuator tests. All values (except  $ST_x$ ) are shown in parts per million.**

$t_r$		$\epsilon^{FEGA}$	$\epsilon^{AL}$	$\epsilon^o$	$w_{TIP}(t/L^2)$	$ST_x$ (%)
0.25	Experiment	176	-57	59.5	116.5	-32
	MMPM	138	-57	40.5	97.5	-41
0.50	Experiment	285	-75	105	180	-26
	MMPM	206	-69	108	177	-34
1.00	Experiment	313	-55	129	184	-18
	MMPM	263	-54	104.5	158.5	-21
2.04	Experiment	331	15	173	158	5
	MMPM	284	-3	140.5	143.5	-1
4.04	Experiment	356	99	227.5	128.5	28
	MMPM	274	61.5	167.75	106.25	22

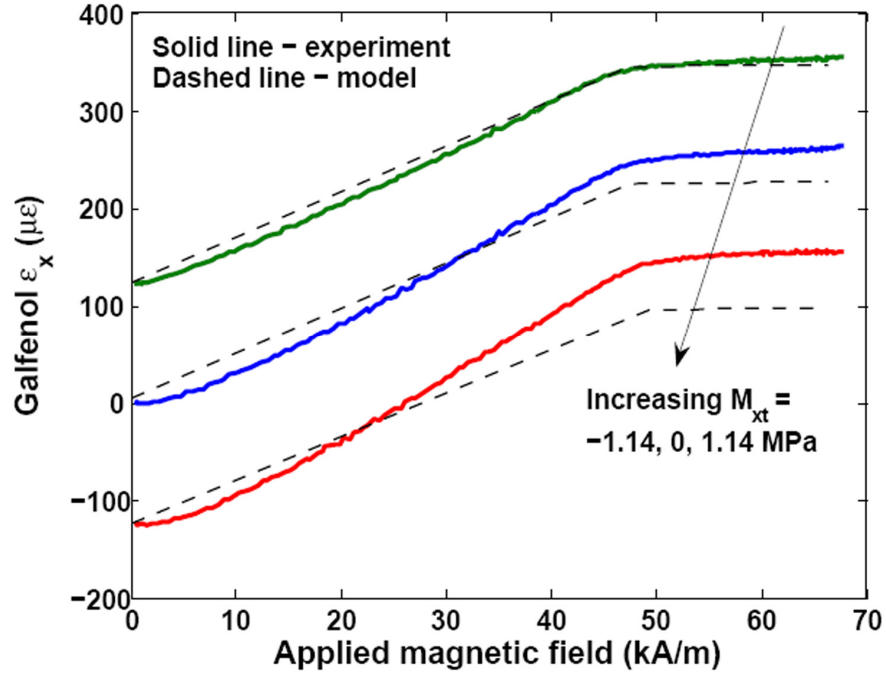


Figure 5.23. Comparison of MMPM prediction with experimental strain data obtained from Galfenol surface in the unimorph with  $t_r = 0.5$  at different  $M_{xt}$ .

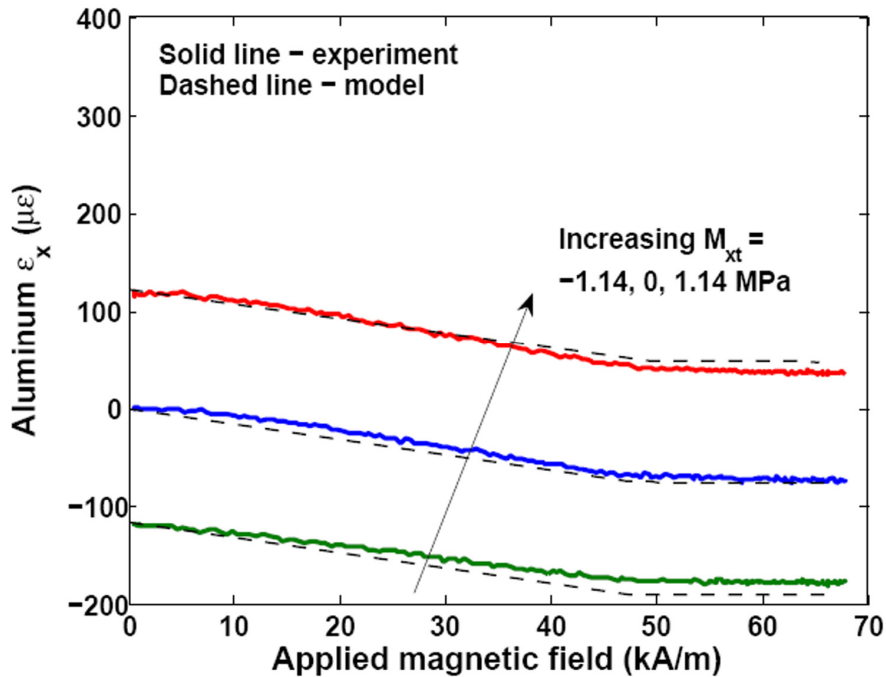
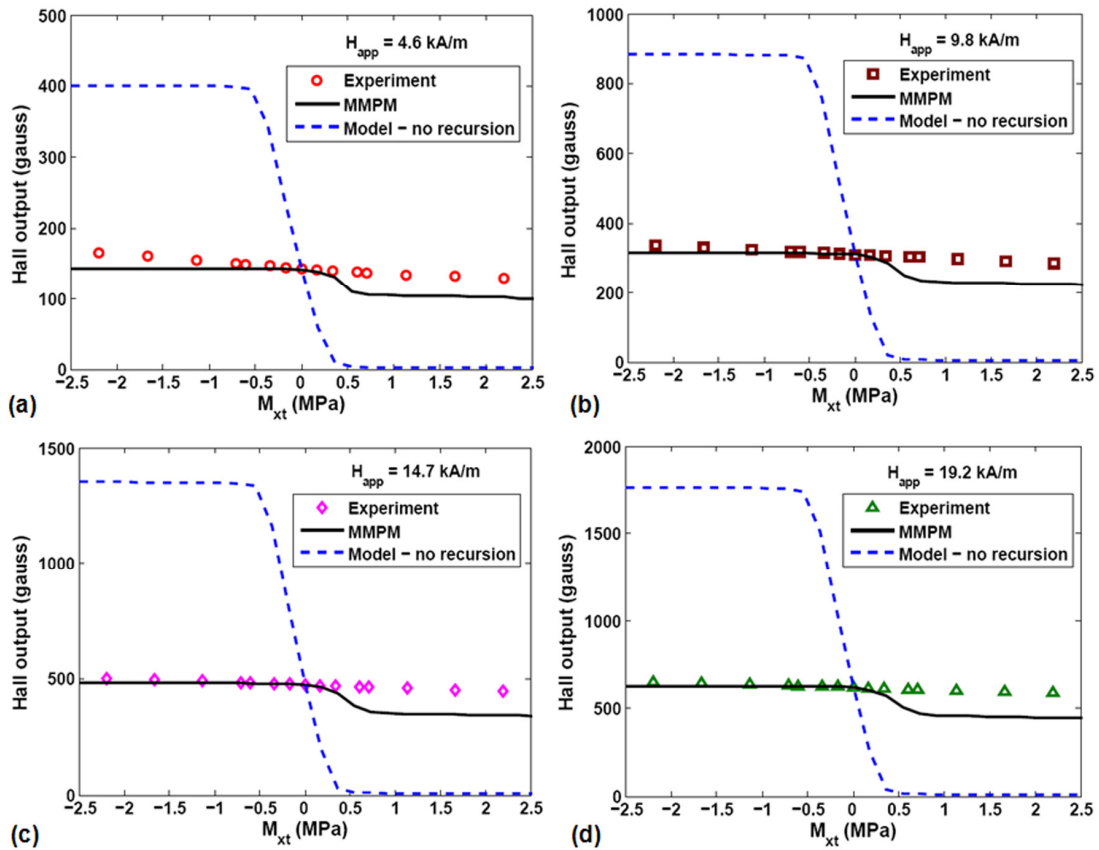


Figure 5.24. Comparison of MMPM prediction with experimental strain data obtained from Aluminum surface in the unimorph with  $t_r = 0.5$  at different  $M_{xt}$ .

Figures 5.23 and 5.24 compare the experimental values and MMPM prediction of variation in strain as a function of magnetic field on the Galfenol and Aluminum surfaces of the unimorph with  $t_r = 0.5$ . Results are shown for zero, negative and positive values of  $M_{xt}$  obtained from the pre-load actuator tests described in Chapter 4. It is evident that the MMPM is able to account for variation in both external mechanical forces (bending moment in this case) and magnetic fields.



**Figure 5.25. Experimental and predicted values of Hall sensor output vs.  $M_{xt}$  at bias applied magnetic fields of (a) 4.6 kA/m, (b) 9.8 kA/m, (c) 14.7 kA/m and (d) 19.2 kA/m in the unimorph with  $t_r = 0.5$ .**

Figure 5.25 compares the experimental values and model prediction of sensor characterization. The results are shown for the Galfenol-Aluminum unimorph with  $t_r$

= 0.5 and at bias applied magnetic fields of 4.6, 9.8, 14.7 and 19.2 kA/m. The MMPM prediction for each case is shown with the solid line. The dashed line shows the modeling results when no recursion was performed, which is similar to prior magnetostrictive sensor modeling approaches [185, 190]. Figure 5.25 clearly shows the benefit of the recursive approach used in MMPM without which the error is nearly 300 % for all cases shown here.

The main challenge in modeling the sensor results was due to the fact that the magnetic field in Galfenol close to the Hall sensor was significantly different from the applied magnetic field at the center of the Galfenol layer along the solenoid axis. Moreover the Hall sensor has a finite surface out of which some area was bonded to the side (i.e.) along the thickness of the Galfenol layer whereas the rest of the surface of the Hall sensor was exposed to air. Hence the experimental data recorded by the Hall sensor is an average of the  $x$ -component of the magnetic flux emanating from the cross-section of Galfenol as well as the flux in air adjacent to the Hall sensor surface. An accurate modeling of such a scenario requires 3D tools. However, Figure 5.25 shows that the MMPM solution which is based on the  $B_x$  calculated at the free surface of Galfenol is at the most 25 % different from the experimental values. In order to account for the spatial variation in magnetic field, the MMPM used values of applied magnetic field which produced the experimental  $B_x$  at  $M_{xt} = 0$ . Since the “no recursion” model cannot use an applied magnetic field as input, appropriate values of internal magnetic field was used such that the bias induction at  $M_{xt} = 0$  matched with the experimental values.

The difference between experimental values and model predictions for all the cases shown above can be attributed to the following causes. Firstly, the experimental values are affected by the bond layer between the Galfenol and Aluminum layer which is not modeled in the MMPM. The effect of bond layer can be significant especially when the Aluminum layer thickness becomes comparable to the bond layer thickness such as for  $t_r = 2.04$  and  $4.04$ . It should be noted that the experimental strain values are average values measured over the area of the strain gage whereas the model values are calculated for a point. Also, the structural component of MMPM (i.e. CLPT) is inherently a 2D model which is less stiff than a 3D structural model. This may affect the results for thick structures such as the ones with  $t_r = 0.25$  and  $0.50$ .

Furthermore, the internal magnetic field calculated by the lumped parameter magnetic model is also a point estimate. Although this should not contribute to a significant error in modeling the actuation behavior if the Galfenol layer is saturated, it is possible though that under experimental conditions, some areas might not have been fully saturated due to spatial variation magnetic field. However, if the spatial variation in magnetic quantities is not accounted for, it may lead to significant error in modeling the sensing behavior. The extent of error would depend on the magnetic circuit and the experimental method of measurement of magnetic quantities.

The maximum error contribution is due the energy-based material constitutive model. As shown in Chapter 2 that although this model is capable of predicting the non-linear magnetomechanical behavior of magnetostrictive materials, the prediction is of a best-fit nature and does not coincide perfectly with experimental behavior at all

operating conditions. Hence the predicted values using this constitutive model are significantly affected by this error. Also note that an error introduced in the first step of recursion due to the values predicted by the constitutive model would also lead to subsequent erroneous predictions of stress, strain and magnetic field by the structural and magnetic models.

#### 5.4. Summary and conclusions

In this chapter a generalized modeling approach for magnetostrictive devices was described. Based on this approach, a magnetomechanical plate model (MMPM) was developed by combining a lumped parameter magnetic model, the classical laminated plate theory and an energy-based non-linear constitutive magnetostrictive model using a recursive algorithm.

The MMPM was used to simulate the quasi-static strain response of Galfenol-based unimorph actuators and the quasi-static magnetic induction response of Galfenol-based unimorph sensors. The effects of applied magnetic field, axial pre-load, active/passive layer thickness ratio and passive layer mechanical properties on the strains and stresses on the free surfaces of the unimorph actuators were studied. The effects of bias applied magnetic fields and the nature of loading on the magnetic induction response of unimorph sensors were also studied. The predictions reflected the non-linear magnetomechanical response as well as the structural and magnetic coupling in the unimorph.

A non-dimensional parameter  $ST_i$  (percentage strain transfer) was introduced to explain the behavior of the unimorph actuators in extension and bending dominated regimes and a critical thickness ratio ( $t_{rc}$ ) was defined to demarcate these two

regimes. It was deduced that  $t_{rc}$  also corresponded to the optimal thickness ratio for maximum sensitivity in a unimorph sensor.

Similarly, a condition for obtaining maximum out-of-plane tip displacement was also obtained. The out-of-plane displacements of cantilevered unimorph beams normalized with respect to the thickness and length of the unimorphs were calculated as function of magnetic field, thickness ratio and stiffness ratio. It was shown that for any active/passive layer combination, a particular thickness ratio ( $t_{rw}$ ) which produces the maximum curvature in the structure would produce the maximum tip displacement.

This model presents a significant improvement over other existing models as it accounts for the effect of stress developed in the magnetostrictive layer under its own actuation effect and recalculates the magnetostriction as a function of the magnetic field as well as the stress in the magnetostrictive patch. The effect of stress on the internal magnetic field for a given applied magnetic field is also implemented by considering stress and magnetic field-dependent permeability in Galfenol. The effect of shape anisotropy is implemented using a bulk demagnetization factor.

Existing models [183-185] which do not consider the coupling between stress and internal magnetic field in Galfenol would either over-predict or under-predict the actuation forces and moments depending on the internal magnetic field and stress developed in the Galfenol layer. It was shown that other models [180-182] which predict tip displacement of magnetostrictive unimorph are only suitable for thin films and they largely over-predict at thickness ratios above 0.05.

The model simulations of unimorph sensor showed that the sensitivity, operating range and linearity of a unimorph sensor can be tuned by varying the bias applied magnetic field. The trends were explained using energy principles.

Finally, the MPPM was used to simulate representative experimental cases presented earlier in Chapter 4. The model predictions showed good correlation with the experimental results. Possible reasons for difference between model predictions and experimental values were also discussed.

The generalized modeling approach presented in this chapter is not only restricted to modeling of magnetostrictive devices but can also be used for other smart materials. For example, a piezoelectric device can use a combination of a structural model, an electrostatic or electrodynamic model and an appropriate non-linear electromechanical constitutive model. The key difference of this modeling approach with other models lie in the recursive technique used in the algorithm which can account for bi-directional coupling effects of one input parameter (stress) on other input parameters (magnetic or electric field) in the device. This generalized approach is expected to be helpful in modeling active vibration control, morphing structures, structural health monitoring devices and energy harvesting devices.

## Chapter 6: Conclusions

In conclusions, a summary of the research carried out as part of this dissertation is presented. The original contributions of this dissertation and their significance are stated and suggestions for future work to expand or improve upon this research are made.

### 6.1. Summary of research

Prior work on high performance rare-earth magnetostrictive materials such as Terfenol-D had focused on material characterization in axial mode because these materials could not be used in bending due to their brittleness. Although bending characterization has been performed on amorphous magnetostrictive alloys, a comprehensive literature survey showed that a lack of consistency in experimental design and terminology and limitation in physical understanding of magnetomechanical coupled mechanics requires further in-depth research in this area. Galfenol was considered as a suitable active material because of its unique combination of magnetostrictive and mechanical properties which could be utilized in bending applications.

The main objectives of this dissertation were to understand the effect of operating conditions on the actuator and sensor performance of magnetostrictive Galfenol alloys and to use this information for further studies and understanding of the actuation and sensing behavior of Galfenol in bending mode.

Chapter 2 described the use of well-established material characterization and non-linear modeling techniques in axial mode to study the effect of stress, magnetic

field and alloy composition on figures of merit such as energy density, magnetomechanical coupling factor and sensing gage factor. Results showed that maximum energy density could be obtained at magnetic saturation under the simultaneous influence of a compressive stress collinear to magnetic field, which is sufficient to align all the magnetic moments in the material normal to the stress direction in the absence of magnetic field.

The maximum coupling factor and sensing gage factor was observed at small values of magnetic fields and compressive stresses. It was deduced from the spatial energy distribution in this range of stress/magnetic field that a peak in the magnetomechanical transduction takes place at such operating conditions when a small perturbation in either magnetic field or stress can lead to the reorientation of a large number of magnetic moments.

The experimental work in Chapter 2 provided information consistent with prior work describing material behavior under compressive stresses. Using the model parameters obtained from these experiments, the behavior of the material under tensile stresses could be extrapolated. The understanding of material behavior under both tension and compression and at small as well as relatively large (saturating) magnetic fields was extremely useful in understanding Galfenol's response under bending.

The information from this work also helped in determining alloy composition and operating conditions for further tests and aided in the design of the bending experiments described in Chapters 3 and 4. The experimental characterization also

provided the model parameters which were used in the energy-based constitutive model in Chapter 5.

Chapters 3 and 4 described experimental work involving bending characterization of Galfenol under the influence of magnetic field. Chapter 3 described the simplest bending scenario when only a Galfenol member was subjected to bending while Chapter 4 described experimental characterization of laminated Galfenol-Aluminum structures subjected to bending. The results from Chapter 3 highlighted the usefulness of Galfenol bending members in sensing applications. The results from Chapter 4 showed the interaction of Galfenol with other passive structural materials. This information is necessary for fabricating Galfenol-based magnetomechanical transducers which can work under bending loads.

Chapter 3 also discussed the challenges in designing a magnetic flux path for a magnetostrictive device operating in bending. A four-point bending test was proposed, designed and performed on a Galfenol beam under different bias applied magnetic fields. The results showed that a Galfenol member can be used as a sensor in bending but a critical bias magnetic field is required for operation of such a sensor. Moreover, the net sensing response is due to the compressive stresses in the Galfenol member rather than the tensile stresses. These results were qualitatively explained using the balance of magnetocrystalline anisotropy energy, Zeeman energy and stress-induced anisotropy energy in the material. The results from Chapter 3 determined the sensing response of only a Galfenol member as opposed to the Galfenol being attached to a passive structural material which was described in Chapter 4.

Chapter 4 discussed the concept of laminated magnetostrictive composites using Galfenol and other passive structural materials. Extensive finite element and analytical simulations were performed to design experiments which were conducted on cantilevered Galfenol-Aluminum unimorph actuators and sensors. The experiments studied the effect of three parameters; applied magnetic field, tip loading and Aluminum layer thickness. The experimental results demonstrated non-linearity in the magnetomechanical response of the structure and also exhibited structural coupling between the extensional and bending modes of the structure. In order to investigate these observations and perform a wider range of parametric study, an appropriate coupled modeling technique was developed in Chapter 5. Besides performing a parametric study on Galfenol-Aluminum unimorphs, a number of useful evaluation criteria for sensors were defined and calculated in Chapter 4. These sensing criteria could be used in future work for comparing the sensing performance of magnetostrictive unimorphs.

Chapter 5 described a generalized recursive modeling algorithm which can be applied to any smart material device by appropriate choice of component models. Unlike previous models which assume stress and magnetic field as fundamental independent inputs in magnetostrictive models, this approach assumes a mechanical force and a magnetizing source as the fundamental inputs. It was discussed how stress and magnetic field can affect each other in a magnetostrictive device which motivated the use of a recursive approach. A magnetomechanical plate model (MMPM) was developed based on this approach.

The MMPM simulations were compared to existing modeling techniques to emphasize on the importance of the algorithm described in Chapter 5. The MMPM was used to perform simulations over a wide range of variation in magnetic field, axial mechanical forces and bending moments and active/passive layer thickness ratio. These simulation results were helpful in determining certain optimal configurations and conditions for Galfenol-based unimorph actuators and sensors. Finally, the MMPM simulations were compared with the experimental results from Chapter 4.

The work in this dissertation was focused on experimental study and modeling of quasi-static behavior of single crystal Galfenol in order to spend more effort in understanding the physics of the problem, setting up standard experimental techniques and providing baseline results. This work can be extended to polycrystalline Galfenol alloys and can be implemented in dynamic settings. However, additional experimental challenges related to eddy currents and hysteresis will have to be addressed using careful magnetic circuit design, transducer structural design and processing of active materials.

## 6.2. *Contributions of this research*

The original contributions of this dissertation are stated below.

- Magnetomechanical transducer figures of merit were experimentally evaluated for a particular composition of single crystal Galfenol ( $\text{Fe}_{84}\text{Ga}_{16}$ ). The effect of stress and magnetic field on these figures of merit was also shown.

- A non-linear energy-based magnetostrictive constitutive model was used to predict these figures of merit not only as a function of stress and magnetic field but also as a function of composition of Galfenol. The model can be used to obtain the figures of merit at any desired operating condition without performing experiments at those precise conditions. This database of figures of merit is expected to aid in the design of adaptive transducers. This database can be used for choosing appropriate Galfenol composition, operating range and bias conditions.
- Statistical methods were developed and used to quantify error estimates between experimental and model simulation values of figures of merit. The error estimates are useful for providing a bound on the deviation in performance of a device based on simulated figures of merit compared to using experimental values for device design.
- Experimental values of Young's modulus at constant induction and relative permeability at constant strain were calculated for single crystal Galfenol. The effect of magnetic induction and stress on the modulus and the effect of magnetic field and strain on the permeability values were shown using experimental data. This is the first published values of these material properties.
- A classical four-point bending test concept was extended for bending characterization in the presence of magnetic field to measure the sensing performance of Galfenol beams under bending loads and at different bias applied magnetic fields. This method ensured that the location and size of the

device measuring the magnetic induction changes in Galfenol beam does not influence the evaluation of sensing performance thereby providing an experimentally consistent technique.

- Experimental studies were designed and performed on cantilevered Galfenol-Aluminum unimorph beams. The actuation performance of these beams was quantified by the normalized out-of-plane tip displacement calculated from the strains measured from the surface of Galfenol and Aluminum layers. The sensor performance was quantified using several parameters which were defined. This study focused on the effect of magnetic field, bending loads and Aluminum layer thickness on the actuator and sensor performance of the unimorphs and provided information on optimizing the configuration and operating condition for Galfenol-based unimorph actuators and sensors.
- A magnetomechanical plate model was developed to predict actuator and sensor behavior of magnetostrictive laminated composites. The model simulations were used to perform a wider range of parametric studies. The model predictions were also compared with the results from the experimental studies on Galfenol-Aluminum unimorphs. It was demonstrated that the model can not only capture the non-linear magnetostrictive behavior but also the structural couplings in a magnetostrictive laminated composite and can estimate the internal magnetic field in Galfenol under the influence of any applied magnetic field and mechanical forces and moments.

### 6.3. Recommendations and future work

This section will make certain recommendations and suggest future work on Galfenol devices based on the understanding and experience gained through the course of working on this dissertation research.

Although single crystal alloys exhibit superior magnetomechanical properties, it is desirable to use processed polycrystalline alloys for future commercial applications. That would require the knowledge of figures of merit of those specifically processed materials. The figures of merit described in Chapter 2 for single crystal Galfenol alloys could serve as an upper bound but the same experimental procedures may be used for getting accurate information on figures of merit of processed polycrystalline materials. Such a database does not exist at this point of time. A database of stress and magnetic field-dependent figures of merit for not only single crystals but also processed polycrystalline Galfenol would be extremely useful for transducer designers.

The results from Chapter 2 showed that there can be significant error between the energy-based magnetostrictive model and experimental data if a constant ( $\Omega$ ) is used as a fitting parameter in the model for all operating conditions. Such error can contribute to higher errors in other modeling approaches which use the energy-based constitutive model such as the one discussed in Chapter 5. This issue has not been addressed by any work that has used similar energy-based models. Since it was explained in Chapter 2 that  $\Omega$  is merely a statistical fitting parameter, there is no reason why it should be assumed to be a constant. Therefore, a multivariate regression analysis should be performed to evaluate  $\Omega$  as a function of stress and

magnetic field and henceforth a variable  $\Omega$  should be used to provide more accurate values of magnetostriction and magnetic induction at different operating stresses and magnetic fields.

Although sufficient work exists on quasi-static magnetomechanical transduction characterization of single crystal and polycrystalline Galfenol alloys, no published work exist on dynamic characterization of Galfenol. Since it is expected that most real-life applications using Galfenol would be of dynamic nature, it is extremely important to focus on dynamic characterization of Galfenol. Dynamic characterization may involve its own challenges such as eddy current losses, skin-effect, inductive losses in drive coil and structural design of a transducer with appropriate inertial effects. Dynamic characterization results are expected to exhibit the variation in magnetomechanical properties as a function of drive frequency and will also reveal whether Galfenol could be a useful magnetostrictive transducer in dynamic conditions inspite of possessing a higher permeability under most operating conditions than rare-earth based magnetostrictive materials. Such dynamic experimental data will also be useful for validating dynamic models.

Similarly, there is a need to develop a dynamic non-linear magnetostrictive constitutive model. The current form of the energy-based model and its variants are not suitable for predicting the dynamic behavior of the material as there are no strain rate or magnetization rate terms in the energy kernel used in the models. As of now, the only approach for dynamic modeling is using the micromagnetic LLG equation [160, 164] which is accurate but computationally intensive. Hence it would be beneficial to attempt a modification of the energy-based model shown here by adding

strain rate and magnetization rate and possibly internal damping in the energy kernel so that magnetization and magnetostriction can be predicted as a function of not only stress and magnetic field but also their frequencies.

The four-point bending test under magnetic field described in Chapter 3 could serve as a standardized test for sensor characterization of any magnetostrictive material under bending. It would be easier to perform the tests using a longer sample as prescribed in ASTM C1161 [176], than the one used in this work. Also, a better magnetic flux path may be designed by introducing several thin chips of high permeability Metglas to fill the small air gap between the electromagnet poles and the sample.

Further experiments based on the ones shown in Chapter 4 may be conducted with processed polycrystalline Galfenol to evaluate the performance of specific materials as unimorph actuators and sensors. A laser-based technique may be used to directly measure the tip displacement of cantilevers instead of using the measured strain values to indirectly calculate the displacement using beam theory assumptions. However since the area around Galfenol will always be covered by a solenoid in such experiments, resistive strain gages might still be the best method for measuring strains.

Other lay-ups using different combinations of active/passive layers may be used in such unimorphs. Note that a bimorph configuration might end up producing a pure extension if the extension-bending coupling is reduced to zero through appropriate choice and thickness of materials. In particular, it would be interesting to find the response of an active laminated composite with one layer having positive

magnetostriction (e.g. Galfenol) and the other layer having negative magnetostriction (e.g. Nickel). Another interesting combination such as Galfenol/PZT [191] might lead to the formation of magnetoelectric laminated composite. Other such interesting lay-ups can also be considered by depositing thin films for application in magnetostrictive MEMS devices. It should be noted that for all these cases, the most important design parameter would be the aspect ratio which controls the shape anisotropy and demagnetization factor.

The unimorph sensor characterization shown in Chapter 4 could be modified to develop a standard measurement technique such that magnetic induction changes measured from different unimorphs can be directly compared. Also, to further investigate the sensor response of unimorphs at higher bias fields (close to or beyond saturation), the sensor characterization could be performed with Hall-effect sensors having higher ranges. However, such Hall-effect sensors would also have poor resolution that will affect the linearity and accuracy of the results.

Further work needs to be done on the model presented in Chapter 5 to extend its capabilities firstly to 3D quasi-static scenario and finally to 3D dynamic scenarios. A finite element approach could be used to replace the CLPT and lumped parameter magnetic model but that would also involve extreme computational challenge to solve the energy-based constitutive model recursively coupled with a finite element model having three components of the magnetic field vector and 6 components of the stress tensor at each node. Recent works by Mudivarthi *et al.* [166] and Graham *et al.* [192] have shown significant advantages of using finite element structural and magnetic

models in this modeling framework. However it has not been possible yet to account for the effect of all components of magnetic field and stress using a 3D model.

As Galfenol exhibits very low hysteresis, the anhysteretic version of Armstrong's [153] model was used in Chapter 5. For other materials that exhibit significant hysteresis, energy-based hysteretic models developed by Armstrong [154], Atulasimha [157] or Evans [193] can be used to replace the anhysteretic model shown here.

Finally, it should be clearly stated that this model is valid in the regime of continuum mechanics. Although this model can be used for prediction involving extremely small thickness ratio, the actual thickness effects might not be negligible at very small length scales where surface tension and other forces play significant role in controlling the structural deformations. Therefore, to model magnetostrictive MEMS or nano-scale devices, the component models should be replaced with more appropriate ones while keeping the same framework and recursive algorithm.

## References

- [1] I. Chopra, "Review of State of Art of Smart Structures and Integrated Systems" *AIAA Journal*, vol. 40, pp. 2145-2187, 2002.
- [2] R. C. Smith, *Smart Material Systems: Model Development*. Philadelphia: SIAM, 2005.
- [3] J. N. Kudva, "Overview of the DARPA Smart Wing Project," *Journal of Intelligent Material Systems and Structures*, vol. 15, pp. 261-267, 2004.
- [4] B. Sanders, R. Crowe, and E. Garcia, "Defense Advanced Research Projects Agency - Smart Materials and Structures Demonstration Program Overview," *Journal of Intelligent Material Systems and Structures*, vol. 15, pp. 227-233, 2004.
- [5] K. Wakha, M. A. Majed, A. Dasgupta, and D. J. Pines, "Multifunctional piezoelectric stiffness/energy for monitoring the health of structures," in *Smart Structures and Integrated Systems*, San Diego, CA, 2003, Proc. of SPIE, Vol. 5056, pp. 60-72.
- [6] K. Wakha, P. Samuel, and D. J. Pines, "A smart composite patch for the repair of aircraft structures," in *Nondestructive Evaluation and Health Monitoring of Aerospace Materials, Composites, and Civil Infrastructure IV*, San Diego, CA, 2005, Proc. of SPIE, Vol. 5767, pp. 344-355.
- [7] J.-S. Bae, N.-H. Kyong, T. M. Seigler, and D. J. Inman, "Aeroelastic Considerations on Shape Control of an Adaptive Wing," *Journal of Intelligent Material Systems and Structures*, vol. 16, pp. 1051-1056, 2005.

- [8] F. Austin, W. C. V. Nostrand, and M. J. Rossi, "Shape control of structures with semi-definite stiffness matrices for adaptive wings," in *Smart Structures and Materials 1993: Smart Structures and Intelligent Systems*, Albuquerque, NM, 1993, Proc. of SPIE, Vol. 1917, pp. 419-425.
- [9] F. Austin and W. C. V. Nostrand, "Shape control of an adaptive wing for transonic drag reduction," in *Smart Structures and Materials 1995: Industrial and Commercial Applications of Smart Structures Technologies*, San Diego, CA, 1995, Proc. of SPIE, Vol. 2447, pp. 45-55.
- [10] S. Ugrina, "Experimental Analysis and Analytical Modeling of Synthetic Jet-Cross Flow Interactions," PhD dissertation, Aerospace Engineering, University of Maryland, College Park, MD, 2007.
- [11] S. John, "Development of a Magneto-Rheological Fluid Based Actuation System," PhD dissertation, Aerospace Engineering, University of Maryland, College Park, MD, 2007.
- [12] S. M. Peelamedu, G. Naganathan, and S. J. Buckley, "Impact analysis of automotive structures with distributed smart material systems," in *Smart Structures and Materials 1999: Mathematics and Control in Smart Structures*, 1999, Proc. of SPIE, Vol. 3667, pp. 813-824.
- [13] J. Shieh, J. E. Huber, N. A. Fleck, and M. F. Ashby, "The selection of sensors," *Progress in Materials Science*, vol. 46, pp. 461-504, 2001.
- [14] N. G. Elvin, A. A. Elvin, and M. Spector, "A self-powered mechanical strain energy sensor," *Smart Materials and Structures*, vol. 10, pp. 293-299, 2001.

- [15] E. Häslér, L. Stein, and G. Harbauer, "Implantable physiological power supply with PVDF film," *Ferroelectrics*, vol. 60, pp. 277 - 282, 1984.
- [16] K. Uchino, Y. Tsuchiya, S. Nomura, T. Sato, H. Ishikawa, and O. Ikeda, "Deformable mirror using the PMN electrostrictor," *Applied Optics*, vol. 20, pp. 3077-3080, 1981.
- [17] A. Chaudhuri, "Self-contained Hybrid Electro-hydraulic Actuators Using Magnetostrictive and Electrostrictive Materials," PhD dissertation, Aerospace Engineering, University of Maryland, College Park, MD, 2008.
- [18] F. E. Scoppe, "Magnetostrictive torque transducer," *Instrumentation Technology*, vol. 16, pp. 95-99, 1969.
- [19] K. Harada, I. Sasada, T. Kawajiri, and M. Inoue, "A new torque transducer using stress sensitive amorphous ribbons," *Magnetics, IEEE Transactions on*, vol. 18, pp. 1767-1769, 1982.
- [20] I. J. Garshelis and C. R. Conto, "A magnetoelastic torque transducer utilizing a ring divided into two oppositely polarized circumferential regions," *Journal of Applied Physics*, vol. 79, pp. 4756-4758, 1996.
- [21] S. Bitar, J. S. Probst, and I. J. Garshelis, "Development of a Magnetoelastic Torque Sensor for Formula 1 and CHAMP Car Racing Applications " in *Sensors and Actuators 2000*: SAE, 2000.
- [22] H. Wakiwaka and M. Mitamura, "New magnetostrictive type torque sensor for steering shaft," *Sensors and Actuators A: Physical*, vol. 91, pp. 103-106, 2001.

- [23] I. Giouroudi, C. Orfanidou, and E. Hristoforou, "Circumferentially oriented Ni cylindrical thin films for torque sensor applications," *Sensors and Actuators A: Physical*, vol. 106, pp. 179-182, 2003.
- [24] J. Mora, A. Diez, J. L. Cruz, and M. V. Andres, "A magnetostrictive sensor interrogated by fiber gratings for," *Photonics Technology Letters, IEEE*, vol. 12, pp. 1680-1682, 2000.
- [25] H. T. Savage and M. L. Spano, "Theory and application of highly magnetoelastic Metglas 2605SC (invited)," *Journal of Applied Physics*, vol. 53, pp. 8092-8097, 1982.
- [26] F. Seco, J. M. Martín, A. R. Jiménez, and L. Calderón, "A high accuracy magnetostrictive linear position sensor," *Sensors and Actuators A: Physical*, vol. 123-124, pp. 216-223, 2005.
- [27] J. Kosel, H. Pfützner, L. Mehnen, E. Kaniusas, T. Meydan, M. Vázquez, M. Rohn, A. M. Merlo, and B. Marquardt, "Non-contact detection of magnetoelastic bilayer position sensors," *Sensors and Actuators A: Physical*, vol. 123-124, pp. 349-353, 2005.
- [28] D. K. Kleinke and H. M. Uras, "A noncontacting magnetostrictive strain sensor," *Review of Scientific Instruments*, vol. 64, pp. 2361-2367, 1993.
- [29] A. Ludwig, M. Tewes, S. Glasmachers, M. Lohndorf, and E. Quandt, "High-frequency magnetoelastic materials for remote-interrogated stress sensors," *Journal of Magnetism and Magnetic Materials*, vol. 242-245, pp. 1126-1131, 2002.

- [30] J. L. Butler, S. C. Butler, and A. E. Clark, "Unidirectional magnetostrictive/piezoelectric hybrid transducer," *The Journal of the Acoustical Society of America*, vol. 88, pp. 7-11, 1990.
- [31] J. L. Butler, A. L. Butler, and S. C. Butler, "Hybrid magnetostrictive/piezoelectric Tonpilz transducer," *The Journal of the Acoustical Society of America*, vol. 94, pp. 636-641, 1993.
- [32] J. E. Miesner and J. P. Teter, "Piezoelectric/magnetostrictive resonant inchworm motor," in *Smart Structures and Intelligent Systems*, Orlando, FL, 1994, Proc. of SPIE, Vol. 2190, pp. 520-527.
- [33] C. A. Teolis and J. Loncaric, "A Rotary Magnetostrictive Motor for Robotics," University of Maryland, College Park, Technical Report 1993.
- [34] M. Anjanappa and Y. Wu, "Magnetostrictive particulate actuators: configuration, modeling and characterization," *Smart Materials and Structures*, vol. 6, pp. 393-402, 1997.
- [35] H. Oduncu and T. Meydan, "A novel method of monitoring biomechanical movements using the magnetoelastic effect," *Journal of Magnetism and Magnetic Materials*, vol. 160, pp. 233-236, 1996.
- [36] F. Claeysen, N. Lhermet, R. Le Letty, and P. Bouchilloux, "Actuators, transducers and motors based on giant magnetostrictive materials," *Journal of Alloys and Compounds*, vol. 258, pp. 61-73, 1997.
- [37] R. Guntupalli, J. Hu, R. S. Lakshmanan, T. S. Huang, J. M. Barbaree, and B. A. Chin, "A magnetoelastic resonance biosensor immobilized with polyclonal

antibody for the detection of Salmonella typhimurium," *Biosensors and Bioelectronics*, vol. 22, pp. 1474-1479, 2007.

[38] M. R. J. Gibbs, "Applications of magnemems," *Journal of Magnetism and Magnetic Materials*, vol. 290-291, pp. 1298-1303, 2005.

[39] F. Austin, M. J. Siclari, M. Kesselman, and G. N. Weisensel, "Smart TERFENOL-D-powered trailing-edge experiment," in *Industrial and Commercial Applications of Smart Structures Technologies*, San Diego, CA, 1998, Proc. of SPIE, Vol. 3326, pp. 282-293.

[40] F. T. Calkins, A. B. Flatau, and M. J. Dapino, "Overview of Magnetostrictive Sensor Technology," *Journal of Intelligent Material Systems and Structures*, vol. 18, pp. 1057-1066, October 1, 2007 2007.

[41] H. Kwun and K. A. Bartels, "Magnetostrictive sensor technology and its applications," *Ultrasonics*, vol. 36, pp. 171-178, 1998.

[42] A. Hernando, M. Vazquez, and J. M. Barandiaran, "Metallic glasses and sensing applications," *Journal of Physics E: Scientific Instruments*, vol. 21, pp. 1129-1139, 1988.

[43] ETREMA Products, "Terfenol-D data sheet," 2009. <http://www.etrema-usa.com/documents/Terfenol.pdf>

[44] R. A. Kellogg, "Development and modeling of iron-gallium alloys," PhD dissertation, Engineering Mechanics, Iowa State University, Ames, IA, 2003.

[45] J. Atulasimha, "Characterization and Modeling of the Magnetomechanical Behavior of Iron-Gallium Alloys," PhD dissertation, Aerospace Engineering, University of Maryland, College Park, MD, 2006.

- [46] Boedeker Plastics, "Kynar® PVDF (PolyVinylidene Fluoride) Specifications," 2009. [http://www.boedeker.com/pvdf\\_p.htm](http://www.boedeker.com/pvdf_p.htm)
- [47] Electrochemistry Encyclopedia, "ELECTROACTIVE POLYMERS (EAP)," 2009. <http://electrochem.cwru.edu/ed/encycl/art-p02-elact-pol.htm>
- [48] S.-E. E. Park and W. Hackenberger, "High performance single crystal piezoelectrics: applications and issues," *Current Opinion in Solid State and Materials Science*, vol. 6, pp. 11-18, 2002.
- [49] H. C. Materials Corporation, "Properties of Piezoelectric PMN-PT Crystal," 2009. [http://www.hcmat.com/Pmn\\_Properties.html](http://www.hcmat.com/Pmn_Properties.html)
- [50] L. M. Ewart, E. A. McLaughlin, H. C. Robinson, A. Amin, and J. J. Stace, "Mechanical and Electromechanical Properties of PMN-PT Single Crystals for Naval Sonar Transducers," in *Applications of Ferroelectrics, 2007. ISAF 2007. Sixteenth IEEE International Symposium on*, 2007, pp. 553-556.
- [51] MachineDesign.com, "Precision Moves With Magnetostriction." vol. 2009, 2009. <http://machinedesign.com/article/precision-moves-with-magnetostriction-1118>
- [52] TiNi Alloy Company, "Introduction to Shape Memory Alloys," 2009. <http://www.tinialloy.com/pdf/introductiontosma.pdf>
- [53] "ASTM A 340 – 03a: Standard Terminology of Symbols and Definitions Relating to Magnetic Testing," 2003.
- [54] M. Nelkon and P. Parker, *Advanced Level Physics*, 7<sup>th</sup> ed. New Delhi: CBS Publishers and Distributors, 1995.
- [55] D. J. Griffiths, *Introduction to Electrodynamics*, 2<sup>nd</sup> ed. New Jersey: Prentice-Hall Inc., 1989.

- [56] E. Warburg, "Magnetische Untersuchungen," *Annalen der Physik*, vol. 249, pp. 141-164, 1881.
- [57] J. A. Ewing, *Magnetic Induction in Iron and other Metals*, 3<sup>rd</sup> ed. London: The Electrician series, 1900.
- [58] S. Chikazumi, *Physics of Ferromagnetism*. New York: Oxford University Press Inc., 1997.
- [59] R. M. Bozorth, *Ferromagnetism*. Princeton: D. Van Nostrand Company Inc., 1951.
- [60] A. Aharoni, "Demagnetizing factors for rectangular ferromagnetic prisms," *Journal of Applied Physics*, vol. 83, pp. 3432-3434, 1998.
- [61] ALAG3, "FluxGate vs. FluxSet Magnetometers," 2009.  
<http://alag3.mfa.kfki.hu/magnet/fluxset/gate2set.htm>
- [62] M. Beleggia and M. De Graef, "On the computation of the demagnetization tensor field for an arbitrary particle shape using a Fourier space approach," *Journal of Magnetism and Magnetic Materials*, vol. 263, pp. L1-L9, 2003.
- [63] D. C. Jiles, *Introduction to Magnetism and Magnetic Materials*, 2<sup>nd</sup> ed. London: CRC Press, 1998.
- [64] W. D. Callister, *Materials Science and Engineering : An Introduction*, 6<sup>th</sup> ed.: John Wiley & Sons, Inc., 2003.
- [65] R. A. Serway and R. J. Beichner, *Physics for Scientist and Engineers* 5<sup>th</sup> ed. vol. 2. Florence, KY: Thomson Learning, 2003.
- [66] R. C. O'Handley, *Modern Magnetic Materials: Principles and Applications*. New York: John Wiley & Sons Inc. , 2000.

- [67] P. Langevin, "Magnetisme et Theorie des Electrons," *Annales de Chimie et de Physique*, vol. 5, pp. 70-127, 1905.
- [68] P.-E. Weiss, "L'hypothèse du champ moléculaire et la propriété ferromagnetique," *Journal of Physics*, vol. 6, pp. 661-690, 1907.
- [69] F. Bitter, "On Inhomogeneities in the Magnetization of Ferromagnetic Materials," *Physical Review*, vol. 38, pp. 1903-1905, 1931.
- [70] L. Landau and E. Lifshitz, "On the theory of the dispersion of magnetic permeability in ferromagnetic bodies," *Physikalische Zeitschrift der Sowjetunion*, vol. 8, pp. 153-169, 1935.
- [71] F. Bloch, "Zur Theorie des Austauschproblems und der Remanenzerscheinung der Ferromagnetika," *Zeitschrift für Physik*, vol. 74, pp. 295-335, 1932.
- [72] L. Néel, "Les lois de l'aimantation et de la subdivision en domaines élémentaires d'un monocristal de fer," *Journal de Physique et le Radium*, vol. 5, pp. 241-251, 1944.
- [73] W. Heisenberg, "Zur Theorie des Ferromagnetismus," *Zeitschrift für Physik*, vol. 49, pp. 619-636, 1928.
- [74] H. Brooks, "Ferromagnetic Anisotropy and the Itinerant Electron Model," *Physical Review*, vol. 58, pp. 909-918, 1940.
- [75] K. Honda and S. Kaya, "On the magnetization of single crystals of iron," *Scientific Reports of Tohoku Imperial University*, vol. 15, pp. 721-753, 1926.
- [76] J. P. Joule, "On a new class of magnetic forces," *Ann. Electr. Magn. Chem.*, vol. 8, pp. 219-224, 1842.

- [77] E. Villari, "Change of Magnetization by tension and by electric current," *Ann. Phys. Chem.*, vol. 126, pp. 87-122, 1865.
- [78] G. Wiedemann, "Über die Torsion und die Beziehung derselben zum Magnetismus," *Pogg. Ann.*, vol. 106, pp. 161-201, 1860.
- [79] W. F. Barrett, "On the Alterations in the Dimensions of the Magnetic Metals by the Act of Magnetisation " *Nature*, vol. 26, pp. 585-586, 1882.
- [80] E. du Trémolet de Lacheisserie, *Magnetostriction – Theory and Applications of Magnetoelasticity*. Boca Raton: CRC Press, 1993.
- [81] G. Engdahl, *Handbook of Giant Magnetostrictive Materials*. San Diego: Academic Press, 2000.
- [82] B. D. Cullity, *Introduction to Magnetic Materials*. Reading, MA: Addison-Wesley, 1972.
- [83] E. W. Lee, "Magnetostriction and Magnetomechanical Effects," *Reports on Progress in Physics*, vol. 18, pp. 184-229, 1955.
- [84] A. E. Clark, J. B. Restorff, M. Wun-Fogle, T. A. Lograsso, and D. L. Schlagel, "Magnetostrictive properties of body-centered cubic Fe-Ga and Fe-Ga-Al alloys," *Magnetics, IEEE Transactions on*, vol. 36, pp. 3238-3240, 2000.
- [85] S. Guruswamy, N. Srisukhumbowornchai, A. E. Clark, J. B. Restorff, and M. Wun-Fogle, "Strong, ductile, and low-field-magnetostrictive alloys based on Fe-Ga," *Scripta Materialia*, vol. 43, pp. 239-244, 2000.
- [86] O. Kubaschewski, *Iron - Binary Phase Diagrams*. New York: Springer-Verlag Berlin Heidelberg, 1982.

- [87] N. Kawamiya, K. Adachi, and Y. Nakamura, "Magnetic Properties and Mössbauer Investigations of Fe-Ga Alloys " *Journal of the Physical Society of Japan*, vol. 33, pp. 1318-1327, 1972.
- [88] C. Dasarathy and W. Hume-Rothery, "The System Iron-Gallium," *Proceedings of the Royal Society of London. Series A, Mathematical and Physical Sciences*, vol. 286, pp. 141-157, 1965.
- [89] W. Köster and T. Gödecke, "Über den Aufbau des Systems Eisen-Gallium zwischen 10 und 50 At.-% Ga und dessen Abhängigkeit von der Wärmebehandlung: I. Das Diagramm der raumzentrierten Phasen," *Zeitschrift für Metallkunde*, vol. 68, pp. 582-589, 1977.
- [90] W. Köster and T. Gödecke, "Über den Aufbau des Systems Eisen-Gallium zwischen 10 und 50 At.-% Ga und dessen Abhängigkeit von der Wärmebehandlung: II. Des Gleichgewichtsdiagramm," *Zeitschrift für Metallkunde*, vol. 68, pp. 661-666, 1977.
- [91] W. Köster and T. Gödecke, "Über den Aufbau des Systems Eisen-Gallium zwischen 10 und 50 At.-% Ga und dessen Abhängigkeit von der Wärmebehandlung: III. Ein Unterkühlungsdiagramm und Diagramme für die Vorgänge beim Anlassen ofengekühlter und abgeschreckter Legierungen," *Zeitschrift für Metallkunde*, vol. 68, pp. 758-765, 1977.
- [92] O. Ikeda, R. Kainuma, I. Ohnuma, K. Fukamichi, and K. Ishida, "Phase equilibria and stability of ordered b.c.c. phases in the Fe-rich portion of the Fe-Ga system," *Journal of Alloys and Compounds*, vol. 347, pp. 198-205, 2002.

- [93] T. A. Lograsso, A. R. Ross, D. L. Schlagel, A. E. Clark, and M. Wun-Fogle, "Structural transformations in quenched Fe-Ga alloys," *Journal of Alloys and Compounds*, vol. 350, pp. 95-101, 2003.
- [94] D. Viehland, J. F. Li, T. A. Lograsso, A. Ross, and M. Wuttig, "Structural studies of Fe<sub>0.81</sub>Ga<sub>0.19</sub> by reciprocal space mapping," *Applied Physics Letters*, vol. 81, pp. 3185-3187, 2002.
- [95] Q. Xing, Y. Du, R. J. McQueeney, and T. A. Lograsso, "Structural investigations of Fe-Ga alloys: Phase relations and magnetostrictive behavior," *Acta Materialia*, vol. 56, pp. 4536-4546, 2008.
- [96] R. C. Hall, "Single Crystal Anisotropy and Magnetostriction Constants of Several Ferromagnetic Materials Including Alloys of NiFe, SiFe, AlFe, CoNi, and CoFe," *Journal of Applied Physics*, vol. 30, pp. 816-819, 1959.
- [97] A. E. Clark, K. B. Hathaway, M. Wun-Fogle, J. B. Restorff, T. A. Lograsso, V. M. Keppens, G. Petculescu, and R. A. Taylor, "Extraordinary magnetoelasticity and lattice softening in bcc Fe-Ga alloys," *Journal of Applied Physics*, vol. 93, pp. 8621-8623, 2003.
- [98] J. Cullen, P. Zhao, and M. Wuttig, "Anisotropy of crystalline ferromagnets with defects," *Journal of Applied Physics*, vol. 101, p. 123922, 2007.
- [99] R. Wu, "Origin of large magnetostriction in FeGa alloys," *Journal of Applied Physics*, vol. 91, pp. 7358-7360, 2002.
- [100] M. P. Ruffoni, S. Pascarelli, R. Grossinger, R. S. Turtelli, C. Bormio-Nunes, and R. F. Pettifer, "Direct Measurement of Intrinsic Atomic Scale Magnetostriction," *Physical Review Letters*, vol. 101, p. 147202, 2008.

- [101] C. Mudivarthi, *Personal Communication*, 2009.
- [102] A. G. Khachaturyan and D. Viehland, "Structurally Heterogeneous Model of Extrinsic Magnetostriction for Fe-Ga and Similar Magnetic Alloys: Part I. Decomposition and Confined Displacive Transformation," *Metallurgical and Materials Transactions A*, vol. 38, pp. 2308-2316, 2007.
- [103] A. G. Khachaturyan and D. Viehland, "Structurally Heterogeneous Model of Extrinsic Magnetostriction for Fe-Ga and Similar Magnetic Alloys: Part II. Giant Magnetostriction and Elastic Softening," *Metallurgical and Materials Transactions A*, vol. 38, pp. 2317-2328, 2007.
- [104] A. E. Clark, M. Wun-Fogle, J. B. Restorff, T. A. Lograsso, and J. R. Cullen, "Effect of quenching on the magnetostriction on  $\text{Fe}_{1-x}\text{Ga}_x$  ( $0.13 < x < 0.21$ )," *Magnetics, IEEE Transactions on*, vol. 37, pp. 2678-2680, 2001.
- [105] S. Datta, M. Huang, J. Raim, T. A. Lograsso, and A. B. Flatau, "Effect of thermal history and gallium content on magneto-mechanical properties of iron gallium alloys," *Materials Science and Engineering: A*, vol. 435-436, pp. 221-227, 2006.
- [106] R. A. Kellogg, A. B. Flatau, A. E. Clark, M. Wun-Fogle, and T. A. Lograsso, "Temperature and stress dependencies of the magnetic and magnetostrictive properties of  $\text{Fe}_{0.81}\text{Ga}_{0.19}$ ," *Journal of Applied Physics*, vol. 91, pp. 7821-7823, 2002.
- [107] R. A. Kellogg, A. Flatau, A. E. Clark, M. Wun-Fogle, and T. Lograsso, "Quasi-static Transduction Characterization of Galfenol," *Journal of Intelligent Material Systems and Structures*, vol. 16, pp. 471-479, 2005.

- [108] J. Atulasimha and A. B. Flatau, "Experimental Actuation and Sensing Behavior of Single-crystal Iron-Gallium Alloys," *Journal of Intelligent Material Systems and Structures*, vol. 19, pp. 1371-1381, 2008.
- [109] N. Srisukhumbowornchai and S. Guruswamy, "Influence of ordering on the magnetostriction of Fe--27.5 at. % Ga alloys," *Journal of Applied Physics*, vol. 92, pp. 5371-5379, 2002.
- [110] E. M. Summers, T. A. Lograsso, J. D. Snodgrass, and J. C. Slaughter, "Magnetic and mechanical properties of polycrystalline Galfenol," in *Active Materials: Behavior and Mechanics*, San Diego, CA, 2004, Proc. of SPIE, Vol. 5387, pp. 448-459.
- [111] J. Atulasimha, A. B. Flatau, and E. Summers, "Characterization and energy-based model of the magnetomechanical behavior of polycrystalline iron-gallium alloys," *Smart Materials and Structures*, vol. 16, pp. 1265-1276, 2007.
- [112] J. Atulasimha, A. B. Flatau, and R. A. Kellogg, "Sensing Behavior of Varied Stoichiometry Single Crystal Fe-Ga," *Journal of Intelligent Material Systems and Structures*, vol. 17, pp. 97-105, 2006.
- [113] M. Wuttig, L. Dai, and J. Cullen, "Elasticity and magnetoelasticity of Fe--Ga solid solutions," *Journal of Applied Physics*, vol. 80, pp. 1135-1137, 2002.
- [114] G. Petculescu, K. B. Hathaway, T. A. Lograsso, M. Wun-Fogle, and A. E. Clark, "Magnetic field dependence of galfenol elastic properties," *Journal of Applied Physics*, vol. 97, p. 10M315, 2005.

- [115] R. A. Kellogg, A. M. Russell, T. A. Lograsso, A. B. Flatau, A. E. Clark, and M. Wun-Fogle, "Tensile properties of magnetostrictive iron-gallium alloys," *Acta Materialia*, vol. 52, pp. 5043-5050, 2004.
- [116] J.-H. Yoo and A. B. Flatau, "Measurement of field-dependence elastic modulus of iron--gallium alloy using tensile test," *Journal of Applied Physics*, vol. 97, p. 10M318, 2005.
- [117] H. M. Schurter and A. B. Flatau, "Elastic properties and auxetic behavior of Galfenol for a range of compositions," in *Behavior and Mechanics of Multifunctional and Composite Materials*, San Diego, CA, 2008, Proc. of SPIE, Vol. 6929, p. 69291U.
- [118] S. Rafique, J. R. Cullen, M. Wuttig, and J. Cui, "Magnetic anisotropy of FeGa alloys," *Journal of Applied Physics*, vol. 95, pp. 6939-6941, 2004.
- [119] J. M. Hill, R. J. McQueeney, R. Wu, K. Dennis, R. W. McCallum, M. Huang, and T. A. Lograsso, "Low temperature heat capacity of  $\text{Fe}_{1-x}\text{Ga}_x$  alloys with large magnetostriction," *Physical Review B*, vol. 77, p. 014430, 2008.
- [120] J. B. Restorff, M. Wun-Fogle, A. E. Clark, T. A. Lograsso, A. R. Ross, and D. L. Schlagel, "Magnetostriction of ternary Fe--Ga--X alloys (X = Ni,Mo,Sn,Al)," *Journal of Applied Physics*, vol. 91, pp. 8225-8227, 2002.
- [121] A. E. Clark, J. B. Restorff, M. Wun-Fogle, K. B. Hathaway, T. A. Lograsso, M. Huang, and E. Summers, "Magnetostriction of ternary Fe--Ga--X (X = C,V,Cr,Mn,Co,Rh) alloys," *Journal of Applied Physics*, vol. 101, p. 09C507, 2007.

- [122] E. Summers, T. Lograsso, and M. Wun-Fogle, "Magnetostriction of binary and ternary Fe–Ga alloys," *Journal of Materials Science*, vol. 42, pp. 9582-9594, 2007.
- [123] M. Huang, T. A. Lograsso, A. E. Clark, J. B. Restorff, and M. Wun-Fogle, "Effect of interstitial additions on magnetostriction in Fe–Ga alloys," *Journal of Applied Physics*, vol. 103, p. 07B314, 2008.
- [124] R. A. Kellogg, A. B. Flatau, A. E. Clark, M. Wun-Fogle, and T. A. Lograsso, "Texture and grain morphology dependencies of saturation magnetostriction in rolled polycrystalline Fe<sub>83</sub>Ga<sub>17</sub>," *Journal of Applied Physics*, vol. 93, pp. 8495-8497, 2003.
- [125] S.-M. Na and A. B. Flatau, "Secondary recrystallization, crystallographic texture and magnetostriction in rolled Fe–Ga based alloys," *Journal of Applied Physics*, vol. 101, p. 09N518, 2007.
- [126] S.-M. Na and A. B. Flatau, "Deformation behavior and magnetostriction of polycrystalline Fe–Ga–X (X = B,C,Mn,Mo,Nb,NbC) alloys," *Journal of Applied Physics*, vol. 103, p. 07D304, 2008.
- [127] M. Wun-Fogle, J. B. Restorff, A. E. Clark, D. Erin, and S. Eric, "Stress annealing of Fe–Ga transduction alloys for operation under tension and compression," *Journal of Applied Physics*, vol. 97, p. 10M301, 2005.
- [128] J. B. Restorff, M. Wun-Fogle, A. E. Clark, and K. B. Hathaway, "Induced Magnetic Anisotropy in Stress-Annealed Galfenol Alloys," *Magnetics, IEEE Transactions on*, vol. 42, pp. 3087-3089, 2006.

- [129] J. H. Yoo, J. B. Restorff, M. Wun-Fogle, and A. B. Flatau, "The effect of magnetic field annealing on single crystal iron gallium alloy," *Journal of Applied Physics*, vol. 103, p. 07B325, 2008.
- [130] J. L. Weston, A. Butera, T. Lograsso, M. Shamsuzzoha, I. Zana, G. Zangari, and J. Barnard, "Fabrication and characterization of Fe<sub>81</sub>Ga<sub>19</sub> thin films," *Magnetics, IEEE Transactions on*, vol. 38, pp. 2832-2834, 2002.
- [131] A. Butera, J. Gomez, J. L. Weston, and J. A. Barnard, "Growth and magnetic characterization of epitaxial Fe<sub>81</sub>Ga<sub>19</sub>/MgO (100) thin films," *Journal of Applied Physics*, vol. 98, p. 033901, 2005.
- [132] R. R. Basantkumar, B. J. H. Stadler, W. P. Robbins, and E. M. Summers, "Integration of Thin-Film Galfenol With MEMS Cantilevers for Magnetic Actuation," *Magnetics, IEEE Transactions on*, vol. 42, pp. 3102-3104, 2006.
- [133] J. R. Hattrick-Simpers, D. Hunter, C. M. Craciunescu, K. S. Jang, M. Murakami, J. Cullen, M. Wuttig, I. Takeuchi, S. E. Lofland, L. Benderksy, N. Woo, R. B. V. Dover, T. Takahashi, and Y. Furuya, "Combinatorial investigation of magnetostriction in Fe--Ga and Fe--Ga--Al," *Applied Physics Letters*, vol. 93, p. 102507, 2008.
- [134] P. D. McGary and B. J. H. Stadler, "Electrochemical deposition of Fe<sub>1-x</sub>Ga<sub>x</sub> nanowire arrays," *Journal of Applied Physics*, vol. 97, p. 10R503, 2005.
- [135] P. D. McGary, L. Tan, J. Zou, B. J. H. Stadler, P. R. Downey, and A. B. Flatau, "Magnetic nanowires for acoustic sensors (invited)," *Journal of Applied Physics*, vol. 99, p. 08B310, 2006.

- [136] J.-H. Yoo, U. Marschner, and A. B. Flatau, "Preliminary Galfenol vibratory gyro-sensor design," in *Smart Structures and Integrated Systems*, San Diego, CA, 2005, Proc. of SPIE, Vol. 5764, pp. 111-119.
- [137] P. R. Downey and A. B. Flatau, "Magnetoelastic bending of Galfenol for sensor applications," *Journal of Applied Physics*, vol. 97, p. 10R505, 2005.
- [138] P. R. Downey, A. B. Flatau, P. D. McGary, and B. J. H. Stadler, "Effect of magnetic field on the mechanical properties of magnetostrictive iron-gallium nanowires," *Journal of Applied Physics*, vol. 103, p. 07D305, 2008.
- [139] S. Datta and A. B. Flatau, "Magnetostrictive Vibration Sensor based on Iron-Gallium Alloy," in *Materials and Devices for Smart Systems II*, Boston, MA, 2005, Proc. of MRS, Vol. 888, p.V4.9.
- [140] K. Hale and A. Flatau, "Galfenol tactile sensor array and visual mapping system," in *Smart Structures and Integrated Systems*, San Diego, CA, 2006, Proc. of SPIE, Vol. 6173, p. 61730Y.
- [141] M. J. Parsons, S. Datta, C. Mudivarthi, S. M. Na, and A. Flatau, "Torque sensing using rolled galfenol patches," in *Smart Sensor Phenomena, Technology, Networks, and Systems*, San Diego, CA, 2008, Proc. of SPIE, Vol. 6933, p. 693314.
- [142] M. Ghodsi, T. Ueno, H. Teshima, H. Hirano, T. Higuchi, and E. Summers, "'Zero-power" positioning actuator for cryogenic environments by combining magnetostrictive bimetal and HTS," *Sensors and Actuators A: Physical*, vol. 135, pp. 787-791, 2007.

- [143] T. Ueno, C. S. Keat, and T. Higuchi, "Linear Step Motor Based on Magnetic Force Control Using Composite of Magnetostrictive and Piezoelectric Materials," *Magnetics, IEEE Transactions on*, vol. 43, pp. 11-14, 2007.
- [144] T. Ueno and T. Higuchi, "Miniature Magnetostrictive Linear Actuator Based On Smooth Impact Drive Mechanism," *International Journal of Applied Electromagnetics and Mechanics*, vol. 28, pp. 135-141, 2008.
- [145] T. Ueno and T. Higuchi, "Two-DOF Micro Magnetostrictive Bending Actuator for Wobbling Motion," *Magnetics, IEEE Transactions on*, vol. 44, pp. 4078-4080, 2008.
- [146] T. Ueno, T. Higuchi, C. Saito, N. Imaizumi, and M. Wun-Fogle, "Micromagnetostrictive vibrator using a U-shaped core of iron-gallium alloy (Galfenol)," *Journal of Applied Physics*, vol. 103, p. 07E904, 2008.
- [147] L. D. Landau and E. M. Lifshitz, *Electrodynamics of Continuous Media*. Oxford: Pergamon, 1960.
- [148] F. Falk, "Landau Theory and Martensitic Phase Transitions," *Le Journal de Physique Colloques*, vol. 43, pp. C4-3-C4-15, 1982.
- [149] A. Bergqvist and G. Engdahl, "A stress-dependent magnetic Preisach hysteresis model," *Magnetics, IEEE Transactions on*, vol. 27, pp. 4796-4798, 1991.
- [150] D. C. Jiles, "Theory of the magnetomechanical effect," *Journal of Physics D: Applied Physics*, vol. 28, pp. 1537-1546, 1995.
- [151] D. C. Jiles and L. Li, "A new approach to modeling the magnetomechanical effect," *Journal of Applied Physics*, vol. 95, pp. 7058-7060, 2004.

- [152] D. P. Ghosh and S. Gopalakrishnan, "Role of Coupling Terms in Constitutive Relationships of Magnetostrictive Materials," *Computers, Materials and Continua*, vol. 1, pp. 213-227, 2004.
- [153] W. D. Armstrong, "Magnetization and magnetostriction processes in  $\text{Tb}_{(0.27 - 0.30)}\text{Dy}_{(0.73 - 0.70)}\text{Fe}_{(1.9 - 2.0)}$ ," *Journal of Applied Physics*, vol. 81, pp. 2321-2326, 1997.
- [154] W. D. Armstrong, "A directional magnetization potential based model of magnetoelastic hysteresis," *Journal of Applied Physics*, vol. 91, pp. 2202-2210, 2002.
- [155] E. C. Stoner and E. P. Wohlfarth, "A Mechanism of Magnetic Hysteresis in Heterogeneous Alloys," *Philosophical Transactions of the Royal Society of London. Series A, Mathematical and Physical Sciences*, vol. 240, pp. 599-642, 1948.
- [156] J. Atulasimha, A. B. Flatau, and J. R. Cullen, "Analysis of the effect of gallium content on the magnetomechanical behavior of single-crystal FeGa alloys using an energy-based model," *Smart Materials and Structures*, vol. 7, p. 025027, 2008.
- [157] J. Atulasimha, G. Akhras, and A. B. Flatau, "Comprehensive three dimensional hysteretic magnetomechanical model and its validation with experimental  $\langle 110 \rangle$  single-crystal iron-gallium behavior," *Journal of Applied Physics*, vol. 103, p. 07B336, 2008.
- [158] R. C. Smith, M. J. Dapino, T. R. Braun, and A. P. Mortensen, "A homogenized energy framework for ferromagnetic hysteresis," *Magnetics, IEEE Transactions on*, vol. 42, pp. 1747-1769, 2006.

- [159] P. G. Evans and M. J. Dapino, "State-Space Constitutive Model for Magnetization and Magnetostriction of Galfenol Alloys," *Magnetics, IEEE Transactions on*, vol. 44, pp. 1711-1720, 2008.
- [160] W. F. Brown Jr., *Micromagnetics*: Interscience Publishers, 1963.
- [161] B. Zhu, C. C. H. Lo, S. J. Lee, and D. C. Jiles, "Micromagnetic modeling of the effects of stress on magnetic properties," *Journal of Applied Physics*, vol. 89, pp. 7009-7011, 2001.
- [162] H. Kronmüller and M. Fähnle, *Micromagnetism and the microstructure of ferromagnetic solids*: Cambridge University Press, 2003.
- [163] Y. C. Shu, M. P. Lin, and K. C. Wu, "Micromagnetic modeling of magnetostrictive materials under intrinsic stress," *Mechanics of Materials*, vol. 36, pp. 975-997, 2004.
- [164] J. X. Zhang and L. Q. Chen, "Phase-field microelasticity theory and micromagnetic simulations of domain structures in giant magnetostrictive materials," *Acta Materialia*, vol. 53, pp. 2845-2855, 2005.
- [165] R. Hu, A.-K. Soh, G.-P. Zheng, and Y. Ni, "Micromagnetic modeling studies on the effects of stress on magnetization reversal and dynamic hysteresis," *Journal of Magnetism and Magnetic Materials*, vol. 301, pp. 458-468, 2006.
- [166] C. Mudivarthi, S. Datta, J. Atulasimha, and A. B. Flatau, "A bidirectionally coupled magnetoelastic model and its validation using a Galfenol unimorph sensor," *Smart Materials and Structures*, vol. 17, p. 035005, 2008.

- [167] J. Atulasimha, A. B. Flatau, and J. R. Cullen, "Energy-based quasi-static modeling of the actuation and sensing behavior of single-crystal iron-gallium alloys," *Journal of Applied Physics*, vol. 103, p. 014901, 2008.
- [168] "Single crystal synthesized at the Materials Preparation Center, Ames Laboratory, USDOE. See [www.mpc.ameslab.gov](http://www.mpc.ameslab.gov)," 2008.
- [169] C. Kittel, "Physical Theory of Ferromagnetic Domains," *Reviews of Modern Physics*, vol. 21, p. 541, 1949.
- [170] C. Mudivarthi, S. Datta, J. Atulasimha, A. B. Flatau, P. G. Evans, and M. J. Dapino, "Equivalence of magnetoelastic, elastic, and mechanical work energies with stress-induced anisotropy," in *Behavior and Mechanics of Multifunctional and Composite Materials*, San Diego, CA, 2008, Proc. of SPIE, Vol. 6929, p. 69291X.
- [171] M. Wun-Fogle, J. B. Restorff, and A. E. Clark, "Magnetomechanical Coupling in Stress-Annealed Fe–Ga (Galfenol) Alloys," *Magnetics, IEEE Transactions on*, vol. 42, pp. 3120-3122, 2006.
- [172] M. Wun-Fogle, H. T. Savage, and M. L. Spano, "Enhancement of Magnetostrictive Effects for Sensor Applications," *Journal of Materials Engineering* vol. 11, pp. 103-107, 1989.
- [173] M. E. Staley and A. B. Flatau, "Characterization of energy harvesting potential of Terfenol-D and Galfenol," in *Smart Structures and Integrated Systems*, San Diego, CA, 2005, Proc. of SPIE, Vol. 5764, pp. 630-640.
- [174] D. Mauri, V. S. Speriosu, T. Yogi, G. Castillo, and D. T. Peterson, "Magnetoelastic properties of very thin Co-alloy films," *Magnetics, IEEE Transactions on*, vol. 26, pp. 1584-1586, 1990.

- [175] J. N. Reddy, *Energy and Variational Methods in Applied Mechanics*. New York: John Wiley and Sons, 1984.
- [176] ASTM, *Annual Book of ASTM Standards*: American Society for Testing and Materials, 2001.
- [177] J. E. Shigley and L. D. Mitchell, *Mechanical Engineering Design*, 4<sup>th</sup> ed. New York: McGraw-Hill Book Company, 1983.
- [178] T. Ueno and T. Higuchi, "Investigation of Micro Bending Actuator using Iron-Gallium Alloy (Galfenol)," in *Micro-NanoMechatronics and Human Science, International Symposium on MHS*, 2007, pp. 460-465.
- [179] L. Ristic, *Sensor Technology and Devices*. Norwood, MA: Artech House Publishers, 1994.
- [180] E. Klokholm, "The measurement of magnetostriction in ferromagnetic thin films," *Magnetics, IEEE Transactions on*, vol. 12, pp. 819-821, 1976.
- [181] E. du Trémolet de Lacheisserie and J. C. Peuzin, "Magnetostriction and internal stresses in thin films: the cantilever method revisited," *Journal of Magnetism and Magnetic Materials*, vol. 136, pp. 189-196, 1994.
- [182] E. Klokholm and C. V. Jahnes, "Comments on "Magnetostriction and internal stresses in thin films: the cantilever method revisited"," *Journal of Magnetism and Magnetic Materials*, vol. 152, pp. 226-230, 1996.
- [183] R. C. Wetherhold and H. D. Chopra, "Beam model for calculating magnetostriction strains in thin films and multilayers," *Applied Physics Letters*, vol. 79, pp. 3818-3820, 2001.

- [184] V. H. Guerrero and R. C. Wetherhold, "Magnetostrictive bending of cantilever beams and plates," *Journal of Applied Physics*, vol. 94, pp. 6659-6666, 2003.
- [185] M. Wun-Fogle, H. T. Savage, and A. E. Clark, "Sensitive, wide frequency range magnetostrictive strain gage," *Sensors and Actuators*, vol. 12, pp. 323-331, 1987.
- [186] D. P. Ghosh and S. Gopalakrishnan, "Coupled analysis of composite laminate with embedded magnetostrictive patches," *Smart Materials and Structures*, vol. 14, pp. 1462-1473, 2005.
- [187] L. P. Kollar and G. S. Springer, *Mechanics of Composite Structures*. Cambridge: Cambridge University Press, 2003.
- [188] K. Bhaskar and T. K. Varadan, "The Contradicting Assumptions of Zero Transverse Normal Stress and Strain in the Thin Plate Theory: A Justification," *Journal of Applied Mechanics*, vol. 68, pp. 660-662, 2001.
- [189] MEMSNET, "Material index," 2007. <http://www.memsnet.org/material>
- [190] P. Downey, "Characterization of Bending Magnetostriction in Iron-Gallium Alloys for Nanowire Sensor Applications," PhD dissertation, Aerospace Engineering, University of Maryland, College Park, 2008.
- [191] J. Atulasimha, G. Akhras, and A. B. Flatau, "A generalized energy model for the behavior of single-crystal magneto-electric composites," in *Behavior and Mechanics of Multifunctional and Composite Materials*, San Diego, CA, 2007, Proc. of SPIE, Vol. 6526, p. 65260V.
- [192] F. Graham, C. Mudivarthi, S. Datta, and A. B. Flatau, "Development and Validation of a Bidirectional Magneto-Mechanical Coupled Actuator Model," in *Ist*

*ASME Conference on Smart Materials, Adaptive Structures and Intelligent Systems*  
Ellicott City, MD, 2008.

[193] P. G. Evans and M. J. Dapino, "Fully-coupled model for the direct and inverse effects in cubic magnetostrictive materials," in *Behavior and Mechanics of Multifunctional and Composite Materials*, San Diego, CA, 2008, Proc. of SPIE, Vol. 6929, p. 692922.